Neutrino radiation hydrodynamics in hot and dense nuclear matter
and
the role of microphysics in simulations of massive stars

Inauguraldissertation

zur
Erlangung der Würde eines Doktors der Philosophie
vorgelegt der
philosophisch-naturwissenschaftlichen Fakultät
der Universität Basel
von

Tobias   Fischer

aus   Rötha   Sachsen (Deutschland)

Basel, 2010

Genehmigt von der philosophisch-naturwissenschaftlichen Fakultät

auf Antrag von

Prof. Dr. Friedrich-Karl Thielemann,
Prof. Dr. Matthias Liebendörfer,
Prof. Dr. Jürgen Schaffner-Bielich

Basel, den   15. September 2009

Prof. Dr. Eberhard Parlow

Dekanin/Dekan

Dedication

This dissertation is dedicated to my grand mother
Marie-Luise Pestner.

Preface

During my undergraduate studies in Leipzig and Stockholm, astrophysics was a subject of rare interest to me. It was most likely due to the lack of qualified tuition available at the University of Leipzig where I started my studies. I made the first contact with astrophysical processes and their description in a seminar program course at the Royal Institute of Technology in Stockholm where a student fellow of mine presented the subject of core collapse supernovae of massive stars on a very general basis. The subject immediately caught my interest, especially the complex underlying physical processes that are required to describe such a system. To name only a few, these are neutrinos, their transport and interactions, matter at extreme conditions, hydrodynamics and general relativity. It was around that time when Matthias Liebendörfer, who was working at at the CITA in Toronto/Canada, announced Ph.D. position opening in his new project that was about to start in autumn 2005 in Basel/Switzerland. The project was content about core collapse supernovae and related topics. Though I had not quite completed my undergraduate studies in Sweden, I applied for the position. I was very happy to be the successful candidate. By that time, my interest in astrophysics had increased tremendously and I picked a topic for my masters thesis related to the evolution of galactic stellar systems. Due to a lack of time I had to finish my undergraduate studies while the project in Basel had already started, which left very little time to make myself familiar with the subject before the beginning of 2006. After that, I started to investigate more deeply important neutrino matter interactions which were meant to be important in core collapse supernova simulations but not taken into account in our model. This branch of our work has continued over the past 4 years of my doctoral studies.

Furthermore, general relativity and in particular the properties as well as the formation of black holes has always been fascinating to me. For that reason, my undergraduate studies in Leipzig focused on the mathematical description of axisymmetric and stationary spacetime. The general relativistic aspects of my doctoral studies did not come off too badly at all. The numerical model I was able to develop is based on general relativistic radiation hydrodynamics in spherical symmetry. It can simulate the dynamical evolution of astronomical objects that will collapse to a black hole due to the presence of strong gravitational fields until the formation of the apparent horizon.

Although the involved microphysics is highly uncertain, this method provides up to now the only insight into the state of matter during gravitational collapse until the formation of a black hole. Generally, the emitted neutrino signal is of particular interest in modeling core collapse supernovae.

Neutrino detector facilities such as Super-Kamiokande and SNO might resolve a future event at high precision, i.e. resolving millisecond events. The emitted neutrinos provide in fact the only reliable information from stellar interiors by the present knowledge, since matter is opaque to light and the emitted gravitational waves have proven difficult to detect. Furthermore, it turned out to be extremely useful to continually develop and improve the microphysics that is used to describe matter at extreme conditions which are found in stellar interiors and even explore new physics in the context of simulations of massive stars. Future observations as well as experiments and the correlation to the description of microphysics might provide a powerful technique to explore new physics. This strategy turned out to be the main guide of my doctoral research. It is of great importance for researchers to improve the general picture of physics and challenge even long agreed standards, while modeling physical processes (sometimes based on phenomenological approaches) trying to explain observations and experimental results.

Acknowledgments

Abstract

The main results of my doctoral studies were obtained from core collapse simulations of massive stars using a numerical model based on radiation hydrodynamics and three-flavour Boltzmann neutrino transport in spherical symmetry. It was continuously further developed with respect to the involved microphysics, such as neutrino-matter interactions, a nuclear reaction network for low temperatures and densities and the equation of state (EoS) for hot and dense nuclear matter.

These improvements made it possible to extend the simulation times from about 1 second to more than 20 seconds of physical time and allowed a detailed and for the first time consistent radiation hydrodynamics investigation of the neutrino driven wind, which develops during the early post-explosion phase of massive stars due to the continued neutrino energy deposition. The neutrinos that diffuse out of the central object, a protoneutron star (PNS), heat the material on top of the PNS surface. This heat is partly converted into kinetic energy which drives a matter outflow, known as the neutrino driven wind. Neutrino driven explosions of massive Fe-core progenitors of 10 and 18 $M_\odot$ were modelled using enhanced neutrino opacities. This was necessary because the explosion mechanism of such stars is a subject of active research and by present standard knowledge only working in multi-dimensional models. In the case of a special progenitor star, the less massive 8.8 $M_\odot$ O-Ne-Mg-core, the explosion in spherical symmetry was found even without enhanced opacities. The obtained post-explosion evolution is in qualitative agreement with previous static steady-state and parametrized dynamic wind models. On the other hand, we find generally smaller neutrino luminosities and mean energies, the neutrino driven wind is proton-rich for more then 10 seconds and the PNS properties and the contraction behaviour differ from the assumptions made in previous wind studies. Despite the moderately large entropies of about 100 k_B/baryon and the fast expansion timescale, the conditions found are unlikely to favour r-process nucleosynthesis.

In addition, we discuss the formation of stellar mass black holes via PNS collapse. The simulations are launched from several massive progenitors of 40 and 50 $M_\odot$. In the absence of an earlier explosion, the PNS collapses to a black hole due to the continued mass accretion. We analyse the electron-neutrino luminosity dependencies and construct a simple approximation for the electron-neutrino luminosity. Furthermore,

we analyse different (μ, τ)-neutrino pair-reactions separately and compare the differences during the post-bounce phase. We also investigate the connection between the increasing (μ, τ)-neutrino luminosity and the PNS contraction during the accretion phase before black hole formation. Comparing the different post-bounce phases of the progenitor models under investigation, we find large differences in the emitted neutrino spectra. These differences and the analysis of the electron-neutrino luminosity indicate a strong progenitor model dependency of the emitted neutrino signal.

Including an EoS for strange quark matter based on the simple and widely used MIT bag model, we are able to study the appearance of quark matter in core collapse simulations. The transition from hadronic matter to quark matter is modelled via a Gibbs construction which results in an extended mixed phase. Assuming small bag constants, the phase transition occurs during the early post-bounce phase of massive progenitor stars at densities near nuclear saturation which are found at the PNS centre. The simulations are launched from 10, 13 and 15 $M_\odot$ stars, where in the absence of an earlier explosion the PNSs contract due to the continued mass accretion on a timescale of 100 ms. A direct consequence of the phase transition is the formation of a strong second accretion shock at the phase boundary between the mixed and the pure hadronic phases. It even turns into a dynamic shock and overtakes the first shock, which remained unaffected from the happenings inside the PNS. In other words, a new explosion mechanism is discovered, where moderate explosion energies of 1×10^{51} erg are obtained. As soon as this second shock propagates over the sphere of last scattering where neutrinos decouple from matter, a second neutrino burst is released which may possibly be detectable for a future Galactic event, if a quark phase transition has taken place.

Contents

Chapter 1

Introduction

Core collapse supernovae and the understanding of the physical phenomena involved kept scientists from various different fields of research busy for more than half a century. One of the most important issues is the relation of the production of the elements in core collapse supernova explosions, especially heavy elements such as uranium as well as the involved nuclear processes. The so-called explosive nucleosynthesis provides only an indirect insight into stellar interiors. Since the material is optically opaque, the only direct observables are gravitational waves and neutrinos, both of which are emitted on a timescale of several seconds. However, gravitational waves have proven difficult to detect. Hence, the most promising source of information leaving a stellar core are in fact the neutrinos. A neutrino burst was detected from SN1987a, documented in Hirata et al. (1988). It is up to now the only observed core collapse supernova event at such short distance from the Earth which has produced a neutrino signal. Although the measurement only provided very few data points (neutrino events), it nevertheless probed the theoretically predicted scenario of core collapse supernovae to some extent including the relevance of neutrinos. Their relevance and importance is not only due to the detectability of core collapse supernova events but also in order to explain the explosion mechanism. From simple energetic considerations it can be shown that neutrinos carry away energy of the order of several 10^{53} erg on a timescale of several minutes. This energy exceeds the typical kinetic explosion energy of a few 10^{51} erg by two orders of magnitude. Already less than 1% of the energy in the neutrino radiation field is sufficient in order to obtain an explosion. Hence, neutrino driven explosions represent at present the most reliable explosion mechanism of massive stars which unfortunately has only been working in axially symmetric models for massive Fe-core progenitors and in spherical symmetry for the low-mass 8.8 $M_\odot$ O-Ne-Mg-core. Additional explosions have been obtained due to the dumping of acoustic energy and magnetically driven, both of which require multi-dimensional models as well. In the following section, the reader will be introduced to the supernova problem, which is related to the explosion mechanism of massive stars. It is an active subject of research

to which we were able to contribute a new hypothesis by reviving an old idea that is related to the involved microphysics.

1.1 Phenomenology of core collapse supernovae

Massive stars in the range of 8 to $\simeq 75$ M$_\odot$ evolve on the main sequence for millions of years through the different nuclear burning phases. The final state of nuclear burning of such massive progenitor stars is obtained when a reasonable amount of heavy Fe-group nuclei, such as $^{52-56}$Fe, ^{56}Ni and ^{60}Zn, are produced. Since these nuclei are the most stable elements with respect to the smallest mass per nucleon, nuclear burning processes stop and heavier elements can not be produced in stellar cores that way. Above temperatures of 0.5 MeV ($\simeq 6 \times 10^9$K), the production of heavy nuclei and their destruction are in equilibrium and nuclear burning proceeds towards nuclear statistical equilibrium. In addition, the importance of electron capture reactions increases. Electron captures on nuclei and free protons reduce the number of electrons, because the densities at the final stage of nuclear burning are low enough to allow the emitted neutrinos to escape freely. In other words, the stellar core deleptonises and the number of electron leptons Y_L and the number of electrons per baryon Y_e reduce. Consequently the pressure of the degenerate electron gas, which is the dominant contribution to the pressure at the end of stellar evolution, decreases and the stellar core starts to contract. The contraction proceeds into a collapse during which density and temperature increase and hence electron capture reactions become even more important. Above densities of $\rho \simeq 10^{11}$ g/cm^3, neutrinos are not free-streaming and neutrino transport becomes important. At even higher densities of $\rho \simeq 10^{13}$ g/cm^3 neutrinos are in equilibrium with matter and hence can be considered trapped. At the trapping density, the lepton number is fixed at a value of $Y_L \simeq 0.35$ whereas the central electron fraction continues to decrease to values below 0.35 according to the thermodynamic state. The collapse finally halts at nuclear densities of the order $\rho \simeq 2 - 4 \times 10^{14}$ g/cm^3 ($n_B \simeq 0.15 - 0.17$ fm^{-3} in nuclear units), which depends on the equation of state (EoS). The collapse is divided into a supersonically collapsing outer core and a subsonically collapsing inner core, spatially connected at the *sonic point*. Information about the stalling collapse at the centre cannot propagate from the inner part to the outer part across the sonic point. Hence, the outer collapse continues while at the centre a stagnation wave forms which propagates outwards. At the sonic point, the stagnation wave turns into a shock front. This defines the moment of *bounce* when the central density reaches its maximum. At bounce, the central electron fraction has a value slightly below 0.3 which defines the mass enclosed inside the bouncing core, see Goldreich and Weber (1980). The electron capture scheme used sensitively tunes the position of shock formation and hence the initial energy of the forming shock front. The standard reaction rates from Bruenn (1985) are based on the simplification of a single average nucleus with average atomic mass and charge. An

improved description has been published by Langanke et al. (2003) and Hix et al. (2003) where they address a nuclei distribution for the calculation of the electron capture rates based on shell-model calculations for the Gammov-Teller transition. Simulations using this improved scheme result in a slightly higher degree of deleptonisation during collapse and at core bounce.

After bounce, the shock front propagates further outwards and loses energy due to the dissociation of heavy nuclei into light nuclei and nucleons. In this expanding regime the shock continues to propagate into regions with lower and lower densities. The shock propagation across the neutrinospheres, i.e. the neutrino energy and flavour dependent spheres of last scattering, define the physical state where the neutrino radiation field decouples from matter. This corresponds to a release (out-burst) of a large number of electron-neutrinos emitted via additional electron captures. These electron-neutrinos carry away energy of $4 - 5 \times 10^{53}$ erg/s (depending on the progenitor model) on a timescale of $5 - 10$ ms. These two sources of energy loss turn the expanding shock front into a standing accretion shock (SAS) which expands to a few 100 km at about 5 ms after bounce. In this sense, there is no evidence for a *prompt explosion*. All massive progenitor stars follow the same fate shortly after bounce. Depending on the progenitor mass, only the magnitude of the observables (such as the time before the expanding shock front turns into the SAS, the neutrino luminosities and energies, the enclosed mass inside the SAS) differ.

The central object that has formed immediately after bounce is a *protoneutron star* (PNS). The neutrinos which diffuse out of the hot and dense PNS on timescales of several seconds, have long been investigated whether they can revive the SAS and lead to *neutrino driven explosions* (see for example Bethe and Wilson (1985)). The absorption of neutrinos behind the SAS transfers energy from the radiation field into the fluid on timescales of 100 ms, when the neutrino luminosities and energies are still sufficiently high. This corresponds to an increase of the thermal energy of the matter, i.e. matter is heated. This heat is partly converted into kinetic energy. Unfortunately, up to now this energy transfer has proven to be not efficient enough to revive the SAS in spherically symmetric core collapse models. Even models that are based on accurate neutrino transport and involve a sophisticated EoS for the description of nuclear matter at high densities and temperatures could not explain explosions in spherical symmetry. An exception is the spherically symmetric explosion of the 8.8 $M_\odot$ O-Ne-Mg-core from Nomoto (1983,1984,1987) by Kitaura et al. (2006). On the other hand, multi-dimensional models have become available only recently. Multi-dimensional phenomena such as rotation and the development of fluid instabilities have been shown to increase the neutrino heating efficiency, see for example Miller et al. (1993), Herant et al. (1994), Burrows et al. (1995) and Janka and Mueller (1996). They help us to understand aspherical explosions, see for example Bruenn et al. (2006), Marek and Janka (2009) and Janka et al. (2008).

1.2   Aims of the present work

Despite the recent success of multi-dimensional core collapse models with respect to the actual task of exploring the explosion mechanism of massive stars, such models suffer from various problems. For example, the obtained explosion energies can barely be related to observations because the simulations are not carried out for long enough. A comparison of different multi-dimensional explosion models is difficult. In addition, it is difficult to exclude numerical effects, such as grid effects, causing the launch of the explosion. A comparison of the composition of the explosion ejecta depends on the explosive nucleosynthesis model. Hence, we belief it is important to constantly improve the *input (micro)physics* involved as well. These are the neutrino physics, the equation of state (EoS) and the progenitor star as the initial model. Next to the development of fluid instabilities and the possible shock revival explored in multi-dimensional models, the improvements of neutrino-matter interactions and different EoSs have been speculated to help to understand the explosion mechanism as well (Horowitz (2002), Itoh et al. (2004)). To improve the input physics and investigate the improvements to a high precision, multi-dimensional models are not ideally suited for due to the large computational resources such simulations typically consume. Hence, we choose a spherically symmetric approach based on the highly advanced numerical model AGILE-BOLTZTRAN. It was designed by Mezzacappa and Bruenn (1993a-c) based on Newtonian radiation-hydrodynamics using three-flavour Boltzmann neutrino transport. It was updated by Liebendörfer et al. (2001a,b) to solve the general relativistic equations. A lot of effort was devoted to implementing an adaptive grid as documented in Liebendörfer et al. (2002) and to accurately conserve Lepton number, momentum and energy, see Liebendörfer et al. (2004). The advantage of spherically symmetric over multi-dimensional models is the possibility of improving neutrino-matter interactions and investigating these using accurate neutrino transport, where multi-dimensional models have to approximate neutrino transport for computational reasons. Furthermore, simulations can be carried out for several seconds of physical time using simulation times of only up to a few weeks. Present state-of-the-art multi-dimensional simulations are limited to not much more then 1 second of physical time and can run for years.

1.2.1   Neutrino-matter interactions

Neutrino-matter interactions are taken into account via reaction rates that are calculated interactively, because the rates depend on the thermodynamic state which changes during the dynamical evolution. The dominant reactions are the electronic charged current reactions, which are the electron(positron) and electron-(anti)neutrino captures at free the nucleons and nuclei. During the collapse of the stellar core, the degeneracy of matter is too low for the presence of positrons. Only electron capture reactions can take place and hence there are only electron-neutrinos and all other flavours are suppressed.

Only as the temperature increases due to shock heating post-bounce, positrons appear as well which allow then also for the production of electron-antineutrinos via positron captures at free neutrons and (μ/τ)-(anti)neutrinos via pair reactions. In principle, the muonic charged current reactions contribute as well. However, the large rest mass of the muon of about 107 MeV would allow muon capture reactions only at a extremely high degeneracy. Hence, such reactions are suppressed and typically ignored in core collapse supernova models. Next to the charged current reactions, neutral current reactions such as various scattering and pair reactions are considered. Most important for the determination of the neutrinospheres are neutrino-nucleon and neutrino-nuclei scattering, due to the small mean-free paths. Reactions such as neutrino-electron(positron) scattering thermalise the neutrinos on their trajectory out before they reach the neutrinospheres where neutrinos decouple from matter. Pair reactions, such as electron-positron annihilation, nucleon-nucleon-Bremsstrahlung and the annihilation of trapped electron flavour neutrino pairs produce (μ/τ)-(anti)neutrinos. To summarise, the following reactions are considered:

$$\text{Charged current reactions} \begin{cases} e^- + p \leftrightarrow n + \nu_e, \\ e^- + \langle A, Z \rangle \leftrightarrow \langle A, Z - 1 \rangle + \nu_e, \\ e^+ + n \leftrightarrow p + \bar{\nu}_e, \end{cases}$$

$$\text{Neutral current reactions} \begin{cases} \left. \begin{array}{l} \nu + N \leftrightarrow \nu + N \quad (N = n, p), \\ \nu + \langle A, Z \rangle \leftrightarrow \nu + \langle A, Z \rangle, \\ \nu + e^\pm \leftrightarrow \nu + e^\pm, \end{array} \right\} \text{scattering} \\ \\ \left. \begin{array}{l} e^- + e^+ \leftrightarrow \nu + \bar{\nu}, \\ N + N \leftrightarrow N + N + \nu + \bar{\nu} \;\; (N = n, p,), \\ \nu_e + \bar{\nu}_e \leftrightarrow \nu_{\mu/\tau} + \bar{\nu}_{\mu/\tau}, \end{array} \right\} \text{pair reactions} \end{cases}$$

where $\nu = (\nu_e, \bar{\nu}_e, \nu_{\mu/\tau}, \bar{\nu}_{\mu/\tau},)$ unless stated otherwise and $\langle A, Z \rangle$ represents heavy nuclei via a single nucleus approximation with average mass A and charge Z.

The electron-flavour neutrinos are the dominant sources for cooling and heating matter via the emission and absorption processes respectively. At large densities which correspond to PNS interiors, the neutrino emission is dominant. The emitted neutrinos are highly trapped and can only diffuse out of the PNS on timescales of seconds. This deleptonises and cools the PNS, which leads to a contraction on the same timescales. The neutrinos thermalise on their way out of the PNS, which reduces the mean energy of the neutrinos. At low enough neutrino energies this allows for the reverse reactions, i.e. the neutrino absorption processes, to dominate which in turn results in a net-heating rate taking place close to the neutrinospheres. The radius at which this occurs defines the *gain region*, where outside this radius the neutrino energy deposition is meant to be the origin of power which drives neutrino driven explosions. Fig. 1.1 which was taken from Janka (2001) illustrates the typical post bounce situation.
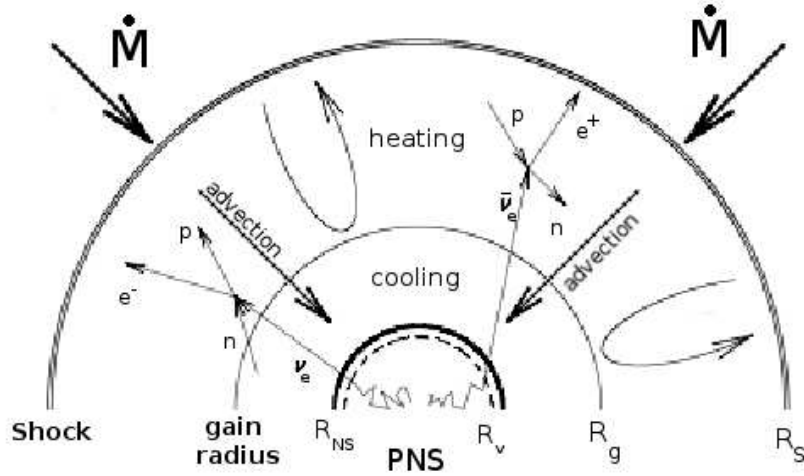
Figure 1.1: Illustration of the post bounce situation, including mass accretion from the progenitor star, the shock position, heating and cooling regions and the gain radius.

The transport of neutrinos becomes important in the regime near the neutrinospheres, essentially in order to model the transition between the neutrino trapping and free streaming regimes where we solve the Boltzmann equation for ultra-relativistic massless fermions. This is computationally very expensive and can only be done in spherically symmetric models. At present, multi-dimensional models have to rely on some neutrino transport approximation scheme. The current and most successful axially symmetric models of our time apply either the multi-group flux limited diffusion approximation (see Bruenn (1985)) or the ray-by-ray approximation (see Janka and Mueller (1995)), where the latter one calculates Boltzmann transport for each angular ray. Recently, Liebendörfer et al. (2009) developed a new algorithm based on the separation of trapped and free-streaming neutrinos, which is computationally less expensive and can even be applied in 3-dimensional models (see Whitehouse and Liebendörfer (2010)).

1.2.2   The equation of state

The equation of state (EoS) in core collapse supernova models is much more than a relation between matter pressure and baryon density. It describes general properties of matter including the composition for various different thermodynamic regimes, which can be distinguished as follows.

1. At low densities and temperatures, typically below $T \simeq 0.5$ MeV which corresponds to $T \simeq 6 \times 10^9$ K, nuclei are present and the evolution of the thermo-

dynamic quantities is determined by the changing composition and hence time-dependent thermonuclear and weak reactions. Matter properties such as pressure, entropy and internal energy, are dominated by the degenerate electron gas. Our core collapse model used previously the simplification of an ideal gas of Si-nuclei. This lead to an increasingly inaccurate energy evolution, especially in explosion models after 500 ms post bounce when the explosion shock reached the Si-layer and simplifications could not be extended beyond ~ 1 second post bounce. In order to describe the baryon properties in such a regime accurately, a nuclear reaction network can be used. The implementation of the nuclear reaction network now makes it possible to include more mass (up to and even including a large fraction of the He-layer) of the progenitor star into the physical domain and follow the dynamical evolution for one order of magnitude longer.

2. For temperatures $T > 0.5$ MeV, the destruction and production of nuclei are in equilibrium, i.e. nuclear statistical equilibrium, and given by the thermodynamic state temperature T, baryon density n_B and electron fraction Y_e. Heavy nuclei are approximated by a single representative nucleus with average atomic mass and charge $\langle A, Z \rangle$, in addition to α-particles, which represent the light nuclei in our model, and the free nucleons. The EoS in that regime for matter at high baryon densities and temperatures is relatively unknown. The calculation of the EoS has to rely on theoretical models, which are typically based on phenomenological approaches and include various nuclear effects where the commonly used EoSs for hot and dense nuclear matter in core collapse simulations of massive stars are from Lattimer and Swesty (1991) and more recently Shen et al. (1998a).

Up to now, contributions from exotic particles such as strangeness in the nucleon sector and quarks are only starting to be explored in the context of core collapse supernovae. The study of their possible appearance in a radiation-hydrodynamics context and the consequent relevance with respect to possible observables are major subjects of the present work. Therefore, we employ a quark matter EoS that is based in the simple and widely used MIT-bag model, developed by Sagert et al. (2009a). It describes the transition from hadronic matter to (u,d,s)-quark matter via an extended co-existence region,i.e. the mixed phase, modelled via the Gibbs construction. The additional quarks (t,b,c) are suppressed due to their large rest masses. The phase transition causes a collapse of the PNS in the regime above nuclear saturation due to the softening of the EoS in the mixed phase. A second standing accretion shock forms due to the stiffening of the EoS for matter in the pure quark phase. This second standing accretion shock accelerates along the decreasing density gradient at the PNS surface, overtaking the first SAS and leading to an explosion even in spherical symmetry where otherwise no explosions could have been obtained. It becomes also observable in the emitted neutrino spectra as a second outburst of neutrinos, due to the lifted degeneracy

of the additionally shock heated hadronic material. The results of this investigation are published in Sagert et al. (2009b) and will be discussed further in §3.3.

1.2.3   The progenitor model

The third part of the input physics in core collapse supernova simulations is the progenitor model as initial conditions. The stellar life of a massive star with an initial mass between 8 and $\simeq 75$ $M_\odot$ on the main sequence is modelled using quasi-static spherically symmetric fluid dynamics combined with an EoS valid for the thermodynamic conditions applied in such simulations. It includes a treatment of nuclear reactions, weak reactions and mixing. Such stellar evolution models are provided by for example Nomoto and Hashimoto (1988), Woosley and Weaver (1995), Woosley et al. (2002), Umeda and Nomoto (2008) and Hirschi (2007). The star is evolving on the main sequence over millions of years (depending on its initial mass and metallicity) though H-burning which produces a core composed of He where the core temperature is not high enough to start He-burning. The loss of internal energy and pressure support (i.e. contributions from radiation, burning and baryons) cause the He-core to become gravitationally unstable which results in a contraction during which the temperature increases. As soon as the temperature is sufficiently high enough to ignite He-burning, the contraction halts due to the contribution from the nuclear burning to the internal energy and pressure where quasi-hydrostatic equilibrium is re-establishment. He-burning on the other hand produces a C-O-core where again the temperatures are not high enough to ignite C-O-burning and nuclear burning stops - this again results in a gravitational contraction during which the temperature increases until C-O-burning starts and quasi-hydrostatic equilibrium is obtain. In other words, the ash from each nuclear burning process sinks towards the centre and initiates the next higher burning process, after a contraction during which the temperature increases sufficiently high enough for the next higher burning processes to be ignited. Hence, nuclei with larger atomic mass are found closer to the stellar core. Massive star develop this way an onion-like shapes (see Fig. 1.2) where the different layers determine the nuclear burning history of the star. At the end of C-O-burning, ^{28}Si and ^{32}S nuclei have been produced dominantly and Si- and S-burning produces Fe-group nuclei (for illustration, see Fig. 1.2 at the example of a 15 $M_\odot$ progenitor model) Furthermore, the timescale for each burning process reduces reduces. Where the star evolves over millions of years on the main sequence through H-burning, He-burning lasts for a couple of 10^5 years and C-O-burning only a couple of 100 years. The shortest burning process is Si-S-burning, which lasts only a couple of days.

However, Fe-group nuclei and in particular ^{56}Fe is the most stable nuclei with respect to the smallest mass per nucleon and hence Fe-burning does not take place. Heavier elements cannot be produced in stellar cores via nuclear burning. Consequently, as soon as a reasonable amount of Fe-group nuclei are produced at the core of the Si-S-
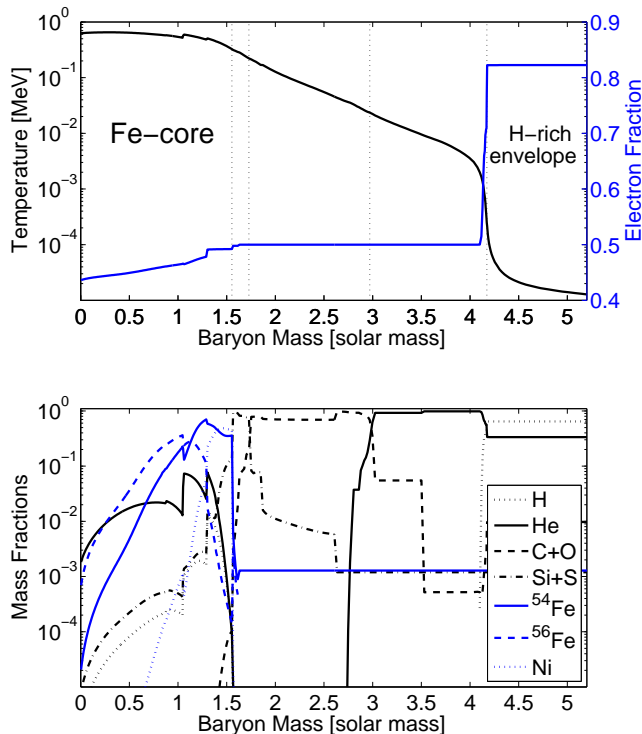
Figure 1.2: The non-rotating 15 $M_\odot$ progenitor model from Woosley et al. (2002), illustrating at the top the temperature (in log-scale at the left side) and the electron fraction (linear-scale at the right side) as well as the dominant composition at the bottom at the end of stellar evolution for the innermost 5 $M_\odot$ of the remaining mass of the star, i.e. the H-rich envelope extends up to 12.6421 $M_\odot$. About 2.3579 $M_\odot$ have been lost into the interstellar medium during stellar evolution via stellar winds. The dashed vertical lines (top) illustrate the onion-like structure of the progenitor due to the composition.

burning shell, nuclear burning stops again. This time, the loss of energy support from the nuclear burning in combination with the increasing importance of electron captures cause the stellar core to contract during which quasi-hydrostatic equilibrium cannot be obtained anymore and the contraction proceeds into the collapse of the Fe-core. At that stage, stellar evolution models cannot be used anymore due to the lack of neutrino transport which becomes more and more important as density and temperature increase. Instead, the progenitors are used as input in core collapse supernova models where the continuous evolution is simulated. In this sense, all massive progenitor stars follow the same fate at the end of stellar evolution.

Less massive stars, such as our own sun, do not reach high enough core temperatures to continuously ignite the next higher burning processes up to Si-S-burning. Such stars do not produce extended Fe-cores at the final stage of nuclear burning that collapses and explodes leaving a neutron star or a black hole. Instead, such cores develops an electron degenerate ^{12}C-enriched white dwarf. An intermediate progenitor between these two mass ranges is the 8.8 $M_\odot$ O-Ne-Mg-core from Nomoto (1983,1984,1987). The core of this progenitor contains only a small fraction ($\simeq 0.1$ $M_\odot$ of the core) of Fe-group nuclei at the end of stellar evolution, where C-O-burning is still proceeding during the core collapse. This progenitor will be further discussed below as well as its post-bounce evolution, for which we were able to obtain an explosion in spherical symmetry which is in qualitative agreement with Kitaura et al. (2006).

Organisation of the manuscript

In §2 I will briefly introduce the fundamental physical concept behind the modeling of core collapse supernovae, which is general relativistic neutrino radiation hydrodynamics based on three-flavour Boltzmann neutrino transport in spherical symmetry. I will also explain the improvements made during my doctoral studies. These are the implementation of improved nuclear input physics, such as additional neutrino reactions for neutrino-positron scattering and the annihilation of trapped electron-flavour neutrino pairs, an equation of state (EoS) for hot and dense asymmetric nuclear matter which is in nuclear statistical equilibrium (NSE) developed by Shen et al. (1998a) and a nuclear reaction network for matter which is not in NSE developed by Thielemann et al. (2004). Since the explosion mechanism of massive progenitor stars is an active subject of research, we model explosions in spherical symmetry by enhancing the electronic charged current reaction rates artificially. For such explosion models (using the improvements of the nuclear physics) it is now possible to follow the explosion dynamics and the dynamical evolution of the PNS up to 20 seconds post-bounce. On the timescale of several seconds, the *neutrino driven wind* will appear as a consequence of continuous neutrino energy deposition on top of the PNS surface after the explosion has been launched. In §3.1 I will discuss and illustrate the neutrino driven wind at two different Fe-core progenitor models and the O-Ne-Mg-core. Massive progenitors above a certain threshold (typically 40 $M_\odot$, depending on the explosion mechanism) will not explode but proceed into an extended PNS accretion phase during which the continuous mass accretion causes the PNS to become gravitationally unstable and collapse to a solar mass black hole on timescales of several 100 ms. Such scenarios will be discussed in §3.2 for several massive progenitors. Of special interest is the emitted neutrino signal from such events. In collaboration with Sagert et al. (2009a) formerly from the University of Frankfurt and now at the University of Heidelberg, we additionally explore the possibility and consequences of a phase transition from hadronic matter to strange quark matter. I will present the basic concept that can be applied to describe quark matter (e.g. based on the MIT-bag model) and illustrate the resulting quark EoS as well as the transition between the hadronic and the quark phases in §2.2. The consequences of this work with respect to dynamical simulations, including the quark-hadron phase transition induced explosion mechanism, will be further discussed in §3.3.

Chapter 2

Radiation hydrodynamics in spherical symmetry

A wide range of exact solutions to Einsteins field equation have been formulated, see for example Stephani et al. (2003). Most of these analytical solutions describe astronomical objects and astrophysical processes only to a very limited degree. The simplifications of nature as of e.g. perfect gas, perfect fluids and rigidly rotating dust discs leave out important aspects. The whole physical picture is much more complex. It involves, next to gravity and electromagnetism, for instance an equation of state (EoS) as well as nuclear reactions (strong and weak interactions) and even radiation transport. In this sense, the modeling of core collapse supernovae requires a description that takes the four fundamental forces of nature into account. On the other hand, there is no analytical model that describes the dynamical evolution of a collapsing star taking at least the dominant microphysical effects into account. It is a system that requires the combination of general relativistic hydrodynamics and radiation transport. At present, there are no analytical solutions to such a description. Numerical solutions are required in order to calculate the dynamical evolution of such systems. It is thereby important to accurately fulfill the conservation laws of physics, e.g. energy, momentum and lepton number conservation. Since the numerical solutions of such systems go far beyond the mathematically approved domain of the theories beneath, they can only be understood as an attempt to understand the fundamental physical processes involved and not as a mathematically complete theory. For example, the gravitational collapse of an ideal fluid can be solved analytically in the general relativistic framework. Coupling a physical (i.e. non-polytropic) equation of state including composition to the system, introduces physical dependencies for which analytical solutions cannot be extended. The same holds for the inclusion of radiation transport and nuclear interactions, both of which are additionally required for the modeling of core collapse supernovae. On the other hand in addition to experiments, astronomical observations can be used to limit certain parameters of the used input physics. This results in a powerful correla-

tion between observations and the fundamental understanding of the involved physical processes. It creates a scientifically fruitful environment.

The numerical model I have been working with during my doctoral studies is AGILE-BOLTZTRAN. It was developed by Mezzacappa and Bruenn (1993a-c) based on spherically symmetric Newtonian hydrodynamics including three-flavour Boltzmann neutrino transport. Liebendörfer (2001a,b) extended this model to solve the general relativistic equations. An adaptive grid, described in Liebendörfer et al. (2002), was included and a lot of effort has been devoted to conserve the lepton number, momentum and energy (see Liebendörfer et al. (2004)). I will elucidate in the following sections the physical theories that stand behind AGILE-BOLTZTRAN, which are general relativistic fluid dynamics, (neutrino) radiation transport, both their coalescence as well as various neutrino-matter interactions.

2.1   General relativistic hydrodynamics

In the standard framework of general relativity based on Riemannian geometry, the equations for energy and momentum conservation are obtained from the divergence of the stress-energy tensor $T(X, Y)$ as follows

$$\nabla_X T(X, Y) = 0,$$

where ∇ is the covariant derivative. In a chart, the covariant derivative defines a connection on the Manifold M as follows

$$\nabla_i \partial_j = \Gamma_{ij}^k \partial_k,$$

where $\{\partial_i\}$, given by a local chart $\{x_i\}$ on M, is the basis in the tangent space to M, i.e. $T_p M = \mathrm{span}\{\partial_i\} \; \forall p \in M$ and the vector fields $X, Y \in T_p M$. Γ_{ij}^k are the Christoffel symbols given implicitly by the metric g_{ij} of the Riemannian manifold. The system is closed with the conservation of the number of particles with rest mass density ρ (in the sense of a system composed of conserved microscopic particles with 4-velocity u)

$$\nabla_X \left(\rho \, u(X) \right) = 0.$$

Writing these relations in coordinate form as well as introducing the stress energy tensor in coordinate form, one obtains

$$\frac{1}{\sqrt{-g}} \frac{\partial}{\partial x^i} \left(\sqrt{-g} T^{ij} \right) = -\Gamma_{ik}^j T^{ki}, \tag{2.1}$$

and

$$\frac{1}{\sqrt{-g}} \frac{\partial}{\partial x^i} \left(\sqrt{-g} \rho u^i \right) = 0,$$

where $g = \det(g_{ij})$[1]. These equations determine the dynamical evolution and are in a sense equivalent to the equations of motion and energy conservation. Introducing the stress-energy tensor of a perfect fluid, i.e.

$$T^{ij} = \mu u^i u^j + p(g^{ij} + u^i u^j), \tag{2.2}$$

where μ is the energy density, p is the pressure and u^i is the 4-velocity vector, applying (2.2) to Eq. (2.1), the following expression for the time component can be obtained

$$u^i \frac{\partial \mu}{\partial x^i} + (\mu + p) \frac{1}{\sqrt{-g}} \frac{\partial}{\partial x^i} \left(\sqrt{-g} u^i \right) = 0, \tag{2.3}$$

and for the space component

$$(\mu + p) u^i \left(\frac{\partial u^\tau}{\partial x^i} + \Gamma^\tau_{ij} u^j \right) + \left(g^{\tau i} + u^\tau u^i \right) \frac{\partial p}{\partial x^i} = 0. \tag{2.4}$$

These equations can be written explicitly for a spherically symmetric and non-stationary spacetime with coordinate time t, radial coordinate a (baryon mass) and the two angles (ϑ, φ) that describe a 2-sphere of radius $r(t, a)$. Using the following line element[2],

$$ds^2 = -e^{2\Phi(t,a)} dt^2 + e^{2\Lambda(t,a)} da^2 + r(t,a)^2 \left(d\vartheta^2 + \sin^2 \vartheta d\varphi^2 \right), \tag{2.5}$$

and writing the zero-component of the stress-energy tensor in terms of the internal energy density e, i.e. $T^{tt} = \rho(1 + e)$, Eqs. (2.3) and (2.4) take the following form

$$\frac{1}{\rho} \nabla_i T^{it} = \frac{\partial e}{\alpha \partial t} + p \frac{\partial}{\alpha \partial t} \left(\frac{1}{\rho} \right) = 0,$$

$$\frac{r'}{\Gamma} \frac{1}{\rho} \nabla_i T^{ia} = \frac{p'}{\rho} + \left(1 + e + \frac{p}{\rho} \right) \Phi' = 0,$$

(see for example Liebendörfer et al. (2001a) without radiative contributions) using the following setting for the metric coefficient functions, i.e. $\alpha = e^\Phi$ is the lapse function and $r'/\Gamma = e^\Lambda$. The dotted quantities denote partial derivative with respect to the coordinate time t and the primed quantities denote partial derivatives with respect to the radial coordinate (baryon mass), i.e.

$$\dot{} = \frac{\partial}{\alpha \partial t}, \qquad ' = \frac{\partial}{\partial a}.$$

---

[1]In the following I use the convention where Latin indexes denote space-time inducers $(i, j, k) = (0, ..., 3)$ and Greek indexes denote spatial ones only.

[2]It goes back to May and White (1966) who were the first to perform general relativistic simulations based on the equations derived in Misner and Sharp (1964)

The equations that are required to describe the system are obtained from the Einstein equation, i.e.

$$G_{ij} = 8\pi T_{ij},$$

as follows (see Misner and Sharp (1964),Liebendörfer et al. (2001a))

$$G^{tt} = \frac{1}{r^2}(1 + u^2 - \Gamma^2) - \frac{2\Gamma}{r}\left\{\frac{\Gamma'}{r'} - \frac{u}{\alpha\Gamma}\left(\frac{\dot{r}'}{r'} - \frac{\dot{\Gamma}}{\Gamma}\right)\right\} = 8\pi\rho(1 + e), \qquad (2.6)$$

$$G^{at} = \frac{2\Gamma}{r}\left\{\frac{u'}{r'} - \frac{1}{\alpha}\left(\frac{\dot{r}'}{r} - \frac{\dot{\Gamma}}{\Gamma}\right)\right\} = 0, \qquad (2.7)$$

$$G^{aa} = -\frac{2m}{r^3} - \frac{2}{r}\left(\frac{\dot{u}}{\alpha} - \frac{\Gamma^2}{\alpha}\frac{\alpha'}{r'}\right) = 8\pi p, \qquad (2.8)$$

where $u = \dot{r}/\alpha$ is the radial velocity. In combination with the expression that relates the radius, baryon mass and matter density in spherical symmetry,

$$\frac{\partial r}{\partial a} = \frac{\Gamma}{4\pi r^2 \rho}, \qquad (2.9)$$

the Eqs. (2.6), (2.7) and (2.8) can be simplified as follows (Liebendörfer et al. (2001a))

$$\frac{\partial}{\partial a}\left(\frac{r}{2}\left(1 + u^2 - \Gamma^2\right)\right) = 4\pi r^2 r' \rho(1 + e), \qquad (2.10)$$

$$\frac{1}{\alpha}\left(\frac{\dot{r}'}{r'} - \frac{\dot{\Gamma}}{\Gamma}\right) = \frac{u'}{r'}, \qquad (2.11)$$

$$\frac{\partial u}{\alpha \partial t} = \frac{\Gamma^2}{\alpha}\frac{\alpha'}{r'} - \frac{m}{r^2} - 4\pi r p. \qquad (2.12)$$

Combining Eqs. (2.9) with (2.11), one obtains the evolution equation for the rest mass density (Liebendörfer et al. (2001a))

$$\frac{\partial}{\alpha \partial t}\left(\frac{1}{\rho}\right) = \frac{\partial}{\Gamma \partial a}\left(4\pi r^2 u\right), \qquad (2.13)$$

which is the continuity equation. All the expressions (2.8)-(2.13) have been obtained in the absence of any radiation field. They will be modified if a radiation field is present and coupled to the system.

2.2 Boltzmann neutrino transport

The type of radiation considered in core collapse supernovae are neutrinos, due to the presence of weak reactions like the capture of leptons on nucleons as well as scattering processes. The emission and absorption as well as thermalisation processes are subject to the theory of weak interactions based on the theory by Weinberg-Salam-Glashow (Greiner and Müller), see for example Dicus (1972), Tubbs and Schramm (1975), Yueh and Buchler (1976a), Yueh and Buchler (1976b), Schinder and Shapiro (1982) and Bruenn (1985).

Although most of the progenitors physical domain corresponds to the free-streaming regime form neutrinos, the physical conditions found inside stellar interiors belong to the regime where neutrinos are highly trapped. Neutrinos can be considered as trapped particles at densities above 10^{13} g/cm^3. The most important region for neutrino-fluid interactions with respect to heating and cooling lays inside the density domain between $10^{10} - 10^{13}$ g/cm^3. There, neutrinos are not trapped anymore but also not free streaming yet and hence their transport is of importance. We apply accurate three flavour Boltzmann neutrino transport for the whole domain considered, where no assumptions are required with respect to trapping(diffusion) or free streaming. These conditions are determined automatically via the mean free paths, which are calculated interactively and enter the Boltzmann transport equation for massless ultra-relativistic (i.e. $v = c$) Fermions. In the following subsections, I will introduce the general relativistic Boltzmann transport equation which goes back to Lindquist (1966). Below that, I will draw down the equations used in spherical symmetry.

2.2.1 Mathematical remarks

The equations for radiation transport must obey a general relativistic form in order to be able to couple them to a general relativistic fluid dynamics system. The theory of classical mechanical systems is one of the best known and most elegant mathematical descriptions in physics. It is related to *Hamiltonian systems* (M, w, H) which is a reformulation of a classical mechanical system. It describes the structures defined on a symplectic manifold (in classical physics terms the phase-space) (M, w) where an additional structure, the Hamilton function H, is given. M is an ordinary manifold and $w(p) : T_m M \times T_m M \to \mathbb{R}$ ($\forall m \in M$) is a symplectic 2-form. Lindquist (1966) applies such a representation to formulate the transport equation.

In general, the basis of the tangent space $T_x M$ over a 4-dimensional Riemannian manifold M ($x \in M$) with coordinates $\{x^i\}$ ($i = 0, 1, 2, 3$) can be defined on some open set $U \subset M$ as $\{\partial/\partial x^i\}$. The tangent vectors $\mathbf{p} \in U$ can be written as (Lindquist (1966))

$$\mathbf{p} = p^i \frac{\partial}{\partial x^i},$$

where p^i are the coefficient functions. Defining a new set of local coordinates $\{x^i, p^i\}$ in the section of the tangent bundle TM that lays over U, $TM|_U := TU$, gives a natural basis in the tangent space over TU via (Lindquist (1966))

$$\left\{ \frac{\partial}{\partial x^i}, \frac{\partial}{\partial p^i} \right\}.$$

In the following paragraph, the path towards a presentations of vectors in such a context will be sketched in terms of a differentiable map that relates the tangent space $T_x M$ for any $x \in M$ with $T_b U$ for any $b \in TU$, $\psi_* : T_b U \rightarrow T_x M$.

Splitting up $T_b U$ in a horizontal $(H_b U)$ and a vertical part $(V_b U)$ in a coordinate-free way as follows (Lindquist (1966))

$$T_b U = H_b U \oplus V_b U,$$

each vector $\mathbf{t}' \in T_b U$ can be expresses as a sum of horizontal and vertical components (Lindquist (1966))

$$\mathbf{t}' = \mathbf{t}'_H + \mathbf{t}'_V,$$

where $\mathbf{t}'_H \in H_b U$ and where $\mathbf{t}'_V \in V_b U$. Then (Lindquist (1966))

$$\psi_*^{-1}(\mathbf{t}) = \mathbf{t}'_H$$

is the horizontal vector whose projection gives the tangent vector $\mathbf{t}$ at x. Furthermore following the introduction by Lindquist (1966), $C(\tau)$ is a curve in M passing through $x_0 = \psi(b)$ and $b_0 = (x_0, \mathbf{p}_0) \in TU$. Constructing a unique curve in TM denoted as $C'(\tau) = \{x^i, \mathbf{p}^i\}$, which describes both a curve $x^i(\tau)$ and a vector field $\mathbf{p}(\tau) = \mathbf{p}^i \partial/\partial x^i$ which is parallel-transported along C. Denote the tangent vector to $C(\tau)$ as (Lindquist (1966)),

$$\mathbf{t} = \frac{dx^i}{d\tau} \frac{\partial}{\partial x^i},$$

the corresponding tangent vector to $C'(\tau)$ is given by (Lindquist (1966))

$$\mathbf{t}' = \frac{dx^i}{d\tau} \frac{\partial}{\partial x^i} + \frac{dp^j}{d\tau} \frac{\partial}{\partial p^j}.$$

Because $\mathbf{p}(\tau)$ is parallel-transported along C, one can write the coefficient function of the momentum direction of the tangent vector in terms of the connection(Christoffel symbols) as follows (Lindquist (1966))

$$\frac{dp^j}{d\tau} = -\Gamma^j_{ik} p^k \frac{dx^i}{d\tau},$$

which yields (Lindquist (1966))

$$\mathbf{t}' = \frac{dx^i}{d\tau} D_i,$$

where

$$D_i = \frac{\partial}{\partial x^i} - \Gamma^j_{ik} p^k \frac{\partial}{\partial p^j}.$$

A tangent vector in TU will be expressed in this form, if it is horizontal. The set of independent vectors $\{D_{x^i}\}$ spans $H_b U$. Combining this with the vectors $\{\partial/\partial p^i\}$ that span $V_b U$, the following basis

$$\left\{ \mathbb{R}D_{x^i}, \frac{\partial}{\partial p^i} \right\}$$

spans $T_b U$ (Lindquist (1966)). Hence any vector $\mathbf{u} \in T_b U$ can be written as (Lindquist (1966))

$$\mathbf{u} = u^i_H D_i + u^i_V \frac{\partial}{\partial p^i}.$$

2.2.2 The general relativistic transport equation

Introducing a distribution function $f(x, \mathbf{p})$, which is a probability function defining the number of particles dN in a certain spacelike volume element dV at position x with 4-momentum $\mathbf{p}$. The momenta lay in a corresponding 3-surface element dP of the momentum-space.

Let $d_1\mathbf{p}, d_2\mathbf{p}, d_3\mathbf{p}$ be three displacements of the vector $\mathbf{p}$, which span a 3-surface on the mass shell through $\mathbf{p}$ whose normal is $\mathbf{p}$ itself, where $\mathbf{p} \cdot \mathbf{p} = -m^2$. Conserving orthogonality the following expression (Lindquist (1966)),

$$\sqrt{-g}\epsilon_{ijkl} d_1 p^i d_2 p^j d_3 p^k = \text{const.}\, p_l = dP\, p_l,$$

defines an invariant volume element dP orthogonal to $\mathbf{p}$, where $g = \det|g_{ij}|$ and where ϵ_{ijkl} is the Levi-Civita symbol(anti-symmetric tensor). This expression can be written as follows (Lindquist (1966))

$$dP = \sqrt{-g}\epsilon_{ijkl} \frac{p^l}{m^2} d_1 p^i d_2 p^j d_3 p^k = \sqrt{-g}\epsilon_{ijkl} \frac{d_1 p^i d_2 p^j d_3 p^k}{-p_0},$$

where $p_0 = g_{0i} p^i$. If dN defines the number of world lines crossing dV at x with 4-momenta in the range dP, one can use the following relation to define the distribution function (Lindquist (1966)),

$$dN = f(x, \mathbf{p})(-\mathbf{p} \cdot \mathbf{u})dV\, dP,$$

where $\mathbf{u}$ is any arbitrary timelike unit vector for which $\mathbf{u} \cdot \mathbf{u} \equiv u^i u_i = -1$ and $u^0 > 0$ holds. The necessity of the additional factor $(-\mathbf{p} \cdot \mathbf{u})$ is explained in Lindquist (1966).

Assuming the particles paths are geodesics leads to the following expressions for the particle trajectory and momentum as follows (Lindquist (1966)),

$$\frac{dx^i}{d\tau} = p^i$$

$$\frac{dp^i}{d\tau} = -\Gamma^i_{jk}p^k p^j.$$

Denote dW the 4-volume element spanned by dV and dP. Furthermore be $\mathbf{dx} = \mathbf{p}\delta\tau$ an infinitesimal displacement along a family of world lines, the following identity can be applied to express the 4-volume element (Lindquist (1966))

$$dW = (-\mathbf{u} \cdot \mathbf{dx})dV = (-\mathbf{p} \cdot \mathbf{u})dV d\tau.$$

Lindquist (1966) showed that $(-\mathbf{p} \cdot \mathbf{u})dV dP$ remains invariant along a given set of trajectories (Louisville's Theorem). It follows from this expression that the total change in the number of world lines within $dW dP$ can be expressed in terms of the change of the distribution function due to (a) transport (Lindquist (1966)),

$$\begin{aligned}
\delta(dN) &= \left(\frac{\partial f}{\partial x^i}dx^i + \frac{\partial f}{\partial p^i}dp^i\right)(-\mathbf{p} \cdot \mathbf{u})dV dP \\
&= \left(p^i\frac{\partial f}{\partial x^i} - \Gamma^i_{jk}p^k p^j\frac{\partial f}{\partial p^i}\right)dW dP,
\end{aligned}$$

and (b) interactions within dW that destroy and create particles and change the particle number via scattering, denoted as *collision term* on the right hand side. This leads to the Boltzmann transport equation (Lindquist (1966)),

$$p^i D_i(f) = \left(\frac{df}{d\tau}\right)_{\text{collisions}}, \tag{2.14}$$

using the derivative D_i defined in the section above. The left hand side of this expression is the directional derivative of f along the phase flow and denotes the phase-space transport of f. The collision term will be further discussed at the example of neutrino transport in spherical symmetry in §2.1.3.

2.2.3   Boltzmann transport in spherical symmetry

The above expressions for the transport of particles(radiation) can be written in an explicit way for the spherical symmetry case based on the line-element (2.5). The following representation of the 4-momenta is used,

$$p^0 = E, \quad p^1 = E\,\cos\theta, \quad p^2 = E\,\sin\theta\,\cos\varphi, \quad p^3 = E\,\sin\theta\,\sin\varphi,$$

for which the following useful relations hold

$$
\begin{aligned}
d^3p &= p^2 dE \sin\theta\, d\theta\, d\varphi, = E^2\, dE\, d\mu\, d\varphi, \\
p^0 d^3p &= E^3 dE\, d\mu\, d\varphi, \\
\frac{p^1}{p^0} d^3p &= E^2 dE\, \mu d\mu\, d\varphi, \\
p^1 d^3p &= E^3 dE\, \mu d\mu\, d\varphi,
\end{aligned}
$$

where $\mu = \cos\theta$ is the cosine of the propagation angle. The distribution function $f(t, a, E, \mu)$ depends on the spacetime and the momentum space coordinates, which in spherical symmetry are the time and baryon density (t, a) and the particle energy and the cosine of the propagation angle (E, μ) respectively. Applying this representation to the transport equation (2.14), the following form can be obtained (Lindquist (1966))

$$
\begin{aligned}
e^{-\phi}\frac{\partial f}{\partial t} &= \frac{e^{-\Lambda}}{r'}\mu\frac{\partial f}{\partial a} \\
&+ (1-\mu^2)\left[-\frac{\Gamma}{r'}\frac{\partial\phi}{\partial a} + \frac{\Gamma}{r} + \mu\left(\frac{u}{r} - e^{-\phi}\frac{\partial\Lambda}{\partial t}\right)\right]\frac{\partial f}{\partial\mu} \\
&- E\left(\mu\frac{e^{-\Lambda}}{r'}\frac{\partial\phi}{\partial a} + \mu^2 e^{-\phi}\frac{\partial\Lambda}{\partial t} + (1-\mu^2)\frac{u}{r}\right)\frac{\partial f}{\partial E} \\
&- \left(e^{-\phi}\frac{df}{dt}\right)_{\text{collision}}.
\end{aligned}
$$

This equation was expressed in terms of Lagrangian coordinates by Castor (1972) and Yamada et al. (1999). They obtained the following form of the Boltzmann equation in spherical symmetry

$$
\begin{aligned}
\frac{\partial F}{\alpha\partial t} &= \frac{\mu}{\alpha}\frac{\partial}{\partial a}\left(4\pi r^2\alpha\rho F\right) \\
&+ (1-\mu^2)\left\{\mu\left(\frac{3u}{r} + \frac{\partial\ln\rho}{\alpha\partial t}\right) + \Gamma\left(\frac{1}{r} - \frac{1}{\alpha}\frac{\partial\alpha}{\partial r}\right)\right\}\frac{\partial F}{\partial\mu} \\
&+ \left\{(1-3\mu^2)\left(\frac{\partial\ln\rho}{\alpha\partial t} + \frac{3u}{r}\right) - 2\mu\Gamma\left(\frac{1}{r} - \frac{1}{\alpha}\frac{\partial\alpha}{\partial r}\right)\right\}F \\
&- \mu\Gamma\frac{1}{\alpha}\frac{\partial\alpha}{\partial r}\frac{1}{E^2}\frac{\partial}{\partial E}\left(E^3 F\right) \\
&+ \left[\mu^2\left(\frac{\partial\ln\rho}{\alpha\partial t} + \frac{3u}{r}\right) - \frac{u}{r}\right]\frac{1}{E^2}\frac{\partial}{\partial E}\left(E^3 F\right) \\
&+ \left(\frac{dF}{\alpha dt}\right)_{\text{collision}}
\end{aligned}
\tag{2.15}
$$

$$
\begin{aligned}
=\ & \frac{\mu}{\alpha}\frac{\partial}{\partial a}\left(4\pi r^2 \alpha\rho F\right)\\[2mm]
+\ & \Gamma\left(\frac{1}{r}-\frac{1}{\alpha}\frac{\partial\alpha}{\partial r}\right)\frac{\partial}{\partial\mu}\left[\left(1-\mu^2\right)F\right]\\[2mm]
+\ & \left(\frac{\partial\ln\rho}{\alpha\partial t}+\frac{3u}{r}\right)\frac{\partial}{\partial\mu}\left[\mu\left(1-\mu^2\right)F\right]\\[2mm]
-\ & \mu\Gamma\frac{1}{\alpha}\frac{\partial\alpha}{\partial r}\frac{1}{E^2}\frac{\partial}{\partial E}\left(E^3 F\right)\\[2mm]
+\ & \left[\mu^2\left(\frac{\partial\ln\rho}{\alpha\partial t}+\frac{3u}{r}\right)-\frac{u}{r}\right]\frac{1}{E^2}\frac{\partial}{\partial E}\left(E^3 F\right)\\[4mm]
+\ & \left(\frac{dF}{\alpha dt}\right)_{\text{collision}},
\end{aligned}
\tag{2.16}
$$

for the specific distribution function $F(t,a,E,\mu) = f(t,a,E,\mu)/\rho$ and the settings defined already in the previous section, i.e. $\alpha = e^\phi$ and $\Gamma = e^\Lambda$ (see for example Liebendörfer et al. (2001a) and Liebendörfer et al. (2004)).

2.2.4   The moment equations

Following the standard framework applied for the derivation of the Boltzmann transport equation above, one can define a particle(radiation) flux 4-vector in the general relativistic framework as follows (Lindquist (1966))

$$
n^i(x) = \int_{-\infty}^{\infty} d^3p\, p^i f(x, \mathbf{p}).
$$

Furthermore, integrating over the Boltzmann equation with the same measure of integration yields (Lindquist (1966))

$$
\int_{-\infty}^{\infty} d^3p\left\{p^i\frac{\partial f}{\partial x^i}-\Gamma_{ik}^j p^i p^k\frac{\partial f}{\partial p^j}\right\} = \frac{\partial n^i}{\partial x^i}+\Gamma_{ik}^i n^k
\tag{2.17}
$$

$$
= \nabla_i n^i = \int_{-\infty}^{\infty} d^3p\left(\frac{df}{d\tau}\right)_{\text{collision}}.
\tag{2.18}
$$

This is the first momentum equation of the Boltzmann transport equation. It relates the changes in the particle(radiation) flux to the source terms on the right hand side. This continuity equation is not zero, in other words the particle(radiation) flux is by definition not conserved, because of the emission and absorption of particles(radiation) as a consequence of interactions with the background matter field taken into account in the collision term. Integrating over the Boltzmann equation with a different measure and using the definition of the stress-energy tensor for the particles(radiation)

introduced in Lindquist (1966) as follows,

$$T^{ik}(x) = \int_{-\infty}^{\infty} d^3p \, p^i p^k f(x, \mathbf{p}),$$

one finds the following relations for the equation of energy and momentum conservation for the radiation field (Lindquist (1966))

$$
\begin{aligned}
\int_{-\infty}^{\infty} d^3p \left\{ p^m p^k \frac{\partial f}{\partial x^k} - p^m \Gamma^j_{ik} p^i p^k \frac{\partial f}{\partial p^j} \right\} &= \frac{\partial T^{mk}}{\partial x^k} + \Gamma^i_{ik} T^{mk} + \Gamma^m_{ik} T^{ik} \\
&= \nabla_k T^{mk} = \int_{-\infty}^{\infty} d^3p \, p^m \left(\frac{df}{d\tau} \right)_{\text{collision}}.
\end{aligned}
$$

The stress-energy tensor is not conserved for the same reasons that apply for the particle(radiation) flux.

These phase-space integral expressions can be written in spherical symmetry in terms of the zeroth and first μ moments (number moments) of the distribution function defined as follows (Liebendörfer et al. (2004))

$$
\begin{aligned}
J^{\text{N}} &= \int_{-1}^{+1} d\mu \int_0^{\infty} E^2 dE \; F(t, a, \mu, E), & (2.19) \\
H^{\text{N}} &= \int_{-1}^{+1} \mu d\mu \int_0^{\infty} E^2 dE \; F(t, a, \mu, E). & (2.20)
\end{aligned}
$$

Using these expressions and integrating over the Boltzmann equation (2.16), the continuity equation takes the following form in the spherically symmetric case (Liebendörfer et al. (2004))

$$
\frac{\partial J^{\text{N}}}{\partial t} + \frac{\partial}{\partial a} \left(4\pi r^2 \alpha \rho H^{\text{N}} \right) = \alpha \int_{-1}^{+1} d\mu \int_0^{\infty} E^2 dE \; \left(\frac{dF}{dt} \right)_{\text{collision}}, \qquad (2.21)
$$

for the particle number density J and the particle flux H. Note that integrating over the Boltzmann equation, the terms containing $(1 - \mu^2)$ do not contribute because these terms vanish for $\mu = \pm 1$. The same holds for the terms containing $E^3 F$ which vanish at $E = 0$ and $E = \infty$.

The same argumentation applied using different integral measures leads to the evolution equations for the energy moments of the distribution function (Liebendörfer et al.

(2004))

$$J = \int_{-1}^{+1} d\mu \int_0^\infty E^3 dE \; F(t, a, \mu, E),$$

$$H = \int_{-1}^{+1} \mu d\mu \int_0^\infty E^3 dE \; F(t, a, \mu, E),$$

$$K = \int_{-1}^{+1} \mu^2 d\mu \int_0^\infty E^3 dE \; F(t, a, \mu, E),$$

$$Q = \int_{-1}^{+1} \mu^3 d\mu \int_0^\infty E^3 dE \; F(t, a, \mu, E).$$

Integrating the Boltzmann equation (2.16) applying the integration measure E^3, leads to the equation for the radiation energy (Castor (1972), Liebendörfer et al. (2004))

$$\frac{\partial J}{\alpha \partial t} = \frac{1}{\alpha} \frac{\partial}{\partial a} \left(4\pi r^2 \alpha \rho H \right) + \frac{\partial \ln \rho}{\alpha \partial t} K - \frac{u}{r}(J - 3K) - 2\Gamma \frac{\partial \alpha}{\alpha \partial r} H$$
$$+ \int_{-1}^{+1} d\mu \int_0^\infty E^3 dE \left(\frac{dF}{dt} \right)_{\text{collision}},$$

where applying the integration measure μE^3 leads to the the radiative contribution to the lapse function (Castor (1972), Liebendörfer et al. (2004))

$$\frac{\partial H}{\alpha \partial t} = \frac{1}{\alpha} \frac{\partial}{\partial a} \left(4\pi r^2 \alpha \rho K \right) - \Gamma \left(\frac{1}{r} - \frac{\partial \alpha}{\alpha \partial r} \right) (J - K) + \Gamma \frac{\partial \alpha}{\alpha \partial r} K$$
$$+ \int_{-1}^{+1} \mu \, d\mu \int_0^\infty E^3 dE \left(\frac{dF}{dt} \right)_{\text{collision}},$$

where the terms with μ^3 which correspond to Q cancel each other and hence Q does not appear in the final expression. Furthermore, using the integral measure $E^3(u + \Gamma \mu)$ leads to the momentum evolution equation (Liebendörfer et al. (2004))

$$\frac{\partial}{\partial t}(uJ + \Gamma H) = -\frac{\partial}{\partial a} \left(4\pi r^2 \alpha \rho (\Gamma K + uH) \right)$$
$$- \frac{\alpha}{r} \left\{ (J + 3K)\frac{m}{r} - \left(1 - \frac{2m}{r} \right)(J - 3K) - 2K \right\}$$
$$- \frac{\alpha}{r} \left\{ 4\pi r^2 \left(J(p + \rho K) + (1 + e + J)\rho K - 2\rho H^2 \right) \right\}$$
$$+ \alpha u \int_{-1}^{+1} d\mu \int_0^\infty E^3 dE \left(\frac{df}{dt} \right)_{\text{collision}}$$
$$+ \alpha \Gamma \int_{-1}^{+1} \mu d\mu \int_0^\infty E^3 dE \left(\frac{dF}{dt} \right)_{\text{collision}}.$$

The system of equations is far from being complete. Most importantly, the coupling of the radiation field to the fluid equations is missing. This will be done in the next section, in combination with radiation-matter interactions which determine the collision term on the right hand side of the Boltzmann equation and hence the integrals of the collision terms in the momentum equations.

2.3 Coupling between radiation field and matter

In the following subsections I will first sketch the derivation of the full set of radiation-hydrodynamics equations. Below I will introduce the various neutrino-matter interactions that are used in core collapse supernova models.

2.3.1 The full picture

The stress-energy tensor of the hydrodynamic system (2.2) is modified due to the additional presence of radiative contributions as follows (Liebendörfer et al. (2004))

$$
\begin{aligned}
T^{tt} &= \rho(1 + e + J), \\
T^{aa} &= p + \rho K, \\
T^{\vartheta\vartheta} = T^{\varphi\varphi} &= p + \frac{1}{2}\rho(J - K).
\end{aligned}
$$

The additional contribution for the antisymmetric component accounting for the energy flux (Liebendörfer et al. (2004))

$$
T^{ta} = T^{at} = \rho H.
$$

The hydrodynamic quantities (ρ, e, p), density, internal energy and pressure have already been defined above. The radiation contributions, i.e. (J, K, H), are the neutrino moments and represent the internal energy density, pressure and energy exchange contributions. Following the same procedure as above, the equations for energy and momentum conservation take the following now modified form due to the appearance of additional terms from the radiation contributions (Liebendörfer et al. (2001a))

$$
\frac{1}{\rho}\nabla_i T^{it} = \frac{\partial}{\alpha\partial t}(e+J)+(p+\rho K)\frac{\partial}{\alpha\partial t}\left(\frac{1}{\rho}\right)+\frac{1}{\alpha^2}\frac{\partial}{\partial a}\left(4\pi r^2\rho H\alpha^2\right)+\frac{u}{r}(J-3K) = 0, \quad (2.22)
$$

$$
\frac{r'}{\Gamma}\frac{1}{\rho}\nabla_i T^{ia} = \frac{1}{\rho}\frac{\partial}{\partial a}(p + \rho K) + \left(1 + e + \frac{p+\rho K}{\rho}\right)\Phi' + \frac{r'}{r}(J - 3K) = 0. \quad (2.23)
$$

The full set of equations are given in Liebendörfer et al. (2004), where the conservation equations for the neutrino momenta (the momentum equations) are subtracted from the

corresponding radiation-hydrodynamics conservation equations to achieve the evolution of the pure hydrodynamic quantities. The resulting set of conservation equations for the hydrodynamic variables, such as total and internal energy, momentum, gravitational mass and the lapse function, also contain contributions from radiation-matter interactions due to energy and momentum exchange. The collision term becomes important and its specific form will be discussed in the following subsection.

2.3.2 The collision term

The most important neutrino-matter interactions that are typically considered in core collapse supernova models go back to the early 1970th as explored in Tubbs and Schramm (1975), Yueh and Buchler (1976a), Yueh and Buchler (1976b) and Yueh and Buchler (1977) which are further developed by Schinder and Shapiro (1982) and later Bruenn (1985). These interactions are calculated via the momentum integrated reaction rates $R_{p_i + p_j \to p_k + p_l}$ weighted by the particles distribution functions f and correspondingly the blocking factors $(1 - f)$ as follows [3]

$$\int \frac{d^3 p_i}{(2\pi)^3} \int \frac{d^3 p_j}{(2\pi)^3} \int \frac{d^3 p_k}{(2\pi)^3} \left(f_i f_j \left(1 - f_k \right) \left(1 - f_l \right) R_{p_i + p_j \to p_k + p_l} \right.$$
$$\left. + \left(1 - f_i \right) \left(1 - f_j \right) f_k \, f_l R_{p_k + p_l \to p_i + p_j} \right).$$

In the standard framework used in the literature, the integration of the final state neutrino f_ν or blocking $(1 - f_\nu)$ is taken into account when the reaction rates are implemented into the collision term on the right hand side of the transport equation as follows

$$\left(\frac{dF(\mu, E)}{dt} \right)_{\text{collision}} = \Omega(F)_{\text{AE}} + \Omega(F)_{\text{IS}} + \Omega(F)_{\text{NLS}} + \Omega(F)_{\text{PAIR}},$$

where the different contributions are given as follows:

1. Neutrino emission and absorption:

$$\Omega(F)_{\text{AE}} = j(E) \left(\frac{1}{\rho} - F(\mu, E) \right) - \chi(E) F(\mu, E) = \frac{j(E)}{\rho} - \tilde{\chi}(E) F(\mu, E)$$

2. Iso-energetic neutrino-nucleon/nuclei scattering:

$$\Omega(F)_{\text{IS}} = \frac{E^2}{c(hc)^3} \int_{-1}^{+1} d\mu' \, R_{\text{IS}}(\mu', \mu, E) \, F(\mu', E) - \frac{E^2 F(\mu, E)}{c(hc)^3} \int_{-1}^{+1} d\mu' \, R_{\text{IS}}(\mu', \mu, E)$$

---

[3]Since the leptons and baryons involved obey Fermi-Dirac statistics, the particles distribution function are given as follows $f_i \equiv f_i(E_i) = \left(\exp \left\{ \frac{E_i - \mu_i}{k_{\text{B}} T} \right\} + 1 \right)^{-1}$ with particle energy E_i, chemical potential μ_i and temperature T

3. Neutrino-lepton (electron/positron) scattering:

$$
\Omega(F)_{\mathrm{NLS}} = \left(\frac{1}{\rho} - F(\mu, E) \right) \frac{1}{c(hc)^3} \int_0^\infty E'^2 \, dE' \int_{-1}^{+1} d\mu' \, R_{\mathrm{NLS}}^{\mathrm{in}}(\mu, \mu', E, E') \, F(\mu', E')
$$
$$
- F(\mu, E) \frac{1}{c(hc)^3} \int_0^\infty E'^2 \, dE' \int_{-1}^{+1} d\mu' \, R_{\mathrm{NLS}}^{\mathrm{out}}(\mu, \mu', E, E') \left(\frac{1}{\rho} - F(\mu', E') \right)
$$

4. Neutrino pair processes:

$$
\Omega(F)_{\mathrm{PAIR}} = \left(\frac{1}{\rho} - F(\mu, E) \right) \frac{1}{c(hc)^3} \int_0^\infty E'^2 \, dE' \int_{-1}^{+1} d\mu' F(\mu', E')
$$
$$
R_{\mathrm{PAIR}}^{\mathrm{p}}(E, E', \mu, \mu') \left(\frac{1}{\rho} - \bar{F}(\mu', E') \right)
$$
$$
- F(\mu, E) \frac{1}{c(hc)^3} \int_0^\infty E'^2 \, dE' \int_{-1}^{+1} d\mu' \, R_{\mathrm{PAIR}}^{\mathrm{a}}(E, E', \mu, \mu') \bar{F}(\mu', E'),
$$

where $\bar{F}$ is the antineutrino distribution function entering the pair-production kernel integration for the corresponding neutrino.

The angle θ defines the angle between the incident and emergent neutrino angle and is given by the following relation (Bruenn (1985))

$$
\cos \theta \equiv \omega = \mu \mu' + \sqrt{(1 - \mu^2)(1 - \mu'^2)} \cos \phi,
$$

where ϕ is the relative azimuthal angle of one neutrino to the other.

The calculation of the reaction rates, emissivity j, absorptivity χ, the scattering kernels for iso-energetic neutrino-nucleon/nuclei scattering R_{IS}, neutrino lepton scattering R_{NLS} (which is the sum of neutrino electron and positron scattering $R_{\mathrm{NES/NPS}}$) and the pair production kernels R_{PAIR} will be sketched in the subsection below. Note that the rates $R_{\mathrm{NES/NPS}}$ and R_{PAIR} depend not only on μ' and E' which are integrated as shown above, but the rates depend also on ϕ. The dimensional reductions must be performed before being placed in the Boltzmann equation.

2.4   Neutrino matter interactions

In the following subsections, I will introduce and sketch the derivation of the neutrino-matter interaction rates used in our model as well as their explicit form.

2.4.1   The charged current reactions

The charged current reaction rates, e.g. the emission and absorption of electron flavour neutrinos on the free nucleons and nuclei, are calculated via the neutrino energy E dependent absorptivity χ and emissivity j as follows (see Yueh and Buchler (1976b),Bruenn (1985))

$$
\begin{aligned}
\chi(E) \quad &\equiv \quad \frac{1}{c}\, n_n\, \langle \sigma v \rangle \\
&= \quad \int \frac{d^3 p_n}{(2\pi)^3} 2 f_n(E_n)\; R_{p_{\nu_e}+p_n \to p_e+p_p} \int \frac{d^3 p_p}{(2\pi)^3} \int \frac{d^3 p_e}{(2\pi)^3} \left\{ (1 - f_p(E_p))(1 - f_e(E_e)) \right\}, \\
j(E) \quad &\equiv \quad \frac{1}{c}\, n_e n_p\, \langle \sigma v \rangle \\
&= \quad \int \frac{d^3 p_p}{(2\pi)^3} \int \frac{d^3 p_n}{(2\pi)^3} \int \frac{d^3 p_e}{(2\pi)^3} \left\{ 2 f_p(E_p)\, 2 f_e(E_e)\, (1 - f_n(E_n))\; R_{p_e+p_p \to p_n+p_{\nu_e}} \right\},
\end{aligned}
$$

where $\langle \sigma v \rangle$ are the cross sections and the number densities have been expressed in terms of the distribution functions as follows (equivalent for all fermions)

$$
\begin{aligned}
dn(p) &= \frac{d^3 p}{(2\pi)^3}\, 2\, f_n(E), \\
dn(p') &= \frac{d^3 p}{(2\pi)^3}\, (1 - f_n(E)),
\end{aligned}
$$

and the factor 2 relate to the spin degeneracy of the initial state (Tubbs and Schramm (1975)). Emissivity and absorptivity are reverse reactions and can be related via the detailed balance relation (Bruenn (1985)) as follows

$$
\chi(E) = \exp \left\{ \frac{E - (\mu_p - \mu_n + \mu_e)}{kT} \right\} j(E),
$$

which follows from the expression that relates the spin of the interacting particles, i.e. $(2s_i + 1)(2s_j + 1) R_{p_i+p_j \to p_k+p_l} = (2s_k + 1)(2s_l + 1) R_{p_k+p_l \to p_i+p_j}$. Note that the chemical potentials contain the kinetic contributions and the rest mass. They can be written as follows

$$
\begin{aligned}
\mu_n &= \mu_n^0 + m_n, \\
\mu_p &= \mu_p^0 + m_p.
\end{aligned}
$$

The same integrals hold for the emission and absorption of *electron-antineutrinos*, by replacing the corresponding distribution functions and the chemical potentials in the expression above and hence the following expression for the detailed balance can be obtained

$$
\bar{\chi}(E) = \exp \left\{ \frac{E - (\mu_n - \mu_p - \mu_e)}{kT} \right\} \bar{j}(E),
$$

for the electron-antineutrinos. The calculation of the reaction rates is based on the theory of weak interactions. The total emissivity and opacity for electron-(anti)neutrinos are obtained by summing up the contributions from capture reactions on the free nucleons and nuclei, i.e.

$$
\begin{aligned}
j &= j_{\text{nucleons}} + j_{\text{nuclei}}, \\
\bar{j} &= \bar{j}_{\text{nucleons}} + \bar{j}_{\text{nuclei}},
\end{aligned}
$$

where detailed balance is applied for the calculation of the reverse reaction rates $(\chi, \bar{\chi})$.

Reaction 1 $\nu_e + n \leftrightarrow p + e^-$ $(j_{nucleons},\ \chi_{nucleons})$

Electron captures and the reverse reaction, i.e. electron-neutrino captures, are charged currents which are due to the exchange of a W^--boson. The weak interaction process can be related to the $\beta^\pm$-decay, where the substructure of the nucleons (i.e. up-quarks and down-quarks) change flavour via the emission of a $W^\pm$-boson as follows

$$
\begin{aligned}
d &\rightarrow d \\
u &\rightarrow u \\
d &\rightarrow u \quad + \quad W^- \rightarrow e^- + \nu_e,
\end{aligned}
$$

and

$$
\begin{aligned}
u &\rightarrow u \\
d &\rightarrow d \\
u &\rightarrow d \quad + \quad W^+ \rightarrow e^+ + \bar{\nu}_e,
\end{aligned}
$$

where the $W^\pm$-bosons decay into an electron(positron) and an electron-(anti)neutrino[4]. Electron captures can be understood in the same way, where the interaction of an electron with a up-quark inside the proton cause the electron to decay into a W^--boson which in turn changed the quark flavour from an up- to a down-quark and emits an electron-neutrino.

The matrix element for the absorption of electron-neutrinos on free neutrons is given by (Bruenn (1985))

$$
M = \frac{G}{\sqrt{2}} \bar{u}_p(p_p) \gamma^k \left(g_V - g_A \gamma^5 \right) u_n(p_n) \bar{u}_e(p_{e^-}) \gamma_k \left(1 - \gamma_5 \right) u_{\nu_e}(p_{\nu_e}), \tag{2.24}
$$

where $g_V = 1$ is the vector coupling constant and $g_A = 1.23 \pm 0.03$ is the axial-vector coupling constant in the limit of zero momentum transfer and where γ^μ are the usual

---

[4]The W-boson was discovered experimentally by C. Rubbia and S. Van der Meer at the CERN facility in 1983. It has a mass of $\simeq 80$ GeV.

$\gamma - 4 \times 4$-matrices used in the standard theory of weak interactions. The spin-averaged and squared matrix element follows straight forward (Bruenn (1985))

$$
\begin{aligned}
\frac{1}{2} \sum_s |M|^2 \;=\;& 16 G^2 \left\{ (g_V + g_A)^2 \, (p_p \cdot p_{e^-}) \, (p_n \cdot p_{\nu_e}) \right. \\
&+ \; (g_V - g_A)^2 \, (p_p \cdot p_{\nu_e}) \, (p_n \cdot p_{e^-}) \\
&- \; \left. (g_V^2 - g_A^2) \, m_n m_p \, (p_{e^-} \cdot p_{\nu_e}) \right\},
\end{aligned}
$$

and the reaction rate can be obtained as follows (Bruenn (1985))

$$
R_{p_{\nu_e} + p_n \to p_{e^-} + p_p} = \frac{\frac{1}{2} \sum_s |M|^2}{16 E E_{e^-} E_p E_n} (2\pi)^4 \delta^4 \left(p_{\nu_e} + p_n - p_{e^-} - p_p \right),
$$

where E is the neutrino energy and E_e, E_p, E_n denote the electron, proton and neutron energy respectively. The momentum-space integration has been performed analytically in Bruenn (1985), by assuming zero momentum transfer and hence replacing

$$
\delta^4 \left(p_{\nu_e} + p_n - p_{e^-} - p_p \right) \to \delta^3 \left(\vec{p}_n - \vec{p}_p \right) \delta \left(E + E_n - E_{e^-} - E_p \right),
$$

and $|\vec{p}_p| \ll m_p$, $|\vec{p}_n| \ll m_n$. The resulting opacity can be calculated as follows (Bruenn (1985))

$$
\chi(E)_{\text{nucleons}} = \frac{G^2}{\pi} \frac{(2\pi)^4}{(hc)^4} \int \frac{2 d^3 p}{(2\pi)^3} f_n(E) \left(1 - f_p(E) \right) \left(g_V^2 + 3 g_A^2 \right) \left(1 - f_{e^-}(E + Q) \right) \times
$$

$$
\times (E + Q)^2 \sqrt{1 - \frac{m_e^2}{(E + Q)^2}}
$$

$$
= \frac{G^2}{\pi} \frac{(2\pi)^4}{(hc)^4} \frac{1}{e^{\frac{\mu_p^0 - \mu_n^0}{kT}} - 1} \int \frac{2 d^3 p}{(2\pi)^3} \left(f_p(E) - f_n(E) \right) \left(g_V^2 + 3 g_A^2 \right) \left(1 - f_{e^-}(E + Q) \right) \times
$$

$$
\times (E + Q)^2 \sqrt{1 - \frac{m_e^2}{(E + Q)^2}}
$$

$$
= \frac{G^2}{\pi} \frac{(2\pi)^4}{(hc)^4} \frac{n_p - n_n}{e^{\frac{\mu_p^0 - \mu_n^0}{kT}} - 1} \left(g_V^2 + 3 g_A^2 \right) \left(1 - f_{e^-}(E + Q) \right) (E + Q)^2 \sqrt{1 - \frac{m_e^2}{(E + Q)^2}}
$$

$$
= \frac{G^2}{\pi} \frac{(2\pi)^4}{(hc)^4} \eta_{np} \left(g_V^2 + 3 g_A^2 \right) \left(1 - f_{e^-}(E + Q) \right) (E + Q)^2 \sqrt{1 - \frac{m_e^2}{(E + Q)^2}},
$$

where n_p and n_n are the number densities for protons and neutrons respectively. $Q = m_n - m_p$ is the restmass difference between neutrons and protons and where $w = p^2/2m$ ($m_n \simeq m_p \equiv m$). The quantity η_{np} takes into account the final state nucleon blocking (degeneracy factor). From this expression and the expression for the detailed balance introduced above, the emissivity can be calculated (Bruenn (1985))

$$j(E)_{\text{nucleons}} = \frac{G^2}{\pi} \frac{(2\pi)^4}{(hc)^4} \eta_{pn}(g_V^2 + 3g_A^2) f_{e^-}(E+Q)(E+Q)^2 \sqrt{1 - \frac{m_e^2}{(E+Q)^2}}.$$

The factor G is the Fermi constant given by the following expression applying the correct units (Bruenn (1985))

$$\frac{G^2(2\pi)^4}{(hc)^4} = 5.18 \times 10^{-44} \text{cm}^2 \text{MeV}^{-2},$$

and hence the units of j and χ are cm^{-1}.

Reaction 2 $\bar{\nu}_e + p \leftrightarrow n + e^+$ $\left(\bar{j}_{nucleons}, \bar{\chi}_{nucleons}\right)$

The capture of electron-antineutrinos is calculated via the exchange of a W^+-boson. Here I will following the same procedure as for the capture of electron-neutrinos based on Bruenn (1985) and list the important quantities for the derivation of the reaction rate. The matrix element for the absorption of electron-antineutrinos on free protons is given by (Bruenn (1985))

$$M = \frac{G}{\sqrt{2}} \bar{u}_n(p_n)\gamma^k \left(g_V - g_A\gamma^5\right) u_p(p_p)\bar{u}_e(p_{e^+})\gamma_k \left(1 - \gamma_5\right) u_{\bar{\nu}_e}(p_{\bar{\nu}_e}),$$

and the squared and spin-averaged matrix element becomes (Bruenn (1985))

$$\begin{aligned}
\frac{1}{2}\sum_s |M|^2 &=& 16G^2 \left\{ (g_V + g_A)^2 \left(p_p \cdot p_{\bar{\nu}_e}\right)\left(p_n \cdot p_{e^+}\right) \right. \\
&& + \quad (g_V - g_A)^2 \left(p_n \cdot p_{\bar{\nu}_e}\right)\left(p_p \cdot p_{e^+}\right) \\
&& \left. - \quad \left(g_V^2 - g_A^2\right) m_n\, m_p \left(p_{e^+} \cdot p_{\bar{\nu}_e}\right) \right\}.
\end{aligned}$$

The reaction rate is given by the following expression (Bruenn (1985))

$$R_{p_{\bar{\nu}_e} + p_p \to p_{e^+} + p_n} = \frac{\frac{1}{2}\sum_s |M|^s}{16 E E_{e^+} E_p E_n} (2\pi)^4 \delta^4 \left(p_{\bar{\nu}_e} + p_p - p_{e^+} - p_n\right).$$

Integrating the reaction rate over the momentum space gives again the expression for the opacity and emissivity for neutrino energies with $E - Q > m_e$ as follows

$$\bar{\chi}(E)_{\text{nucleons}} = \frac{G^2}{\pi} \frac{(2\pi)^4}{(hc)^4} \eta_{pn}(g_V^2 + 3g_A^2)\left(1 - f_{e^+}(E - Q)\right)(E - Q)^2\sqrt{1 - \frac{m_e^2}{(E - Q)^2}},$$

$$\bar{j}(E)_{\text{nucleons}} = \frac{G^2}{\pi} \frac{(2\pi)^4}{(hc)^4} \eta_{np}(g_V^2 + 3g_A^2)f_{e^+}(E - Q)(E - Q)^2\sqrt{1 - \frac{m_e^2}{(E - Q)^2}}.$$

The expressions are similar in comparison to the electron-neutrino absorptivity and emissivity. The difference in the sign for the neutrino energy is due to the different sign of the electron-antineutrino chemical potential which in turn is due to the different sign of the charged (neutron-proton) and positron chemical potentials which are given by the following relations

$$\mu_{e^-} = -\mu_{e^+} \equiv \mu_e$$
$$\mu_{\nu_e} = \mu_e - (\mu_n - \mu_p)$$
$$\mu_{\bar{\nu}_e} = -\mu_e - (\mu_p - \mu_n) = -\mu_{\nu_e}.$$

Here, the nucleon chemical potentials contain the rest mass contributions.

Reaction 3 $\nu_e + A' \leftrightarrow A + e^-$ *(j_{nuclei}, χ_{nuclei})*

The presence of a distribution of nuclei is simplified by a single average nucleus with average atomic mass $A = (N, Z)$ and charge Z and where the configuration of the final nucleus is given by $A' = (N - 1, Z + 1)$. The neutrino and electron capture rates on nuclei can be approximated in a crucial way. Based on the (current)vector operator $J^\mu = \langle A'|J^\mu(0)|A\rangle$, the matrix element is given by the following expression (Bruenn (1985))

$$M = \frac{G}{\sqrt{2}}J^\mu \bar{u}_{\nu_e}(p_{\nu_e})\gamma_\mu(1 - \gamma_5)u_e(p_e),$$

and the spin averaged and squared matrix element becomes (Bruenn (1985))

$$\frac{1}{2}\sum_s |M|^2 = \frac{G^2}{2} \frac{1}{2J_A + 1}\sum_{m_A}\sum_{m_{A'}} J^\mu J^{*\alpha}\left((p_{\nu_e})_{\mu_e}(p_e)_\alpha + (p_{\nu_e})_\alpha(p_e)_\mu\right.$$
$$\left. - p_{\nu_e} \cdot p_e \ g_{\mu\alpha} - i\epsilon_{\beta\mu\delta\alpha}(p_{\nu_e})^\beta(p_e)^\delta\right)$$
$$= \frac{G^2}{2} \frac{1}{2J_A + 1}\sum_{m_A}\sum_{m_{A'}}\left\{|J^0|^2(1 + \vec{u}_e)\cdot\vec{p}_{\nu_e} + |\vec{J}|^2\left(1 - \frac{1}{3}\vec{u}_e \cdot \hat{p}_{\nu_e}\right)\right\},$$

where $\vec{u}_e = \vec{p}_e/E_e$, $\hat{p}_{\nu_e} = \vec{p}_{\nu_e}/E$ and ϵ is a completely asymmetric tensor with $\epsilon_{0123} = 1$. Following the procedure above, the reaction rate is given by the following expression (Bruenn (1985))

$$R_{p_e + p_A \to p_{\nu_e} + p_{A'}} = \frac{\frac{1}{2} \sum_s |M|^2}{E E_e} (2\pi)^4 \delta^4(p_e + p_A - p_{\nu_e} - p_{A'}).$$

Following the argumentation in Bruenn (1985), only contributions with $|\vec{J}|^2$ provide allowed electron captures on nuclei in the ground state which are dominated by $1f_{7/2} \to 1f_{5/2}$ Gammov-Teller resonances, unless the neutron holes are absent (which is the case for $N > 40$). Fuller et al. (1982) estimated the spin summation as follows

$$\frac{1}{2J_A + 1} \sum_{m_A} \sum_{m_{A'}} |\vec{J}|^2 = \frac{N_p N_h}{2J_{A'} + 1} \frac{12}{7} = \frac{2}{7} N_p N_h,$$

where N_p is the number of protons in the single-particle $1f_{5/2}$ level and where N_h is the number of neutron holes in the single-particle $1f_{7/2}$ level. These numbers are predicted from shell-model calculations as follows

$$N_p(Z) = \begin{cases} 0, & Z < 20 \\ Z - 20, & 20 < Z < 28 \\ 8, & Z > 28 \end{cases}$$

$$N_h(N) = \begin{cases} 6, & N < 34 \\ 40 - N, & 34 < N < 40 \\ 0, & N > 40. \end{cases}$$

Applying these simplifications to the calculations, the emissivity takes the following form (Bruenn (1985))

$$j(E) = \frac{2}{7} \frac{G^2}{\pi} \frac{(2\pi)^4}{(hc)^4} n_A g_A^2 N_p(Z) N_h(N) f_e(E + Q')(E + Q')^2 \sqrt{1 - \frac{m_e^2}{(E + Q')^2}},$$

where $n_A = \rho X_A/(m_B A)$ is the number density of the heavy nuclei. For the mean average nucleus A then the following expression holds (Bruenn (1985))

$$Q' = M_{A'}^* - M_A = M_{A'} - M_A + \Delta,$$

where $\Delta \simeq 3$ MeV is the energy of the neutron $1f_{5/2}$ state above the ground state for the nuclei considered. Applying the detailed balance to the emissivity, one obtains the absorptivity as follows (Bruenn (1985))

$$\chi(E) = \frac{2}{7} \frac{G^2}{\pi} \frac{(2\pi)^4}{(hc)^4} n_A g_A^2 N_p(Z) N_h(N) (1 - f_e(E + Q'))(E + Q')^2 \sqrt{1 - \frac{m_e^2}{(E + Q')^2}}$$

$$\times \exp\left\{\frac{\mu_n - \mu_p - Q'}{kT}\right\}.$$

Remark 1 *The simplification of a single nucleus with average atomic mass and charge $\langle A, Z \rangle$ has recently been extended by G.Martinez-Pinedo and K.-H. Langanke, introducing a distribution of nuclei based on NSE-network calculations. They calculate the allowed $1f_{7/2}$ to $1f_{5/2}$ Gammov-Teller transitions using a shell model and tabulate the values for Δ for a large number of nuclei. This improved electron capture scheme has first been used in stellar evolution models in Woosley et al. (2002) where it has been shown to increase the amount of deleptonisation at the end of stellar evolution which was confirmed during the Fe-core collapse phase in core collapse simulations (see Langanke et al. (2003), Hix et al. (2003)).*

2.4.2 Neutral currents 1: scattering reactions

The scattering kernels for in and out scattering are explicitly given by the momentum integration of the corresponding reaction rates including blocking factors as follows (Bruenn (1985))

$$R^{\text{in}}_{\text{NES(NPS),IS}} = \int \frac{d^3 p_t}{(2\pi)^3} \int \frac{d^3 p'_t}{(2\pi)^3} (1 - f_t(E_t)) \, 2 \, f(E'_t) R_{p'_t + p'_\nu \to p_t + p_\nu}$$

$$R^{\text{out}}_{\text{NES(NPS),IS}} = \int \frac{d^3 p_t}{(2\pi)^3} \int \frac{d^3 p'_t}{(2\pi)^3} 2 \, f_t(E_t) \, (1 - f(E'_t)) R_{p_t + p_\nu \to p'_t + p'_\nu}.$$

The neutrino reactions considered here are neutrino-electron(positron) scattering (NES, NPS) and the iso-energetic scattering of neutrinos on nuclei and free nucleons (IS). For the latter reactions I will not distinguish the different neutrino types because the reaction rates are the same.

Reaction 4 $\nu + N \leftrightarrow \nu + N$ (R^N_{IS})

For the iso-energetic scattering of neutrinos on nucleons, the matrix element and the reaction rate take the following form in the standard theory of weak interactions given via the exchange of the neutral Z^0-boson, (Bruenn (1985))

$$M = \frac{G}{\sqrt{2}} \left(\bar{u}_N(p'_N) \, \gamma^k \, \left(h^N_V - h^N_A \gamma_5 \right) \right) \left(\bar{u}_\nu(p'_\nu) \, \gamma_k \, (1 - \gamma_5) u_\nu(p_\nu) \right),$$

$$\begin{aligned}
R_{p_\nu + p_N \to p'_\nu + p'_N} = \quad & \frac{G^2}{E E' E_N E'_N} (2\pi)^4 \delta^4(p_\nu + p_N - p'_\nu - p'_N) \, \times \\
\times \quad & \left\{ \left(h^N_V + h^N_A \right)^2 (p_N \cdot p_\nu) \, (p'_N \cdot p'_\nu) \right. \\
+ \quad & \left(h^N_V - h^N_A \right)^2 (p'_N \cdot p_\nu) \, (p_N \cdot p'_\nu) \\
- \quad & \left. \left((h^N_V)^2 - (h^N_A)^2 \right) m^2_N \, (p_\nu \cdot p'_\nu) \right\},
\end{aligned}$$

where

$$
\begin{aligned}
h_V^p &= \frac{1}{2} - 2\sin^2\theta_{\mathrm{W}}, \\
h_A^p &= \frac{1}{2}\, g_A, \\
h_V^n &= -\frac{1}{2}, \\
h_A^n &= -\frac{1}{2}\, g_A,
\end{aligned}
$$

are the neutral current nucleon form factors which arise from virtual strong interaction processes in the limit of zero-momentum transfer. θ_{W} is the Weinberg-angle. Performing the momentum integration and assuming $\delta^4(p_\nu + p_N - p'_\nu - p'_N) \to \delta\,(E - E')\delta(\vec{p}_N - \vec{p'}_N)$ (zero-momentum transfer), the scattering kernel becomes (Bruenn (1985))

$$
\begin{aligned}
R_{\mathrm{IS}} \left\{\begin{array}{c} \text{in} \\ \text{out} \end{array}\right\}(E,\omega) &\equiv R_{\mathrm{IS}}^N(E,\omega) \\
&= \frac{2\pi G^2}{h}\eta_{NN}\left\{(h_V^N)^2 + 3(h_A^N)^2 + \left((h_V^N)^2 - (h_A^N)^2\right)\omega\right\}\delta(E - E'),
\end{aligned}
$$

where

$$
\begin{aligned}
\eta_{NN} &= \int \frac{2d^3p_N}{(2\pi)^3} f_N(E_N)\left(1 - f_N(E_N)\right) \\
&= \int \frac{2d^3p_N}{(2\pi)^3} \frac{e^{\frac{E_N - \mu_N}{kT}}}{\left(1 + \exp\left\{\frac{E_N - \mu_N}{kT}\right\}\right)^2} \\
&= kT\frac{\partial n_N}{\partial \mu_N} \to \left\{\begin{array}{ll} n_N & \text{non-degenerate } N \\[2mm] \frac{3}{2}kT\frac{n_N}{\mu_N} & \text{degenerate } N. \end{array}\right.
\end{aligned}
$$

Because the derivative can be numerically unstable for degenerate and non-relativistic nucleons, Mezzacappa and Bruenn (1993a) replaced the derivatives and showed that the following expressions are numerically stable

$$
\begin{aligned}
\eta_{NN} &= \frac{3}{2}kT\frac{n_N}{\epsilon_{\mathrm{F}}^N} \\
&= \frac{\frac{3}{2}kT\frac{n_N}{\epsilon_{\mathrm{F}}^N}}{\sqrt{n_N^2 + \left(\frac{3}{2}kT\frac{n_N}{\epsilon_{\mathrm{F}}^N}\right)^2}}n_N \\
&= \frac{\frac{3}{2}\frac{kT}{\epsilon_{\mathrm{F}}^N}}{\sqrt{1 + \left(\frac{3}{2}\frac{kT}{\epsilon_{\mathrm{F}}^N}\right)^2}}n_N.
\end{aligned}
$$

The scattering kernel has to be integrated over ϕ to get the form which enters the Boltzmann equation. Following again Mezzacappa and Bruenn (1993a), the integration results in the following expression for the scattering kernel

$$R_{IS}^N(\mu,\mu',E) = \frac{8\pi^3 G^2}{h}\eta_{NN}\left\{(h_V^N)^2 + 3(h_A^N)^2 + \left((h_V^N)^2 - (h_A^N)^2\right)\mu'\mu\right\},$$

which is the sum of neutrons and protons $NN = (nn, pp)$, i.e.

$$
\begin{aligned}
R_{IS}^N(\mu,\mu',E) &= \frac{8\pi^3 G^2}{h}\left\{\eta_{nn}\left((h_V^n)^2 + 3(h_A^n)^2 + \left((h_V^n)^2 - (h_A^n)^2\right)\mu'\mu\right)\right. \\
&+ \left.\eta_{pp}\left((h_V^p)^2 + 3(h_A^p)^2 + \left((h_V^p)^2 - (h_A^p)^2\right)\mu'\mu\right)\right\}.
\end{aligned}
$$

Reaction 5 $\nu + A \leftrightarrow \nu + A$ (R_{IS}^A)

The iso-energetic scattering of neutrinos on nuclei can be calculated among similar lines. The reaction rate is given by the following expression (Bruenn (1985))

$$
\begin{aligned}
R_{p_\nu + p_A \to p'_\nu + p'_A} &= G^2(2\pi)^4\delta^4(p_\nu + p_A - p'_\nu - p'_A) \\
&\times \frac{1}{2J_A+1}\sum_{m_A}\sum_{m_{A'}}\left\{(J_z^0)^2\left(1 + \hat{p}_\nu\cdot\hat{p}'_\nu\right) + |\vec{J}|^2\left(1 - \frac{1}{3}\hat{p}_\nu\cdot\hat{p}'_\nu\right)\right\},
\end{aligned}
$$

where J_z^k is the neutral current. Following the calculations in Bruenn (1985), the following expression was found for the scattering kernel

$$
\begin{aligned}
R_{IS}\left\{\begin{array}{c}\text{in}\\\text{out}\end{array}\right\}(E,\omega) &\equiv R_{IS}^A(E,\omega) \\
&= \frac{(2\pi)^2 G^2}{h}n_A A^2\left(C_{V,0} + \frac{1}{2}\frac{N-Z}{A}C_{V,1}\right)^2(1-\omega)e^{-4bE^2(1-\omega)} \\
&\times \delta(E - E'),
\end{aligned}
$$

where $C_{i,0} = \frac{1}{2}(h_i^p + h_i^n)$ and $C_{i,1} = \frac{1}{2}(h_i^p - h_i^n)$ for $i = (V,A)$ and where $n_A = \rho X_A/m_B A$ is the number density of nuclei. The quantity b is given by $b = 4.8\times10^{-6}A^{2/3}$. Performing the ϕ-integration to obtain the the scattering kernel which is used in the Boltzmann equation, one obtains (Bruenn (1985))

$$
\begin{aligned}
R_{IS}^A(\mu,\mu',E) &= \frac{8\pi^3 G^2}{h}n_A A^2\left(C_{V,0} + \frac{1}{2}\frac{N-Z}{A}C_{V,1}\right)^2 e^{-4bE^2(1-\mu\mu')} \\
&\times \left\{(1-\mu\mu')I_0\left(4bE^2\sqrt{(1-\mu^2)(1-\mu'^2)}\right)\right. \\
&+ \left.\sqrt{(1-\mu^2)(1-\mu'^2)}I_1\left(4bE^2\sqrt{(1-\mu^2)(1-\mu'^2)}\right)\right\},
\end{aligned}
$$

where $I_{0,1}$ are the Bessel-functions of the first kind of order (0,1) which appear from the ϕ-integration.

Remark 2 *Corrections from ion-ion-correlations for the scattering of neutrinos at nuclei are included via a multiplicative factor, the s-factor, following Itoh et al. (2004).*

Reaction 6 $\nu_e + e^- \leftrightarrow \nu'_e + e'^-$ $(R_{NES}^{in/out})$

Let us first consider the in-scattering kernel for the electron-neutrinos. The matrix elements for the exchange of a W- and a Z-boson are given by the following two expressions (Bruenn (1985))

$$M_W = \frac{G}{\sqrt{2}} \left(\bar{u}_{\nu_e}(p'_{\nu_e})\gamma^k(1-\gamma_5)u_{e^-}(p_{e^-}) \right) \left(\bar{u}_{e^-}(p'_{e^-})\gamma_k(1-\gamma_5)u_{\nu_e}(p_{\nu_e}) \right),$$

$$M_Z = \frac{G}{\sqrt{2}} \left(\bar{u}_{\nu_e}(p'_{\nu_e})\gamma^k(1-\gamma_5)u_{\nu_e}(p_{\nu_e}) \right) \left(\bar{u}_{e^-}(p'_{e^-})\gamma_k(a-b\gamma_5)u_{e^-}(p_{e^-}) \right),$$

where $a = -\frac{1}{2}\sin\theta_W$ and $b = -\frac{1}{2}$ and hence the total matrix element reads (Bruenn (1985))

$$M = \frac{G}{\sqrt{2}} \left(\bar{u}_{\nu_e}(p'_{\nu_e})\gamma^k(1-\gamma_5)u_{\nu_e}(p_{\nu_e}) \right) \left(\bar{u}_{e^-}(p'_{e^-})\gamma_k(C_V-C_A\gamma_5)u_{e^-}(p_{e^-}) \right),$$

where the vector and axial-vector coupling constants are given as follows (Bruenn (1985))

$$C_V = a+1 = \frac{1}{2} + 2\sin\theta_W,$$
$$C_A = b+1 = \frac{1}{2}.$$

The squared and spin-averaged matrix element is given by the following expression (Bruenn (1985))

$$\sum_{\text{spin}} |M|^2 = 32G^2 \left\{ (C_V+C_A)^2 (p_{\nu_e} \cdot p_{e^-})(p'_{\nu_e} \cdot p'_{e^-}) \right.$$
$$+ (C_V-C_A)^2 (p_{\nu_e} \cdot p'_{e^-})(p'_{\nu_e} \cdot p_{e^-})$$
$$\left. - (C_V^2-C_A^2)m_e^2 (p_{\nu_e} \cdot p'_{\nu_e}) \right\},$$

and the transition rate reads

$$R_{p_{\nu_e}+p_{e^-}\to p'_{\nu_e}+p'_{e^-}} = \frac{G^2}{EE'E_{e^-}E'_{e^-}}(2\pi)^4\delta^4(p_{\nu_e}+p_{e^-}-p_{\nu_e}-p_{e^-})$$
$$\times \left(\beta_1(p_{e^-} \cdot p_{\nu_e})(p'_{e^-} \cdot p'_{\nu_e}) + \beta_2(p'_{e^-} \cdot p_{\nu_e})(p_{e^-} \cdot p'_{\nu_e}) - \beta_3 m_e^2(p_{\nu_e} \cdot p'_{\nu_e}) \right)$$

where $\beta_1 = (C_V + C_A)^2$, $\beta_2 = (C_V - C_A)^2$, $\beta_3 = C_V^2 - C_A^2$ and where the Fermi constant G^2 is given by (Bruenn (1985))

$$G^2 \equiv \left[c(\hbar c)^2 \right] G^2 = 1.55 \times 10^{-33} \text{cm}^3 \text{MeV}^{-2}\text{s}^{-1}.$$

An expression for the scattering kernel can be obtained directly from the integration of the reaction rate over the corresponding initial and final electron momenta (Schinder and Shapiro (1982))

$$R_{\text{NES}}^{\text{out}}(E, E', \omega) = \frac{1}{2} \frac{1}{(2\pi)^3} \frac{\pi\sigma_0 c}{(m_e c^2)^2} \frac{1}{EE'} \left(\beta_1 I_1(E, E', \omega) + \beta_2 I_2(E, E', \omega) + \beta_3 I_3(E, E', \omega) \right),$$

where (see Tubbs and Schramm (1975))

$$\sigma_0 = \frac{4G^2 m_e^2 \hbar^2}{\pi c} = 1.764 \times 10^{-44} \text{cm}^2.$$

The I_i are the phase-space integrated products of the momenta of the squared and spin averaged matrix element, weighted with the electron distribution functions and blocking factors, as follows (Schinder and Shapiro (1982))

$$I_i = \int \frac{d^3 p_{e^-}}{2E_{e^-}} f(E_{e^-}) \int \frac{d^3 p'_{e^-}}{2E'_{e^-}} (1 - f(E'_{e^-})) \int \frac{d^3 p_{\nu_e^-}}{2E'} M_i \, \delta^4(p_{\nu_e} + p_{e^-} - p_{\nu_e} - p_{e^-}),$$

where the products of the momenta are give by

$$
\begin{aligned}
M_1 &= (p_{e^-} \cdot p_{\nu_e}) \left(p'_{e^-} \cdot p'_{\nu_e} \right), \\
M_2 &= (p'_{e^-} \cdot p_{\nu_e}) \left(p_{e^-} \cdot p'_{\nu_e} \right), \\
M_3 &= m_e^2 \left(p_{\nu_e} \cdot p'_{\nu_e} \right).
\end{aligned}
$$

The integrations are done in the rest frame of the fluid and following Tubbs and Schramm (1975), Tubbs (1978) and Yueh and Buchler (1976a) the following expressions are obtained

$$
\begin{aligned}
I_1(E, E', \omega) &= \frac{2\pi k_{\text{B}} T E^2 E'^2 (1-\omega)^2}{\Delta^5} f(E' - E) \times \\
&\times \left\{ A(k_{\text{B}}T)^2 \left(G_2(y) + 2yG_1(y) + y^2 G_0(y) \right) \right. \\
&+ B(k_{\text{B}}T) \left(G_1(y) + yG_0(y) \right) + C G_0(y) \} \\
I_2(E, E', \omega) &= I_1(E \to -E', E' \to -E, \omega) \\
I_3(E, E', \omega) &= \frac{2\pi(k_{\text{B}}T)EE'(1-\omega)(m_e c^2)^2}{\Delta} f(E' - E) G_0(y),
\end{aligned}
$$

where

$$
\begin{aligned}
\Delta &= \sqrt{E^2 + E'^2 - 2EE'\omega}, \\
y &= \frac{1}{k_{\mathrm{B}}T}\left(-\frac{E - E'}{2} + \frac{\Delta}{2}\sqrt{1 + \frac{2(m_e c^2)^2}{EE'(1 - \omega)}}\right), \\
A &= E^2 + E'^2 + EE'(3 + \omega), \\
B &= E\left(2E^2 + EE'(3 - \omega) - E'^2(1 + 3\omega)\right), \\
C &= E^2\left((E - E'\omega)^2 - \frac{E'^2(1 - \omega^2)}{2} - \frac{(1 + \omega)(m_e c^2)^2\Delta^2}{2(1 - \omega)E^2}\right), \\
f(x) &= \frac{1}{e^{\frac{x}{kT}} - 1}, \\
G_i(y) &= F_i\left(\frac{\mu_e - (E - E')}{k_{\mathrm{B}}T} - y\right) - F_i\left(\frac{\mu_e}{k_{\mathrm{B}}T} - y\right), \\
F_i(z) &= \int_{-\infty}^{+\infty} dx\, \frac{x^i}{e^{x-z} + 1}.
\end{aligned}
$$

The F_i are Fermi-integrals and, following Mezzacappa and Bruenn (1993a), can be related to the polylogarithm function[5]

$$
F_i(z) = -i!\, S_{i+1}(-e^z),
$$

where

$$
S_i(z) = \frac{x}{(i - 1)!}\int_0^\infty dt\, \frac{t^{i-1}}{e^t - z},
$$

and hence

$$
\begin{aligned}
S_2(z) &= -S_2\left(\frac{1}{z}\right) - \frac{1}{2}\log^2(-z) - \frac{\pi^2}{6}, \\
S_3(z) &= S_3\left(\frac{1}{z}\right) - \frac{1}{6}\log^3(-z) - \frac{\pi^2}{6}\log(-z).
\end{aligned}
$$

Remark 3 *For $E = E'$, the expressions for the I_i can be simplified as follows (Mezza-*

---

[5]The polylogarithm function and other related complex-valued functions, such as the whole theory on zeta-functions, are by present standards included in most numerical mathematics programs such as MATHEMATICA.

cappa and Bruenn (1993a))

$$
\begin{aligned}
I_1(E,\omega) &= \frac{2\pi(k_BT)E^4(1-\omega)^2}{\Delta^5} \times \\
&\times \left\{ A(k_BT)^2 \left(2F_1\left(\frac{\mu_e}{k_BT}-y\right) + 2yF_0\left(\frac{\mu_e}{k_BT}-y\right) + y^2F_{-1}\left(\frac{\mu_e}{k_BT}-y\right) \right) \right. \\
&+ \left. B(k_BT)\left(F_0\left(\frac{\mu_e}{k_BT}-y\right) + yF_{-1}\left(\frac{\mu_e}{k_BT}-y\right) \right) \right. \\
&+ \left. CF_{-1}\left(\frac{\mu_e}{k_BT}-y\right) \right\} \\
I_2(E,\omega) &= I_1(E,\omega) \\
I3(E,\omega) &= \frac{2\pi(k_BT)E^2(1-\omega)(m_ec^2)^2}{\Delta} F_{-1}\left(\frac{\mu_e}{k_BT}-y\right),
\end{aligned}
$$

including the simplifications in the expressions for Δ, y, A, B, C and where

$$
F_{-1}(z) = \frac{1}{e^z+1}.
$$

The final expressions for the scattering kernel depends on E, E', μ, μ' and on ϕ. To obtain the form of these kernels that can be used in the collision term at the right hand side of the Boltzmann transport equation, the dimensional reduction with respect to ϕ must be performed. A simple approach would be the integration of ϕ, which yields

$$
R_{\mathrm{NES}}^{\mathrm{out}}(E, E', \mu, \mu') = \int_0^{2\pi} d\phi\, R_{\mathrm{NES}}^{\mathrm{out}}(E, E', \omega). \tag{2.25}
$$

An additional approach was introduced by Mezzacappa and Bruenn (1993a) who follow the derivations from Schinder and Shapiro (1982) and Bruenn (1985) and expand the kernels in a Legendre series as follows

$$
R_{\mathrm{NES}}^{\mathrm{out}}(E, E', \omega) = \sum_{l=0}^{\infty} \frac{2l+1}{2} \Phi_{\mathrm{NSE},l}^{\mathrm{out}}(E, E')\, P_l(\omega),
$$

with the Legendre coefficients

$$
\Phi_{\mathrm{NSE},l}^{\mathrm{out}}(E, E') = \int_{-1}^{+1} d\omega\, P_l(\omega)\, R_{\mathrm{NES}}^{\mathrm{out}}(E, E', \omega).
$$

Following the addition theorem for Legendre polynomials[6], the full scattering kernel can be written as follows

$$
\begin{aligned}
R_{\text{NES}}^{\text{out}}(E, E', \omega) &= \sum_{l=0}^{\infty} \frac{2l+1}{2} \Phi_{\text{NES},l}^{\text{out}}(E, E') P_l(\mu) P_l(\mu') \\
&+ \sum_{l=0}^{\infty} \frac{2l+1}{2} \Phi_{\text{NES},l}^{\text{out}}(E, E') \, 2 \sum_{m=1}^{l} \frac{(l-m)!}{(l+m)!} \left(P_l(\mu)\right)^m \left(P_l(\mu')\right)^m \cos(m\phi).
\end{aligned}
$$

Integrating this expression over ϕ gives (Mezzacappa and Bruenn (1993a))

$$
R_{\text{NES}}^{\text{out}}(E, E', \mu, \mu') = 2\pi \sum_{l=0}^{\infty} \frac{2l+1}{2} \Phi_{\text{NES},l}^{\text{out}}(E, E') P_l(\mu) P_l(\mu'). \tag{2.26}
$$

A problem occurs for both approaches, either Exp. (2.25) or (2.26), which is that the expressions for forward scattering, i.e. $E = E'$ and $\mu = \mu'$, become singular. This has been pointed out by Mezzacappa and Bruenn (1993a). To avoid this problem the μ'-integration of the scattering kernel can be done without loosing generality as follows,

$$
\begin{aligned}
\int_{-1}^{+1} d\mu' R_{\text{NES}}^{\text{out}}(E, E', \mu, \mu') &= 2\pi \sum_{l=0}^{\infty} \frac{2l+1}{2} \Phi_{\text{NES},l}^{\text{out}}(E, E') P_l(\mu) \int_{-1}^{+1} d\mu' P_l(\mu') \\
&= 2\pi \Phi_{\text{NES},0}^{\text{out}}(E, E'),
\end{aligned}
$$

giving the isotropic forward scattering contribution, which is the zero order Legendre expansion. Furthermore, these expressions are realised numerically with discrete neutrino energies E and direction cosine μ. Mezzacappa and Bruenn (1993a) use this fact, i.e. that the scattering kernels are numerically averaged over a discrete μ-grid, and therefor interpret the kernels as integrable finite. They split the discrete direction cosine $\mu_{j+1/2}$ into forward and non-forward scattering as follows

$$
\begin{aligned}
\sum_{l=1}^{j_{\max}} w_j R_{\text{NES}}^{\text{out}}(E_{k+1/2}, E_{k+1/2}, \mu_{j+1/2}, \mu_{l+1/2}) &= w_{j+1/2} R_{\text{NES}}^{\text{out}}(E_{k+1/2}, E_{k+1/2}, \mu_{j+1/2}, \mu_{j+1/2}) \\
&+ \sum_{j \neq l} w_l R_{\text{NES}}^{\text{out}}(E_{k+1/2}, E_{k+1/2}, \mu_{j+1/2}, \mu_{l+1/2}),
\end{aligned}
$$

---

[6]The following expression for $P_l(\omega)$ can be obtained

$$
P_l(\omega) = P_l(\mu) P_l(\mu') + 2 \sum_{m=1}^{l} \frac{(l-m)!}{(l+m)!} \left(P_l(\mu)\right)^m \left(P_l(\mu')\right)^m \cos(m\phi).
$$

where the w_j are the corresponding weights and where the left hand side is the numerical discretisation of the μ' integration. Combining the two expressions above, the resulting scattering kernel can be used for forward scattering (Mezzacappa and Bruenn (1993a))

$$w_{j+1/2}\, R_{\text{NES}}^{\text{out}}(E_{k+1/2}, E_{k+1/2}, \mu_{j+1/2}, \mu_{j+1/2}) = 2\pi \Phi_{\text{NES},0}^{\text{out}}(E_{k+1/2}, E_{k+1/2})$$

$$- \sum_{j \neq l} w_l R_{\text{NES}}^{\text{out}}(E_{k+1/2}, E_{k+1/2}, \mu_{j+1/2}, \mu_{l+1/2}).$$

We are left with the calculation of the isotropic scattering kernel. There one can avoid the singular behaviour by integrating first over ω and than over the electron energy E_{e^-} as follows (see Bruenn (1985))

$$\Phi_{\text{NES},0}^{\text{out}}(E, E') = \frac{G^2}{\pi} \frac{1}{E^2 E'^2} \int_0^\infty dE_{e^-} f_{e^-}(E_{e^-})(1 - f_{e^-}(E_{e^-} + E - E'))$$

$$\times \left(\beta_1 H_0^I(E, E', E_{e^-}) + \beta_2 H_0^{II}(E, E', E_{e^-}) \right),$$

where the same definition(units) for the Fermi constant G are used as above and where the contributions from the electron rest mass term (β_3) are expected to be small assuming relativistic(degenerate) electrons and are hence neglected. The functions H_0^i are given in Yueh and Buchler (1976a), Bruenn (1985) and Mezzacappa and Bruenn (1993a) as follows

$$H_0^I = \begin{cases} \frac{4}{15}E_{e^-}^5 + \frac{4}{3}E_{e^-}^4 E + \frac{8}{3}E_{e^-}^3 E^2 + \Theta(E' - E)\Gamma_0^I(E, E'), & E' > E_{e^-}, \\ a_0^I(E, E') + b_0^I(E, E')E_{e^-} + c_0^I(E, E')E_{e^-}, & E' < E_{e^-}, \end{cases}$$

$$H_0^{II} = \begin{cases} \frac{4}{15}E_{e^-}^5 - \frac{4}{3}E_{e^-}^4 E' + \frac{8}{3}E_{e^-}^3 E'^2 + \Theta(E' - E)\Gamma_0^{II}(E, E'), & E' > E_{e^-}, \\ a_0^{II}(E, E') + b_0^{II}(E, E')E_{e^-} + c_0^{II}(E, E')E_{e^-}, & E' < E_{e^-}, \end{cases}$$

where

$$
\begin{aligned}
a_0^I(E, E') &= \left(\frac{8}{3} E^2 E'^3 - 4EE'^4 + \frac{8}{5} E'^5 \right) \Theta(E - E') + \frac{4}{15} E^5 \Theta(E' - E), \\
b_0^I(E, E') &= \left(\frac{16}{3} EE'^3 - 4E'^4 \right) \Theta(E - E') + \frac{4}{3} E^4 \Theta(E' - E), \\
c_0^I(E, E') &= \frac{8}{3} E'^3 \Theta(E - E') + \frac{8}{3} E^3 \Theta(E' - E), \\
a_0^{II}(E, E') &= a_0^I(E', E), \\
b_0^{II}(E, E') &= b_0^I(E', E), \\
c_0^{II}(E, E') &= c_0^I(E', E), \\
\Gamma_0^I(E, E') &= \frac{8}{3} E_{e-}^2 (E^3 - E'^3) + 4 E_{e-}^2 (E - E')^2 \left(\frac{E^2}{3} + \frac{2EE'}{3} + E'^2 \right) \\
&+ 4(E - E')^3 \left(\frac{E^2}{15} + \frac{EE'}{5} + \frac{2E'^2}{5} \right).
\end{aligned}
$$

Remark 4 *The scattering kernel for in-scattering is obtained from the detailed balance, similar to the charged current reactions and in accordance to the general form of the scattering kernels, as follows*

$$
R_{NES}^{in}(E, E', \mu, \mu') = \exp\left\{ \frac{E - E'}{k_B T} \right\} R_{NES}^{out}(E, E', \mu, \mu').
$$

Reaction 7 $\nu_e + e^+ \leftrightarrow \nu_e' + e'^+$ $(R_{NPS}^{in/out})$

The difference of electron-neutrino positron scattering to electron scattering is the exchange of the electron contributions by the corresponding positron contributions in the matrix elements. The squared and spin averaged matrix element can be written as follows (Yueh and Buchler (1976b),Hannestad and Madsen (1995))

$$
\begin{aligned}
\sum_{\text{spin}} |M|^2 &= 32 G^2 \left\{ (C_V + C_A)^2 (p_{\nu_e} \cdot p_{e+}')(p_{e+} \cdot p_{\nu_e}') \right. \\
&+ (C_V - C_A)^2 (p_{\nu_e} \cdot p_{e+})(p_{e+} \cdot p_{\nu_e}') \\
&- \left. (C_V^2 - C_A^2) m_e^2 (p_{\nu_e} \cdot p_{\nu_e}') \right\}.
\end{aligned}
$$

The calculation of the reaction rate for electron-neutrino positron scattering (NPS) can be done in the same way as for NES of electron-neutrinos

$$
\begin{aligned}
R_{p_{\nu_e}+p_{e+}\rightarrow p'_{\nu_e}+p'_{e+}} &= \frac{G^2}{EE'E_{e+}E'_{e+}}(2\pi)^4\delta^4(p_{\nu_e}+p_{e+}-p_{\nu_e}-p_{e+}) \\
&\times \left((C_V+C_A)^2(p_{\nu_e}\cdot p'_{e+})(p'_{\nu_e}\cdot p_{e+})\right. \\
&+ (C_V-C_A)^2(p_{\nu_e}\cdot p_{e+})(p'_{\nu_e}\cdot p'_{e+}) \\
&- \left.(C_V^2+C_A^2)m_e^2(p_{\nu_e}\cdot p'_{\nu_e})\right).
\end{aligned}
$$

Hence, the out-scattering kernel is given by the following expression

$$
R_{\mathrm{NPS}}^{\mathrm{out}}(E,E',\omega) = \frac{1}{2}\frac{1}{(2\pi)^3}\frac{\pi\sigma_0 c}{(m_e c^2)^2}\frac{1}{EE'}\left(\beta_1\tilde{I}_1(E,E',\omega)+\beta_2\tilde{I}_2(E,E',\omega)+\beta_3\tilde{I}_3(E,E',\omega)\right),
$$

where the electron chemical potential is replaced by the positron chemical potential in each of the phase-space integrated products of momenta, which are due to symmetry considerations of the matrix element in comparison to NES given by the following expressions (Yueh and Buchler (1976b))

$$
\begin{aligned}
\tilde{I}_1(E,E',\omega,\mu_e) &= I_2(E,E',\omega,-\mu_e), \\
\tilde{I}_2(E,E',\omega,\mu_e) &= I_1(E,E',\omega,-\mu_e), \\
\tilde{I}_3(E,E',\omega,\mu_e) &= I_3(E,E',\omega,-\mu_e).
\end{aligned}
$$

The ϕ-integration can be done exactly as discussed above for NES. To obtain the isotropic scattering kernel, the positron energy integration is performed in the same way as for NES, i.e.

$$
\Phi_{\mathrm{NPS},0}^{\mathrm{out}}(E,E') = \frac{G^2}{\pi}\frac{1}{E^2 E'^2}\int_0^\infty dE_{e+}\, f_{e+}(E_{e+})(1-f_{e+}(E_{e+}+E-E'))
$$

$$
\times\left(\beta_1\tilde{H}_0^I(E,E',E_{e+})+\beta_2\tilde{H}_0^{II}(E,E',E_{e+}),\right),
$$

where again the contributions from the rest mass term are ignored. Following again symmetry considerations, the functions H_0^i ($i \in I, II$) are given by the following expressions (Yueh and Buchler (1976b)),

$$
\begin{aligned}
\tilde{H}_0^I(E,E',E_{e+}) &= H_0^{II}(E,E',E_{e-}) \\
\tilde{H}_0^{II}(E,E',E_{e+}) &= H_0^I(E,E',E_{e-}),
\end{aligned}
$$

where the same coefficient functions a_0^i, b_0^i, c_0^i $(i \in I, II)$ and Γ_0^I are used as for NES. The in-scattering kernel is again obtained from the detailed balance

$$R_{\mathrm{NPS}}^{\mathrm{in}}(E, E', \mu, \mu') = \exp\left\{\frac{E - E'}{k_B T}\right\} R_{\mathrm{NPS}}^{\mathrm{out}}(E, E', \mu, \mu').$$

Reaction 8 $\bar{\nu}_e + e^\pm \leftrightarrow \bar{\nu}'_e + e'^\pm$ $(R_{NES/NPS}^{in/out})$

The scattering kernels for the electron-antineutrino can be obtained using the following argumentation from Bruenn (1985), where the neutrino momenta dependency of the matrix element is modified applying the following replacement

$$p_{\nu_e} \rightarrow -p'_{\bar{\nu}_e}$$
$$p'_{\nu_e} \rightarrow -p_{\bar{\nu}_e},$$

which is equivalent to the setting

$$C_A \leftrightarrow -C_V.$$

The reaction rates and hence the scattering kernel can be written as follows (Bruenn (1985))

$$
\begin{aligned}
R_{\mathrm{NES}}^{\mathrm{out}}(E, E', \omega) &= \frac{1}{2}\frac{1}{(2\pi)^3}\frac{\pi\sigma_0 c}{(m_e c^2)^2}\frac{1}{EE'}\left(\beta_2 I_1(E, E', \omega) + \beta_1 I_2(E, E', \omega) + \beta_3 I_3(E, E', \omega)\right) \\
R_{\mathrm{NPS}}^{\mathrm{out}}(E, E', \omega) &= \frac{1}{2}\frac{1}{(2\pi)^3}\frac{\pi\sigma_0 c}{(m_e c^2)^2}\frac{1}{EE'}\left(\beta_2 \tilde{I}_1(E, E', \omega) + \beta_1 \tilde{I}_2(E, E', \omega) + \beta_3 \tilde{I}_3(E, E', \omega)\right).
\end{aligned}
$$

The same holds for the isotropic scattering kernels

$$
\begin{aligned}
\Phi_{\mathrm{NES},0}^{\mathrm{out}}(E, E') = \frac{G^2}{\pi}\frac{1}{E^2 E'^2}\int_0^\infty dE_{e^-} f_{e^-}(E_{e^-})(1 - f_{e^-}(E_{e^-} + E - E')) \\
\times \left(\beta_2 H_0^I(E, E', E_{e^-}) + \beta_1 H_0^{II}(E, E', E_{e^-})\right)
\end{aligned}
$$

$$
\begin{aligned}
\Phi_{\mathrm{NPS},0}^{\mathrm{out}}(E, E') = \frac{G^2}{\pi}\frac{1}{E^2 E'^2}\int_0^\infty dE_{e^+} f_{e^+}(E_{e^+})(1 - f_{e^+}(E_{e^+} + E - E')) \\
\times \left(\beta_2 \tilde{H}_0^I(E, E', E_{e^+}) + \beta_1 \tilde{H}_0^{II}(E, E', E_{e^+})\right),
\end{aligned}
$$

using the same conventions as above. The in-scattering kernel is again calculated via the detailed balance.

Remark 5 *Comparing the above expressions for NES and NPS for the electron-flavour neutrinos and by symmetry considerations of the reactions itself, one finds that the electron-antineutrino scattering kernel for NES is equivalent to the electron-neutrino scattering kernel for NPS by replacing $\mu_e = -\mu_e$. The same holds for the electron-antineutrino scattering kernel for NPS and the electron-neutrino scattering kernel for NES.*

Reaction 9 $\nu_{\mu/\tau} + e^{\pm} \leftrightarrow \nu'_{\mu/\tau} + e'^{\pm}$ ($R_{NES/NPS}^{in/out}$)

The scattering of μ/τ-(anti)neutrinos proceeds via the exchange of a Z^0-boson only (no charged currents are involved). The squared and spin-averaged matrix elements are given by the following expressions for NES and NPS respectively (Hannestad and Madsen (1995))

$$\sum_{\text{spin}} |M|^2_{\text{NES}} = 32G^2 \left\{ (C_V + C_A - 2)^2 (p_\nu \cdot p_{e^-})(p'_\nu \cdot p'_{e^-}) + (C_V - C_A)^2 (p_\nu \cdot p'_{e^-})(p_{e^-} \cdot p'_\nu) \right.$$
$$\left. - ((C_V - 1)^2 + (C_A - 1)^2) m_e^2 (p_\nu \cdot p'_\nu). \right\},$$

$$\sum_{\text{spin}} |M|^2_{\text{NPS}} = 32G^2 \left\{ (C_V + C_A - 2)^2 (p_\nu \cdot p'_{e^+})(p_{e^+}.p'_\nu) + (C_V - C_A)^2 (p_\nu \cdot p_{e^+})(p'_{e^+} \cdot p'_\nu) \right.$$
$$\left. - ((C_V - 1)^2 + (C_A - 1)^2) m_e^2 (p_\nu \cdot p'_\nu). \right\}.$$

Applying the same argumentation as above, the following replacements (Bruenn (1985))

$$C_V \rightarrow C_V - 1,$$
$$C_A \rightarrow C_A - 1,$$

give the final expressions for the scattering kernels $R^{\text{in}}_{\text{NEP/NPS}}(E, E', \omega)$ and $\Phi^{\text{in}}_{\text{NES/NPS}}(E, E')$, where the detailed balance is applied again for the in-scattering.

Remark 6 *The total scattering kernel for NLS which enters the collision term on the right hand side of the Boltzmann equation is given by the sum of the contributions from NES and NPS, i.e.*

$$R_{NLS}^{in/out} = R_{NES}^{in/out} + R_{NPS}^{in/out},$$

for each neutrino flavour.

2.4.3 Neutral currents 2: pair processes

Pair processes play a fundamental role in core collapse supernovae. μ/τ-(anti)neutrinos can only be produced via pair reactions since the muonic-charged current reactions are suppressed due to the absence of μ or τ. In the following paragraphs, I will discuss the pair-processes used in our model. The standard reaction is the annihilation of electron-positron pairs as well as $N - N$-Bremsstrahlung. Recently we have implemented an additional process which was pointed out by Buras et al. (2003) to be of relevance, that is the annihilation of trapped electron-flavour neutrino pairs.

Reaction 10 $e^- + e^+ \leftrightarrow \nu_e + \bar{\nu}_e$ $(R^{a/p}_{PAIR,e^-e^+})$

The classical pair production process is the annihilation of electron-positron pairs. The reaction kernel is given by the electron momentum and positron momentum integration of the reaction rate $R_{p_{e^-}+p_{e^+}\leftrightarrow p_{\nu_e}+p_{\bar{\nu}_e}}$, scaled with the corresponding electron and positron distribution functions for the emission of neutrinos or the blocking factors for the absorption of neutrinos as follows (Bruenn (1985))

$$R^{\mathrm{p}}_{\mathrm{PAIR},e^-e^+}(E, E', \omega) = \int \frac{d^3 p_{e^-}}{(2\pi)^3} \int \frac{d^3 p_{e^+}}{(2\pi)^3} 2 f_{e^-}(E_{e^-}) 2 f_{e^+}(E_{e^+}) R_{p_{e^-}+p_{e^+}\to p_{\nu_e}+p_{\bar{\nu}_e}},$$

$$R^{\mathrm{a}}_{\mathrm{PAIR},e^-e^+}(E, E', \omega) = \int \frac{d^3 p_{e^-}}{(2\pi)^3} \int \frac{d^3 p_{e^+}}{(2\pi)^3} (1 - f_{e^-}(E_{e^-}))(1 - f_{e^+}(E_{e^+})) R_{p_{\nu_e}+p_{\bar{\nu}_e}\to p_{e^-}+p_{e^+}},$$

where similar to the considerations above, detailed balance can be used to calculate the reverse reaction kernel as follows (Bruenn (1985))

$$R^{a}_{\mathrm{PAIR},e^-e^+}(E, E', \omega) = \exp\left\{\frac{E_{e^-} + E_{e^+}}{k_{\mathrm{B}}T}\right\} R^{p}_{\mathrm{PAIR},e^-e^+}(E, E', \omega).$$

The spin-averaged and squared matrix element can be written as follows (Hannestad and Madsen (1995))

$$\begin{aligned}
\sum_{\mathrm{spin}} |M|^2 &= 32 G^2 \left\{ (C_V + C_A)^2 (p_{e^+} \cdot p_{\nu_e})(p_{e^-} \cdot p_{\bar{\nu}_e}) \right. \\
&+ (C_V - C_A)^2 (p_{e^-} \cdot p_{\nu_e})(p_{e^+} \cdot p_{\bar{\nu}_e}) \\
&+ \left. (C_V^2 - C_A^2) m_e (p_{\nu_e} \cdot p_{\bar{\nu}_e}) \right\}.
\end{aligned}$$

Following Yueh and Buchler (1976b) and Schinder and Shapiro (1982), the calculation of the pair reaction kernels for the electron-flavour neutrinos can be done in a similar way as NES for electron-neutrinos applying the following replacements

$$\begin{aligned}
p'_{e^-} &= -p_{e^+}, \\
p_{\nu_e} &= -p_{\nu_e},
\end{aligned}$$

and relabel the initial electron and positron and the final electron-neutrino and antineutrino momenta as given in the squared and spin-averaged matrix element. Following the same calculations as for NES above, the resulting reaction rate becomes (Bruenn (1985))

$$
\begin{aligned}
R_{e^-+e^+\leftrightarrow\nu_e+\bar{\nu}_e} &= \frac{1}{2}\frac{G^2}{EE'E_{e^-}E_{e^+}}(2\pi)^4\delta^4(e^-+e^+-\nu_e-\bar{\nu}_e) \\
&\times \quad (C_V+C_A)^2(p_{e^+}\cdot p_{\nu_e})(p_{e^-}\cdot p_{\bar{\nu}_e}) \\
&+ \quad (C_V-C_A)^2(p_{e^-}\cdot p_{\nu_e})(p_{e^+}\cdot p_{\bar{\nu}_e}) \\
&+ \quad (C_V^2-C_A^2)m_e(p_{\nu_e}\cdot p_{\bar{\nu}_e}),
\end{aligned}
$$

Integrating over the electron and positron momenta and assuming relativistic electrons and positrons, an expression for the pair-reaction kernel can be obtained, which depends on the neutrino in and out going energies E and E' respectively and on ω as follows (Schinder and Shapiro (1982))

$$
R^{\mathrm{p}}_{\mathrm{PAIR},e^-e^+}(E,E',\omega) = \frac{1}{(2\pi)^5}\frac{1}{2}\frac{\pi\sigma_0}{(m_ec^2)^2}\frac{1}{EE'}\times
$$

$$
\times\left\{(C_V+C_A)^2 J_1(E,E',\omega)+(C_V-C_A)^2 J_2(E,E',\omega)+(C_V^2-C_A^2)J_3(E,E',\omega)\right\}.
$$

Remark 7 *Note that*

$$
\frac{1}{2}\frac{1}{(2\pi)^2}\frac{\sigma_0 c}{(m_ec^2)^2} = \frac{2G^2}{2\pi},
$$

where again

$$
\sigma_0 = \frac{4G^2 m_e^2\hbar^2}{\pi c} = 1.764\times 10^{-44}\,cm^2,
$$

and hence the integral kernel scaling factor does not contain an explicit electron rest mass dependency.

The J_i correspond to the integrated products of the momenta given by the squared and spin-averaged matrix element. The integration has been performed in Schinder and Shapiro (1982) where the following results were obtained

$$
\begin{aligned}
J_1(E,E',\omega) &= -\frac{2\pi k_{\mathrm{B}}T(E+E')E^2 E'^2(1-\omega)^2}{\Delta^5}f(E+E')\times \\
&\times \quad \left\{A(k_{\mathrm{B}}T)^2\left(G_2(y_{\max})-G_2(y_{\min})+2y_{\max}G_1(y_{\max})-2y_{\min}G_1(y_{\min})\right.\right. \\
&\quad\quad + \left. y_{\max}^2 G_0(y_{\max})-y_{\min}^2 G_0(y_{\min})\right) \\
&\quad + \quad B(k_{\mathrm{B}}T)\left(G_1(y_{\max})-G_1(y_{\min})+y_{\max}G_0(y_{\max})-y_{\min}G_0(y_{\min})\right) \\
&\quad + \quad \left. C\left(G_0(y_{\max})-G_0(y_{\min})\right)\right\}, \\
J_2(E,E',\omega) &= J_1(E',E,\omega), \\
J_3(E,E',\omega) &= -\frac{2\pi k_{\mathrm{B}}T(m_ec^2)^2 E^2 E'^2(1-\omega)^2}{\Delta}f(E+E')\left(G_0(y_{\max})-G_0(y_{\min})\right),
\end{aligned}
$$

where

$$
\begin{aligned}
A &= E'^2 + E^2 - EE'(3+\omega) \\
B &= E\left(EE'(3-\omega) + E'^2(3\omega+1) - 2E^2\right) \\
C &= E^2\left((E+E'\omega)^2 - \frac{1}{2}E'^2(1-\omega^2) - \frac{1}{2}\frac{(m_ec^2)^2}{E^2}\Delta\frac{1+\omega}{1-\omega}\right) \\
\Delta &= \sqrt{E^2 + E'^2 + 2EE'\omega} \\
f(x) &= \frac{1}{e^{\frac{x}{k_\mathrm{B}T}} - 1} \\
G_n(y) &\equiv F_n(\eta'-y) - F_n(\eta-y) \\
\eta &= \frac{\mu_e}{k_\mathrm{B}T} \\
\eta' &= \eta + \frac{E+E'}{k_\mathrm{B}T},
\end{aligned}
$$

and where $F_n(x)$ are again Fermi-Dirac integrals as introduced in the section on NES above. The arguments are given by

$$
y_{\mathrm{min/max}} = \frac{\frac{E+E'}{2} \mp \frac{\Delta}{2}\sqrt{1 - \frac{2(m_ec^2)^2}{EE'(1-\omega)}}}{k_\mathrm{B}T}.
$$

The similarity to the NES kernel becomes obvious. Hence, the pair emission and absorption kernels become singular with respect to the forward direction, i.e. $E \to E'$, $\mu \to \mu'$. Applied the same dimensional reduction as for NES and expanding the scattering kernel in a Legendre series (Messer (2000))

$$
R^p_{\mathrm{PAIR},e^-e^+}(E,E',\omega) = \sum_{l=0}^{\infty} \frac{2l+1}{2}\Phi^\mathrm{p}_{\mathrm{PAIR},e^-e^+,l}(E,E')P_l(\omega),
$$

where (using again the addition theorem for Legendre polynomials)

$$
\int_{-1}^{+1} d\mu' R^p_{\mathrm{PAIR}}(E,E',\mu,\mu') = 2\pi\Phi^\mathrm{p}_{\mathrm{PAIR},e^-e^+,0}(E,E'),
$$

is the isotropic zero order Legendre expansion of the pair production kernel. The same technique used for NES, namely separating forward and non-forward (i.e. $j = j_{\max}+1-j'$, Messer (2000)) direction cosine in the discrete form of the μ'-integrated scattering kernel and combine it with the above expression for $\Phi^\mathrm{p}_{\mathrm{PAIR},0}$, one obtains (Messer (2000))

$$
\frac{1}{w_{j+1/2}}R^\mathrm{p}_{\mathrm{PAIR},e^-e^+}(E_{k+1/2}, E_{k+1/2}, \mu_{j+1/2}, \mu_{j_{\max}+1-j+1/2}) = 2\pi\Phi^p_{\mathrm{PAIR},0}(E_{k+1/2}, E_{k+1/2})
$$

$$- \sum_{l \neq j_{\max}+1-j} w_l R^{\mathrm{p}}_{\mathrm{PAIR},e^-e^+}(E_{k+1/2}, E_{k+1/2}, \mu_{j+1/2}, \mu_{l+1/2}).$$

The zero order Legendre expansion is calculated in Bruenn (1985), avoiding the singular behaviour by integrating first over ω and then over the electron and positron momenta. Using the same definition for G^2 as above, one obtains

$$
\begin{aligned}
\Phi^{\mathrm{p}}_{\mathrm{PAIR},e^-e^+,0}(E, E') &= \frac{G^2}{\pi} \int_0^{E+E'} dE_{e^-} f_{e^-}(E_{e^-}) f_{e^+}(E + E' - E_{e^-}) \times \\
&\times \; \left((C_V + C_A)^2 J_0^I(E, E', E_{e^-}) + (C_V - C_A)^2 J_0^{II}(E, E', E_{e^-}) \right),
\end{aligned}
$$

where again the rest mass term is considered to be small and hence neglected. The coefficients are given by the following expressions (see Messer (2000) based on Bruenn (1985))

$$
\begin{aligned}
J_0^I(E, E', E_{e^-}) &= \Theta(E + E' - E_{e^-}) \times \\
&\times \; \{ a(E, E', E_{e^-}) \left(\Theta(E - E_{e^-})\Theta(E' - E) + \Theta(E' - E_{e^-})\Theta(E - E') \right) \\
&+ \; b(E, E', E_{e^-}) \left(\Theta(E_{e^-} - E')\Theta(E' - E) + \Theta(E_{e^-} - E)\Theta(E - E') \right) \\
&+ \; c(E, E', E_{e^-}) \left(\Theta(E_{e^-} - E)\Theta(E' - E_{e^-}) \right) \\
&+ \; d(E, E', E_{e^-}) \left(\Theta(E_{e^-} - E')\Theta(E - E_{e^-}) \right) \}, \\
J_0^{II}(E, E', E_{e^-}) &= J_0^I(E', E, E_{e^-}),
\end{aligned}
$$

where

$$
\begin{aligned}
a(E, E', E_{e^-}) &= \frac{1}{EE'} \left(\frac{4}{15} E^5 E'^3 - \frac{4}{3} E_{e^-}^4 E' + \frac{8}{3} E_{e^-}^3 E'^2 \right), \\
b(E, E', E_{e^-}) &= \frac{1}{EE'} \left(-a(E, E', E_{e^-}) + \frac{8}{3} E_{e^-}(E^3 + E'^3) \right. \\
&- \; \frac{4}{3} E_{e^-}(E + E')^2 (E'^2 - 2EE' + 3E^2) \\
&+ \; \left. \frac{4}{15}(E + E')^3 (E'^2 - 3EE' + 6E^2) \right), \\
c(E, E', E_{e^-}) &= \frac{E^2}{E'} \left(\frac{8}{3} E'^2 + 4EE' + \frac{8}{3} E^2 \right) - E_{e^-} \left(\frac{16}{3} E^2 + 4 \frac{E^3}{E'} \right) + \frac{8}{3} \frac{E_{e^-} E^2}{E'}, \\
d(E, E', E_{e^-}) &= \frac{4}{15} \frac{E'^4}{E^4} - \frac{4}{3} \frac{E_{e^-} E'^3}{E} + \frac{8}{3} \frac{E_{e^-}^2 E'^2}{E}.
\end{aligned}
$$

Reaction 11 $e^- + e^+ \leftrightarrow \nu_{\mu/\tau} + \bar{\nu}_{\mu/\tau}$ $\left(R^{a/p}_{PAIR,e^-e^+} \right)$

The pair reaction kernel for the annihilation and emission of μ/τ neutrino pairs is a cross over channel from ν_e-pair emission and can be done following the argumentation applied above for NES(NPS) using the same relations, namely (Bruenn (1985))

$$
\begin{aligned}
C_V &\rightarrow C_V - 1, \\
C_A &\rightarrow C_A - 1.
\end{aligned}
$$

Reaction 12 $N + N \leftrightarrow N + N + \nu + \bar{\nu}$ $(R^{a/p}_{PAIR,NN})$

The calculation of the pair processes due to nucleon-nucleon Bremsstrahlung goes back to the work by Hannestad and Raffelt (1998). They rewrite the collision term as follows

$$
\Omega(f)_{\text{PAIR, brems}} = C_A^2 G_F^2 n_B \int_{-1}^{+1} d\mu' \int_0^\infty E'^2 dE' \, (3 - \mu\mu') \times
$$
$$
\times \left((1 - f_\nu)(1 - f_{\bar{\nu}}) \, S_\sigma(-E' - \bar{E}') - f_\nu f_{\bar{\nu}} \, S_\sigma(E' + \bar{E}') \right),
$$

where f_ν and $f_{\bar{\nu}}$ are the neutrino and antineutrino distribution functions respectively and C_A is the coupling constant, n_B is the baryon density. The scattering kernel is given as follows

$$
R^{\text{p}}_{\text{PAIR},NN}(\mu, \mu', E, E') = C_A^2 G_F^2 n_B (3 - \mu\mu') S_\sigma(E', \bar{E}', T, n_B, X_n, X_p).
$$

This expresses the calculation of the pair reaction rate in terms of S_σ, which depends on the neutrino energy E' and the antineutrino energy $\bar{E}'$ of the out-scattering neutrino-antineutrino pair, the temperature T, the baryon density n_B and the nucleon fractions X_p and X_n. Here I would like to summarise the final results from Hannestad and Raffelt (1998), who find

$$
\begin{aligned}
S_\sigma(E) &= \frac{1}{T} \frac{\gamma}{x^2 + \frac{\gamma g(y,\eta_*)}{2}^2} s(x), \\
x &= \frac{E}{T}, \\
y &= \frac{m_\pi^2}{m_N T} = 1.94 \, T_{10}^{-1}, \\
\gamma &= \frac{\Gamma_\sigma}{T} = 1.63 \, \eta_*^{3/2} T_{10} = 8.6 \, \rho_{14} T_{10}^{-1/2}, \\
\Gamma_\sigma &= \frac{8\sqrt{2\pi} \, \alpha_\pi^2}{3\pi^2} \eta_*^{3/2} \frac{T^2}{m_N}, \\
\eta_* &= \frac{p_F^2}{2 m_N T} = \frac{(2\pi)^{2/3}}{2 m_N T} \left(\frac{\rho}{m_N} \right),
\end{aligned}
$$

where $\alpha_\pi = (2m_N/m_\pi)^2/4\pi$ is the pion-nucleon fine structure constant and η_* is the effective degeneracy parameter with Fermi-momentum p_F. This reduces the calculation of $S_\sigma(E)$ to find expressions for $s(x)$ and $g(y, \eta_*)$. The derivation is given in details in Hannestad and Raffelt (1998). The reaction kernels contribute to both, the production and absorption of electron and μ/τ neutrino pairs, equivalently.

Reaction 13 $\nu_e + \bar{\nu}_e \leftrightarrow \nu_{\mu/\tau} + \bar{\nu}_{\mu/\tau}$ $(R^{a/p}_{PAIR,\nu_e\bar{\nu}_e})$

In addition to the standard process of μ/τ neutrinos pair emission via electron-positron annihilation and N-N-Bremsstrahlung, the annihilation of trapped electron-flavour neutrino pairs has been studied by Buras et al. (2003). They point out the importance of this reaction especially in the regime of high matter densities and temperatures, becoming as important as Bremsstrahlung. The squared and spin-averaged matrix element is a cross-over from the traditional pair-emission process. It can be obtained by replacing the corresponding electron-positron distributions and momenta by the μ/τ neutrino distributions and momenta. The following matrix element is used (Hannestad and Madsen (1995))

$$\sum_{\text{spin}} |M|^2 = 32G^2 \left\{ (C_V + C_A)^2 (p_{\bar{\nu}_\mu} \cdot p_{\nu_e})(p_{\nu_\mu} \cdot p_{\bar{\nu}_e}) + (C_V - C_A)^2 (p_{\nu_\mu} \cdot p_{\nu_e})(p_{\bar{\nu}_\mu} \cdot p_{\bar{\nu}_e}) \right\},$$

where again, similar to the considerations above, the rest mass term does not contribute because the neutrinos are considered to be mass less. The scattering kernels can be written as follows, replacing the electron and positron distribution functions and the momenta

$$R^{\text{p}}_{\text{PAIR},\nu_e\bar{\nu}_e}(E, E', \omega) = \int \frac{d^3p_{\nu_e}}{(2\pi)^3} \int \frac{d^3p_{\bar{\nu}_e}}{(2\pi)^3} 2f_{\nu_e}(E) 2f_{\bar{\nu}_e}(\bar{E}) R_{p_{\nu_e}+p_{\bar{\nu}_e}\to p_{\nu_\mu}+p_{\bar{\nu}_\mu}}$$

$$R^{\text{a}}_{\text{PAIR},\nu_e\bar{\nu}_e}(E, E', \omega) = \int \frac{d^3p_{\nu_e}}{(2\pi)^3} \int \frac{d^3p_{\bar{\nu}_e}}{(2\pi)^3} (1 - f_{\nu_e}(E))(1 - f_{\bar{\nu}_e}(\bar{E})) R_{p_{\nu_\mu}+p_{\bar{\nu}_\mu}\to p_{\nu_e}+p_{\bar{\nu}_e}}.$$

The main difference to electron-positron annihilation lays in the coupling constants. These are

$$C_V = C_A = +\frac{1}{2},$$

and hence

$$\sum_{\text{spin}} |M|^2 = 32G^2 \ (p_{\bar{\nu}_\mu} \cdot p_{\nu_e})(p_{\nu_\mu} \cdot p_{\bar{\nu}_e}).$$

Following the calculations from above for electron-positron annihilation, the integration of the single term of the products of momenta yields the pair production kernel as follows

$$R^{\text{p}}_{\text{PAIR},\nu_e\bar{\nu}_e}(E, E', \omega) = \frac{1}{(2\pi)^5} \frac{1}{2} \frac{\pi\sigma_0}{(m_ec^2)^2} \frac{1}{EE'} \tilde{J}(E, E', \omega),$$

where

$$\tilde{J} = J_1(m_e = 0, \mu_e = \mu_{\nu_e}),$$

i.e. all electron rest mass dependency has been canceled and the electron chemical potential is replaced by the electron-neutrino chemical potential. The annihilation of electron-flavour neutrino pairs is only favourable in the presence of large electron-flavour neutrino numbers, where typically local thermodynamic equilibrium (LTE) can be assumed. Hence, the neutrino chemical potentials are given explicitly by the electron chemical potential μ_e and the charged chemical potentials $\hat{\mu}$ as follows

$$\mu_{\nu_e} = \mu_e - (\mu_n - \mu_p) = \mu_e - \hat{\mu},$$
$$\mu_{\bar{\nu}_e} = -\mu_{\nu_e}.$$

The dimensional reduction, i.e. the ϕ-integration of the kernel, is done in the same way as for electron-positron annihilation, taking into account the singular forward direction. The reverse reaction, i.e. the emission of electron-neutrino pairs via the annihilation of μ/τ-neutrino pairs, is calculated applying detailed balance.

Remark 8 *The total contribution of pair reactions that enters the collision term of the Boltzmann equation is the sum of all contributions discussed above, e.g.*

$$R_{PAIR}^{a/p} = R_{PAIR,e^-e^+}^{a/p} + R_{PAIR,NN}^{a/p} + R_{PAIR,\nu_e\bar{\nu}_e}^{a/p}.$$

2.4.4   Comparison of the different pair reaction rates

The reaction rates depend on the thermodynamic state, especially a strong direct temperature and density dependency becomes clear from the above expressions. To be able to compare the reaction rates with respect to the incoming neutrinos, integrating the reaction kernels with respect to the outgoing neutrino phase space dependency as it is done for the collision term of the Boltzmann equation, one obtains

$$R_{\mathrm{PAIR}}^{\mathrm{p/a}}(\mu, E) = \frac{1}{c} \frac{2\pi}{(hc)^3} \int_{-1}^{+1} d\mu' \int_0^\infty E'^2 dE' \, R_{\mathrm{PAIR}}^{\mathrm{p/a}}(\mu, \mu', E, E').$$

This gives the correct units of $\mathrm{cm^3 s^{-1}}$. Comparing now the spectrum, one has to get rid of the angular dependency which can be done as follows

$$R_{\mathrm{PAIR}}^{\mathrm{p/e}}(E) = \frac{E^2}{h^3 c^2} \int_{-1}^{+1} d\mu \, R_{\mathrm{PAIR}}^{\mathrm{p/a}}(\mu, E),$$

which leads to the neutrino energy dependent scattering kernel in units of $\mathrm{cm^{-3} MeV^{-1} s^{-1}}$. Ignoring effects from neutrino fluxes and neutrino occupation or blocking, one can analyse the phase space integrated reaction rates for different thermodynamic conditions since $E_{\mathrm{PAIR}}(E, T, n_{\mathrm{B}}, Y_e)$.

The integrated kernels for all there considered reactions are plotted with respect to the incoming neutrino energy E in Fig. 2.1, for zero chemical potentials, i.e. $\mu_e = \mu_{\nu_e} = 0$. The left panel shows the thermodynamic conditions given in Table 2.1 (first line) and represent a high density, high temperature and deleptonised environment found typically inside PNSs where neutrino trapping applies. There, N-N-Bremsstrahlung dominates over the other two pair reaction rates by a factor of 2 for the electron-neutrino pairs and a factor of 4-5 for the μ/τ-neutrino pairs. This behaviour has already been pointed out in a previous study by Messer and Bruenn (2003). Analysing the reaction rates for slightly lower densities and temperatures in the right panel of Fig. 2.1 for the conditions given in Table 2.1 (second line), the strong temperature dependency of the N-N-Bremsstrahlung leads to a vanishing of the rates while electron-positron annihilations dominate the production(absorption) of electron flavour neutrino pairs. For the production of μ/τ-neutrino pairs, the annihilation of trapped electron-neutrino pairs is the dominant reaction at these conditions. Since the calculation of this reaction rate is based on the assumption of local thermodynamic equilibrium (LTE), at conditions outside the electron-neutrinosphere where LTE does not apply, the reaction rate vanishes as neutrinos start to decouple from matter. For conditions found outside the electron-neutrinosphere, the annihilation of electron-positron pairs is the dominant source for the production of neutrino pairs of all flavours.

Table 2.1: Thermodynamic conditions for the pair reaction rates illustrated in Fig. 2.1 and 2.2.

T [MeV]	ρ [g/cm^3]	Y_e	η_e	η_{ν_e}	X_n	X_p
12	5×10^{13}	0.35	0	0	0.20	0.09
5	1×10^{12}	0.35	0	0	0.59	0.29
12	5×10^{13}	0.35	10.86	9.67	0.20	0.09
5	1×10^{12}	0.35	6.82	6.32	0.59	0.29

A similar comparison of the reaction rates under "physical" conditions found in core collapse supernovae is difficult. The reaction kernels depend not only on the thermodynamic state given by the triplet $(T, n_{\mathrm{B}}, Y)_e)$, but also on the chemical potentials and the composition. Both of which are implicitly given by the thermodynamic state. Hence, an EoS must be applied to analyse the effects of non-vanishing chemical potentials. The EoS will be introduced in the next section. For that reason, Table. 2.1 gives the same conditions for which the pair reaction rates are illustrated in Fig. 2.1 for vanishing chemical potentials, now involving an EoS for hot and dense nuclear matter that calculates the chemical potentials for these conditions. Demonstrating that for neutron rich conditions which are found in PNS interiors,

$$\mu_e > \mu_{\nu_e},$$

Figure 2.1: Reaction rates for the emission and absorption of neutrino pairs with respect to the incoming neutrino energy for different thermodynamic conditions with $\mu_e = \mu_{\nu_e} = 0$ listed in Table 2.1 (line 1 & 2).
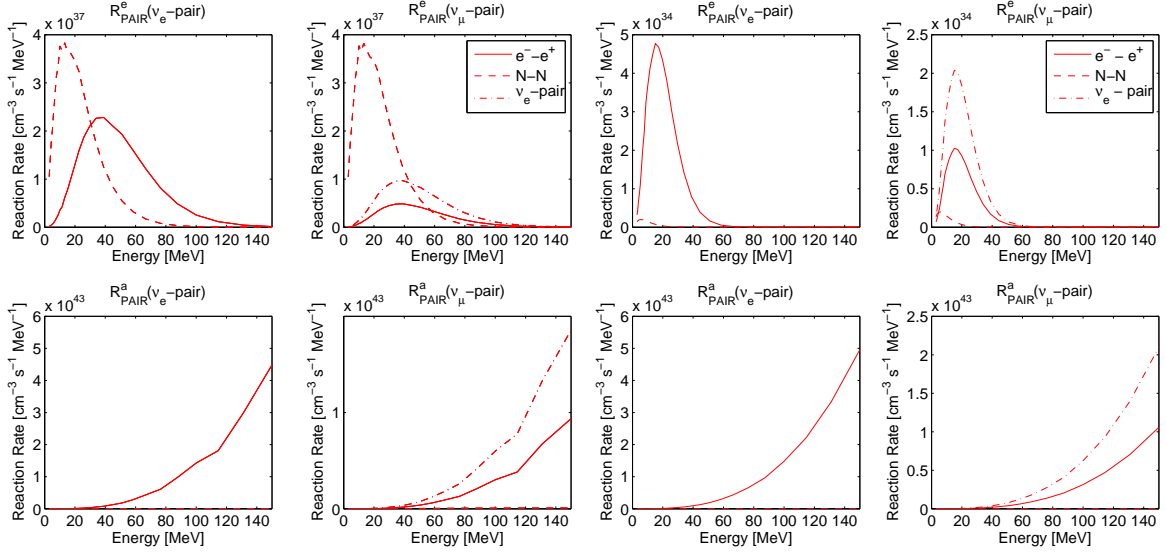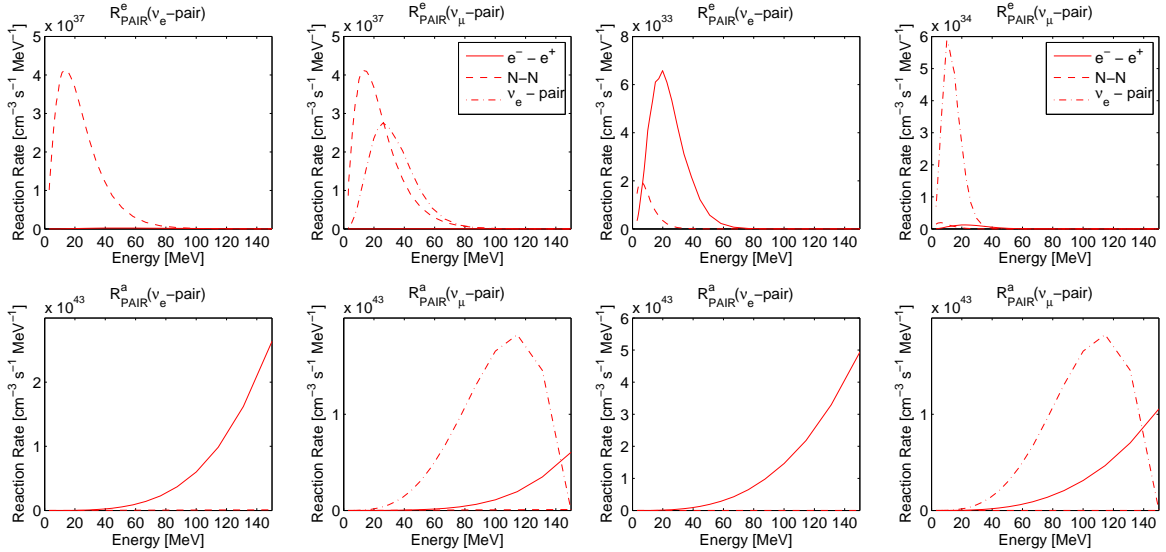

Figure 2.2: Reaction rates for the emission and absorption of neutrino pairs with respect to the incoming neutrino energy for different thermodynamic conditions with non-vanishing chemical potential as listed in Table 2.1 (line 3 & 4).

since $\mu_n - \mu_p > 0$. The annihilation of trapped electron favour neutrino pairs is always more important then electron-positron annihilation, for the production of μ/τ-neutrino pairs. For the same conditions but now using the non-vanishing chemical potentials, the reaction rates are illustrated in Fig. 2.2 (left panel: Table 2.1 third line, (right panel: Table 2.1 fourth line). At high densities and temperatures (left panel), it becomes clear that N-N-Bremsstrahlung is as important as ν_e-pair annihilation for the production of μ/τ-neutrino pairs. At lower densities and temperatures but still at conditions valid for PNS interiors where LTE holds (right panel), N-N-Bremsstrahlung does not contribute to the production of μ/τ-neutrino pairs. The annihilation of trapped ν_e-neutrino pairs dominates over the annihilation of electron-positrons.

With the inclusion of the additional pair production source via the annihilation of trapped electron-flavour neutrino pairs, an important reaction with a non-negligible effect has been added. The influence of this additional pair reaction to the observable neutrino spectra and to the fluid dynamics in the context of core collapse supernova simulations of massive stars will be further discussed and illustrated in §3.2 of the manuscript.

2.5 Conservation of lepton number and the electron fraction

The conservation equation for the electron flavour lepton number, in combination with the Boltzmann transport equation, can be used to derived the evolution equation of the electron fraction. The electron fraction is an important quantity in core collapse supernova models. It determines the number of charges per baryon and, since muons are suppressed due to their large rest mass of 107 MeV, the number of electrons (electron minus positrons) per baryon. The electron fraction is determined via a differential equation in time and given by the balance between the emission and absorption of electron flavour neutrinos as well as electrons and positrons and by the flux of neutrinos.

In addition to the coupling of the hydrodynamics equations and radiation transport, it must be explicitly ensured that such systems conserve the lepton number Y_L for each lepton species, i.e.

$$
\begin{aligned}
Y_{L_e} &= Y_{e^-} - Y_{e^+} + Y_{\nu_e} - Y_{\bar{\nu}_e}, \\
Y_{L_{\mu/\tau}} &= Y_{\mu/\tau^-} - Y_{\mu/\tau^+} + Y_{\nu_{\mu/\tau}} - Y_{\bar{\nu}_{\mu/\tau}}.
\end{aligned}
$$

The μ/τ-lepton number is conserved by definition in our model, because μ/τ-neutrinos are only considered via neutral current reactions. The conservation of the electron lepton number will be discussed in the following paragraph [7].

---

[7]In the following, I use the same conventions as above, where $Y_e := Y_{e^-} - Y_{e^+}$ is the total number of charges per baryon.

Applying the conservation law to the spherically symmetric system introduced in the sections above, the conservation of the lepton number is given by the continuity equation as follows (Mezzacappa and Bruenn (1993b))

$$\frac{\partial Y_L}{\partial t} + m_{\mathrm{B}} \frac{\partial}{\partial a} \left(4\pi r^2 \rho N_L \right) = 0,$$

where N_L is the lepton flux. It is given by the sum of the corresponding lepton contributions from electrons, positrons and electron flavour neutrinos (similar to the lepton number) as follows (Mezzacappa and Bruenn (1993b))

$$N_L \;\; = \;\; N_{e^-} - N_{e^+} + N_{\nu_e} - N_{\bar{\nu}_e} = N_{\nu_e} - N_{\bar{\nu}_e}.$$

However, there is no electron or positron flux relative to the fluid taken in the rest frame of the fluid, because electrons(positrons) correspond to the rest frame. Only the neutrinos can move relative to the fluid. The electron and electron-(anti)neutrino fractions are determined via the number densities n_i, i.e. $Y_i = \rho \, n_i / m_{\mathrm{B}}$, $(i \in e, \nu_e, \bar{\nu}_e)$ where the baryon mass is defined as $m_{\mathrm{B}} = 1.674 \times 10^{-24}$g. The neutrino number densities are explicitly given by phase-space integrals related to the zeroth moment of the distribution function (see Eq. 2.20) and hence the neutrino fractions are given by the following expressions (Mezzacappa and Bruenn (1993b))

$$Y_{\nu_e/\bar{\nu}_e}(t, a) \;\; = \;\; m_{\mathrm{B}} \frac{2\pi}{(hc)^3} \int_{-1}^{+1} d\mu \int_0^\infty E^2 dE \, F_{\nu_e/\bar{\nu}_e}(t, a, \mu, E) = \frac{n_{\nu_e/\bar{\nu}_e}}{n_{\mathrm{B}}},$$

where $F_\nu = f_\nu / \rho$ is the specific neutrino distribution function. Furthermore, the neutrino fluxes are given by phase-space integrations of the neutrino distribution functions as well, related to the first neutrino moment of the distribution functions $F_{\nu_e/\bar{\nu}_e}$ (see Eq. 2.20) as follows (Mezzacappa and Bruenn (1993b))

$$N_{\nu_e/\bar{\nu}_e}(t, a) = \frac{2\pi c}{(hc)^3} \int_{-1}^{+1} \mu d\mu \int_0^\infty E^2 dE \, f_{\nu_e/\bar{\nu}_e}(t, a, \mu, E).$$

With these definitions the continuity equations can be expressed for each electron-neutrino flavour explicitly. Integrating over the Boltzmann equation, Mezzacappa and Bruenn (1993b) obtained the following expressions for the conservation of the neutrino numbers (compare with Eq. 2.21)

$$\frac{\partial Y_{\nu_e}}{\partial t} + m_{\mathrm{B}} \frac{\partial}{\partial a} \left(4\pi r^2 \rho N_{\nu_e} \right) = \frac{m_{\mathrm{B}}}{\rho} \frac{2\pi c}{(hc)^3} \int_{-1}^{+1} d\mu \int_0^\infty E^2 dE \left(j_{\nu_e} - \tilde{\chi}_{\nu_e} f_{\nu_e} \right),$$

$$\frac{\partial Y_{\bar{\nu}_e}}{\partial t} + m_{\mathrm{B}} \frac{\partial}{\partial a} \left(4\pi r^2 \rho N_{\bar{\nu}_e} \right) = \frac{m_{\mathrm{B}}}{\rho} \frac{2\pi c}{(hc)^3} \int_{-1}^{+1} d\mu \int_0^\infty E^2 dE \left(j_{\bar{\nu}_e} - \tilde{\chi}_{\bar{\nu}_e} f_{\bar{\nu}_e} \right),$$

where j, χ are in units of cm^{-1}. Using the same definitions, the conservation of lepton number reads

$$\frac{\partial Y_e}{\partial t} + \frac{\partial}{\partial t}(Y_{\nu_e} - Y_{\bar{\nu}_e}) + m_{\mathrm{B}}\frac{\partial}{\partial a}\left(4\pi r^2 \rho \left(N_{\nu_e} - N_{\bar{\nu}_e}\right)\right) = 0.$$

Combining the above expressions, the evolution equation for the electron fraction Y_e can be written as follows (see Mezzacappa and Bruenn (1993b))

$$\frac{\partial Y_e}{\partial t} = -\frac{2\pi \, c \, m_{\mathrm{B}}}{\rho(hc)^3}\int_{-1}^{+1} d\mu \int_0^\infty E^2 dE \left\{(j_{\nu_e} - \tilde{\chi}_{\nu_e} f_{\nu_e}) - (j_{\bar{\nu}_e} - \tilde{\chi}_{\bar{\nu}_e} f_{\bar{\nu}_e})\right\}. \qquad (2.27)$$

This expression is determined by the local change of neutrino numbers given via neutrino absorption, emission and the neutrino flux. The emissivity and absorptivity depend sensitively on the thermodynamic conditions, which evolve dynamically. The rates favour equilibrium, e.g. $Y_e = constant$. This means when the thermodynamic state changes due to for instance adiabatic collapse(expansion) or shock heating, the reaction rates response to re-establish equilibrium again at a different value of Y_e. The value is rather important in core collapse supernovae as it determines for instance the composition of the ejecta during the explosion phase. It is sensitively tuned by the degree of electron degeneracy.

Remark 9 *The above argumentation for the electron flavour leptons which leads to the evolution equation for the electron fraction Eq. 2.27 can be applied to the μ-lepton number as well. A similar expression for the dynamical evolution of Y_μ could be obtained*

$$\frac{\partial Y_\mu}{\partial t} = -\frac{2\pi \, c \, m_B}{\rho(hc)^3}\int_{-1}^{+1} d\mu \int_0^\infty E^2 dE \left\{\left(j_{\nu_\mu} - \tilde{\chi}_{\nu_\mu} f_{\nu_\mu}\right) - \left(j_{\bar{\nu}_\mu} - \tilde{\chi}_{\bar{\nu}_\mu} f_{\bar{\nu}_\mu}\right)\right\}, \qquad (2.28)$$

which depends on the emissivity j and absorptivity χ of μ-(anti)neutrinos on nucleons via the muonic charged current reactions. Following Yueh and Buchler (1976a), the muonic charged current reactions can be trivially obtained from the derivation of the electronic charged current reactions as discussed above in §.2.4.1, applying the following replacements

$$\begin{aligned} f_{e^\pm} &\rightarrow f_{\mu^\pm}, \\ (f_{\nu_e}, f_{\bar{\nu}_e}) &\rightarrow \left(f_{\nu_\mu}, f_{\bar{\nu}_\mu}\right), \\ (\mu_e, m_e) &\rightarrow (\mu_\mu, m_\mu). \end{aligned}$$

It additionally requires the separation of μ and τ neutrinos in the Boltzmann transport equation, both of which are at present treated as one single species.

An alternative approach to calculate the dynamical evolution of the electron fraction has been published in Qian et al. (1993) and Qian and Woosley (1996). Based on the

weak reaction rates λ_{ij} for the reaction partners i and j, which are in a sense (see Remark 11) equivalent to the emissivity j and absorptivity χ used above, the evolution equation for the electron and positron fractions are given by the following relations,

$$\frac{dY_{e^-}}{dt} = -\lambda_{e^-p}Y_{e^-}Y_p + \lambda_{\nu_e n}Y_{\nu_e}Y_n$$

$$\frac{dY_{e^+}}{dt} = -\lambda_{e^+n}Y_{e^+}Y_n + \lambda_{\bar{\nu}_e p}Y_{\bar{\nu}_e}Y_p.$$

In the fully dissociated regime where no lepton-nuclei reactions contribute, i.e. using the following relations $Y_p = Y_e$ and $Y_n = 1 - Y_e$, the two expressions can be combined to calculate the evolution of the total number of charges as follows (Qian and Woosley (1996)),

$$\frac{dY_e}{dt} = \lambda_{e^+n}Y_{e^+} + \lambda_{\nu_e n}Y_{\nu_e} - \left(\lambda_{e^-p}Y_{e^+} + \lambda_{e^+n}Y_{e^+} + \lambda_{\nu_e n}Y_{\nu_e} + \lambda_{\bar{\nu}_e p}Y_{\bar{\nu}_e}\right)Y_e. \qquad (2.29)$$

To this point, the expressions (2.27) and (2.29) are equivalent. Furthermore, Qian and Woosley (1996) (see Eq.(73)) approximated the expression (2.29) in a crucial but powerful way as follows,

$$\begin{aligned} Y_e &\simeq \frac{\lambda_{e^+n}Y_{e^+} + \lambda_{\nu_e n}Y_{\nu_e}}{\lambda_{e^-p}Y_{e^+} + \lambda_{e^+n}Y_{e^+} + \lambda_{\nu_e n}Y_{\nu_e} + \lambda_{\bar{\nu}_e p}Y_{\bar{\nu}_e}} \\ &\simeq \frac{\lambda_{\nu_e n}Y_{\nu_e}}{\lambda_{\nu_e n}Y_{\nu_e} + \lambda_{\bar{\nu}_e p}Y_{\bar{\nu}_e}} \\ &= \left(1 + \frac{\lambda_{\bar{\nu}_e p}Y_{\bar{\nu}_e}}{\lambda_{\nu_e n}Y_{\nu_e}}\right)^{-1}, \end{aligned}$$

ignoring contributions from electron and positron captures and the decoupling of radiation and matter as well as neutrino transport. This expression was then further simplified and expressed in terms of the neutrino luminosities L_ν and the mean neutrino energies $\langle \epsilon_\nu \rangle$ respectively,

$$Y_e \simeq \left(1 + \frac{L_{\bar{\nu}_e}}{L_{\nu_e}} \frac{\langle \epsilon_{\bar{\nu}_e} \rangle - 2Q + \frac{Q^2}{\langle \epsilon_{\bar{\nu}_e} \rangle}}{\langle \epsilon_{\nu_e} \rangle + 2Q + \frac{Q^2}{\langle \epsilon_{\nu_e} \rangle}}\right)^{-1}, \qquad (2.30)$$

where $Q = m_n - m_p = 1.2935$ MeV is the rest mass difference between neutron and proton. This expression is used very often in models which do not relay on accurate Boltzmann transport but approximate neutrino contributions, for instance studies of the neutrino driven wind where neutrino luminosities and energies are assumed and from these the electron fraction can be calculated applying (2.30).

2.6   The equation of state

In the context of pure hydrodynamic simulations, the standard contribution which is determined by the equation of state (EoS) is the relation between matter pressure and matter (baryon) density ρ (n_{B}). In the case of internal structures, such as for instance the matter composition, the matter internal energy, entropy per baryon, the mass fractions of the free nucleons and the (light and heavy) nuclei as well as the chemical potentials

$$(P, e_{\mathrm{int}}, s, x_n, x_p, x_\alpha, x_{Fe}, \mu_n, \mu_p)$$

are given by the EoS as well. These quantities are determined not only for a given density but also for given temperature T and proton-to-baryon ratio given by the electron fraction Y_e, depending on the nuclear physics model applied.

There remains a question about the radiation-hydrodynamics timescales in relation to the timescale for the strong and weak interactions which change the composition and hence the EoS. In the case where the radiation-hydrodynamics timescale is much larger than the timescale for strong interactions, equilibrium is achieved instantaneously. No time dependency enters the EoS and it can be evaluated without loss of generality. This is the case for high temperatures and densities. However, at low densities and temperatures where nuclear burning processes are found to be present (e.g. a large fraction of the simulated domain in core collapse supernova studies are covered by the progenitor star), time dependent reaction rates determine the composition and hence the EoS.

In the following subsections, I will introduce the different thermodynamic regimes for which different EoSs are used in our core collapse supernova simulations. The thermodynamic conditions found in core collapse supernovae span the following 3-dimensional space in (T, n_{B}, Y_e)

$$
\begin{aligned}
T &= 10^{-4}, ..., 100 \text{ MeV}, \\
n_{\mathrm{B}} &= 10^{-12}, ..., 1 \text{ fm}^{-3}, \\
Y_e &= 0, ..., 0.8,
\end{aligned}
$$

where the low temperatures and densities correspond to the outer part of the stellar core, i.e. the Si-S, C-O, He and H-layers, which must be taken into account to some extend as well for the correct dynamic evolution (e.g. the mass accretion onto the Fe-core).

In order to support these numbers, Fig. 2.3 shows data from core collapse simulations of 15 M$_\odot$ (left panel) and 40 M$_\odot$ (right panel) progenitor stars. The figures illustrate the evolution of the Temperature with respect to the baryon density, where color-coded is electron fraction. High baryon densities correspond to the central part of the stellar domain and low densities are the infalling material from the Fe-core surroundings given by the progenitor, where matter is iso-spin symmetric with $Y_e \simeq 0.5$. However, the

highly deleptonised domain where $Y_e < 0.1$ corresponds to densities below saturation of $\rho \simeq 10^{11} - 10^{13}$ g/cm^3 where the neutrinospheres are located. Both models reach high central densities above nuclear saturation. The simulations differ also in the central temperatures obtained, $T \simeq 50$ MeV for the 15 M$_\odot$ progenitor and $T \geq 100$ MeV for the 40 M$_\odot$ progenitor. The domain illustrated in (T, n_{B}, Y_e) must be covered by the EoS valid for core collapse supernova simulations. Please note that the 40 M$_\odot$ model in Fig. 2.3 (left panel) collapses to a black hole after about 550 ms post-bounce.

Remark 10 *The (T, n_B, Y_e) phase space is occupied rather symmetrically for core collapse supernova matter. In other words extreme phase-space asymmetry, such as high baryon densities and low temperatures (e.g. neutron star matter) or vice versa (e.g. the early universe), are not obtained in core collapse supernova simulations on timescales of the order 1 second after bounce. This is illustrated in Fig. 2.3 at the example of the 15 and 40 M$_\odot$ progenitors from Woosley and Weaver (1995). Only at later times and after the explosion has been launched, when the central object becomes a neutrons star via deleptonisation of the PNS, the temperature decreases while the central density increases continuously.*
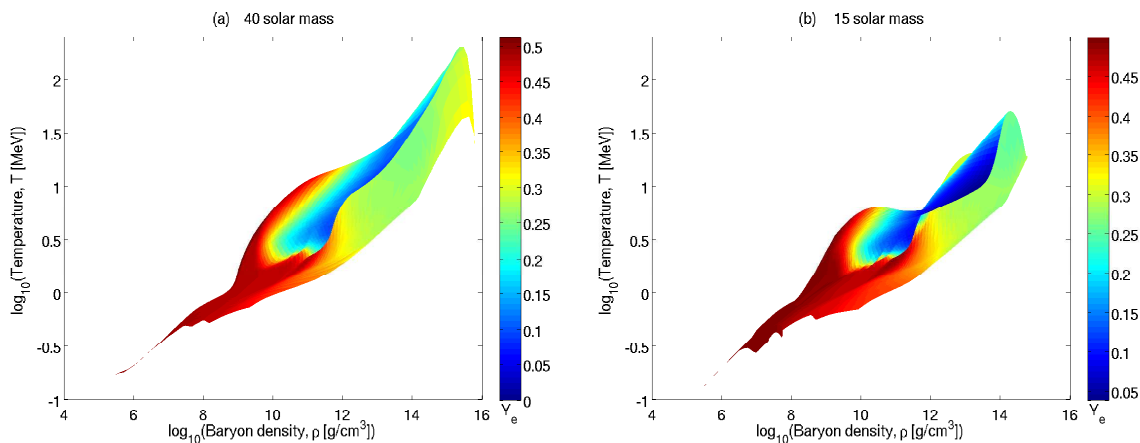
Figure 2.3: Thermodynamic phase space, illustrating the temperature and baryon density domain covered in core collapse supernova simulations of massive progenitor stars; (a): 40 M$_\odot$ and (b): 15 M$_\odot$). Color coded is the electron fraction. The white regions are not covered at all.

2.6.1 The nuclear reaction network for low temperatures and densities

For temperatures below 0.5 MeV, the physical domain is typically governed by the progenitor structure and the presence of heavy nuclei dominates the baryon matter

properties such as pressure, entropy per baryon, internal energy and the nucleon chemical potentials. However, at these conditions the electron(positron) contributions to the EoS dominate over the baryons. In the following subsection, I will describe the baryon EoS used and further below I will briefly sketch the electron-positron contributions to the EoS.

The baryon contributions

Following the notation of Timmes and Arnett (1999), the radiation contributions to the internal energy and the baryon pressure can be calculated based on the photon gas (massless, spin = 1) as follows

$$
\begin{aligned}
e_{\mathrm{B},th} &= \frac{8\pi}{15(hc)^3}(k_{\mathrm{B}}T)^4 = a\,T^4, \\
p_{\mathrm{B},th} &= \frac{1}{3}e_{\mathrm{B},th},
\end{aligned}
$$

where a is the Boltzmann constant. The ion-contributions on the other hand are calculated based on the non-relativistic perfect gas using a Maxwell-Boltzmann distribution as follows (Timmes and Arnett (1999))

$$
\begin{aligned}
e_{\mathrm{B},ion} &= \frac{3}{2}n_{\mathrm{ion}}k_{\mathrm{B}}T, \\
p_{\mathrm{B},ion} &= n_{\mathrm{ion}}k_{\mathrm{B}}T,
\end{aligned}
$$

where the total number density of ions (or nuclei) $n_{\mathrm{B},ion}$ is the sum of all number densities of the nuclei n_i, given explicitly by the mass fractions X_i and the atomic mass A_i or the abundances Y_i as follows

$$
n_i = \frac{\rho X_i}{m_{\mathrm{B}}A_i} = \frac{\rho Y_i}{m_{\mathrm{B}}},
$$

such that $n_{\mathrm{ion}} = \sum_i n_i$. Next to $e_{\mathrm{B},ion}$, the composition contributes to the total internal energy via nuclear burning processes. The generation of energy from nuclear reactions is taken into account via the dynamically changing composition, which in turn is calculated from a nuclear reaction network. The binding energy (or mass excesses m_{mexc}, both are equivalent) of the distribution of N nuclei used are calculated as follows,

$$
e_{\mathrm{B},nuc} = \sum_{i=1}^{N} Y_i\, m_{\mathrm{exc},i}\, c^2,
$$

where the mass excess of each nucleus with mass $m(Z, A)$, charge Z and atomic mass number A is given by (Thielemann)

$$
m_{\mathrm{exc}}(Z, A) = m(Z, A) - A\, m_u,
$$

where $m_u = 931.49432$ MeV is the atomic mass unit. It is defined as the mass of ^{12}C such that $m_{\text{exc},12} = 0$. We use the tabulated mass excesses from Audi et al. (2003). The total internal baryon energy is then given by the sum of all the contributions from above, i.e. (Timmes and Arnett (1999))

$$e_{\text{B}} = e_{\text{B},th} + e_{\text{B},ion} + e_{\text{B},nuc}.$$

To calculate the abundances Y_i dynamically, the following system of equations is used to calculate the number density n_i for each nucleus (Thielemann)

$$\frac{\partial n_i}{\partial t}\bigg|_{\rho=constant} = \sum_j N_j^i \lambda_j n_j + \sum_{j,k} \frac{N_{j,k}^i}{1 + \delta_{jk}} \langle \sigma v \rangle_{j,k} \, n_j n_k, \tag{2.31}$$

due to weak interactions and photodisintegration (first term) and two-particle reactions (second term). The N's are positive or negative numbers and specify how many particles of abundance Y_i are created or destroyed. The number densities can be expressed in terms of the abundances and hence Eq. (2.31) takes the following form (Thielemann)

$$
\begin{aligned}
\frac{\partial Y_i}{\partial t} &= \frac{m_{\text{B}}}{\rho} \frac{\partial n_i}{\partial t} \\
&= \sum_j N_j^i \lambda_j Y_j + \frac{\rho}{m_{\text{B}}} \sum_{j,k} \frac{N_{j,k}^i}{1 + \delta_{jk}} \langle \sigma v \rangle_{j,k} \, Y_j Y_k,
\end{aligned}
$$

assuming $\rho = $ constant. In the following paragraphs, I will sketch the basic equations to calculate the reactions (reaction rates) used in the reaction network. Note, the considered reactions are labeled as follows

$$i + j \to o + m \quad : \quad i(j, o)m.$$

Reaction 14 $i(\gamma, o)m$, *(photodisintegration)*

Photodisintegration is the capture of highly thermalised photons (which translates to high temperatures) on heavy nuclei. The general reaction rate (Thielemann),

$$r_{i,j} = \int dn_i \, dn_j \, \sigma \cdot |\vec{u}_i - \vec{v}_j|,$$

can be written as follows (see Thielemann), applying the Plank distribution for the projectile photon $j = \gamma$ (which has relative speed of light c) and the Maxwell Boltzmann distribution for the target nucleus

$$
\begin{aligned}
r_{i,\gamma} &= n_i \frac{1}{\pi^2} \frac{(2\pi)^3 c}{(hc)^3} \int_0^\infty dE_\gamma^2 \, \sigma_{i,\gamma,o}(E_\gamma) \left(\exp\left\{ \frac{E_\gamma}{k_{\text{B}} T} \right\} - 1 \right)^{-1} \\
&= \lambda_{i,\gamma,o}(T) \, n_i,
\end{aligned}
$$

where λ acts as a temperature T dependent decay constant and $\sigma_{i,\gamma,o}$ is the photodisintegration cross section.

Reaction 15 $i(e^-, \nu_e)m$, $i(\nu_e, e^-)m$ *(electron capture rates, electron-neutrino captures)*

The calculation of the reaction rate has already been demonstrated in §2.1.3 where we discussed the collision term of the Boltzmann equation. For the reaction network a slightly different approach is applied. Following standard statistical mechanics (Thielemann), the reaction rate can be expressed as an integral over the reaction cross section σ_e as follows

$$r_{i,e} = \int dn_i \, dn_e \, \sigma_e \cdot |\vec{v}_i - \vec{v}_e| \, .$$

Rewriting this expression in terms of the centre of mass coordinates (i.e. the nucleus is at rest in the centre of mass system), one obtains the following form for the reaction rate (Thielemann)

$$\begin{aligned} r_{i,e} &= n_i \int dn_e \, \sigma_e(v_e) \, v_e \\ &= \lambda_{i,e}(\rho Y_e, T) \, n_i. \end{aligned}$$

The decay rate $\lambda_{i,e}$ is the integral of the electron capture cross section σ_e and depends on the number density of electrons and hence on the baryon density ρ and the electron fraction Y_e and on the temperature T.

Remark 11 *The same calculations can be done for the reaction rate r_{i,ν_e} and the decay rate λ_{i,ν_e}, i.e. for electron-neutrino captures. However, the conditions of the progenitor stars do not favour neutrino captures and the emitted neutrinos produced via electron captures escape freely. This reaction is only important at high baryon densities above 10^{11-12} g/cm^3 and are hence handled applying Boltzmann neutrino transport as discussed above in §2.1. However, since the neutrino capture reactions are the reverse reactions to electron captures, the calculation of the rates can be done applying detailed balance.*

Remark 12 *Comparing the decay rates with the calculation of the emissivity j and opacity χf_{ν_e} (as defined above, f_{ν_e} is the electron-neutrino distribution function) in the context of electron captures on free protons and electron-neutrino captures on free neutrons, both procedures are in a way equivalent (taking into account the approximations made for the momentum integartion calculating j and χ) as follows*

$$\begin{aligned} \lambda_{p,e} &= \frac{j}{X_p}, \\ \lambda_{n,\nu_e} &= \frac{\chi f_{\nu_e}}{X_n}, \end{aligned}$$

where j and χ are the energy integrated emissivity and absorptivity respectively.

Reaction 16 $i(e^+, \nu_e)m$, $i(\bar{\nu}_e, e^-)m$ *(positron capture rates, electron-antineutrino captures)*

These reactions become only important at large electron degeneracy, which is typically not achieved in progenitor models. Even during the Fe-core collapse such large degeneracy is typically not obtained. Hence, these reactions are suppressed and not considered. However, the same calculation as for $i(e^-, \nu_e)m$ can be applied to obtain the reaction and decay rates, i.e. r_{i,e^+} and λ_{i,e^+}.

Reaction 17 *Decay reactions*

In accordance to electron captures, in the case of decay reactions such as the beta-decay or the alpha-decay, the decay rate for nuclei in the ground state is given by (see Thielemann)

$$r_i = \lambda_i\, n_i,$$

where the decay constant λ_i is given by the inverse of the decay half-life time $\tau_{1/2}$ as follows

$$\lambda_i = \frac{1}{\tau_{1/2}} \ln 2.$$

Remark 13 *At high temperatures where excited states can be populated, the decay constant becomes a function of the temperature. Such considerations are relevant for example in explosive nucleosynthesis investigations.*

Reaction 18 *2-particle interactions with nuclei*

When the interacting particles are nuclei and obey both Maxwell-Boltzmann statistics, the reaction rate $r_{i,j}$ can be expressed as follows (Thielemann)

$$
\begin{aligned}
r_{i,j} &= \int dn_i\, dn_j\, \sigma \cdot |\vec{v}_i - \vec{v}_i| \\
&= n_i\, n_j \int d^3v_i\, d^3v_j\, \sigma\left(|\vec{v}_i - \vec{v}_j|\right) |\vec{v}_i - \vec{v}_i|\, f_i\, f_j \\
&= n_i\, n_j\, \langle \sigma v \rangle_{i,j},
\end{aligned}
$$

where

$$f_i = f(\vec{v}_i) = \frac{m_i^{\frac{3}{2}}}{(2\pi k_{\mathrm{B}} T)^3} \exp\left\{ -\frac{m_i\, v_i^2}{2 k_{\mathrm{B}} T} \right\},$$

are the Maxwell-Boltzmann distribution functions of the nuclei. Changing to the centre of mass coordinates, where the centre of mass nuclei is at rest, the integral expression

for the transition rate $\langle \sigma v \rangle_{i,j}$ can be written in terms of the relative particles energy E and mass μ as follows (Thielemann)

$$\langle \sigma v \rangle (T) = \sqrt{\frac{8}{\mu \pi}} \frac{1}{(k_{\mathrm{B}} T)^{3/2}} \int_0^\infty E \, dE \, \sigma(E) \exp \left\{ -\frac{E}{k_{\mathrm{B}} T} \right\}.$$

From the above considerations it becomes clear the central importance lays in the knowledge of the cross sections for the relevant reactions. With these one is enabled to calculate the transition rates and hence determine the abundances and their changes due to the reactions discussed above, for a given number of nuclei and the thermodynamic state (T, n_{B}).

Remark 14 *Sine nuclear reactions change the composition as discussed above, the electron fraction Y_e changes accordingly. Due to present computational limitations we use only 20 nuclei. Starting with (n, p) the free nucleons and ^3He, we use the 14 symmetric nuclei from ^4He to ^{56}Ni and include additionally a few Fe-group isotopes, i.e. in total*

$$
\begin{aligned}
(n, p) && nucleons \\
\left(^3He, ^4He \right) && light\ nuclei \\
\left(^{12}C, ^{14}N, ^{16}O, ^{20}Ne, ^{24}Mg, ^{28}Si, ^{32}S, ^{36}Ar, ^{40}Ca, ^{44}Ti, ^{48}Cr \right) && \alpha\text{-}chain \\
\left(^{52}Fe, ^{53}Fe, ^{54}Fe, ^{56}Fe, ^{56}Ni \right) && Fe\text{-}group
\end{aligned}
$$

These abundances are included into the state vector of AGILE-BOLTZTRAN to model their advection on the adaptive grid accurately. The state vector reads then as follows,

$$\left(a, r, v, m, \rho, T, Y_e, \alpha, Y_n, Y_p, \ldots, Y_{^{56}Fe} \right),$$

where originally only the first 8 quantities were taken into account, i.e. baryon mass a, radius r, velocity v, gravitational mass m, baryon density ρ, temperature T and the lapse function α. However, the abundances are only required to calculate the internal energy evolution. The impact of the nuclear reaction network to change Y_e is of minor importance to determine the nuclear binding energy. It can not be described in details due to the rather small number of nuclei used and we neglect the effect. Though, it is taken into account in post-processing nucleosynthesis investigations where a much larger (typically $N \sim 1000$) nuclear reaction network is used.

Remark 15 *The chemical potentials in the presence of free nucleons are calculated based on the non-relativistic Maxwell-Boltzman gas (Thielemann)*

$$\mu_{(n,p)} = k_B T \ln \left\{ \frac{n_{(n,p)} h^3}{g} \frac{1}{(2\pi m_{(n,p)} T)^{(3/2)}} \right\} + m_{(n,p)} c^2, \tag{2.32}$$

where $g = 2$ for neutrions and protons, h is Planks constant, $m_{(n,p)}$ are the neutron(proton) mass and $n_{(n,p)} = \rho Y_{(n,p)} / m_B$ are the neutron(proton) number densities.

The electron-positron gas

For the calculation of the electron pressure, internal energy and chemical potential, one can use standard text book statistical physics and apply the equations from the degenerate Fermi-gas (spin $s = 1/2$, weight $g = 2$). The EoS we use is developed by Timmes and Arnett (1999). Applying Fermi-Dirac statistics for the derivation of the number density of electrons, the following expression can be found (for the result, see Timmes and Arnett (1999))

$$
\begin{aligned}
n_{e^-} &= \int_0^\infty dp\,\omega(p)\,f_{e^-}(p) = \int_0^\infty dE\,\omega(E)\,f_{e^-}(E) \\
&= \frac{4\pi}{h^3}\,(2m_e k_{\mathrm{B}}T)^{3/2} \int_0^\infty dx\frac{x^{1/2}}{e^{x-\eta}+1}(1+x)\left(1 + \frac{1}{2}\frac{k_{\mathrm{B}}T}{m_e c^2}x\right) \\
&= \frac{4\pi}{h^3}\,(2m_e k_{\mathrm{B}}T)^{3/2}\left(F_{1/2}(\eta,\beta) + F_{3/2}(\eta,\beta)\right),
\end{aligned}
$$

where $x = E/k_{\mathrm{B}}T$, f_{e^-} is the electron distribution function, $\omega(p)$ is the state density which depends explicitly on the statistical weight and the momentum(energy) [8], $\beta = k_{\mathrm{B}}T/m_e c^2$ and $\eta = \mu_e/k_{\mathrm{B}}T$ is the degeneracy parameter. The Fermi-Dirac-integrals are given as follows (Timmes and Arnett (1999))

$$
F_k(\eta,\beta) = \int_0^\infty dx\frac{x^k}{e^{x-\eta}+1}\left(1 + \frac{1}{2}\beta x\right)^{1/2}.
$$

Replacing the electron chemical potentials by the positron chemical potentials $\mu_{e^+} = -\mu_{e^-}$, where $\mu_{e^-} \equiv \mu_e$, the following expression for the number density of positrons can be found (see Timmes and Arnett (1999))

$$
n_{e^+} = \frac{4\pi}{h^3}\,(2m_e k_{\mathrm{B}}T)^{3/2}\left(F_{1/2}(-\eta - 2/\beta,\beta) + \beta F_{3/2}(-\eta - 2/\beta,\beta)\right).
$$

Combining these expressions with the number density of electrons, i.e.

$$
n_{e^-} - n_{e^+} = \frac{\rho Y_e}{m_{\mathrm{B}}},
$$

which is typically known in an astrophysical context (ρ via the continuity equation and Y_e via electron/positron and electron-(anti)neutrino capture reactions). Combining the

---

[8]The expression for the state density for the calculation is given as follows (Timmes and Arnett (1999))

$$
\omega(E) = \frac{2\pi}{h^3}g(2m_e)^{3/2}E^{1/2}\left(1 + \left(\frac{1}{k_{\mathrm{B}}T} + \frac{1}{2m_e c^2}\right)E + \frac{E^2}{k_{\mathrm{B}}T\,2m_e c^2}\right),
$$

where the statistical weight is $g = 2$, which differs from the standard text book expression by a series expansion in E.

above expressions, it is possible to solve the integral expressions numerically and hence calculate the chemical potentials. The knowledge of these enables us to calculate the electron and positron pressure as follows (see Thielemann, Timmes and Arnett (1999))

$$
\begin{aligned}
p_{e^-} &= \frac{1}{3} \int_0^\infty dp\, p\, v\, \omega(p)\, f_{e^-}(p) \\
&= \frac{8\pi}{3} \frac{(2m_e)^{3/2}(k_{\mathrm{B}}T)^{5/2}}{h^3} \int_0^\infty dx \frac{x^{3/2}}{e^{x-\eta}+1} \left(1 + \frac{1}{2}\frac{k_{\mathrm{B}}T}{m_e c^2}x\right)\left(1 + \frac{1}{2}\frac{k_{\mathrm{B}}T}{m_e c^2}x\right) \\
&= \frac{8\pi}{3} \frac{(2m_e)^{3/2}(k_{\mathrm{B}}T)^{5/2}}{h^3} \left(F_{3/2}(\eta,\beta) + \frac{\beta}{2}F_{5/2}(\eta,\beta)\right), \\
p_{e^+} &= \frac{8\pi}{3} \frac{(2m_e)^{3/2}(k_{\mathrm{B}}T)^{5/2}}{h^3} \left(F_{3/2}(-\eta-2/\beta,\beta) + \frac{\beta}{2}F_{5/2}(-\eta-2/\beta,\beta)\right).
\end{aligned}
$$

The analogue calculation can be applied for the specific internal energy (Timmes and Arnett (1999))

$$
\begin{aligned}
e_{e^-} &= \int_0^\infty dp\, E\, \omega(p)\, f_{e^-}(p) \\
&= \frac{1}{\rho}\frac{4\pi}{h^3}(2m_e)^{3/2}(k_{\mathrm{B}}T)^{5/2}\left(F_{3/2}(\eta,\beta) + \beta F_{5/2}(\eta,\beta)\right), \\
e_{e^+} &= \frac{1}{\rho}\frac{4\pi}{h^3}(2m_e)^{3/2}(k_{\mathrm{B}}T)^{5/2}\left(F_{3/2}(-\eta-2/\beta,\beta) + \beta F_{5/2}(-\eta-2/\beta,\beta)\right) + \frac{1}{\rho}2m_e c^2\, n_{e^+}.
\end{aligned}
$$

Remark 16 *The total EoS is the sum of all contributions discussed above for the internal energy, pressure and entropy as follows*

$$
\begin{aligned}
e &= e_{B,rad} + e_{B,ion} + e_{B,nuc} + e_{e^-} + e_{e^+}, \\
p &= p_{B,rad} + p_{B,ion} + p_{B,nuc} + p_{e^-} + p_{e^+}, \\
s &= s_{B,rad} + s_{B,ion} + s_{B,nuc} + s_{e^-} + s_{e^+}.
\end{aligned}
$$

The composition is initially determined by the progenitor and changes during the dynamical evolution evolved using the nuclear reaction network. Next to the electron and positron chemical potentials, which are determined numerically as shown above, the chemical potentials of the free nucleons are calculated assuming an ideal gas of non-relativistic Fermions where due to $\mu/k_B T \to -\infty$ the Maxwell-Boltzmann statistics can be applied and from (see Thielemann)

$$
n_i = e^{\frac{\mu_i}{k_B T}} \frac{g}{h^c} \left(2\pi m_i k_B T\right)^{3/2}
$$

the chemical potentials can be determined by Eq.(2.32).

2.6.2 Hot and dense nuclear matter

For matter temperatures above 0.5 MeV the production of nuclei via nuclear reactions and the destruction via weak interactions and photodisintegration is found to be in thermal equilibrium, i.e. nuclear statistical equilibrium (NSE). The timescale to establish NSE is typically much shorter than the radiation-hydrodynamic timescale in core collapse supernovae, which are of the order of $1 - 100$ ms. Hence the composition can be calculated statically, i.e. depending only on the baryon density, temperature and the electron fraction. Based on the following equilibrium condition for the nucleus chemical potential μ_A and the free nucleons μ_n, μ_p (Thielemann),

$$\mu_A = N\,\mu_n + Z\,\mu_p,$$

the following relation can be used to calculate the abundance of a nucleus with atomic mass A, charge Z and $N = A + Z$ (Thielemann)

$$Y_A = G_A \left(\frac{\rho}{m_{\mathrm{B}}}\right)^{A-1} \frac{A^{4/2}}{2^A} \left(\frac{2\pi\hbar^2}{m_u k_{\mathrm{B}} T}\right)^{\frac{3}{2}(A-1)} Y_n^N \, Y_p^Z \, \exp\left\{\frac{B_A}{k_{\mathrm{B}} T}\right\}, \qquad (2.33)$$

where G_A is the statistical weight of the nucleus, $B_A := N\,m_n c^2 + Z\,m_p c^2 - m_A c^2$ and where Maxwell-Boltzmann statistics is applied for the calculation of the chemical potentials and the following assumptions have been made to simplify the expression (Thielemann)

$$
\begin{aligned}
m_n \simeq m_p &\simeq m_u, \\
m_A &\simeq A\,m_u.
\end{aligned}
$$

The expression (2.33) can be understood as follows:

(i) high densities favour nuclei with large A due to the dominance of the term ρ^{A-1},

(ii) high temperatures favour light nuclei and free nucleons due to the presence of highly thermalised photons (photodisintegration),

(iii) intermediate conditions favour stable nuclei with the largest binding energies due to the dominance of the exponential term $\exp\{B_A/k_{\mathrm{B}} T\}$.

Together with the relations of charge neutrality and mass conservation, i.e. (Thielemann)

$$
\begin{aligned}
\sum_i X_i = \sum_i A_i Y_i &= 1, \\
\sum_i Z_i Y_i &= Y_e,
\end{aligned}
$$

expression (2.33) can be used instead of expression (2.31) to calculate the nuclear composition. For the construction of an EoS for nuclear matter, NSE is assumed for all thermodynamic conditions. This leads to increasing inaccuracies for low temperatures and densities where the nuclear burning history of the progenitor is used to calculate the EoS as demonstrated in the subsection above and time dependent nuclear reactions must be used.

However, for high densities and temperatures above 0.5 MeV the commonly used EoSs for hot and dense nuclear matter are the EoS from Lattimer and Swesty (1991) (EoS1) and the EoS from Shen et al. (1998a) (EoS2). EoS1 is based on the liquid drop model including surface effects. It already contains contributions from electrons and positrons and is available to the community as a subroutine or a table for the three different incompressibility energies 180, 220 and 375 MeV and a asymmetry energy of 29.3 MeV. These values determine the stiffness or softness of nuclear matter. EoS2 is based on the relativistic mean field (RMF) approach and Thomas-Fermi approximation. It has a incompressibility of 281 MeV and a asymmetry energy of 36.9 MeV, which results in a rather stiff EoS for nuclear matter in comparison to EoS1. EoS2 contains only the baryon contributions and is distributed to the community as a table. Contributions from electrons and positrons as well as ion-ion correlations and photons are added using the same EoS applied for matter in non-NSE as described in the subsection above. It is developed by Timmes and Arnett (1999) and Timmes and Swesty (2000). EoS1 and EoS2 assume NSE for all conditions. Both approximate the composition os heavy nuclei via a single nucleus with average atomic A mass and charge Z, in addition to α-particles which represent light nuclei and the free nucleons. Above the neutron drip line, which is found at intermediate densities of about $\rho \simeq 10^{12}$ g/cm^3, nuclei start to dissolve and nuclear matter appears. At even higher densities, nuclei disappear completely and bulk nuclear matter, which means free nucleons only, is achieved. The EoSs handle the transitions between these different regimes intrinsically.

EoS2 has been added to our core collapse model recently. In the following paragraph I will examine the three different descriptions used for the different nuclear regimes. Relativistic mean field (RMF) theory is applied to calculate the EoS for homogeneous nuclear matter (free nucleons only), the Thomas-Fermi approximation is used for inhomogeneous matter (free nucleons, α-particles, a single representative heavy nucleus) and the ideal gas approximation for low densities and temperatures. The minimisation of the free energy determines which approach is favoured over the other. Note that it is hardly possible to conclude the (dis)appearance of phases to density or temperature effects. It is a correlation of the density, the temperature and the electron fraction. The different thermodynamic regimes can be separated as follows (Shen et al. (1998a))

(a) *homogeneous nuclear matter* for densities and temperatures of

$$
\begin{aligned}
n_\mathrm{B} &= 0.0954, ..., 1.5127 \text{ fm}^{-3}, \\
T &= 15, ..., 100 \text{ MeV},
\end{aligned}
$$

for a mixture of neutrons, protons and initially α-particles which disappear at high densities and temperatures.

(b) *non-uniform matter* at intermediate densities and high enough temperatures for the free nucleons to form clusters that are interpreted as heavy nuclei. The starting density of this phase depends strongly on the temperature where at high densities the temperature dependency decreases. For temperatures $T > 15$ MeV, the non-uniform matter phase disappears independent of the density.

(c) *uniform matter* at low densities and finite temperatures for a mixed gas of neutrons, protons and α-particles.

(d) *the ideal gas* for densities in the range

$$n_{\mathrm{B}} = 7.58 \times 10^{-11}, ..., 10^{-5}\,\mathrm{fm}^{-3},$$

and finite temperatures where, based on the most stable nucleus with atomic mass $A \simeq 56$, heavy nuclei dominate the EoS.

This behaviour is illustrated in Fig. 2.4 for low temperatures where nuclei dominate the EoS. At $T = 0.5$ MeV (left panel) where (supernova) matter is typically only very slightly iso-spoin asymmetric with $Y_e = 0.48$, heavy nuclei have atomic masses around $\langle A \rangle \simeq 60$ and belong to the Fe-group with $\langle Z \rangle \simeq 26$. These nuclei become larger going to higher baryon densities, forming even the extremely massive ('isotopic') nuclei with $\langle A \rangle > 2000$[9], before finally slightly below saturation density bulk (fully dissociated) nuclear matter appears and the heavy nuclei disappear. At low densities, heavy nuclei compete with the appearance of α-particles. Going to higher temperatures of $T = 1$ MeV (right panel), where the asymmetry typically increases and $Y_e = 0.4$, the fraction of heavy nuclei reduces at low densities in favour of α-particles and free nucleons, and the heavy nuclei become larger with $\langle A \rangle \simeq 80$ and $\langle Z \rangle \simeq 30$ before super-heavy nuclei appear slightly below saturation density. Fig. 2.5 illustrates the baryon fractions at higher temperatures where heavy nuclei start to disappear. At about $T = 5$ MeV and $Y_e = 0.3$ (left panel, which are typical bounce conditions), the fraction of heavy nuclei reduces to the density domain where only the super-heavy nuclei exist. The fraction of α-particles reduces at lower densities as well and the EoS is determined by the gas of free nucleons. This phenomenon holds for even higher temperatures of $T = 10$ MeV where typically $Y_e = 0.2$ (right panel, typical post-bounce condition).

Remark 17 *Both EoSs, EoS1 and EoS2, define the internal energy density relative to the nuclear model specific mass unit. These gauge masses $m_g[MeV]$ are the neutron*

---

[9]Such bulk of nuclear matter are no physical nuclei, i.e. they cannot be found in the nuclear chart. They form due to the clustering of nucleons at intermediate densities and belong to the phase known as *pasta*, *spaghetti* and *Swiss cheese*. More precise descriptions for these phases are required in order to take the effects into account constructing an EoS.
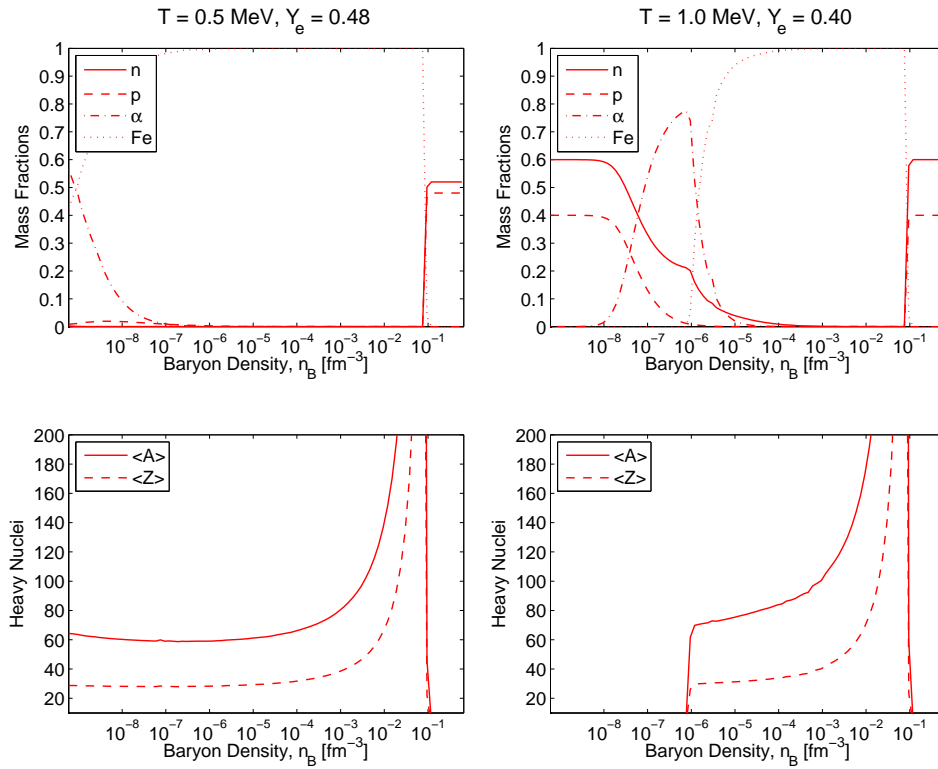
Figure 2.4: Baryon fractions and average atomic mass number and charge with respect to the baryon density for different thermodynamic conditions found in core collapse supernova simulations. The conditions illustrate the regime dominated by a large fraction of heavy nuclei.
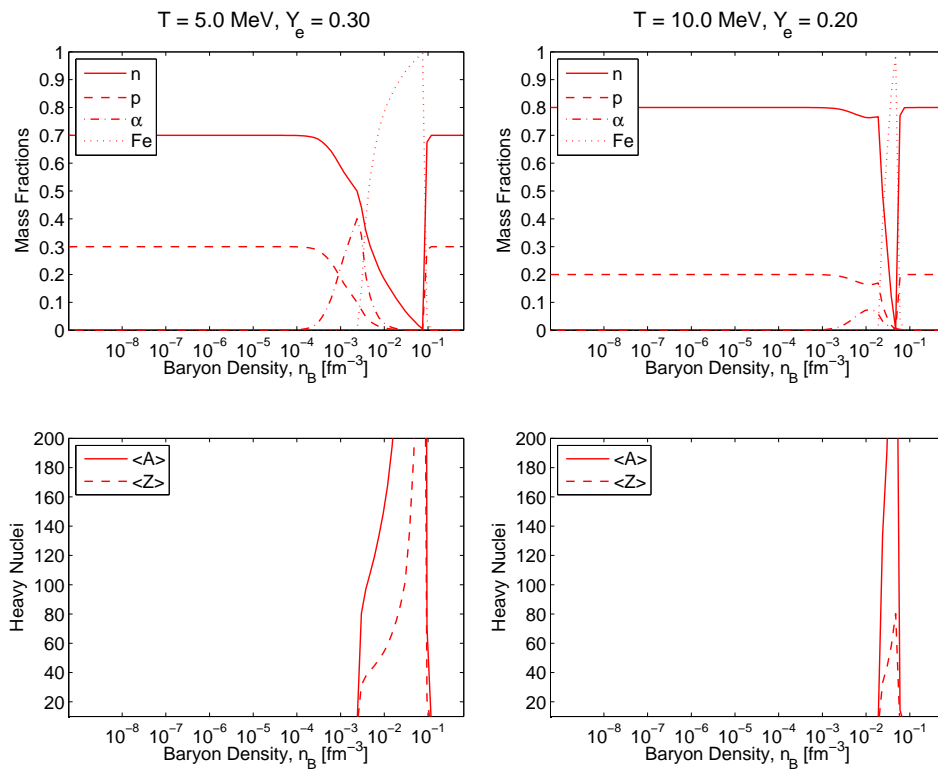
Figure 2.5: The same configuration as Fig. 2.4 but higher temperatures where heavy nuclei disappear.

mass $m_n = 939.5653$ MeV and the atomic mass unit $m_u = 931.49432$ MeV for EoS1 and EoS2 respectively. The internal energy density output of the EoSs is then given by the following expression

$$e_{int}[MeV] = \frac{e}{n_g} - m_g.$$

For each gauge the baryon density is defined as follows

$$\rho = m_g n_g,$$

where n_g is the baryon number density. Since our numerical model Agile-Boltztran uses a different definition of the baryon mass, i.e. $m_B = 1.674 \times 10^{-24}$ g $(= 939.0361$ MeV), the internal energy is re-gauged to m_B as follows

$$e_{AB}[MEV] = e_{int}[MeV] + (m_g - m_B).$$

This value for the internal energy density is then used in our numerical model.

2.7   Matter at and above nuclear saturation density

Although the baryon EoSs from Lattimer and Swesty (1991) and Shen et al. (1998a) describe the properties of matter above nuclear density, the physical state of matter at such high densities relatively uncertain. On the other hand, the saturation point of nuclear matter is known experimentally. Electron-nucleon scattering experiments have shown that the central density of heavy nuclei is almost constant and independent of the atomic mass. This provides values for the saturation density (Durand et al. (2000))

$$n_0 = 0.17 \pm 0.2 \, \text{fm}^{-3},$$

where the binding energy of nuclear matter at saturation density can be estimated to be (Durand et al. (2000))

$$\frac{E}{A_0} = -16 \pm 1 \, \text{MeV}.$$

The saturation point, in other words the EoS of nuclear matter at saturation density, corresponds to the equilibrium point at $T = 0$ MeV. This translates to a vanishing pressure at saturation density.

2.7.1   Heuristic considerations

Assuming an ideal gas of N fermions (nucleons) in a finite volume. The Fermi energy of the gas is defined as the chemical potential at zero temperature, i.e. $E_{\text{F}} = \mu(T = 0)$,

and can be written in terms of the number density n_N of the nucleons as follows

$$
\begin{aligned}
E_{\mathrm{F}} &= \frac{(\hbar c)^2}{2m_N}(3\pi^2)^{2/3}n_N^{2/3} \\
&\simeq 198.716\,\mathrm{MeV} \times \left(\frac{n}{\mathrm{fm}^{-3}}\right)^{2/3},
\end{aligned}
$$

where m_N [MeV] is the nucleon mass. This gives Fermi-energies of $\simeq 42.8$ and $\simeq 125.183$ MeV for baryon densities of 0.1 and 0.5 fm^{-3} respectively. This behaviour of the Fermi energy is illustrated in Fig. 2.6. Increasing the (number) density while keeping the
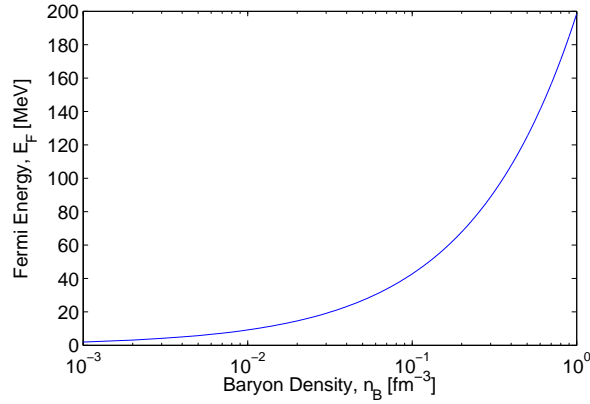

Figure 2.6: Fermi energy with respect to the baryon density.

volume fixed translates to a system where the mean distance between the nucleons reduces. Where the gas to be non-interacting, at some (number) density the wave functions would begin to overlap. This effect is compensated in an interacting nucleon gas by for instance nucleon-nucleon interactions. Such interactions describe generally short range forces and are taken into account for both EoSs discussed above. They are assumed to be strongly repulsive at short distances of ≤ 0.4 fm and attractive at intermediate distances of $\sim 1 - 1.2$ fm. Such interactions determine the compressibility and the asymmetry energy of the EoS and are responsible for the stiffening of the EoS at high densities. However, increasing the baryon density to high values will continuously increase the Fermi energy. There is no upper limit for the baryon density of a nucleon gas. It simply translates to higher Fermi levels of the nucleon states that are occupied. Baryon densities above nuclear saturation might have a deformation effect on the nucleon structure, where the model of a nucleon gas (despite various nucleon-nucleon interactions) might not be applicable anymore. It is physically more appropriate to include the nucleon sub-structure, i.e. the quarks. Their properties are known (to some extend) from high energy $E > 1$ GeV (deep inelastic) electron-nucleon scattering experiments. Electrons (or in general leptons) have a very small mean free

path at such high energies ($\lambda \sim 1/E < 0.2$ fm) and no internal structure. Hence, the scattering cross sections depend only on the internal structure of the scattering target (the nucleon). In addition, these cross sections can be calculated analytically (see for example Greiner and Schäfer) depending on the so called *structure functions*, which can be calculated from theoretical quark models to confirm the experimentally found values for the cross section. From such experiments and from the excited baryon resonances, it is well known that the nucleons consist of three quarks, i.e.

$$ \text{n} = \begin{pmatrix} d \\ u \\ d \end{pmatrix}, \quad \text{p} = \begin{pmatrix} u \\ d \\ u \end{pmatrix}, \tag{2.34} $$

where u and d denote the up- and down-quarks. Today, 6 quark species are known in total. These and a few of their properties are listed in Table 2.2 and 2.3. The quark

Table 2.2: Selected properties of the light quarks taken from the Particle Data Group and Eidelman (2004).

Flavour	Symbol	Mass [MeV]		Charge	Spin	Baryon number
up	u	2.55	$\begin{cases} +0.75 \\ -1.05 \end{cases}$	$+\frac{2}{3}$	$\frac{1}{2}$	$\frac{1}{3}$
down	d	5.04	$\begin{cases} +0.96 \\ -1.54 \end{cases}$	$-\frac{1}{3}$	$\frac{1}{2}$	$\frac{1}{3}$
strange	s	100	$\begin{cases} +26 \\ -34 \end{cases}$	$-\frac{1}{3}$	$\frac{1}{2}$	$\frac{1}{3}$

Table 2.3: Selected properties of the massive quarks taken from the Particle Data Group and Eidelman (2004).

Flavour	Symbol	Mass [GeV]		Charge	Spin	Baryon number
charm	c	1.27	$\begin{cases} +0.07 \\ -0.11 \end{cases}$	$+\frac{2}{3}$	$\frac{1}{2}$	$\frac{1}{3}$
bottom	b	4.20	$\begin{cases} +0.17 \\ -0.07 \end{cases}$	$-\frac{1}{3}$	$\frac{1}{2}$	$\frac{1}{3}$
top	t	171.2 ± 2.1		$+\frac{2}{3}$	$\frac{1}{2}$	$\frac{1}{3}$

spin of $1/2$, the baryon numbers of $1/3$ and the charges must be fulfilled to explain the nucleon quantum numbers. However, since spin-$1/2$ particles obey the Fermi-Dirac statistics two quarks must not be in the same state. Therefore, next to the flavour eigenstates, colour eigenstates are invented.

Although nuclear models that are used to describe nuclear matter and the EoS take quark contributions into account, one of the most prominent question in high energy

nuclear physics remains: *Is there a transition to a gas composed of deconfined quarks and at which conditions does it happen?* This question could not be answered to a satisfying degree by the present knowledge, because there is no model that describes consistently nucleons as the confined state of free quarks at finite densities and temperatures. Furthermore, the transition to a deconfined state and the general understanding of deconfinement is rather uncertain up to now and remains an active subject of research. It would mean solving the (de)confinement problem for the quantumchromodynamic (QCD) equations based on the QCD Lagrangian, taking quark-quark interactions and gluons (strong interaction particles) into account.

The approach to describe quarks as an interacting gas goes back to the theory of quantumelectrodynamics (QED) and its extensions to the theory of weak interactions. This path will be sketched in the following paragraphs. It leads to the formulation of the standard model of particle physics and describes all fundamental interactions of nature (electro-magnetism, weak, strong) by the exchange of specific interaction particles (photons, $W^{\pm}$-,Z^0-bosons, gluons). The electromagnetic interactions are modelled via the exchange of photons (electro-magnetic interaction particles) applying the following Lagrangian density,

$$
\begin{aligned}
L &= L_0 + L_{\text{int}} \\
&= -\frac{1}{4}\,F_{\mu\nu}\,F^{\mu\nu} + \bar{\psi}\,(p_\mu - eA_\mu)\,\gamma^\mu\psi,
\end{aligned}
$$

where ψ are the quantum fields, e is the charge, γ^μ are the gamma matrices and A^μ are the vector potentials. The field tensor is given by the following expression

$$
F_{\mu\nu} = \partial_\mu A_\nu - \partial_\nu A_\mu.
$$

The vector potentials have a benifitful property, they are invariant under gauge transformations which makes it possible to consider the QED as a gauge theory. This makes life a lot easier because one can make use of the well known symmetry group properties for gauge theories and their representations (see for example Greiner and Müller). The gauge group of QED can be achieved directly from the gauge symmetry by for instance replacing the interaction fields $A(x)$ by matrix valued functions $\hat{A}(x)$ and hence (Greiner and Schäfer)

$$
L = -\frac{1}{4}\,\hat{F}_{\mu\nu}\,\hat{F}^{\mu\nu} + \bar{\psi}\left(\hat{p}_\mu - g\hat{A}_\mu\right)\gamma^\mu\psi,
$$

where the coupling constant g has been introduced replacing e and where

$$
\hat{F}_{\mu\nu} = \partial_\mu\hat{A}_\nu - \partial_\nu\hat{A}_\mu + ig\left[\hat{A}_\mu, \hat{A}_\nu\right].
$$

This description for electro-magnetic interactions can be extended for weak interactions by postulating that leptons couple only to their neutrinos (e.g. electrons(positrons)

with electron-(anti)neutrinos, muons(anti-muons) with mu-(anti)neutrinos), which can be modelled via the exchange of charged particles. These interaction particles were given the names $W^{\pm}$-bosons. For the neutral currents (such as scattering and pair processes), the exchange of a neutrally charged particle had to be postulated in addition. It was given the name Z^0-boson. The matrix valued vector or gauge fields $\hat{A}$ are then replaced by the boson fields $\lambda^j W^j$ and B and the Lagrangian density becomes (Greiner and Schäfer)

$$L = -\frac{1}{4} W^j_{\mu\nu} W^{j,\mu\nu} - \frac{1}{4} B_{\mu\nu} B^{\mu\nu} + \bar{\psi} \left(p_\mu - g_1 W^j_\mu \frac{\lambda^j}{2} - g_2 B_\mu \right) \gamma^\mu \psi,$$

where the two coupling constants g_1 and g_2 describe the two different boson exchanges and where

$$
\begin{aligned}
W^j_{\mu\nu} &= \partial_\mu W^j_\nu - \partial_\nu W^j_\mu - g_1 \epsilon_{ijk} W^i_\mu W^k_\nu, \\
B_{\mu\nu} &= \partial_\mu B_\nu - \partial_\nu B_\mu.
\end{aligned}
$$

The matrices λ^j are due to the representation of the gauge group applied to the problem. The exchange of photons for QED leads to the U(1)-symmetry, where here the exchange of the $W^{\pm}$-bosons leads to SU(2)-symmetry and the exchange of Z^0-boson leads to U(1)-symmetry. Hence, the total symmetry group for weak interactions is the SU(2)$\times$U(1) where the following set of matrices (matrix valued vectors)

$$\lambda^1 = \begin{pmatrix} 0 & 1 \\ 1 & 0 \end{pmatrix}, \quad \lambda^2 = \begin{pmatrix} 0 & -\mathrm{i} \\ \mathrm{i} & 0 \end{pmatrix}, \quad \lambda^3 = \begin{pmatrix} 1 & 0 \\ 0 & -1 \end{pmatrix}, \quad \lambda^4 = \begin{pmatrix} 1 & 0 \\ 0 & 1 \end{pmatrix},$$

is a representation (identified as the Pauli matrices) of the gauge group.

The extension of this description to quark-quark interactions is a subject of active research. It has been postulated that the number of leptons must be equal to the number of quarks and hence there are three colour eigenstates. This statement leads to a representation of the symmetry group SU(3) for the QCD and the wave-functions become colour triplets

$$\psi(x) = \begin{pmatrix} \psi_{\mathrm{r}}(x) \\ \psi_{\mathrm{b}}(x) \\ \psi_{\mathrm{g}}(x) \end{pmatrix},$$

where (r,b,g) index the colours (red, blue, green) respectively. Denote the representation of the symmetry group as $\hat{\lambda}^a \in$ SU(3) and identifying the quark interaction particles as gluons, which consist of a colour and anti-colour state. Hence, there are 8 gluons in total. The vector(gauge) fields of the gluons can be written as follows

$$\hat{A}_\mu(x) = \sum_{a=1}^{8} \frac{1}{2} \hat{\lambda}^a A^a_\mu(x),$$

where the Lagrange density follows directly (Greiner and Schäfer)

$$L = -\frac{1}{2} \operatorname{tr} \left\{ \hat{F}_{\mu\nu} \, \hat{F}^{\mu\nu} \right\} + \bar{\psi} \left(\hat{p}_\mu - g\hat{A}_\mu \right) \gamma^\mu \psi.$$

g is the coupling constant for quark interactions and the gluon stress-energy tensor is given by the following expression (Greiner and Schäfer)

$$\hat{F}_{\mu\nu} = \partial_\mu \hat{A}_\nu - \partial_\nu \hat{A}_\mu - ig \left[\hat{A}_\mu, \hat{A}_\nu \right].$$

These equations, including the brief introduction of QED and the theory of weak interactions, form the standard model of particle physics with the fundamental interactions and their particles [10]. However, while the equations for QED and the theory of weak interactions can be solved rather straight forward from for instance perturbation considerations, it is not straight forward to solve the QCD equations based on the Lagrangian density. The following attempts can be found in the literature (Greiner and Schäfer).

1. The most prominent approach is the perturbation ansatz, where the series of Feynman-diagrams that can be constructed from the Lagrangian density converge at high order. This approach has been succeeded for QED and for the theory of weak interactions because the series expansion for the coupling constants converge at some point. The same argument does not apply for QCD. The series expansion in g of Feynman diagrams converges only at high energy scales $\sim$GeV. It is discussed in details in Greiner and Schäfer.

2. Another approach is to model the QCD on a lattice, where the continuous space-time is replaced by a discrete lattice. The equations are then solved numerically which might introduce numerical effects due to the presence of descretoced lattice solutions that could lead to increasing inaccuracies.

3. Most phenomenological approaches (I will not go into details here) work on the actual task of a QCD model that explains(predicts) the QCD phase diagram. The question could be formulated as follows: How many different representations (or phases) of quark matter do exist and which are the thermodynamic conditions in terms of temperature and chemical potential (or equivalent baryon density). Most of these models are based on phenomenological approaches that are similar to what is applied to calculate hadronic EoSs. The phenomenological descriptions predict a cross over from the hadronic regime to a quark-gluon plasma at low

---

[10]The experimental evidence for the presence of the Higgs-boson and the gravitational interactions are predicted theoretically but not included yet.

chemical potentials and high temperatures [11], while a phase transition of first or second order is expected at finite temperatures and large chemical potentials. The concern is a deeper understanding of the appearance of the different quarks and the possible existence of super-conducting phase at high chemical potentials.

In the following subsection, I will introduce the most simple phenomenological approach to describe quark matter and to construct an EoS. This model has been applied to core collapse simulations of massive stars to investigate the phase transition from hadronic matter to quark matter during the PNS evolution. It is meant to explore possible observables and the dynamics of the phase transition itself.

2.7.2   The MIT-bag model

This very simple and widely applied phenomenological approach to describe hadronic matter composed of quarks goes back to the assumption that quarks are enclosed inside the nucleons (which defines here confinement) where otherwise the quarks inside the nucleons can be considered as free Fermions (let me anticipate that there have been no free quarks observed in any experiment). The MIT-bag model suffers from the same variety of mismatches in explaining experimental data as other quark matter descriptions but the big advantage is its simplicity.

The basic idea is to construct a colour flux, given by the product of current vector and density, which fulfills the continuity equation and vanishes at a given (nucleon)surface (i.e. the nucleon radius) identified as the bag as follows (Greiner and Schäfer)

$$n^\mu \cdot \hat{J}^a_\mu \Big|_{\text{surface}} = \vec{n} \cdot \vec{\hat{J}}^a \Big|_{R(\theta,\phi) \subset \mathbb{R}^2} = 0,$$

where n is the density of states and the simplification (restriction) to the spatial surface R has been made. Assuming the different colour quarks can not be separated, the current vector is given by (Greiner and Schäfer)

$$\hat{J}^a_\mu = (\bar{q}_r, \bar{q}_b, \bar{q}_g)\ \lambda^a\ \gamma_\mu \begin{pmatrix} q_r \\ q_b \\ q_g \end{pmatrix},$$

where $\lambda^a \in \text{SU}(3)$ is a representation of the symmetry group and $q_i(x)$ are the quark colour wave functions. By means that the quark flavours can be considered separately,

---

[11]Lattice QCD calculations showed that the critical temperature T_c must be between $100 - 200$ MeV. These calculations predict a *smooth* confinement-deconfinement transition. The calculations can be extended to larger chemical potentials where T_c reduces. However, lattice QCD calculations could only be performed for a very limited amount of data points in the phase diagram due to numerical difficulties and present computational limitations.

the continuity equation takes the following form (Greiner and Schäfer)

$$\vec{n} \cdot \bar{q}\vec{\gamma}q \Big|_{R(\theta,\phi)} = 0,$$

which can be understood as a boundary condition. This leads to an eigenvalue problem for the matrix $\vec{n} \cdot \vec{\gamma}$ where the eigenvectors fulfill the above expression and the only unknown is the size of the bag given by R. The confinement (in other words the quarks inside the bag) produce a pressure acting onto the bag. This pressure must be equivalent to the external vacuum pressure. This is not meant to be a physical pressure but must be taken into account when constructing an EoS from the model assumption of a bag for confined quarks. Starting from the stress-energy tensor for Dirac-particles (i.e. particles that are solutions of the Dirac equation, see Greiner and Schäfer)

$$T_{\mu\nu} = \sum_q \frac{i}{2} \left(\bar{q}\,\gamma_\mu\,\partial_\nu q - q\,\partial_\nu\gamma_\mu\bar{q} \right),$$

the following relation holds (Greiner and Schäfer)

$$
\begin{aligned}
n^\mu T_{\mu\nu}\big|_{\text{surface}} &= \sum_q \frac{i}{2} n^\mu \bar{q}\,\gamma_\mu\,\partial_\nu q - n^\mu q\,\partial_\nu\gamma_\mu\bar{q} \bigg|_{\text{surface}} \\
&= -\sum_q \frac{1}{2}\bar{q}\,\partial_\nu q - q\,\partial_\nu\bar{q} \bigg|_{\text{surface}} \\
&= -\frac{1}{2}\partial_\nu \sum_q \bar{q}q \bigg|_{\text{surface}} \\
&= -n_\nu P_D\big|_{\text{surface}},
\end{aligned}
$$

using the fact that $(\vec{n} \cdot \vec{\gamma})^2 = -1$ and where P_D denotes the Dirac pressure. Hence, this pressure must be equivalent to a constant external pressure B

$$P_D\big|_{\text{surface}} = -\frac{1}{2}n^\nu \partial_\nu \sum_q \bar{q}q \bigg|_{\text{surface}} = -\frac{1}{2}\vec{n} \cdot \vec{\nabla} \sum_q \bar{q}q \bigg|_{R(\theta,\phi)\subset\mathbb{R}^2} = B,$$

where again the simplification(restriction) to only spatial dependencies has been made. This consideration determines the hadron-bag for given parameters B. For a spherically symmetric system, i.e. solving the Dirac equation for the massless quark fields in spherical symmetry, the bag pressure (constant) can be approximated in terms of the bag radius R as follows (Greiner and Schäfer)

$$R^4 = \frac{N_q}{4\pi B}ER,$$

where N_q is the number of quarks inside the bag and ER are the energy eigenvalues of the quark states that are considered. Although this approach has its major advantages in the simplicity, for instance quark-quark interaction (in other words gluons) are not considered and so are other important aspects not taken into account. However, an experimental and theoretical justifications of the MIT-bag model is at presence neither provided nor excluded.

2.7.3   The EoS for three flavour quark matter based on the MIT bag model

Quarks inside the bag can be considered as free particles. The equations for an ideal gas of Fermi-Dirac particles can be applied to calculate the EoS, assuming mass less (u,d)-quarks and massive s-quarks. In addition, the bag constant must be added to the internal baryon energy and subtracted from the baryon pressure.

To construct an EoS from such principles, the criterion that applies to decide which phase (hadronic or free quarks) is favoured is the minimisation of the free energy which was done by Sagert et al. (2009a) for a certain domain given by the independent variables (T, Y_e, n_B). The bag constants are chosen to be $B^{1/4} = 162$ MeV and $B^{1/4} = 165$ MeV, which gives stable maximal gravitational masses for cold ($T = 0$) neutron star matter of 1.56 $M_\odot$ and 1.50 $M_\odot$ respectively. At conditions where the MIT-bag model is favoured over the hadronic model EoS2, a transition from the Hadronic EoS to the quark EoS is constructed. For this purpose, Sagert et al. (2009a) assume global charge neutrality which leads to a Gibbs construction for the transition(coexistence) region between hadrons and quarks and hence to an adiabatic (constant entropy) phase transition. The coexistence region, in other words the onset and the end-point of the phase transition, is shown in Fig. 2.7 for the two choices of the bag constant. We plot the temperature dependency of the coexistence region with respect to the baryon density for different values for the electron fraction. From the graphs it becomes clear that for lower values of Y_e and higher temperatures, the onset of the phase transition happens at lower densities. This is independent of the size of the bag. For the larger bag constant, the onset of the phase transition as well as the end-point is shifted to higher densities and temperatures.

The mixed phase is modelled constructing a quark fraction X_Q, which is illustrated in Fig. 2.8 (lower panel) with respect to the baryon density for different Y_e and entropies per baryon s (see lower panel). X_Q rises slowly as the density increases. The onset of the phase transition is related to the appearance of the quark fraction (e.g. $X_Q > 0$) while it is zero in the hadronic regime ($X_Q = 0$). The end-point is related to the quark fraction reaching $X_Q = 1$. In this sense, the domain within between where $0 < X_Q < 1$ defines the mixed phase (or coexistence region). The upper panel of Fig. 2.8 shows the pressure with respect to the baryon density for the same conditions. There it becomes
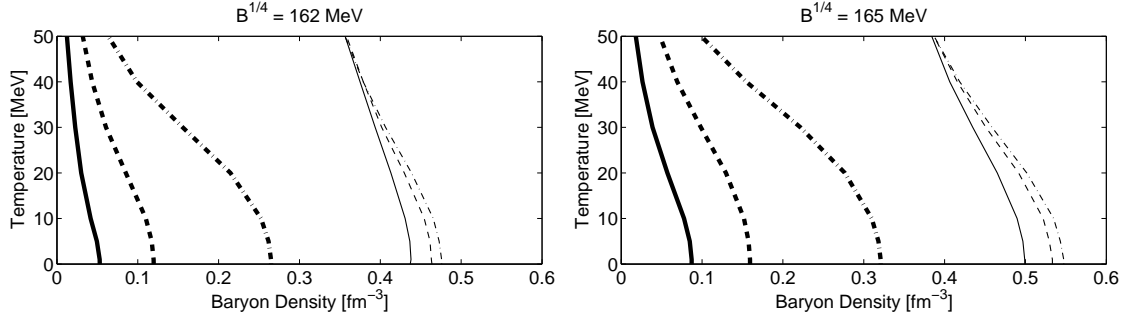
Figure 2.7: Onset and end-point of the mixed phase (coexistence region) for the two quark EoSs used based on the MIT-bag model with $B^{1/4} = 162$ MeV and $B^{1/4} = 165$ MeV for different values of Y_e (solid: 0.1, dashed: 0.3, dash-dotted: 0.5).
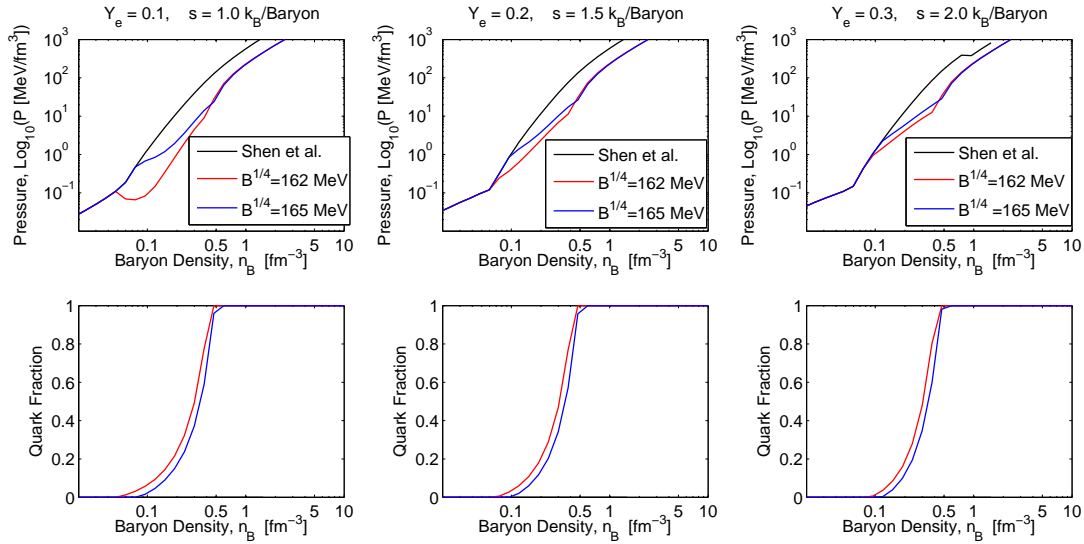

Figure 2.8: Pressure and quark fraction of the quark EoSs in comparison to EoS2.

clear that the mixed phase is characterised by a decreasing pressure gradient[12]. This translates to a decrease of the adiabatic index for matter which is in the mixed phase and hence to a significant softening of the EoS. The consequences of this construction will be discusses and illustrated in the following chapter in §3.3.

---

[12]Note that for the preparation of the quark EoSs and in particular the mixed phase, the lepton contributions are taken into account as well.

Chapter 3

Simulations of massive progenitor stars

In the following sections I will summarise the most important results that have been obtained during the past 4 years of my doctoral studies, using the numerical model AGILE-BOLTZTRAN which has been introduced in §2. including the resent improvements of the input physics. Explosions in spherical symmetry will be discussed at three examples, the low mass 8.8 M$_\odot$ O-Ne-Mg-core from Nomoto (1983,1984,1987) and the 10.8 and 18 M$_\odot$ Fe-core progenitors from Woosley et al. (2002). I will illustrate the differences between the O-Ne-Mg-core and Fe-core progenitors during the explosions phase. I will additionally examine the long term post-bounce evolution which is determined by the appearance of the neutrino driven wind. The second part of this chapter is devoted to the PNS evolution of more massive Fe-core progenitors in the mass range of $40 - 50$ M$_\odot$, where in the absence of an earlier explosion the continuous mass accretion leads to a PNS collapse and the formation of a black hole. Further below, I will discuss the quark-hadron phase transition during the early post bounce evolution of low and intermediate mass Fe-core progenitor stars. The phase transition leads to explosions, where in spherical symmetry otherwise no explosion could have been obtained. Furthermore, it becomes observable in the neutrino spectra

3.1 Neutrino driven explosions and the neutrino driven wind

Massive stars end their life in an explosion event with kinetic energies of the order 10^{51} erg. A region of low density and high entropy forms behind the explosion ejecta immediately after the explosion has been launched, which is continuously subject to neutrino heating. The neutrinos emitted from the remnant at the center, the protoneutron star (PNS), heat the material above the PNS surface. This heat is partly converted into

kinetic energy and the material accelerates to positive velocities, known as the neutrino driven wind. For the first time, we simulate the collapse, bounce, explosion and the neutrino driven wind phases consistently for more than 20 seconds. In simulations where no explosions are obtained naturally, we model neutrino driven explosions for low and intermediate mass Fe-core progenitor stars by enhancing the charged current reaction rates. In the case of a special progenitor star, the 8.8 $M_\odot$ O-Ne-Mg-core, the explosion in spherical symmetry was obtained without enhanced opacities. The post explosion evolution is in qualitative agreement with static steady-state and parametrized dynamic models of the neutrino driven wind. On the other hand, we find generally smaller neutrino luminosities and mean neutrino energies as well as a different evolutionary behavior of the neutrino luminosities and mean neutrino energies. In addition, the neutrino driven wind is proton-rich for more then 10 seconds and the PNS properties and the contraction behaviour differ from the assumptions made for the inner boundary in previous neutrino driven wind studies. Despite the moderately large entropies of about 100 k_B/baryon and the fast expansion timescale, the conditions found are unlikely to favor r-process nucleosynthesis. The simulations are carried out until the neutrino driven wind settles down to a quasi-stationary state. After about 5 seconds post bounce, the peak temperature inside the PNS already starts to decrease due to the continues deleptonization. This moment determines the beginning of the neutrino dominated cooling phase. We discuss the physical conditions of the quasi-static PNS evolution and take the effects of deleptonization and mass accretion of the low density envelope enclosed inside the mass cut into account.

Most of the work that will be presented in this section is collected in Fischer et al. (2009b) and submitted to Astronomy & Astrophysics.

3.1.1   Introduction to the neutrino driven wind

Independent of the explosion mechanism, the mass enclosed inside the mass cut will accrete onto the PNS after the explosion has been launched. The following dynamical evolution of the PNS and hence the properties of the neutrino spectra emitted is determined by the mass accretion and the EoS. On a timescale of several seconds after the explosion has been launched, the region between the expanding explosion shock and the PNS at the center is subject to the formation of the neutrino driven wind as follows. Neutrinos continuously diffuse out of the hot PNS and heat the material on top of the PNS surface before they reach the neutrinospheres. We define the PNS surface to be the radius of the energy-integrated electron-neutrinosphere. The dominant neutrino heating contributions are given by the captures of electron-neutrinos and electron-antineutrinos at free nucleons. Matter is heated by neutrinos where the thermal energy is converted into kinetic energy, which accelerates material on top of the PNS surface to positive velocities. This matter outflow is known as the neutrino driven wind.

In this context, two particular studies are of special importance. The properties of the neutrino driven wind as described in Woosley et al. (1994) are based on the detailed radiation hydrodynamics simulation of a 20 $M_\odot$ Fe-core progenitor applying the numerical model from Wilson and Mayle (1993). The simulation was carried until about 18 seconds after bounce. Another state-of-the-art model of that time was the explosion of the O-Ne-Mg-core by Mayle and Wilson (1988). Both investigations were milestones in the research of core collapse supernovae and are based on detailed neutrino input physics including neutrino transport, developed by J. R. Wilson. The results obtained, in particular the properties of the ejecta and the neutrino observables such as luminosities and energies, were considered the standard reference for more than 10 years. Neutrino driven wind studies used the results as parameters, where the conditions found indicated the possible site for the production of heavy elements via the r-process. In the simulations discussed in here, we follow a similar approach as Wilson and Mayle (1993) and Mayle and Wilson (1988), where we apply the neutrino input physics based on Bruenn (1985). Although we find general agreement with the previous work, in particular the explosion phase, we find significant differences in the properties of the neutrino driven wind. The entropies per baryon are smaller by a factor of 2-3 and the wind stays proton-rich for more than 10 seconds for all our models. In addition, the neutrino luminosities and mean energies are generally smaller. The mean neutrino energies decrease with time, where they remain almost constant in the simulation of Woosley et al. (1994). The largest difference arises in the decreasing difference between the mean electron neutrino and antineutrino energies found in our simulations, i.e. the neutrino spectra become more similar with respect to time. The difference in the neutrino spectra in Woosley et al. (1994) remains large and even increases with time. Using the results from Woosley et al. (1994) as reference, Qian and Woosley (1996) analyzed the neutrino driven wind and formulated approximate analytical expressions for various properties of the neutrino driven wind, e.g. the neutrino heating rate, the electron fraction, the entropy per baryon and the mass outflow rate.

Based on the static wind equations, the results obtained in parameter studies (see e.g. Duncan et al. (1986), Hoffman et al. (1997), Thompson et al. (2001) and Thompson and Burrows (2001)) became known as static steady-state wind models, where Woosley and Baron (1992), Woosley et al. (1994), Takahashi et al. (1994) and Witti et al. (1994) described the neutrino driven wind in a radiation-hydrodynamics context. Of special importance for the neutrino driven wind investigations is the impact on the nucleosynthesis. Most interesting is the possibility to explain the production of heavy elements via the r-process due to the large entropies, the fast expansion timescales and the low electron fraction of $Y_e < 0.5$ in the wind. Otsuki et al. (2000) explored general relativistic effects on the neutrino driven wind and investigated the possible impact on the nucleosynthesis. Recently, Wanajo (2006a) and Wanajo (2006b) investigated the neutrino driven wind with respect to the r- and rp-processes.

The possibility of supersonic wind velocities has been explored in most of the refer-

ences. The supersonically expanding material in the wind collides with the much slower expanding and denser explosion ejecta. The material decelerates and a reverse shock forms which is known as the neutrino driven wind termination shock (first observed by Janka and Mueller (1995) and Burrows et al. (1995)). Recently, Arcones et al. (2007) examined the post bounce phase of core collapse supernovae of several massive progenitor stars. Their models were launched from massive progenitor stars that were previously evolved through the core collapse, bounce and early post bounce phases using sophisticated radiation hydrodynamics based on spectral neutrino transport in spherical symmetry. The simulations are then continued applying a simplified radiation hydrodynamics description (see Scheck et al. (2006)), assuming large luminosities to trigger neutrino driven explosions in spherical symmetry. The neutrino driven wind develops supersonic outflow and the wind termination shock appears in all their models. Like most of the present neutrino driven wind studies, an interior boundary was assumed instead of simulating the PNS interior for the PNS contraction and the diffusion of neutrinos out of the PNS. However, steady-state wind studies could not predict the important dynamical features from the presence of the neutrino driven wind termination shock, especially the deceleration of the wind material and the consequent entropy as well as density and temperature increase during the deceleration. In this respect, the investigation from Arcones et al. (2007) was a milestone in modeling the neutrino driven wind consistently. On the other hand, they were focusing on parameters (luminosities and mean neutrino energies) in agreement with the simulations of Bethe and Wilson (1985) and Woosley et al. (1994). Although the dynamics is in general agreement, several properties of the neutrino driven wind as well as the neutrino spectra emitted differ significantly.

The present investigation follows a different approach. We simulate consistently the dynamical evolution of the collapse, bounce and post bounce phases until the neutrino driven wind phase for more than 20 seconds. The simulations are launched from the 8.8 $M_\odot$ O-Ne-Mg-core from Nomoto (1983,1984,1987) and the 10.8 and 18 $M_\odot$ Fe-core progenitors from Woosley et al. (2002). Our numerical model is based on general relativistic radiation hydrodynamics with spectral three-flavor Boltzmann neutrino transport in spherical symmetry. The explosion mechanism of massive Fe-core progenitors is an active subject of research. To model neutrino driven explosions for such progenitors in spherical symmetry, we enhance the electronic charged current reaction rates artificially which increases the neutrino energy deposition and revives the SAS. The mechanism including the tuned neutrino reaction rates will be further discussed in §2 and §3. Such explosion models were investigated with respect to the nucleosynthesis by Fröhlich et al. (2006 a-c). Here, we report on the formation of the neutrino driven wind and the possibility of the wind developing supersonic velocities and hence the formation of the wind termination shock. In addition, we will also illustrate the explosion and the neutrino driven wind phases of the O-Ne-Mg core, where an explosion is found in spherical symmetry even without artificially enhanced neutrino opacities.

The results are in qualitative agreement with those of Mayle and Wilson (1988) and Kitaura et al. (2006), who used a different EoS.

We find that for low progenitor masses, the neutrino driven wind termination shock will develop, using the tuned neutrino reaction rates. When the neutrino reaction rates are switched back to the standard opacities given in Bruenn (1985), the neutrino driven wind develops only a subsonic matter outflow. For intermediate progenitor masses, the neutrino driven wind remains subsonic even with the artificially enhanced neutrino emission and absorption rates. Since the neutrino driven wind depends sensitively on the emitted neutrino spectra at the neutrinospheres, we believe accurate neutrino transport and general relativity in the presence of strong gravitational fields are essential in order to describe the dynamical evolution. Furthermore, the accurate modeling of the electron fraction in the wind is essential for nucleosynthesis calculations, which can only be obtained using Boltzmann neutrino transport. In addition, it is beyond the present computational capabilities to carry multi-dimensional simulations with neutrino transport to several seconds after bounce. Hence, our investigations are performed in spherical symmetry where we simulate the entire PNS interior rather than approximating an interior boundary. We find significant discrepancies in comparison with the assumptions made in previous wind studies. Material is found to be proton rich for more than 10 seconds, where most wind models assume luminosities and mean neutrino energies such that the neutrino driven wind becomes neutron-rich. We question the validity of the approximations made in such wind studies. We believe that an accurate and consistent modeling of the physical conditions in the wind is essential, especially in order to be able to draw conclusions with respect to nucleosynthesis.

3.1.2 Enhanced neutrino emissivity and opacity

By our choice of a spherically symmetric approach, we implement the explosion mechanism of massive Fe-core progenitor stars artificially to trigger neutrino driven explosions during the post bounce evolution after the deleptonization burst has been launched. Neutrino heating between the neutrinospheres and the SAS transfers energy from the radiation field into the fluid. A part of this energy is converted into kinetic energy which revives the SAS and launches the explosion. The neutrino heating timescale and hence the neutrino driven explosions take place on a timescale of several 100 ms. The resulting neutrino spectra from artificially induced explosions in spherical symmetry are in agreement with the neutrino spectra of the very latest success of axially-symmetric neutrino driven core collapse supernova explosions by Marek and Janka (2009).

During the post bounce evolution, heavy nuclei continue to fall onto the SAS and dissociate into free nucleons. These free nucleons accrete onto the PNS surface. Hence the dominant neutrino heating contributions behind the SAS are due to the electronic charged current reactions. To trigger explosions in spherically symmetric core collapse simulations of massive Fe-core progenitors, we enhance the emissivity j and absorp-

tivity χ by a certain factor (typically $5 - 7$) in the region between the SAS and the neutrinospheres. This corresponds to matter with entropies above 6 k_{B}/baryon and baryon densities below 10^{10} g/cm^3. The entropies ahead of the shock are lower and the central densities of the PNS are higher, such that the artificial heating only applies to the region between the neutrinospheres and the SAS. The artificially enhanced reaction rates do not change the neutrino luminosities and mean neutrino energies significantly for the electron-neutrinos and electron-antineutrinos. Furthermore, β-equilibrium is fulfilled since the reverse reaction rates are obtained via the detailed balance. However, the timescale for weak-equilibrium to be established is reduced and hence the electron fraction changes on a shorter timescale. In combination with the increased neutrino energy deposition, this leads to a deviation of the thermodynamic variables in comparison to simulations using the standard opacities given in Bruenn (1985), which will be further discussed in §3.1.9. The weak neutrino driven explosions obtained have explosion energies of 6.5×10^{50} erg and 2×10^{50} erg for the 10 and the 18 $M_\odot$ progenitor model respectively.

3.1.3   Explosion energy and mass cut

The explosion energy estimate is a quantity which changes during the dynamical evolution of the system. It is given by the total specific energy of the fluid in the laboratory frame expressed in terms of the co-moving frame

$$E_{\mathrm{specific}}(t, a) = \Gamma e + \frac{2}{\Gamma + 1} \left(\frac{u^2}{2} - \frac{m}{r} \right), \tag{3.1}$$

which in turn is the sum of the specific internal energy e [1], the specific kinetic energy given by the fluid velocity $u = \partial r / \alpha \partial t$ squared and the specific gravitational binding energy m/r with gravitational mass m and radius r. $\Gamma(t, a) = \sqrt{1 - 2m/r + u^2}$ and $\alpha(t, a)$ are the metric functions in a non-stationary and spherically symmetric spacetime with coordinate time t, baryon mass a and the two angular coordinates (θ, ϕ) describing a 2-sphere of radius $r(t, a)$ [see Misner and Sharp (1964)]. The explosion is determined by the energy of the ejecta. Integrating $E_{\mathrm{specific}}(t, a)$ with respect to the enclosed baryon mass starting from the progenitor surface M toward the center

$$E_{\mathrm{total}}(t_0, a_0) = - \int_{\mathrm{M}}^{a_0} E_{\mathrm{specific}}(t_0, a) \, da, \tag{3.2}$$

gives the total mass integrated energy, at a given time t_0 and mass a_0. The expression (3.2) is negative during the collapse, bounce and the early post bounce phases

---

[1]The baryon contribution to the internal energy is composed of a thermal and nuclear part, i.e. $e = e_{\mathrm{thermal}} + e_{\mathrm{nuclear}}$. In NSE, e is given implicitly via the EoS of hot and dense nuclear matter. In non-NSE, e_{nuclear} is the binding energy of the nuclei used in the reaction network.

because the progenitor and central Fe-core are gravitationally bound. At some time after bounce, expression (3.2) becomes positive in the region between the shock and the neutrinospheres. It stays negative at large distances and close to the deep gravitational potential of the PNS, because the progenitor and the PNS continue to be gravitationally bound. While the emission and scattering of neutrinos cool the PNS interior, neutrino absorption deposits energy on a timescale τ_{heating} of the order 100 ms into the fluid near the neutrinospheres. This increases the specific internal energy which matches at later (~ 500 ms) post bounce times the gravitational binding energy at a certain distance toward the center. This region is defined as the gain region $\{a_{\mathrm{gain}}\}$ where $E_{\mathrm{total}}(t \geq \tau_{\mathrm{heating}}, a) > 0$, $\forall a \in \{a_{\mathrm{gain}}\}$. On a suggestion by S. Bruenn, material outside this region becomes gravitationally unbound and will be ejected where the enclosed material will accrete onto the central PNS. The *mass cut* defines the transition layer between ejected and non-ejected material as follows

$$a_{\mathrm{cut}} = a\left(\max\left(E_{\mathrm{total}}(t_0, a)\right)\right), \qquad \forall a \in \{a_{\mathrm{gain}}\}, \tag{3.3}$$

and the explosion energy estimate is defined as the total mass integrated energy given at the mass cut

$$E_{\mathrm{expl}} = E_{\mathrm{total}}(t_0, a_{\mathrm{cut}}), \tag{3.4}$$

at a given time t_0 post bounce. It becomes clear from the above expressions that the explosion energy estimate is sensitively determined by the balance of internal and kinetic energies to gravitational binding energy.

From the time post bounce when the shock reaches low enough densities and temperatures such that neutrinos decouple form matter completely, neutrino heating and cooling does not affect the explosion energy estimate anymore. The additional energy deposition from the neutrino driven wind, which will be discussed further below, might affect the explosion estimate at later times. We will illustrate in particular the effect of the formation of a supersonic neutrino driven wind and the wind termination shock to the explosion energy estimate. In other words, only when the neutrino driven wind disappears again the final value of the explosion energy can be obtained.

3.1.4 The neutrino observables

The neutrino radiation hydrodynamics equations are a coupled system which combines the evolution of the matter properties given by the state vector y and the radiation field, as documented in Liebendörfer et al. (2004) and references therein. The neutrino radiation field is taken into account via the phase space distribution function $f_\nu(t, a, \mu, E)$ for each neutrino flavor $\nu = (\nu_e, \bar{\nu}_e, \nu_{\mu/\tau}, \bar{\nu}_{\mu/\tau})$. In spherical symmetry, it depends on the time t, the enclosed baryon mass a as well as on the neutrino energy E and the cosine of the propagation angle $\mu = \cos(\theta)$. The evolution of the distribution function is modeled via solving the Boltztran transport equation. It determines the phase space derivative

of the specific distribution function $F_\nu = f_\nu/\rho$, i.e. the distribution function divided by the matter density ρ, in a co-moving frame (see for example Eq.(8) in **?**) and due to neutrino-matter interactions such as emission and absorption as well as scattering and pair reactions.

In order to compare simulation results, neutrino observables can be defined. Commonly used are the neutrino luminosities, which are given by the phase space integration of the distribution function as follows

$$L_\nu(t,a) = 4\pi r^2 \rho \frac{2\pi c}{(hc)^3} \int_{-1}^{+1} d\mu \int_0^\infty E^3 \, dE \; F_\nu(t,a,\mu,E). \tag{3.5}$$

In the general relativistic framework applied to the present investigation, the quantity is understood as the number of neutrinos of energy E passing through the mass coordinate a at time t taken in a co-moving frame at position $r(t,a)$. Additionally useful quantities are the root-mean-squared (rms) neutrino energies as well as the mean neutrino energies, defined as follows

$$\langle E_\nu(t,a) \rangle_{\mathrm{rms}} = \sqrt{\frac{\int_{-1}^{+1} d\mu \int_0^\infty E^4 \, dE \; F_\nu(t,a,\mu,E)}{\int_{-1}^{+1} d\mu \int_0^\infty E^2 \, dE \; F_\nu(t,a,\mu,E)}}, \tag{3.6}$$

$$\langle E_\nu(t,a) \rangle = \frac{\int_{-1}^{+1} d\mu \int_0^\infty E^3 \, dE \; F_\nu(t,a,\mu,E)}{\int_{-1}^{+1} d\mu \int_0^\infty E^2 \, dE \; F_\nu(t,a,\mu,E)}. \tag{3.7}$$

We will use these three observables to illustrate the dynamical evolution of the radiation field as well as for comparisons with previous studies.

3.1.5   Explosions in spherical symmetry

Progenitor stars more massive than 9 $M_\odot$ develop extended Fe-cores at the end of stellar evolution. The explosion mechanism of such Fe-core progenitors is an active subject of research. In the following section, we will investigate the neutrino driven explosions of the 10.8 and 18 $M_\odot$ Fe-core progenitors from Woosley et al. (2002) in spherical symmetry by enhancing the electronic charged current reaction rates artificially. Further below, we will investigate the explosion phase of the 8.8 $M_\odot$ O-Ne-Mg core from Nomoto (1983,1984,1987), where the explosion is obtained without enhancing the neutrino opacities.

Neutrino driven explosions of Fe-core progenitors

The neutrino luminosities and the rms as well as the mean neutrino energies are shown in Fig.3.1 for the 10.8 (middle panel) and the 18 (right panel) $M_\odot$ progenitor model with respect to time after bounce. Note that the more compact PNS of the 18 $M_\odot$ progenitor
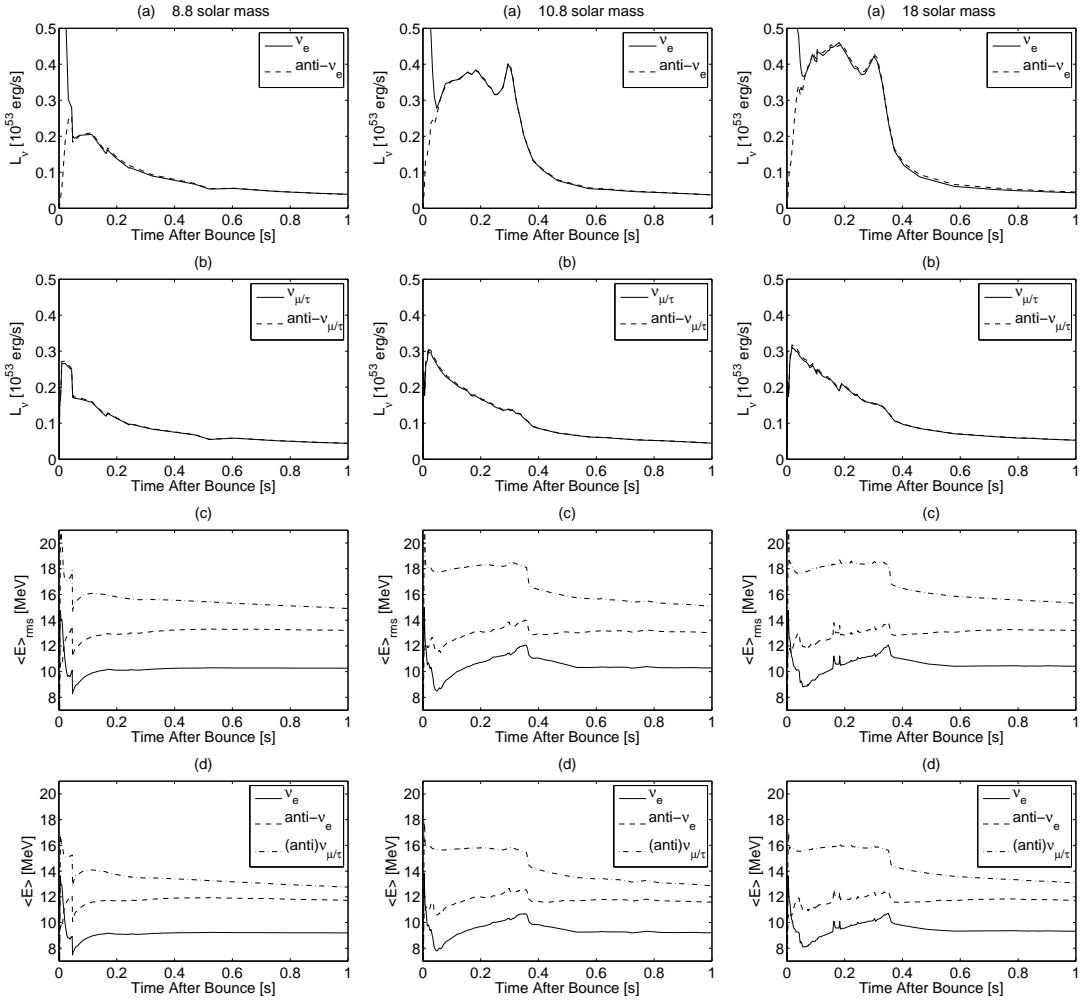
Figure 3.1: Electron-(anti) neutrino luminosities in the graphs (a), μ/τ-(anti)neutrino luminosities in the graphs (b), rms neutrino energies in the graphs (c) and mean neutrino energies in the graphs (d) (ν_e: solid lines, anti-ν_e: dashed lines, $\nu_{\mu/\tau}$: dash-dotted lines), with respect to time after bounce for the 8.8 $M_\odot$ O-Ne-Mg-core progenitor model from Nomoto (1983,1984,1987) (left panel) and the 10.8 $M_\odot$ and 18 $M_\odot$ progenitor model from Woosley et al. (2002) (middle and right panels respectively), measured in a co-moving frame at 500 km distance.

model results in generally larger neutrino luminosities. The oscillating shock position and the consequent contracting and expanding neutrinospheres during the neutrino heating phase of the 10 and 18 $M_\odot$ progenitor models on a timescale of several 100 ms are reflected in the electron-flavor neutrino luminosities, which correspondingly increase or decrease respectively. During the heating phase, the mean neutrino energies of the electron-(anti)neutrinos increase from about 8 (10) MeV after bounce to about 12 (14)
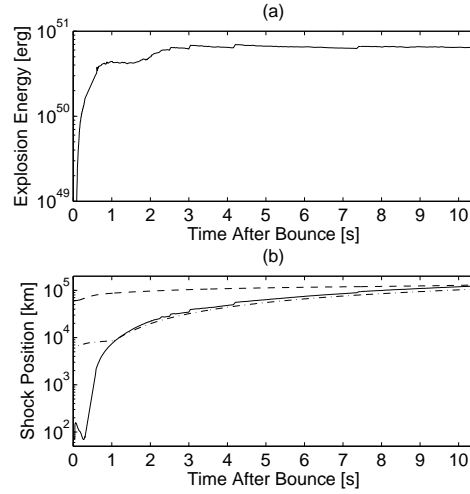
Figure 3.2: Explosion energy estimate and shock position with respect to time after bounce for the 10.8 M$_\odot$ progenitor model from Woosley et al. (2002). In addition, graph (b) illustrates the position of the He-layer (dashed line) and the O-layer (dash-dotted line).

MeV until the explosion is launched. The mean neutrino energy of the μ/τ-neutrinos remains constant at about 18 MeV during the heating phase. The mean neutrino energies are generally smaller than the rms-energies and follow the same behavior. The explosions for both models are launched after about 300 ms post bounce, which defines the neutrino heating timescale for the energy deposition in the gain region to revive the SAS. Matter is accelerated to positive velocities and the SAS turns into the dynamic explosion shock. It continuously propagates through the remaining domain to the progenitor. After the explosions have been launched, the electron flavor neutrino luminosities decay exponentially. Furthermore the jumps in the neutrino energies after 350 ms post bounce for the 10.8 and 18 M$_\odot$ progenitor models are due to the shock propagation over the position of 500 km, because the luminosities and energies are measured in a co-moving reference frame.

In addition, Fig. 3.2 shows the dynamical behavior of the explosion energy estimate in graph (a) and the shock position in graph (b) with respect to time after bounce. These figures illustrate the explosion phase of core collapse supernovae modeled in spherical symmetry. After achieving a convergent value between 600 ms and 2 seconds post bounce of 4.5×10^{50} erg, the explosion energy estimate is lifted slightly to about 6.5×10^{50} erg. This effect co-insides with the additional mass outflow obtained in the neutrino driven and the appearance of the reverse shock, which will be discussed further below. In simulations with a less intense(subsonic) neutrino driven wind, this effect is much weaker and the explosion energy can be obtained already at about 1 second post bounce.
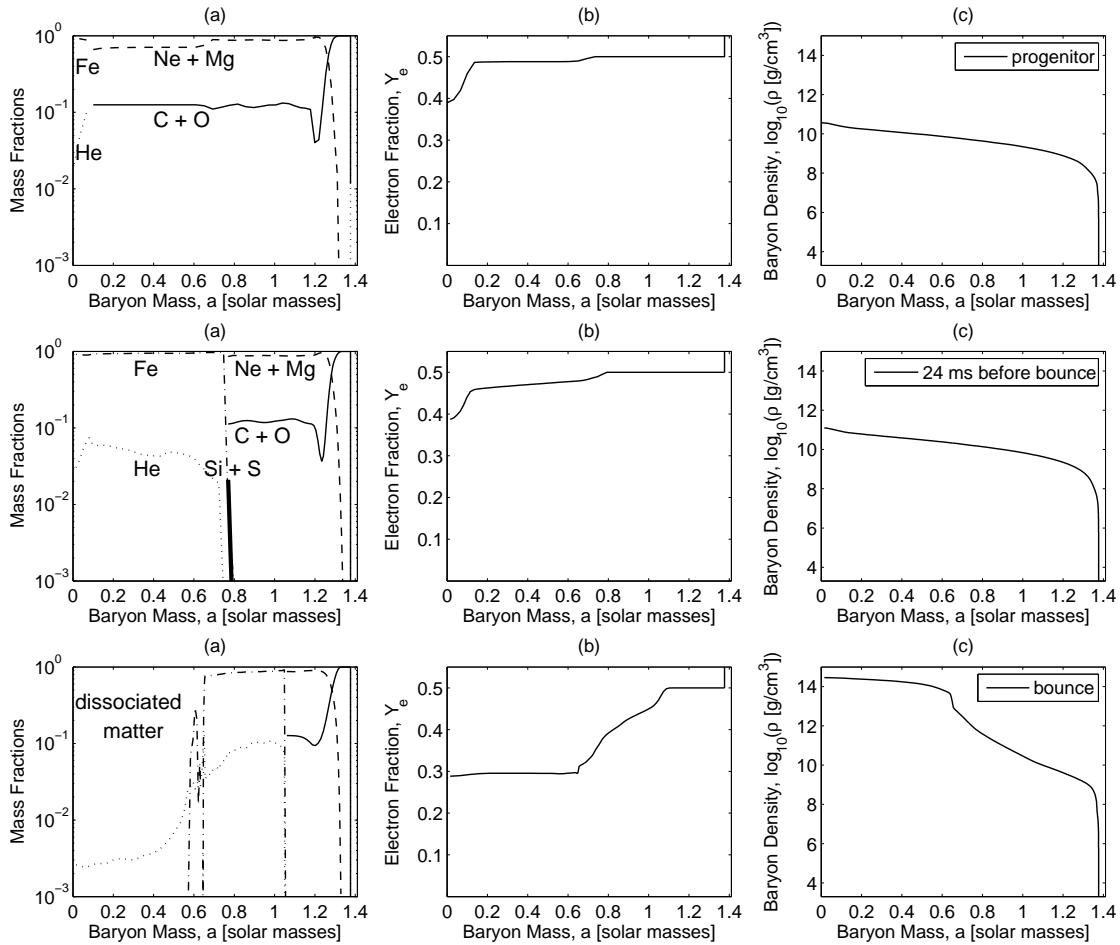
Figure 3.3: Evolution of the 8.8 $M_\odot$ progenitor model from Nomoto (1983,1984,1987) during the collapse phase (top: progenitor configuration, middle: 24 ms before bounce, bottom: at bounce). The composition in the graphs (a) are as follows: thin solid line (C+O), dashed line (Ne+Mg), dash-dotted line (Fe+Ni), dotted line (He) and thick solid line (Si+S).

The O-Ne-Mg-core

A special star is the 8.8 M$_\odot$ progenitor model from Nomoto (1983,1984,1987). The central thermodynamic conditions at the end of stellar evolution are such that only a tiny fraction of about 0.15 M$_\odot$ of Fe-group nuclei are produced, where nuclear statistical equilibrium (NSE) applies (see Fig. 3.3 (a) top panel). Instead, the central composition is dominated by ^{16}O, ^{20}Ne and ^{24}Mg nuclei. Because temperature and density increase during the collapse, these nuclei are burned into Fe-group nuclei and the NSE regime increases (see Fig. 3.3 (a) and (c) middle panel). The core continues to deleptonize, identified at the decreasing Y_e (see Fig. 3.3 (b)). We use our nuclear reaction network as described in §2.2 to calculate the dynamically changing composition, based on the abundances provided by the progenitor model. The size of the bouncing core of $M_{\mathrm{core}} \simeq$ 0.65 M$_\odot$ is significantly larger in comparison with the previous studies by Kitaura et al. (2006) and Liebendörfer (2004), illustrated in Fig. 3.4(a) at different velocity profiles before and at bounce. This is because we do not take the improved electron capture rates from Hix et al. (2003) and Langanke et al. (2003) into account, which are based on the capture of electrons on the distribution of heavy nuclei. It results in a lower central electron fraction at bounce and a consequently more compact bouncing core of about $\simeq$ 0.1 M$_\odot$, in comparison to the standard rates given in Bruenn (1985). The remaining difference is most likely due to the stiff EoS from Shen et al. (1998a) applied to the present study.
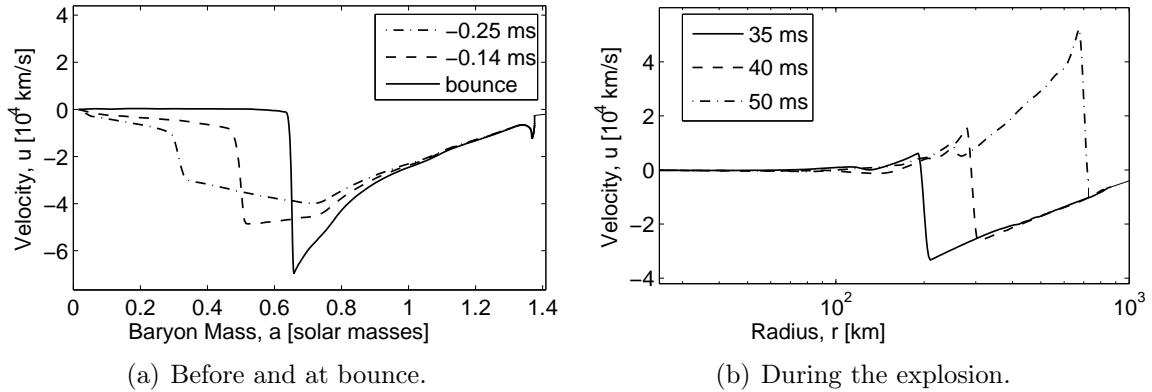

(a) Before and at bounce.   (b) During the explosion.

Figure 3.4: Radial velocity profiles with respect to the baryon mass (a) and with respect to the radius (b) for the 8.8 M$_\odot$ progenitor model from Nomoto (1983,1984,1987)

This progenitor is not only a special case due to the incomplete nuclear burning at the end of stellar evolution but also due to the steep density gradient which separates the dense core from the He- and H-envelope at 1.376 M$_\odot$, see Fig. 3.3 (c). There, the density drops over 13 orders of magnitude which makes it difficult to handle numerically.

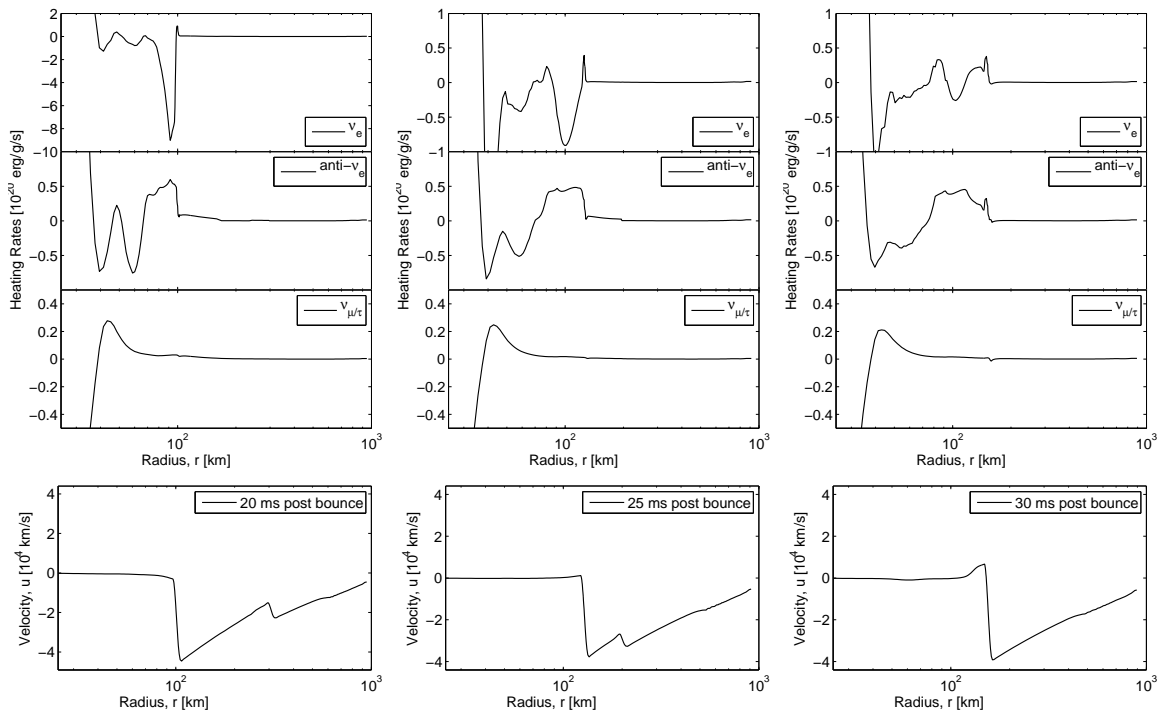The low density of the mass outside the O-Ne-Mg-core makes it possible to obtain

Figure 3.5: Heating (> 0) and cooling (< 0) rates for the 8.8 M$_\odot$ progenitor model from Nomoto (1983,1984,1987) during the explosion phase at 20 ms (left panel), 25 ms (middle panel) and 30 ms (right panel) post bounce. For a better comparison, the velocities are plotted for the same post bounce times.

the explosion in spherical symmetry supported via neutrino heating. Neutrino cooling in the region of dissociated nuclear matter causes the expanding shock front to turn into the SAS with no significant matter outflow. ν_e-cooling dominates over $\bar{\nu}_e$-heating by one order of magnitude. Only at the dissociation line of infalling heavy nuclei, the neutrino energy deposition drives the SAS slowly to larger radii, for illustration see the heating(cooling) rates and velocity profile in Fig. 3.5 (left panel) at 20 ms post bounce. However, the cooling of ν_e still contributes to a large amount at 25 ms post bounce over the heating of $\bar{\nu}_e$ and $\nu_{\mu/\tau}$ in Fig. 3.5 (middle panel) behind the SAS. Only directly at the shock a small net-heating rate remains. Hence the influence of the neutrinos to the explosion itself is of minor importance. More important is the region of C-O-burning which produces Ne and Mg. The hydrodynamic feedback to this thermodynamic transition can be identified already during the collapse phase of the progenitor core at the velocity profiles in Fig. 3.4(a) at about $1.35 - 1.374$ M$_\odot$. As material is shock heated post bounce, the transition layer where Ne and Mg nuclei are burned into NSE propagates together with the expanding shock wave outwards. In other words, NSE burns through the Ne-Mg-layer of the progenitor. Furthermore, the transition (discontinuity) from C-O-burning is falling quickly towards the SAS. It was found to be at about 350 km at 20 ms post bounce and at about 200 km at 25 ms post bounce, illustrated at the velocity profiles (bottom) in Fig. 3.5 (left-right panels). At about 30 ms post bounce, the entire Ne-Mg-layer is converted into NSE due to the temperature increase obtained via shock heating. Hence, C and O nuclei are burned directly into NSE.

In contrast to more massive Fe-core progenitors where O-burning produced an extended Si-S-layer, the amount of ^{28}Si and ^{32}S is less then 1% at the end of nuclear burning for the O-Ne-Mg-core discussed here (see Fig. 3.3 (a) middle panel). This small fraction of Si and S is already converted into NSE during the initial collapse phase, due to the rapid density and temperature increase of the contracting core. Hence, C- and O-nuclei are burned directly into NSE during the post bounce evolution. This sharp transition is related to a jump in the density and the thermodynamic variables. As the SAS propagates over this transition along the decreasing density, the shock accelerates to positive velocities (see Fig. 3.5 right panel). The consequent explosion is hence driven due to the shock propagation over the infalling transition between two different thermonuclear regimes rather then by pure neutrino heating, illustrated at the velocity profiles in Fig. 3.4(b). Although Kitaura et al. (2006) approximated nuclear reactions during the evolution of the O-Ne-Mg-core progenitor, the results of their explosion dynamics are in qualitative agreement with our findings.

The more massive Fe-core progenitors show the same thermo- and hydrodynamic features as discussed above for the O-Ne-Mg-core due to the transition between different thermonuclear regimes. However, the differences are smaller because C-O-burning produces an extended layer composed of ^{28}Si and ^{32}S. The transition of Si-burning into NSE is much smoother than the transition of C-O-burning into NSE. Furthermore, due

to the more massive Si-S and C-O-layers for the Fe-core progenitors, the transitions take more time of the order 100 ms to fall onto the SAS. The presence of neutrino heating becomes important for the more massive Fe-core progenitors to drive the SAS to large radii on a longer timescale. The effects of the shock propagation across the transition between different thermonuclear regimes has been pointed out in Bruenn et al. (2006) with respect to the explosion dynamics in axially-symmetric simulations of massive Fe-core progenitors. In our spherically symmetric model we can not confirm the driving force of explosions of Fe-core progenitors to be the shock propagation across different thermonuclear regimes. It is rather the neutrino energy deposition, although enhanced, which initiates the explosion. The shock is accelerated additionally when crossing different thermonuclear regimes due to the density jumps at the transitions.

Comparison of the neutrino spectra

Striking is the agreement in the mean neutrino energies between all different progenitor models (including the O-Ne-Mg-core and the Fe-core progenitors) during the explosion phase, although the neutrino emissivities and opacities are enhanced for the Fe-core progenitor models (see Fig. 3.1). The explosion phase for the O-Ne-Mg-core lasts only until about 40 ms post bounce and is significantly shorter in comparison to the more massive Fe-core progenitors. Furthermore, the luminosities are also smaller by a factor of 2. For all models, the electron antineutrino luminosity is larger than the electron neutrino luminosity on a timescale of 200 ms after the explosion has been launched. This slight difference reduces again at later times where the electron neutrino luminosity becomes again larger than the electron antineutrino luminosity. However, after the explosion has been launched the behavior of the luminosities are in qualitative agreement for all models. The same holds for the mean neutrino energies which increase continuously during the neutrino heating phase. The electron (anti)neutrinos have rms energies of about 12 (14) MeV where after the explosion has been launched rms energies of about 11 (13) MeV are obtained. The values remain constant on the timescale of 1 second post bounce. The μ/τ-neutrino have rms energies of about 18 MeV during the neutrino heating phase and about 15 MeV after the explosion has been launched. These differences in the mean neutrino energies and luminosities during the neutrino heating, initial and proceeding explosion phases are in correspondence with the electron fraction of the material, as will be illustrated in the following section.

The electron fraction of the early ejecta

During the neutrino heating phase, the neutrino spectra are mainly determined by mass accretion at the neutrinospheres. Neutron rich nuclei from the progenitor star with an electron fraction of $Y_e \simeq 0.45$ are falling onto the oscillating SAS and dissociate into free nucleons and light nuclei, see Fig. 3.6 (d). These nucleons accrete than slowly onto

the PNS surface at the center. Due to the increased electron-degeneracy behind the
SAS in Fig. 3.6 (c), weak-equilibrium is established at a lower value of the electron
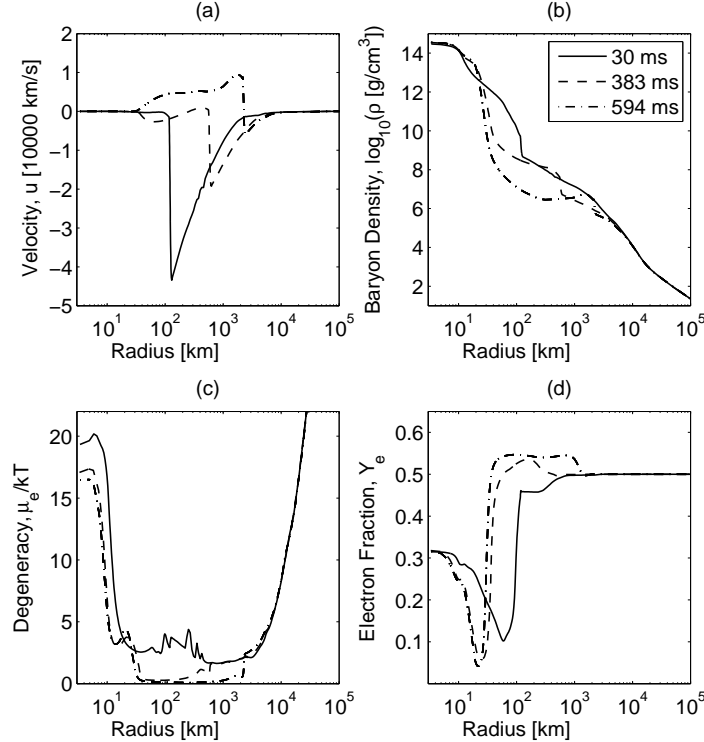fraction of $Y_e \leq 0.15$.

Figure 3.6: Selected hydrodynamic variables during the explosion phase at three differ-
ent times after bounce for the 10.8 $M_\odot$ progenitor model from Woosley et al. (2002).

As soon as the SAS is revived and propagates outward, see the velocity and density
profiles in Fig. 3.6 (a) and (b), the electron degeneracy behind the expanding shock is
reduced and weak-equilibrium is established at a larger value of the electron fraction
of $Y_e > 0.56$ [2]. The capture rates for electron-neutrinos at neutrons are favored over
electron-antineutrino captures at protons. This slight difference results in an electron
and hence proton excess. Consequently the explosion ejecta are found to be initially
proton-rich. This behavior of the electron fraction was found for all our explosion
models, for the 10.8 and 18 $M_\odot$ Fe-core progenitors with artificially enhanced opacities
and for the O-Ne-Mg-core using the standard opacities. Such explosion models were

---

[2]The EoS from Shen et al. (1998a) is limited to a maximum electron fraction of $Y_e \geq 0.564$. The EoS
has been extended by Gögelein (2007) to model asymmetric nuclear matter with an electron fraction
above 0.564. We assume an ideal gas of free nucleons and light nuclei, which is a sufficient assumption
for the conditions found in the region of the extremely proton-rich ejecta.

investigated with respect to the nucleosynthesis in general and with respect to the νp-process by Fröhlich et al. (2006a-c).

One of the main goals of the present investigation is to determine the behavior of the electron fraction for the initially proton-rich ejecta on a long timescale of the order 10 seconds, in a consistent manner. We explore the question if the material ejected in the neutrino driven wind becomes neutron-rich and which are the conditions (e.g. entropy per baryon, and expansion timescale) obtained in the neutrino driven wind. These aspects are of special relevance for the composition of the ejecta, which is determined via explosive nucleosynthesis analysis, in particular in order to be able to draw conclusions with respect to a possible site for the production of heavy elements via the r-process. Therefore, the continues expansion of the explosion ejecta must be simulated, for which the inclusion of a large physical domain of the progenitor up to the He-layer is required. Furthermore, since only the electronic charged current reactions including the neutrino fluxes can determine the electron fraction, the PNS contraction at the center and hence the contraction of the neutrinospheres are essential.

3.1.6   Simulation results of the neutrino driven wind

In this section we will investigate the post explosion evolution with special focus on the properties of the ejecta, in particular the electron fraction. We will explore the problem if the initially proton-rich ejecta become neutron rich at later times of the order 10 seconds and if the conditions might indicate a possible site for the nucleosynthesis of heavy nuclei via the r-process. This has been assumed in static steady-state as well as parametrized dynamic wind models, based on the results obtained by Woosley et al. (1994). The ejected material in their simulations does never become proton-rich, the electron fraction was found to continuously decrease with time after the explosion has been launched. The ejecta were investigated with respect to the nucleosynthesis of heavy elements where conditions could be obtained favorable for the r-process. The stellar models applied to the present investigation of the neutrino driven wind are the 8.8 $M_\odot$ O-Ne-Mg-core and the 10.8 and 18 $M_\odot$ Fe-core progenitors, where for the latter case the explosion is obtained using the artificially enhanced opacities as introduced in S 3.1.3.

After the explosion has been launched, the region between the expanding explosion shock and the neutrinospheres cools rapidly and the density decreases continuously as illustrated in Figs. 3.9 and 3.10 (d) and (h). For most previous studies, the neutrino reaction rates were assumed to freeze out at a distance of typically 10 km outside the neutrinospheres. In terms of distance, we find this till too close to the neutrinospheres to assume frozen neutrino reaction rates. The region where the neutrino reaction rates freeze out depend on the thermodynamic conditions. Since these change continuously during the dynamical evolution (e.g. density and temperature decrease during the expansion), we find such a static approximation to be rather simplified. In addition, the
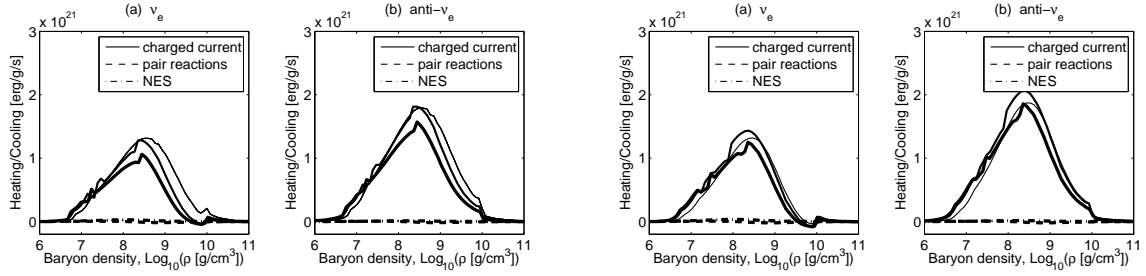
(a) The 10.8 M$_\odot$ progenitor model from Woosley et al. (2002).

(b) The 18 M$_\odot$ progenitor model from Woosley et al. (2002).

Figure 3.7: Net-heating rates of the electron-flavor neutrinos. Including the charged current reactions and neutrino-nucleon scattering (solid lines), the emission of neutrino pairs (dashed lines) and neutrino-electron scattering (NSE, dash-dotted lines) as a function of the baryon density at three different times post bounce (thin: 1 second, intermediate: 2 seconds, thick: 3 seconds) during the formation of the neutrino driven wind.

thermodynamic conditions in the region where the neutrino driven wind develops correspond not to the trapped and not yet to the free-streaming regime for the neutrinos that diffuse out of the hot PNS on a timescale of the order of seconds. Hence, the neutrino fluxes are important in addition to the neutrino reaction rates in order to determine the evolution of the electron fraction Y_e. Since the PNS and hence the neutrinospheres contract continuously due to the deleptonization, the degeneracy increases and matter at the PNS surface is found to be neutron rich where $Y_e \leq 0.1$. This is shown via the contracting neutrinospheres in Fig. 3.8 (a) and the electron fraction at the corresponding neutrinospheres in Fig. 3.8 (b) (thin lines) with respect to time after bounce.

Independent of the progenitor model, the region on top of the PNS surface is continuously subject to neutrino heating during the post explosion phase as shown in Figs. 3.7(a) and 3.7(b) for the 10.8 and the 18 M$_\odot$ progenitor models respectively. The dominant heating sources are the absorption of electron-(anti)neutrinos on free nucleons, due to the large fraction of free nucleons (dissociated nuclear matter) in the region on top of the PNS. In order to be able to compare the heating, we plot the rates with respect to the baryon density in Figs. 3.7(a) and 3.7(b). The neutrino pair production and thermalization processes, such as neutrino electron scattering, have a negligible contribution to the net-heating outside the neutrinospheres. Figs. 3.9 (d) and 3.10 (d) show the contracting PNSs at the center via the radial baryon density profiles and the electron-neutrinospheres. The region of interest corresponds to the density domain of $10^7 - 10^{10}$ g/cm^3. The degeneracy of the early ejecta favors proton-rich matter where a large electron fraction of $Y_e \simeq 0.54$ is obtained. Hence, the absorption of electron-antineutrinos on free protons dominates over electron-neutrino absorption on
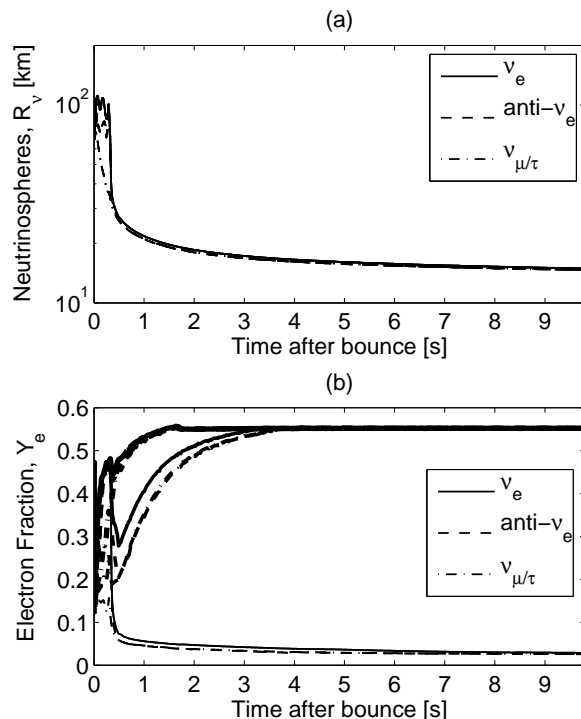
Figure 3.8: Neutrinospheres and electron fraction with respect to time after bounce for the 10.8 $M_\odot$ progenitor model from Woosley et al. (2002). Graph (b) shows the electron fraction from Boltzmann neutrino transport at the neutrinospheres (thin lines), at radii of 5 km (intermediate lines) and 10 km (thick lines) outside the neutrinospheres.

free neutrons. The corresponding radial neutrino luminosities and root -mean-squared (rms) energies are shown in Figs. 3.9 and 3.10 (e) and (g). In addition, for the first time we were able to follow the deleptonization burst from core bounce for several seconds over a large physical domain including several 10^5 km of the progenitor star. It can be identify in the luminosities in the Figs. 3.9 (e) and 3.10(e) at 0.6 seconds after bounce at a distance between 5×10^4 and 10^5 km, leaving the computational domain between $1 - 2$ seconds post bounce.

After the explosion has been launched, the continued energy transfer from the neutrino radiation field into the fluid outside the neutrinospheres drives the matter entropies to large values. The heat deposition at the PNS surface accelerates matter to positive velocities, see Figs. 3.9 (s) and 3.10 (a) after $\simeq 1$ second post bounce. This matter outflow is known as the neutrino driven wind, which proceeds adiabatically at larger radii. This is consistent with the constant radial entropy per baryon profiles in the graphs (c). Furthermore, the rapidly decreasing luminosities reach values below 5×10^{51} erg/s already 1 second after bounce. The luminosities continue to decrease and reach values below 1×10^{51} erg/s at 10 seconds after bounce, see Fig. 3.15 (a) and (b). The same

holds for the mean neutrino energies where values below 10 MeV for the electron-flavor neutrinos and below 12 MeV for the (μ/τ)-neutrinos are obtained.

Several previous wind studies achieved supersonic matter outflow velocities for the neutrino driven wind due to the assumed large luminosities. In any case, the accelerated material of the neutrino driven wind collides with the slower and subsonically expanding explosion ejecta. In the case of a supersonic neutrino driven wind, this leads to the formation of a reverse shock known as the wind termination shock. The formation of the wind termination shock of the 10.8 $M_\odot$ progenitor model is illustrated in Fig. 3.11 and will be discussed in the following paragraph. In order to analyze the dynamical evolution and the consequences of the formation of the reverse shock, steady-state wind models can not be used. Radiation hydrodynamics is required in order to describe the dynamical effects obtained consistently. Our results, obtained using general relativistic radiation hydrodynamics based on spectral three flavor Boltzmann neutrino transport, are in qualitative agreement with the detailed parametrized investigation by Arcones et al. (2007).

During the initial and subsonic wind expansion, the matter entropies in Fig. 3.11 (c) increase slowly from 4 to $5 - 10$ k_B/baryon and the densities in Fig. 3.11 (b) and temperatures in Fig. 3.11 (e) decrease on a long timescale over several seconds. Furthermore, the reduced degeneracy in the wind increases the electron fraction shown in Fig. 3.11 (d) slowly on the same timescale. When the material is accelerated supersonically with velocities of several 10^4 km/s up to radii of a several 10^3 km (see Figs. 3.11 (a) and (f)), the entropies increase from s $\simeq 5 - 10$ k_B/baryon to s $\simeq 40 - 60$ k_B/baryon on a short timescale of the order of 100 ms. During this rapid expansion, the density and temperature decrease drastically from 10^{10} g/cm^3 to $10^4 - 10^2$ g/cm^3 and from 3 MeV to $0.1 - 0.01$ MeV respectively (see Figs. 3.11 (b) and (e)). It also corresponds to a rapid decrease of the degeneracy which in turn is reflected in a rapid increase of the electron fraction of the accelerated material on top of the PNS surface, from $Y_e \simeq 0.1$ to $Y_e \simeq 0.56$ (see Fig. 3.11 (d)). Furthermore, the supersonically expanding neutrino driven wind collides with the explosion ejecta as can bee seen in Fig. 3.11 (a) (solid red line) at radii of several 10^4 km. Consequently, the previously accelerated material decelerates behind the explosion ejecta as can be seen in the velocities in Fig. 3.11 (f). This phenomenon becomes significant after about 2 seconds post bounce and corresponds to the formation of the reverse shock, i.e. the wind termination shock. (see Fig. 3.11 (a) dashed red line at radii of several 10^3 km). It causes an additional entropy increase to the final values of s $\simeq 50 - 100$ k_B/baryon. During the rapid deceleration on the same short timescale of the order 100 ms, the densities in Fig. 3.11 (b) and temperatures in Fig. 3.11 (e) increase again slightly, where the degeneracy increases and hence the electron fraction reduces slightly to values of $Y_e \simeq 0.54$. The following dynamical evolution is given by the subsonic and adiabatic expansion of the explosion ejecta on a longer timescale of the order of seconds. The density and temperature decrease slowly where the entropies of s $\simeq 50 - 100$ k_B/baryon and the electron fraction of about $Y_e = 0.54$
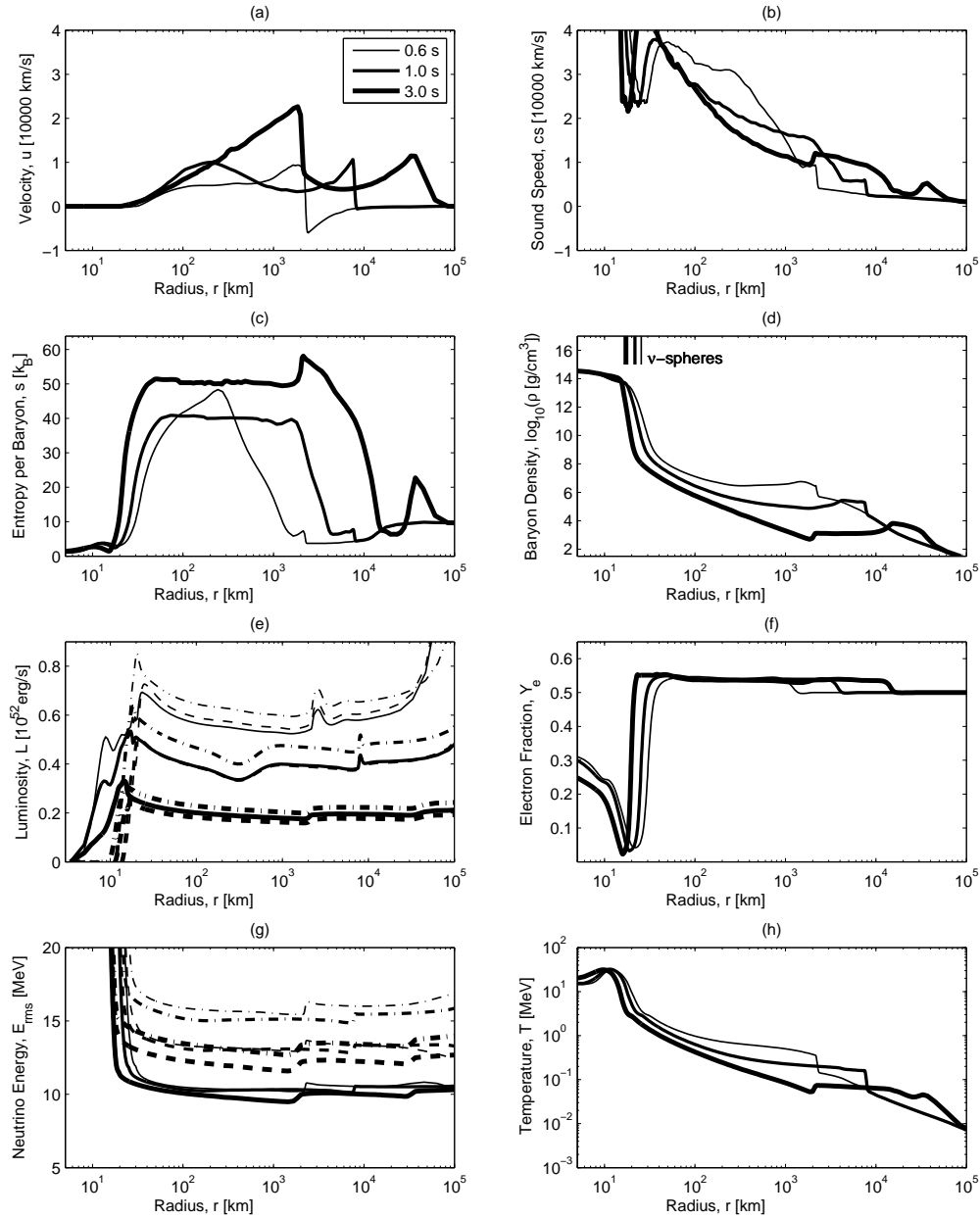
Figure 3.9: Selected hydrodynamic variables during the formation of the neutrino driven wind at three different times after bounce for the 10.8 $M_\odot$ progenitor model from Woosley et al. (2002). In addition, graphs (e) and (g) show the neutrino luminosities and rms neutrino energies (solid lines: ν_e, dashed lines: $\bar{\nu}_e$, dash-dotted lines: $\nu_{\mu/\tau}$). For this progenitor model the neutrino driven wind becomes supersonic, using the enhanced opacities.
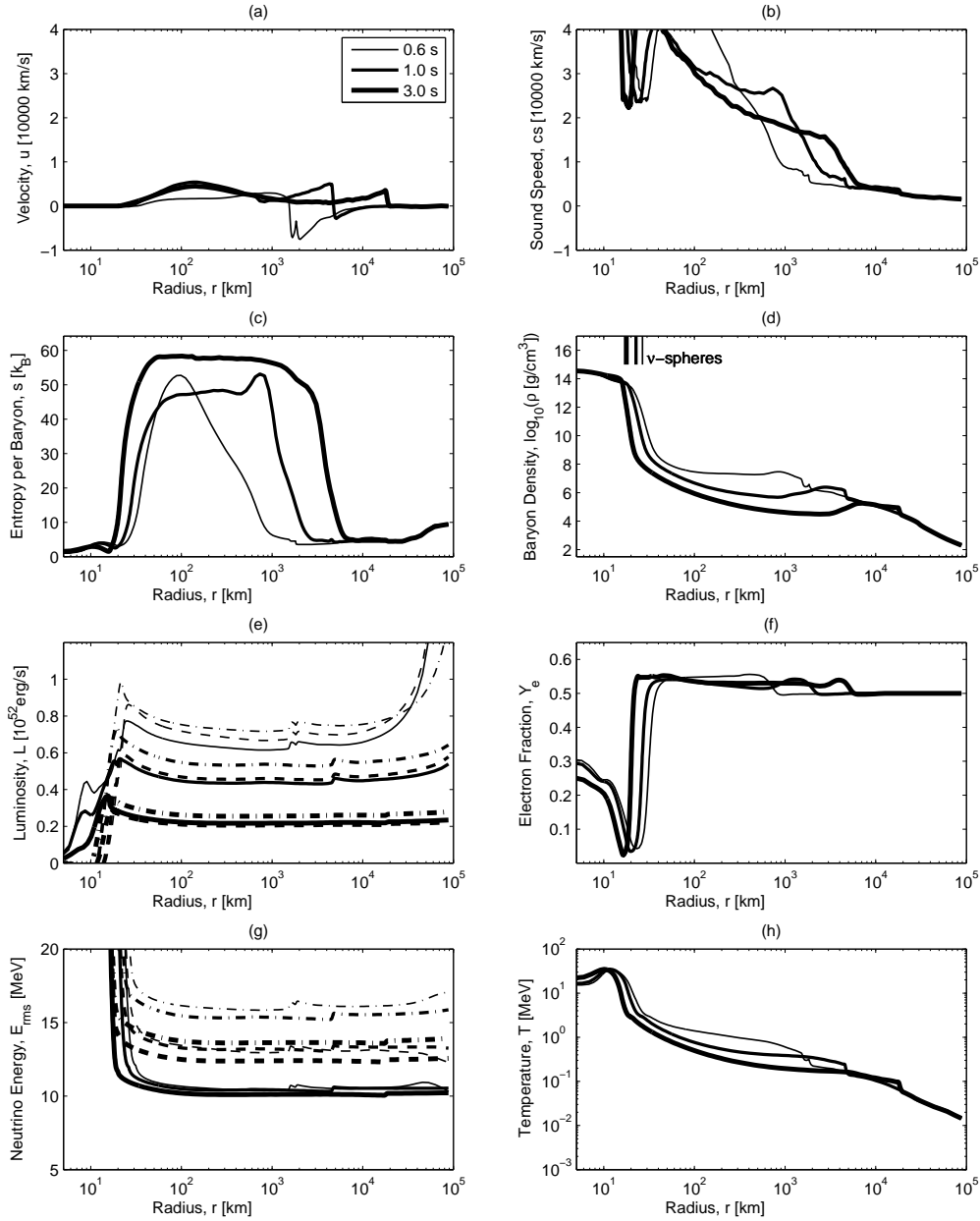
Figure 3.10: The same configuration as Fig. 3.9 for the 18 M$_\odot$ progenitor model from Woosley et al. (2002). The neutrino driven wind remains subsonic for this progenitor model.
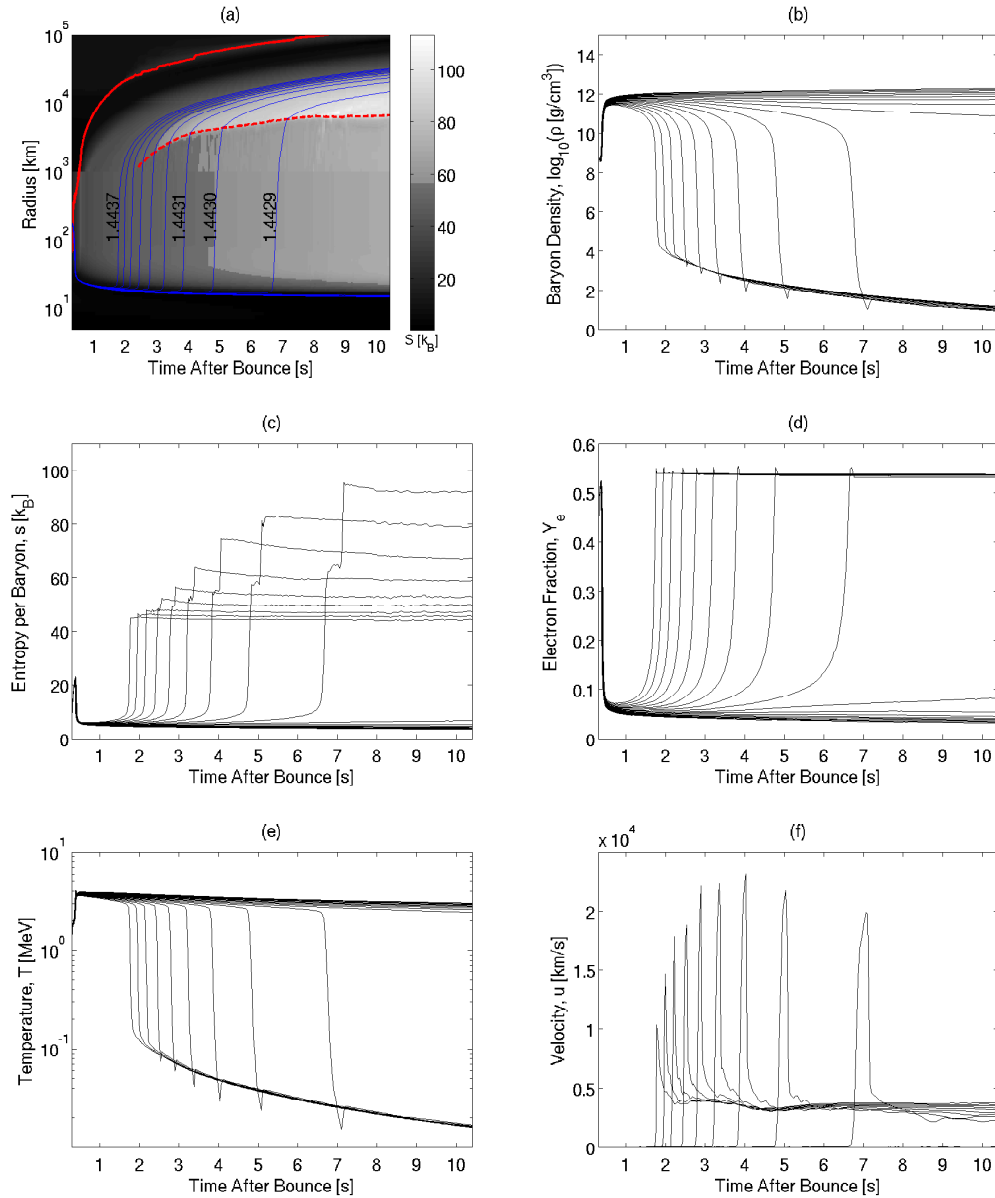
Figure 3.11: Hydrodynamic and thermodynamic properties of selected mass shells in the neutrino driven wind as a function of time after bounce for the 10.8 $M_\odot$ progenitor model from Woosley et al. (2002) where the enhanced opacities are used. Graph (a) shows in addition gray-scaled the entropy per baryon, the position of the expanding explosion shock (thick solid line) and the position of the wind termination shock (thick dashed line).
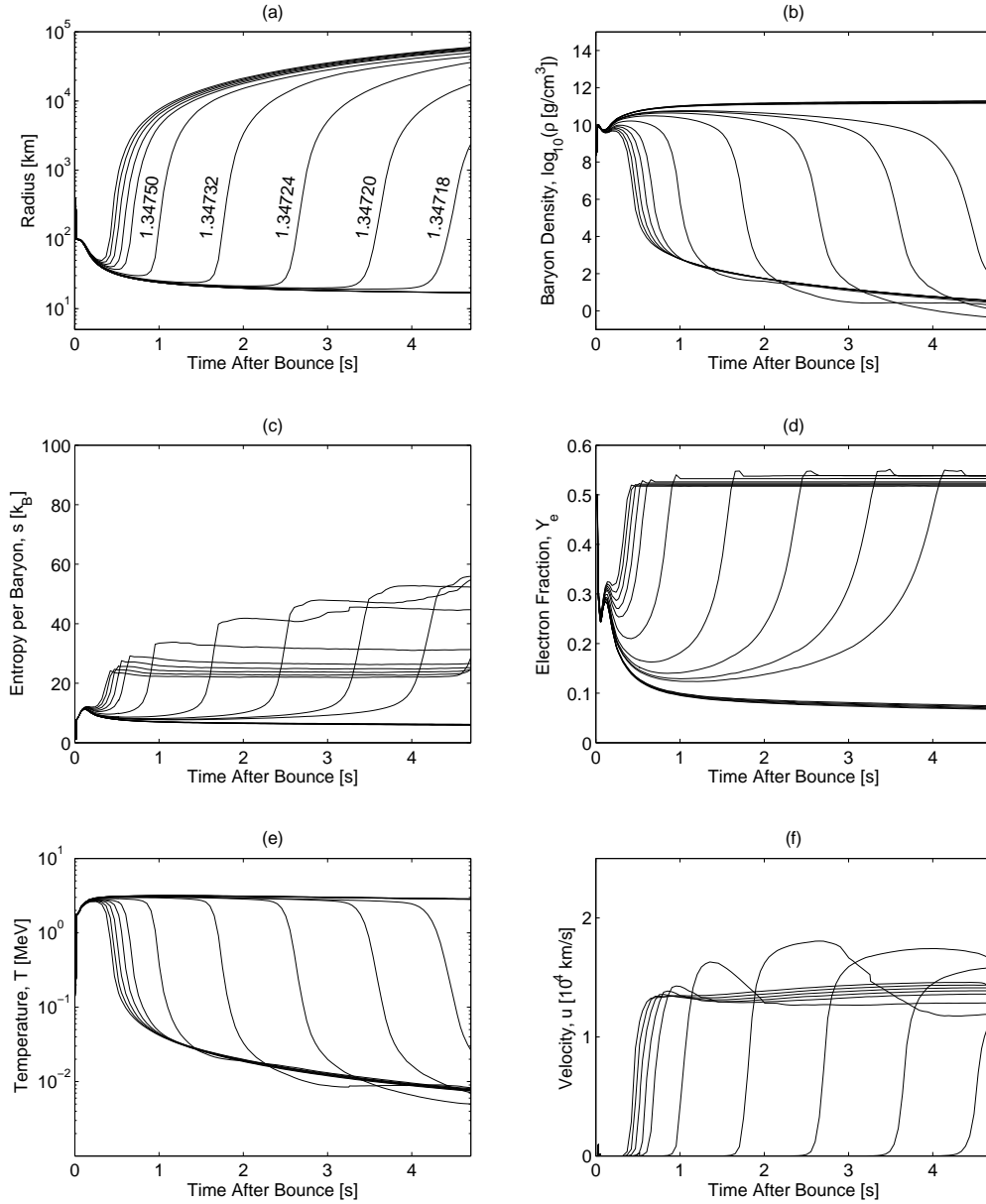
Figure 3.12: Selected mass shells in the neutrino driven wind from 1.3600 to 1.3639 $M_\odot$ for the 8.8 $M_\odot$ progenitor model from Nomoto (1983,1984,1987) where we use the standard emissivities and opacities given in Bruenn (1985). The graphs show the same configurations as Fig. 3.11 for the 10.8 $M_\odot$ progenitor model.
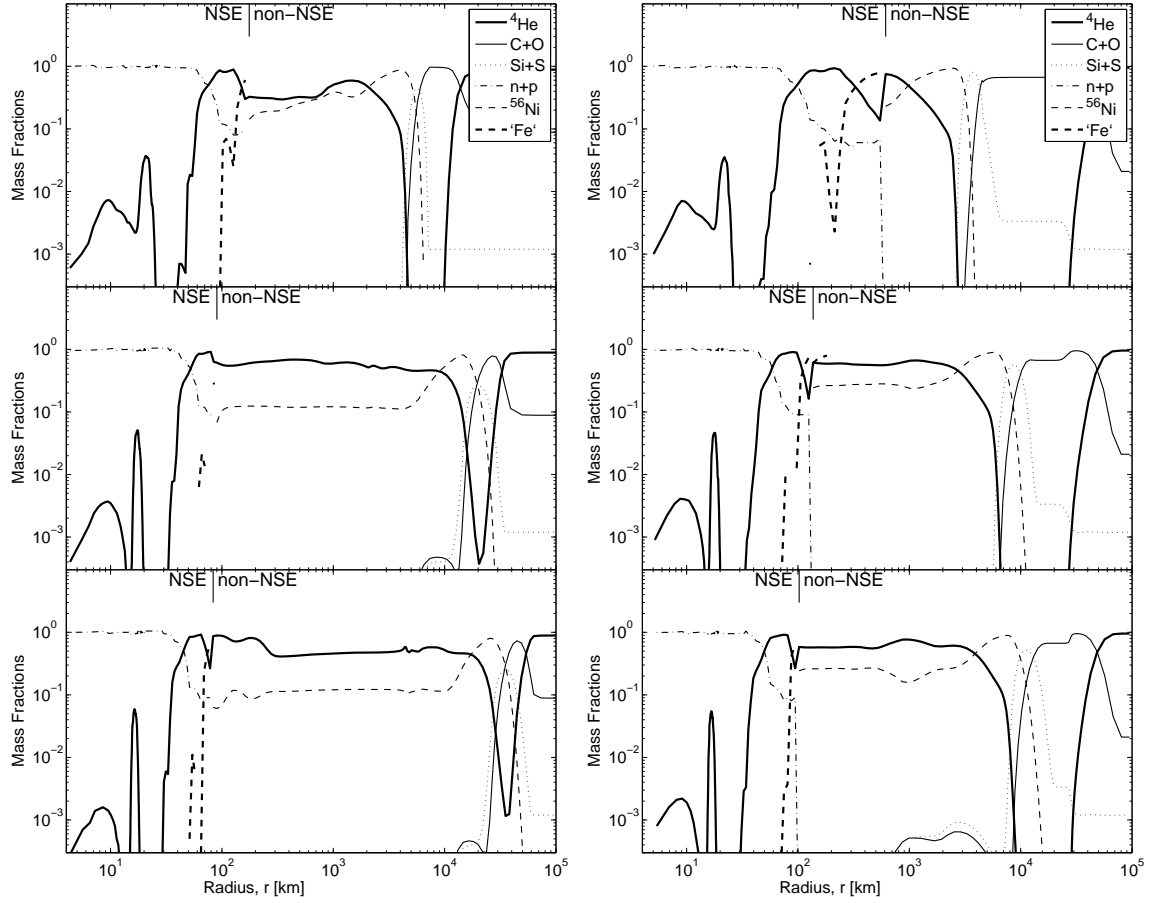
Figure 3.13: Selected radial mass fraction profiles during the neutrino driven wind phase for the 10.8 M$_\odot$ (left panel) and the 18 M$_\odot$ (right panel) progenitor model from Woosley et al. (2002) at 1 second (top), 3 seconds (middle) and 5 seconds (bottom) post bounce. The vertical lines represent the separation of NSE (EoS for hot and dense nuclear matter) where heavy nuclei are represented by a single Fe-group nucleus $'Fe'$ with average atomic mass and charge and non-NSE (nuclear reaction network) where the most abundant Fe-group element is ^{56}Ni, at temperatures of $\simeq 0.5$ MeV.

remain constant. The latter aspects are essential for the nucleosynthesis analysis of the ejecta. It can be understood in the sense that the neutrino reaction rates freeze out and the matter conditions correspond to the neutrino free streaming regime.

Note that the strong neutrino driven wind for the 10.8 $M_\odot$ progenitor model is obtained using the enhanced opacities as introduced in §2.3. We additionally illustrate selected properties of the neutrino driven wind for the 8.8 $M_\odot$ progenitor model in Fig. 3.12 where a strong neutrino driven wind was obtained using the standard emissivities and opacities given in Bruenn (1985). This is due to the low density of the region between the neutrinospheres at the PNS surface and the expanding explosion shock, where neutrino heating via the standard rates is sufficient to drive a strong supersonic matter outflow. Matter entropies increase to s $\simeq 10$ k_B/baryon during the initial acceleration of the wind and the densities and temperatures decrease slowly on a timescale of seconds. The properties during the initial acceleration observed are similar to those of the more massive 10.8 $M_\odot$ Fe-core progenitor. The same holds for the acceleration to supersonic velocities. The timescale is reduced to 100 ms where the entropies increase rapidly to s $\simeq 20 - 50$ k_B/baryon (see Fig. 3.12 (c)) and due to the reduced degeneracy the electron fraction increases from $Y_e = 0.1$ at the PNS surface to $Y_e = 0.56$ (see Fig. 3.12 (d)). Density and temperature decrease to $10 - 100$ g/cm^3 and 0.001 MeV respectively (see Fig. 3.12 (b) and (e)). The difference to the more massive 10.8 $M_\odot$ Fe-core progenitor is due to the less mass enclosed between the PNS surface and the expanding explosion ejecta. For the more massive 10.8 $M_\odot$ Fe-core progenitor in Fig. 3.11 (f), the previously accelerated material collides with the explosion ejecta already after a few 100 ms during the acceleration. Here the supersonic wind expands on a much longer timescale up to several seconds before it collides with the explosion ejecta (see Fig. 3.12 (f)). During this adiabatic expansion, entropy and electron fraction remain constant. The previously accelerated material collides with the much slower expanding explosion ejecta where the material is decelerated and hence the reverse shock appears. This is again similar to the formation of the reverse shock for the more massive 10.8 $M_\odot$ Fe-core progenitor as discussed above. Matter entropies increase to several 100 kB/baryon (see Fig.3.12 (c)), density and temperature increase sightly (see Fig.3.12 (b) and (e)) and the electron fraction reduces slightly to $Y_e \simeq 0.52 - 0.54$ due to the increased degeneracy (see Fig.3.12 (d)). The following evolution is determined by the adiabatic expansion of the explosion ejecta during which the entropy and electron fraction remain constant.

Comparing Figs. 3.9 and 3.10, the more compact wind region of the 18 $M_\odot$ progenitor model produces a less pronounced neutrino driven wind in comparison to the 10.8 $M_\odot$ progenitor model. The densities of the wind region are larger up to two orders of magnitude and the temperatures are higher by a factor of 2. The resulting velocities of the neutrino driven wind outflow are smaller by a factor of 2 and stay below 10^4 km/s. Hence, the neutrino driven wind remains subsonic for all times for the 18 $M_\odot$ progenitor model (see Fig. 3.10 (a)) where the wind develops supersonic velocities for the 10.8 $M_\odot$ progenitor model (see Fig. 3.9 (a)).

In the following paragraph, we will discuss the composition of the neutrino driven wind region to some extend. This is possible due to the recently implemented nuclear reaction network. It includes the free nucleons and the symmetric nuclei from ^{4}He to ^{56}Ni plus ^{53}Fe, ^{54}Fe and ^{56}Fe. The initial composition is given by the progenitor model. Mostly ^{28}Si and ^{30}S are shock-heated and burned to Fe-group nuclei due to the temperature and density jump during the initial expansion of the explosion shock (see Fig. 3.13 and compare with Figs. 3.9 and 3.10 (d) and (f)). The large fraction of these Fe-group nuclei reduces behind the explosion shock due to photodisintegration, indicated by the region of low density and high entropy in Figs. 3.9 and 3.10 (b) and (c). This produces a large fraction of α-particles, which in our model represent light nuclei. The region of α-particle domination behind the expanding explosion shock increases with time. This behaviour is illustrated in Fig. 3.13 for both Fe-core progenitor models under investigation. The position of the explosion shock is indicated by the maximum of the mass fraction of Fe-group nuclei (in particular ^{56}Ni). In addition, density and temperature of the neutrino driven wind on top of the PNS surface decrease continuously with time. The low temperatures and densities in that region do not justify the assumption of NSE already at about 1 second after bounce, where temperatures reach values below 0.5 MeV. Instead, our nuclear reaction network is used to determine the composition in that region. There, the decreasing density and temperature and the presence of a large fraction of free nucleons favor the freeze out of light nuclei. Finally, the entire region between the expanding explosion shock and the PNS surface is found to be dominated in our simulations by α-particles. In Fig. 3.13, the radii of the NSE to non-NSE transitions are indicated by vertical lines. The slight mismatch between the abundances between the heavy 'Fe'-group nuclei (the representative heavy nucleus with average atomic mass and charge in NSE) and ^{56}Ni (non-NSE) as well as between the α's is due to the different nuclear models used for the two regimes. Where in NSE the EoS for hot and dense nuclear matter assumes ^{56}Fe as the most stable nucleus due to the smallest mass per nucleon for low temperatures and densities, the nuclear reaction network applied in non-NSE calculates the composition dynamically based on tabulated reaction rates.

3.1.7   Comparison with previous wind studies

The proton-to-baryon ratio of the wind

The approximations made in previous wind studies is a simplified description of the radiation-hydrodynamics equations, see for example Duncan et al. (1986) and Qian and Woosley (1996). More crucial is the absence of neutrino transport. Neutrino heating and cooling is calculated only based on assumed neutrino luminosities and mean energies. Hence, such models explore the neutrino driven wind by varying the neutrino luminosities and energies, where the simplified radiation-hydrodynamics equations are

solved (see for example Thompson et al. (2001)). Since neutrino transport is neglected, the evolution equation for the electron fraction Eq. (2.27) cannot be solved because the neutrino distribution functions are unknown. Hence, Eq. (2.30) is used in previous static steady-state and parametrized dynamic studies of the neutrino driven wind.
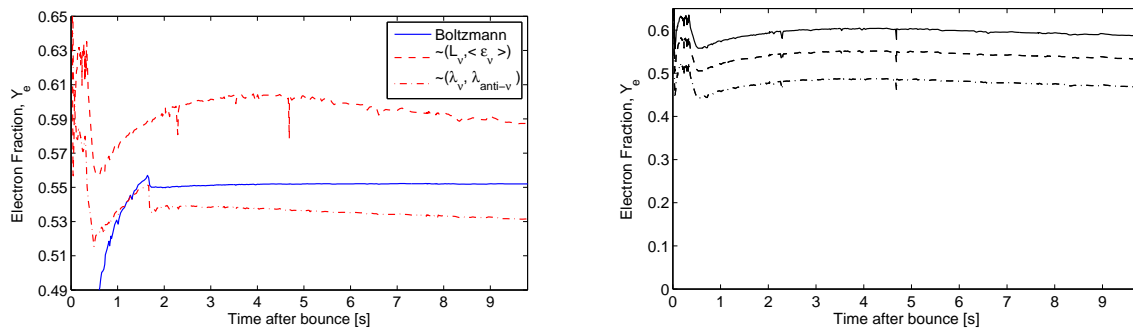
(a) Different electron fraction approximations.

(b) Based on the luminosities and mean neutrino energies Eq. (2.30) for different mean neutrino energy differences.

Figure 3.14: The Electron fraction approximations at a distance of 10 km outside the electron-neutrinosphere for the 10.8 $M_\odot$ progenitor model from Woosley et al. (2002).

Fig. 3.14(a) compares the electron fraction behavior at a distance of 10 km outside the electron-neutrinosphere, from Boltzmann neutrino transport (blue solid line) with the approximations based on the neutrino capture rates (red dashed line) and based on the luminosities and mean neutrino energies (red dash-dotted lines). The approximations are in qualitative agreement with Boltzmann transport. The differences on the longer timescale are most likely due to the presence of light and heavy nuclei which are not taken into account explicitly in the approximations. They change the number of free nucleons available for the reactions. All descriptions agree qualitatively in the prediction of a generally proton-rich material in the wind, based on the neutrino spectra obtained via Boltzmann transport.

The neutrino observables in the wind

Comparing the neutrino spectra in Fig. 3.15 with the spectra assumed in previous static steady-state and dynamic wind studies (see for example Thompson et al. (2001) and Arcones et al. (2007)), we find two major differences: *One*, the neutrino luminosities and mean neutrino energies assumed are significantly larger than those we find and *two*, the assumed behaviour with respect to time is different.

The commonly used assumptions made in static steady-state and parametrised dynamic wind studies go back to the detailed investigation from Woosley et al. (1994), who performed core collapse simulations based on sophisticated input physics. They

investigated the neutrino driven explosion of a 20 $M_\odot$ progenitor star and followed the evolution for 18 seconds post bounce into the neutrino driven wind phase. In their simulations the electron (anti)neutrino luminosities decreased from initially 4×10^{52} (3×10^{52}) erg/s at the onset of the explosion to 6×10^{51} (7.5×10^{50}) erg/s at 10 seconds after bounce, where strictly $L_{\bar{\nu}_e} > L_{\nu_e}$ after the onset of the explosion. The difference between the neutrino and antineutrino luminosities remained small and constant with respect to time up to 3 seconds post bounce and increased only significantly after $4-5$ seconds post bounce, after which the difference reached its maximum of 1.5×10^{50} erg/s at the end of the simulation at about 18 seconds post bounce. The electron flavor neutrino luminosities in our models follow a different behaviour. They reach 1×10^{51} erg/s at about 5, 6 and 8 seconds post bounce for the 8.8, 10.8 and 18 $M_\odot$ progenitor models respectively. The larger electron flavor neutrino luminosities for the more massive progenitors are in correlation with the more massive PNSs and the hence larger number of neutrinos emitted. However, the difference between electron-neutrino and electron-antineutrino luminosities found in the present investigation is significantly smaller than the difference in Woosley et al. (1994). During the initial explosion phase until about 300 ms after the onset of the explosion, the electron antineutrino luminosity is slightly larger than the electron neutrino luminosity by about 1×10^{50} erg/s which explains the electron fraction of $Y_e > 0.5$ of the early explosion ejecta. After about 900 ms post bounce, the luminosities can hardly be distinguished where during the initial neutrino driven wind phase after about 1 second after bonce the electron neutrino luminosity becomes larger than the electron antineutrino luminosity by about 1×10^{50} erg/s. This difference reduces again at later times at about 6 seconds post bounce and the electron flavor neutrino luminosities become more and more similar (see Fig. 3.15(a)).

Even more different are the values and the behavior of the mean neutrino energies, see Fig. 3.15(c) and (d) and compare with Fig. 2 of Woosley et al. (1994). They found (μ/τ)-neutrino energies of about 35 MeV which remained constant with respect to time. Their electron-antineutrino energies increased slightly from about 20 MeV to 22 MeV where the electron-neutrino energies decrease from 14 MeV to 12 MeV. This increasing difference between the electron neutrino and antineutrino spectra favored neutron-rich material, which was consistent with their findings of $Y_e < 0.5$ for the material ejected in the neutrino driven wind in Woosley et al. (1994). We cannot confirm these results for the mean neutrino energies nor the evolution of the spectra. In contrast, all mean neutrino energies decrease with respect to time for all our models, as a consequence of deleptonization of the central PNS where the neutrinos are produced and diffuse out. The electron (anti)neutrino energies decrease from about 10 (12) MeV at the onset of the explosion to about 8.5 (9) MeV and the (μ/τ)-neutrino energies decrease from 16 MeV to 10 MeV at the end of the simulations. Hence, not only the mean energies decrease also the difference between the electron flavor neutrino spectra decreases. The reason for the neutrino spectra to become more similar with respect to time is related to the evolution of the thermodynamic properties at the neutrinospheres, and will be
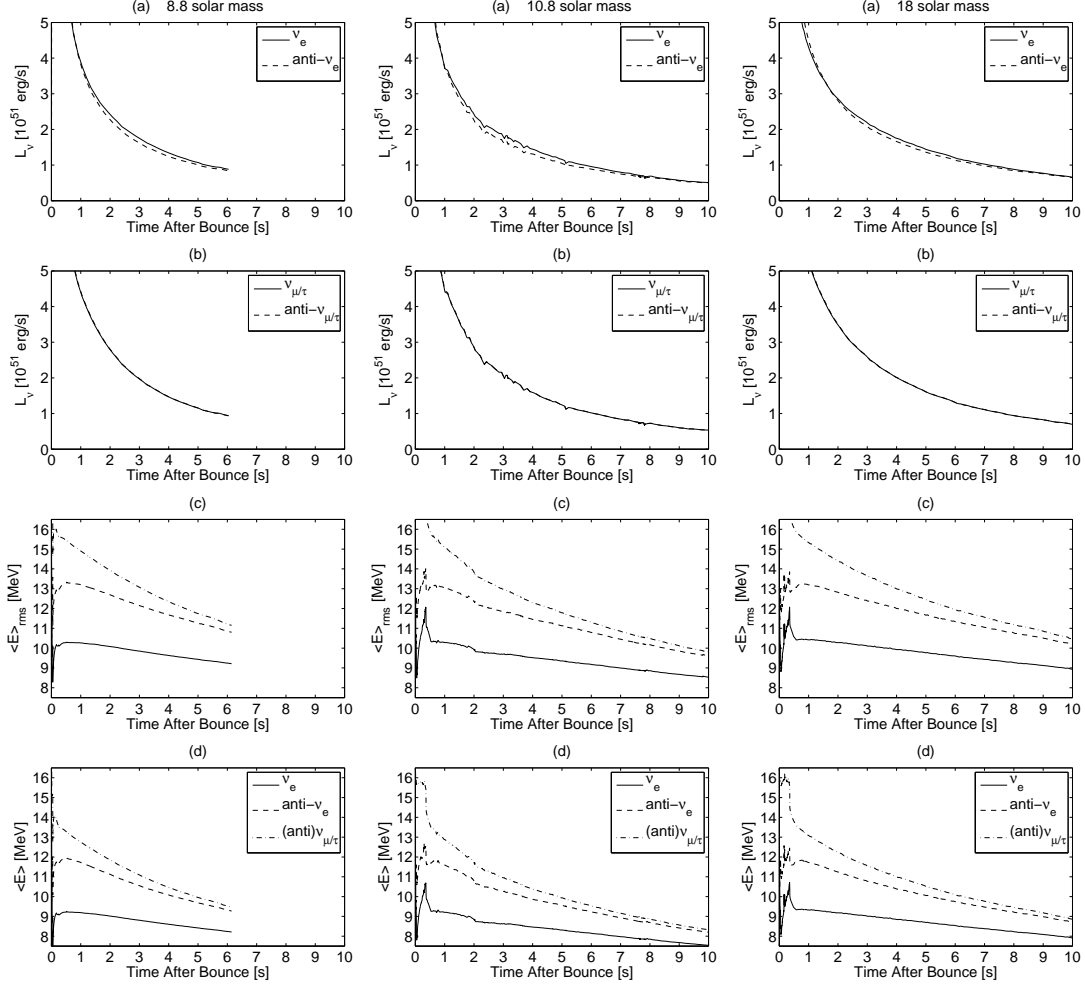
discussed in the following subsection.

Figure 3.15: Neutrino luminosities and mean energies with respect to time after bounce for the 8.8 $M_\odot$ O-Ne-Mg-core from Nomoto (1983,1984,1987) (left panel) and the 10.8 $M_\odot$ (middle panels) and 18 $M_\odot$ (right panel) Fe-core progenitor models from Woosley et al. (2002), measured in a co-moving reference frame at a distance of 500 km.

The PNS contraction

The behaviour of the neutrino spectra and hence the evolution and the properties of the neutrinospheres is related to the PNS contraction. The contraction is caused by a continuous deleptonization and translates to a continued steepening of the density gradient at the PNS surface. Hence, the neutrinosphere radii for the electron flavor neutrinos move closer together with time. The evolution of the neutrinosphere radii for

both electron neutrino and antineutrino are illustrated in Fig. 3.16 (a) for the 10.8 $M_\odot$ progenitor model. Their difference reduces from 740 m at about 1 second post bounce to 370 m at about 5 seconds post bounce and further to 260 m at about 10 seconds post bounce.

This contraction behaviour has consequences for the neutrino spectra, which are determined during the neutrino driven wind phase by diffusion rather than by mass accretion. Hence, the electron flavor neutrino luminosities can be determined as follows

$$L_\nu = \frac{1}{4}\, 4\pi\, r^2\, u_\nu\, |_{R_\nu},$$
(3.8)

where $u_\nu \propto T^4$ is the thermal black body spectrum for ultra-relativistic fermions with temperature T. The matter temperatures at the neutrinospheres decrease with respect to time as shown in Fig. 3.16 (b), which is due to the continuous deleptonization of the PNS. It explains the decreasing electron flavor neutrino luminosities and mean neutrino energies with respect to time. Furthermore, the temperature difference decreases with respect to time from 0.467 MeV at about 1 second post bounce to 0.362 MeV at about 10 seconds post bounce. Consequently the neutrino spectra become more similar with respect to time. As illustrated in Fig. 3.15, the difference in the electron flavor neutrino luminosities and mean neutrino energies decreases for all models under investigation. It becomes additionally clear from the electron fraction approximation Eq. (2.30), not the absolute values for the mean neutrino and antineutrino energies determine whether matter becomes neutron- or proton-rich but their difference.
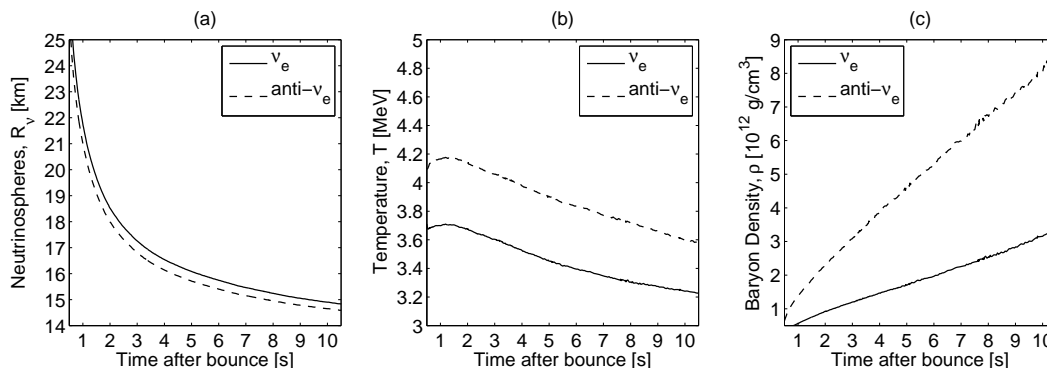

Figure 3.16: Evolution of the neutrinosphere radii in graph (a) and temperature and density at the corresponding neutrinospheres in graphs (b) and (c) respectively for the 10.8 $M_\odot$ progenitor model from Woosley et al. (2002).

Since this difference is small in our simulations, with initially at about 1 second post bounce $\langle E_{\nu_e}\rangle_{\rm rms} \simeq 10$ MeV and $\langle E_{\bar\nu_e}\rangle_{\rm rms} \simeq 13$ MeV and at later times at 10 seconds post bounce only $\langle E_{\nu_e}\rangle_{\rm rms} \simeq 9$ MeV and $\langle E_{\bar\nu_e}\rangle_{\rm rms} \simeq 11$ MeV, the values found for the electron fraction of $Y_e > 0.5$ (solid line in Fig. 3.14(b) for the Y_e-approximation based

on the luminosity and mean neutrino energies) clearly illustrate that the accelerated matter in the neutrino driven wind stays proton-rich for more than 10 seconds. This is in qualitative agreement with Boltzmann transport as discussed above and shown in Fig. 3.14(a). Hence we find Eq.(2.30) to be a good approximation to model the electron fraction in the wind. On the other hand, most of the previous studies select the neutrino luminosities and mean energies to investigate a neutron-rich neutrino driven wind. In order to test the appearance of $Y_e < 0.5$ under such conditions, we increase the difference between the mean neutrino and antineutrino energies by hand. We evaluate expression (2.30) shown in Fig. 3.14(b) at 10 km outside the electron-neutrinosphere for 1.2 (dashed line) and 1.5 (dash-dotted line) times larger electron-antineutrino mean energies. For the first value, Y_e decreases but matter remains slightly proton-rich, where for the latter value matter becomes neutron-rich. In other words, the larger the difference between neutrino and antineutrino spectra are, the smaller becomes the electron fraction in the wind. Please note that the luminosities and electron-neutrino energies remained unmodified for this at-hock approach. Such an increase of the energy difference between neutrinos and antineutrinos could perhaps be related to the uncertainty of the EoS for nuclear matter, which will be discussed in the following paragraph.

The assumed PNS radii in previous wind studies reach about 10 km shortly (≤ 1 second) after the explosion has been launched. We define the radius of the PNS as the position of the electron-neutrinosphere at the steep density gradient at the PNS surface. The approximated inner boundary of the physical domain in most wind models is close to but still inside this radius. The position of the neutrinospheres and the contraction of the PNSs found in the present investigation differ significantly from the assumptions made in most previous wind studies. We find PNS radii of about 40 km at the time of the explosion and 20 km at about 2 seconds after bounce. During the later evolution, the PNS contraction slows down. The PNS profile and hence the position of the neutrinospheres as well as the contraction behavior itself is given implicitly by the EoS for hot and dense nuclear matter as well as the PNS deleptonization. For the stiff EoS from Shen et al. (1998a) and both the 10.8 and 18 $M_\odot$ progenitors, the PNSs reach radii of $14.5-15$ km only at about 10 seconds after bounce (see Fig. 3.16 (a)). The larger radii of the neutrinospheres result in lower neutrino luminosities and mean energies and a smaller differences between neutrino and antineutrino spectra in comparison to the assumptions made in most previous wind models, rather than the PNS contraction only. This is in agreement with Arcones et al. (2007) who additionally assume PNS radii of 15 km and find conditions that differ more from previous wind studies. They obtained significantly larger values for the electron fraction. To summarize, this effects and the different behaviour of the neutrino spectra assumed in the previous wind studies leads to different matter properties of the neutrino driven wind. A detailed comparison study of fast and slow contracting PNSs with respect to the neutrino driven wind, e.g. applying EoSs with different compressibilities and asymmetry energies, would be necessary in the context of radiation hydrodynamics simulations using spectral Boltzmann neutrino

transport.

3.1.8   Long term post bounce evolution

During the neutrino driven wind phase, the neutrino luminosities and mean neutrino energies decrease continuously, which leads to a constant decrease in the net-heating rates. At luminosities below 10^{51} erg/s (see Fig. 3.15), the supersonic matter outflow for the 10 M$_\odot$ progenitor model descents into a subsonic expansion. The wind termination shock turns again into a subsonic neutrino driven wind. At later times, the neutrino driven wind settles down to a quasi-stationary state with no significant matter outflow, illustrated at the example of the 18 M$_\odot$ progenitor model in Fig.3.18 (a). The explosion shock continues to expand and the material enclosed inside the mass cut accretes onto the PNS at the center. In combination with the deleptonization, this leads to the continuous PNS contraction. However, the contraction proceeds on a timescale of seconds and hence the PNS can be considered in a quasi-stationary state. The dense and still hot and lepton rich PNS at the center is surrounded by a low density and high entropy atmosphere, composed of light and heavy nuclei. See for example the abundances of the 18 M$_\odot$ progenitor for the post bounce time of 22 seconds in Fig. 3.18 (e).

The internal temperature profile of the PNS is not constant. The central region of the PNS did not experience shock heating immediately after the Fe-core bounce, since the initial shock forms at the edge of the bouncing core. Its mass scales roughly with Y_e^2 and is typically around values of $0.5-0.6$ M$_\odot$ for low and intermediate mass Fe-core progenitors. Hence, the central temperature after bounce is given by the thermodynamic conditions at bounce. The temperature changes only during the post bounce evolution due to compressional heating and the diffusion of neutrinos. The shock heated material inside the PNS shows significantly higher temperatures than at the center. The temperature decreases again towards the PNS surface where the matter is less dense (for the illustration of the radial temperature profile inside the PNS as well as the dynamical evolution of temperature and density, see Fig.3.18 (f) and (b) at selected post bounce times between $5-22$ seconds). The neutrinos diffuse continuously out of the PNS and carry away energy. This deleptonize the PNS where the central electron fraction reduces from $Y_e \simeq 0.25$ at the onset of the explosion to $Y_e \simeq 0.15$ at 22 seconds after bounce (see Fig.3.18 (d)). It relates to a temperature decrease from about 35 MeV initially (at 3 seconds post bounce) to 23 MeV at about 22 seconds post bounce. This corresponds to the initial and neutrino dominated cooling phase. Unfortunately the achieved temperatures are not representative since important neutrino reactions, such as the direct and modified Urca processes, are not yet taken into account.
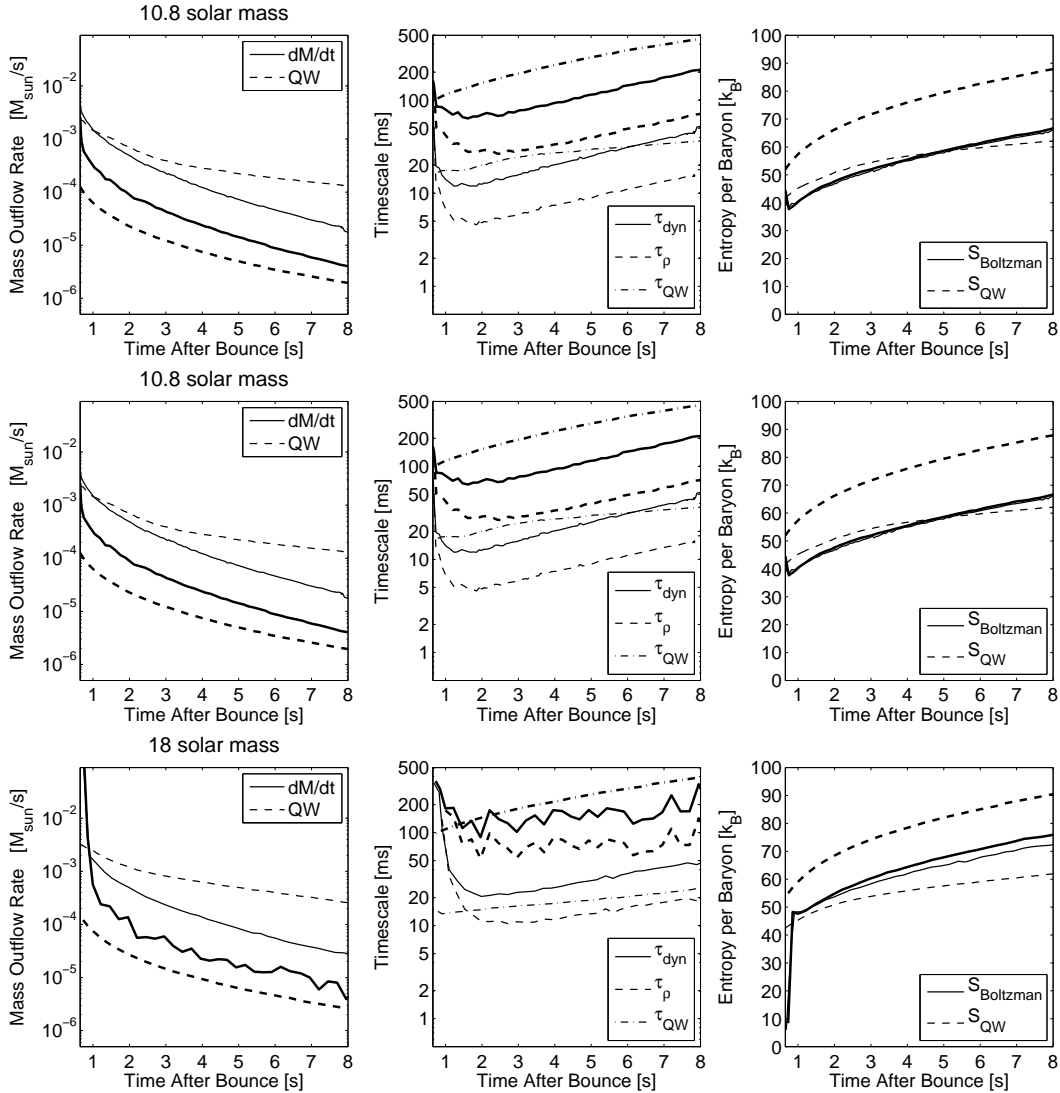
Figure 3.17: Comparing the mass accretion rate, timescale and entropy per baryon approximations from our simulations and the approximations from Qian and Woosley (1996) with respect to time after bounce for 8.8 (top), 10.8 (middle) and 18 M$_\odot$ (bottom) progenitor models.

3.1.9 Justification of the enhanced opacities

The neutrino driven wind was found to occur in all three progenitor models under investigation, the 8.8 $M_\odot$ O-Ne-Mg-core and the 10.8 and 18 $M_\odot$ Fe-core progenitor models. Because the neutrino driven explosions for the Fe-core progenitors are launched using artificially enhanced neutrino reaction rates, one may ask about the impact of these modified rates on the neutrino driven wind. Therefore we performed additional runs for which we switch back to the standard opacities given in Bruenn (1985) after the explosion has been launched. The times when we switch back is about 500 ms after bounce, chosen such that the dynamics of the explosion ejecta does not change anymore significantly due to neutrino heating. However, the lower opacities translate to a significantly smaller net-heating by a factor of $5 - 6$ in the region on top of the PNS where the neutrino driven wind develops. The energy deposition is still sufficient to drive the neutrino driven wind but the matter velocities are smaller by a factor of $2 - 5$ in comparison to the wind velocities using the enhanced reaction rates (see Fig. 3.19 (a)). The main effect of the artificially enhanced reaction rates and the hence increased neutrino heating on the dynamics is clearly the stronger neutrino driven wind. For the 10.8 $M_\odot$ progenitor model, the wind even develops supersonic velocities (as discussed above in §4) in Fig. 3.19(a) (top panel). The supersonic wind collides with the explosion ejecta where matter decelerates and hence the reverse shock forms, which additionally increase the entropy in the wind (see Fig. 3.19(c) (top panel)). This additional entropy increase is absent in the simulations using the standard opacities, where the wind stays subsonic. The same holds for the 18 $M_\odot$ progenitor model (Fig. 3.19, bottom panel), even using the enhanced opacities where the wind stays subsonic. This progenitor dependency of the neutrino driven wind is related to the density of the envelope surrounding the PNS after the explosion has been launched, which is significantly higher for more massive progenitors and hence the neutrino driven wind is weaker. In addition to the neutrino driven wind phase for the Fe-core progenitor models where the enhanced opacities are used, the neutrino driven wind of the O-Ne-Mg-core is illustrated in Fig. 3.12 using the standard rates from Bruenn (1985). The formation of a supersonic neutrino driven wind could be confirmed including the formation of the wind termination shock. Hence, one may speculate whether only low mass progenitors develop a strong neutrino driven outflow where the influence of the wind to the matter properties of the ejecta becomes small for more massive progenitors. The agreement of the time evolution of the mean neutrino energies between all three progenitor models under investigation (using the enhanced and standard opacities) in Fig. 3.15 is striking. In other words, the impact of the artificial heating to the neutrino observables and hence to the electron fraction in the wind is negligible. The influence on the composition of the wind is illustrated via the electron fraction in Fig. 3.19 (d). Using the standard rates, the wind stays slightly more proton-rich. Increasing the charged current reaction rates allows β-equilibrium to be established on a shorter timescale. In addition, matter stays slightly more proton-rich

for the the less intense neutrino driven wind, which develops for the Fe-core progenitors using the standard neutrino opacities. The additional electron fraction reduction in the neutrino driven wind for the models using the enhanced neutrino reactions is found due to the larger degeneracy obtained in the stronger deceleration behind the explosion ejecta. However, the findings of generally proton-rich ejecta as well as the generally proton-rich neutrino driven wind does not change. The corresponding densities and entropies per baryon in the wind are shown in Fig. 3.19 (b) and (c). The effects of the artificial heating are slightly smaller entropies. The higher matter outflow velocities in the wind region using the artificial heating results additionally in lower densities, shown in Fig. 3.19 (b).

The artificially increased charged current reaction rates cannot be justified by physical uncertainties of the rates themselves. Similar to the large luminosities assumed in Arcones et al. (2007), they could rather be seen as a lowest order attempt to take the effects of multi-dimensional phenomena into account. For example, known fluid instabilities increase the neutrino energy deposition efficiency. Convection allows matter to stay for a longer time in the neutrino heating region (see Herant et al. (1994), Janka and Mueller (1996)). Present axially symmetric core collapse models of massive Fe-core progenitor stars (even non-rotating) predict bipolar explosions (see Janka et al. (2008)). The deviation from a spherical description and hence the deformation of the SAS towards different modes due to fluid instabilities takes place during the neutrino heating phase on a timescale of several 100 ms after bounce already during the explosion phase. The luminosities are powered by a significantly larger mass accretion, compared to spherically symmetric models, since the up-streaming neutrino heated matter is accompanied by a large down-stream of cold material. These larger luminosities may power a supersonic neutrino driven wind behind the explosion ejecta while the neutrino driven wind may remain absent in the angular wedges of the accreting material which will not be ejected. However, we use spherically symmetric simulations since we believe that accurate Boltzmann neutrino transport and general relativistic effects are as important for the physical conditions of the neutrino driven wind as the possibility to follow the dynamical evolution for several seconds. This is by present standards beyond the state-of-the-art of multi-dimensional core collapse simulations.

3.1.10 Nucleosynthesis discussion

Previous wind models have long been investigated as a possible site for the production of heavy elements via the r-process, due to the expected neutron rich material ejected, the large entropies in the neutrino driven wind and the short timescale of the neutrino driven wind expansion (see Hoffman et al. (2007) and Panov and Janka (2009) and references therein). The relevant quantities are shown in Figs. 3.11 and 3.12 for the 10.8 $M_\odot$ and 8.8 $M_\odot$ progenitor models respectively. Illustrated are several selected mass shells that are part of the region where the neutrino driven wind develops in our radiation
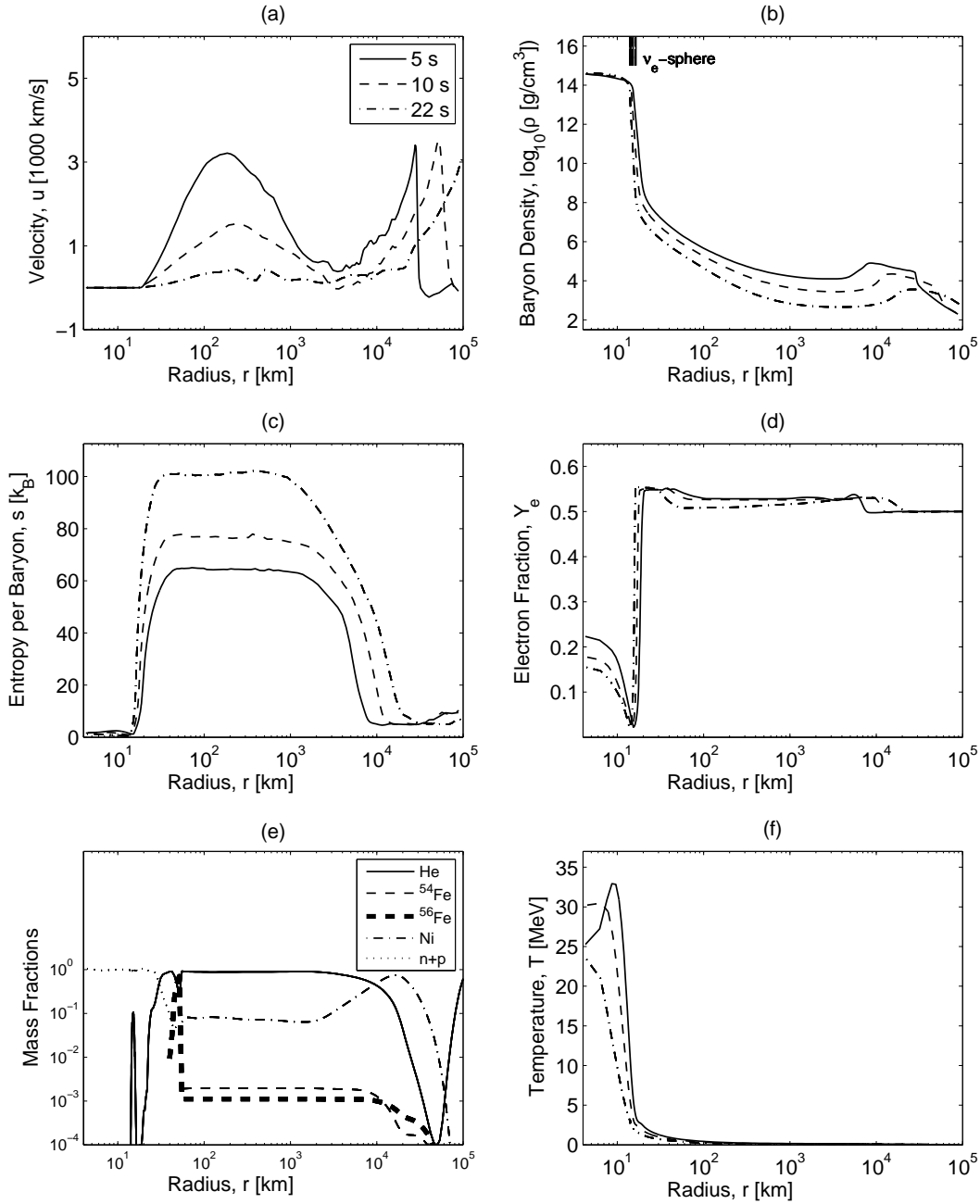
Figure 3.18: Radial profiles of selected hydrodynamic variables for the 18 $M_\odot$ progenitor model at three different post bounce times, illustrating the disappearance of the neutrino driven wind and the PNS cooling and contracting. Graph (e) illustrates the composition at 22 seconds post bounce.
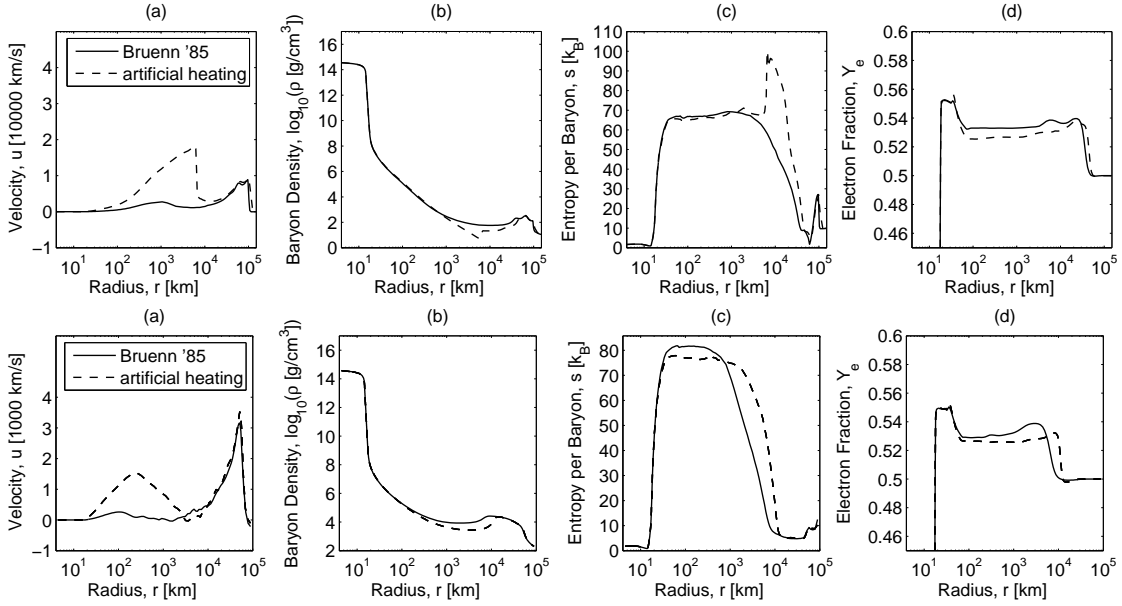
Figure 3.19: Comparing selected hydrodynamic variables using the standard reactions rates of Bruenn (1985) (solid lines) with the artificially enhanced rates (dashed lines) for the 10.8 $M_\odot$ (top) and the 18 $M_\odot$ progenitor model (bottom).

hydrodynamics model based on spectral three flavor Boltzmann neutrino transport. The inclusion of neutrino transport in a dynamical model is essential in order to obtain consistent neutrino spectra which determine the evolution of the electron fraction and the PNS contraction due to deleptonization and mass accretion. In comparison to previous static steady-state and dynamic wind models - where these ingredients were assumed - we confirm several properties of the accelerated material in the neutrino driven wind, such as the fast expansion and the large matter outflow rate shown in Fig. 3.17(a) and (b), the high velocities in the Figs. 3.11(f) and 3.12(f)) and the rapidly decreasing density and temperature of the accelerated material in Fig. 3.11 (b) and (c) respectively. The expansion timescale in Fig. 3.17(b) is given by the following expression

$$\tau_{\mathrm{dyn}} = \left. \frac{r}{v} \right|_{T=0.5\,\mathrm{MeV}},$$

evaluated at the surface of constant temperature of $T = 0.5$ MeV, compared with an alternative definition of the dynamic timescale which has been introduced in Thompson et al. (2001)

$$\tau_\rho = \left| \frac{1}{v} \frac{1}{\rho} \frac{\partial \rho}{\partial r} \right|^{-1}_{T=0.5\mathrm{MeV}},$$

as well as a timescale approximation which has been derived in Qian and Woosley (1996) Eq.(61)

$$\tau_{\mathrm{QW}} \propto \frac{1}{L_{\bar{\nu}_e}} \frac{1}{\epsilon_{\bar{\nu}_e}} R_{\mathrm{PNS}} M_{\mathrm{PNS}},$$

where additionally an approximation for the mass outflow rate is derived as follows

$$\left. \frac{dM}{dt} \right|_{\mathrm{QW}} \propto L_{\bar{\nu}_e}^{5/3} \epsilon_{\bar{\nu}_e}^{10/3} R_{\mathrm{PNS}}^{5/3} M_{\mathrm{PNS}}^{-2},$$

where R_{PNS} and M_{PNS} are the PNS radius and mass respectively, which we take to be given by the electron-antineutrinosphere, and $\epsilon_{\bar{\nu}_e} = \left\langle E_{\bar{\nu}_e}^2 \right\rangle / \left\langle E_{\bar{\nu}_e} \right\rangle$ where $\left\langle E_{\bar{\nu}_e} \right\rangle$ is the mean electron-antineutrino energy and $L_{\bar{\nu}_e}$ is the electron-antineutrino luminosity, both taken at the surface of constant temperature of $T = 0.5$ MeV. In comparison with previous wind studies (see for example Fig. 4 of Arcones et al. (2007)), we find generally a longer timescale of $\tau_{\mathrm{dyn}} = 30 - 100$ ms for the neutrino driven wind which corresponds to a mass outflow rate of $10^{-3} - 10^{-5}$ M$_\odot$ s^{-1} shown in Fig. 3.17 (a) and (b) respectively. However, we find generally a much longer timescale than the approximation τ_{QW} which is of the order $\sim 1 - 5$ ms. The same holds for the mass outflow rate $dM/dt|_{\mathrm{QW}}$ which is smaller by one order of magnitude. This may be related to the crucial assumptions made during the derivation of the above expressions, e.g. hydrostatic equilibrium, $R_{\mathrm{PNS}} = 10$ km, $L_{\nu_e} \simeq L_{\bar{\nu}_e}$, $\epsilon_{\bar{\nu}_e} = 20$ MeV, which differ significantly from our findings. However, the wind entropies of $40 - 100$ k$_{\mathrm{B}}$ found (initially driven due to neutrino heating and additionally due to the deceleration in the reverse shock) are significantly smaller than often assumed in the literature and the previously accelerated matter does not become neutron rich as the neutrino driven wind decelerates behind the explosion ejecta but stays slightly proton-rich where $Y_e \simeq 0.54$ for more than 10 seconds. This, in combination with the much slower PNS contraction illustrated via the neutrinospheres in Fig. 3.16 in comparison to static steady-state and dynamic wind models suggest that the assumptions made in previous wind studies should be carefully reconsidered. These assumptions are based on the detailed investigation of Woosley et al. (1994). They followed a neutrino driven core collapse supernova explosion of a 20 M$_\odot$ progenitor star for 18 seconds after bounce into the neutrino driven wind phase. Their numerical model was developed by J. R. Wilson and is based on sophisticated neutrino radiation hydrodynamics. The behaviour of the neutrino luminosities of all three flavors is in general agreement with our results. However, the mean neutrino energies differ significantly. We find generally smaller mean neutrino energies which decrease with respect to time after bounce, where the mean electron-neutrino energy decreases slightly and the mean electron-antineutrino energy increases slightly in the simulation analysed in Woosley et al. (1994) (see Fig.3). This results in an increasing difference between the electron flavor neutrino mean energies, where in our simulations this difference decreases. This fact in combination with the different PNS properties found in Woosley et al. (1994),

result in a strong neutrino driven wind where high entropies up to 400 k_B/baryon and a low electron fraction of $Y_e \simeq 0.35 - 0.45$ was obtained. These properties of the neutrino driven wind differ quantitatively from our results, where entropies of $60 - 100$ k_B/baryon are obtained and matter stays proton-rich ($Y_e \simeq 0.52 - 0.54$) for more then 10 seconds.

3.2 Protoneutron star evolution of massive Fe-core progenitors

In this section I will report on the emitted neutrino signal from failed core collapse supernova explosions and the formation of black holes via PNS collapse. For a review and previous studies of black hole formation including neutrino transport, see for example Baumgarte et al. (1996), Beacom et al. (2001), Liebendörfer et al. (2004) and Sumiyoshi et al. (2007). We performed general relativistic simulations in spherical symmetry using spectral three-flavour Boltzmann neutrino transport. By our choice of a spherically symmetric approach, we assume that accurate neutrino transport and general relativistic effects are more important for the analysis of the emitted neutrino signal, than multi-dimensional phenomena which are investigated in Marek et al. (2009). The simulations are launched from several massive progenitors stars of 40 and 50 $M_\odot$. I will present results from the investigation of the differences in the emitted neutrino signals for several massive progenitor models from different stellar evolution groups, such as Woosley and Weaver (1995), Heger and Woosley (2002), Umeda and Nomoto (2008) and Tominaga et al. (2007), during the accretion phase before black hole formation. For such progenitors, the presence of strong gravitational fields implements that general relativistic effects are important and must be taken into account.

The emitted neutrino signal depends on the matter conditions during the dynamical evolution of the PNS contraction, which are given by the EoS for hot and dense nuclear matter. Sumiyoshi et al. (2007) compared two different EoSs with respect to the compressibility of nuclear matter and illustrated the different emitted neutrino signals, especially the different timescales for the PNSs to become gravitationally unstable during the accretion phase of failed core collapse supernova explosions. We point out the importance of the progenitor model for the emitted neutrino signal. We demonstrate that it is hardly possible to draw any conclusions from the neutrino signal about the EoS or the progenitor model separately, as both quantities have similar effects on the emitted neutrino spectra. Moreover, we analyse the feasibility of approximating the electron-neutrino luminosity at large distances (typically of the order of a few 100 km and more) depending explicitly on the progenitor model (the mass accretion rate) and the temperature at the neutrinosphere. Liebendörfer (2005) presented a density-parametrized deleptonisation scheme which can be applied in multi-dimensional simulations during the collapse phase. We introduce a simple model to illustrate the dependency of the electron-(anti)neutrino luminosity from the matter conditions at the PNS surface.

(μ/τ)-(anti)neutrinos are assumed to interact via neutral current reactions (as introduced in §2.1.3 above) only as the thermodynamic conditions do not favour the presence of a large fraction of μ/τ. Hence the muonic charged current reactions are suppressed. On the other hand, the (μ/τ)-(anti)neutrino emission is rather important for the cooling at the (μ/τ)-neutrinospheres and needs to be handled carefully. In an

earlier study, Liebendörfer et al. (2004) emphasized the (μ/τ)-(anti)neutrino luminosity increase during the accretion phase of a 40 M$_\odot$ progenitor model. Fischer et al. (2007) extended this study and presented preliminary results investigating the connection between the (μ/τ)-(anti)neutrino luminosity increase and the contraction of the PNS during the accretion phase. Here, we compare selected pair creation reactions separately and analyse the consequences of these different reactions to the post-bounce evolution of massive progenitors before black hole formation.

The work which is summarised in the following sections has already been published in Fischer et al. (2009a).

3.2.1 Aspects of PNS evolution and black hole formation

Fig. 3.20 illustrates the physical conditions during the collapse of a PNS to a black hole. The PNSs are modelled as the central object in failed core collapse supernova explosions of massive progenitors of (40 and 50 M$_\odot$). As the central density in Fig. 3.20 (b) exceeds a certain critical value (depending on the EoS), nuclear forces and neutron pressure fail to keep the PNS stable against gravity and the central part of the PNS starts to contract. This can be identified at the radial velocities in Fig. 3.20 (a). During the subsequent compression, the central matter density in Fig. 3.20 (b) continues to rise above 10^{15} g/cm^3 while the shock position remains almost unaffected at $30 - 35$ km. In addition, the hydrodynamical timescale for the PNS to become gravitationally unstable and to collapse to a black hole is reduced to milliseconds.

The moment of black hole formation is reached when the central lapse function (α in Fig. 3.20 (c)) approaches zero with respect to time. Due to our co-moving coordinate choice, no stable solutions of the differential equations for momentum and energy conservation can be found. In addition, Fig. 3.20 (d) shows the relativistic factor $\Gamma = \sqrt{1 - 2m/r + u^2}$ and α as a function of the enclosed baryon mass a for three snapshots directly before and during the PNS collapse, illustrating the region where relativistic effects become important.

The neutrino signal from PNS accretion from two different EoSs

In the following paragraphs, I compare the soft EoS from Lattimer and Swesty (1991) (formerly EoS1) with the compressibility of 180 MeV with the stiff EoS from Shen et al. (1998a) (formerly EoS2) with the compressibility of 281 MeV during the accretion phase of a core collapse simulation of the 40 M$_\odot$ progenitor model from Woosley and Weaver (1995) before black hole formation.

Fig. 3.21 compares the neutrino luminosities in graph (a) and the mean neutrino energies in graph (b) as a function of time after bounce for EoS1 and EoS2. The larger electron-neutrino luminosity slightly before and at bounce is due to the different thermodynamic conditions achieved at bounce as illustrated in Fig. 3.22. These different
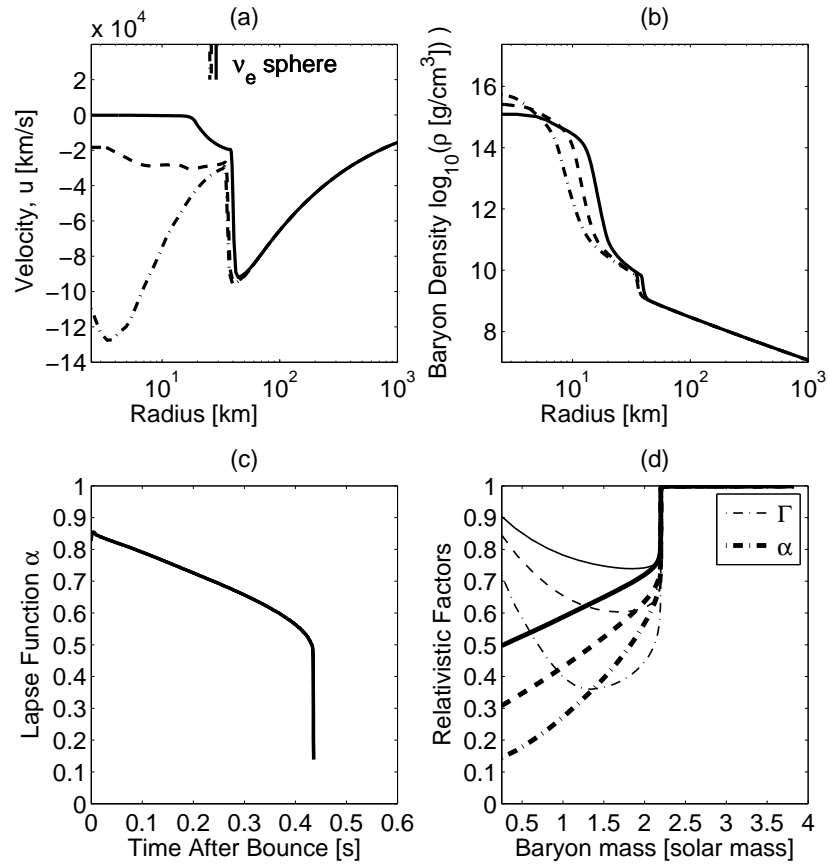
Figure 3.20: Radial velocity and density profiles as a function of the radius. The relativistic factor Γ and the lapse function α as a function of the enclosed baryon mass at three different times after bounce during the PNS collapse (solid line 433.6 ms, dashed 435.4 ms, dash-dotted 435.5 ms), at the example of a 40 $M_\odot$ progenitor from Woosley and Weaver (1995). In addition, the lapse function at the centre is plotted with respect to time after bounce.

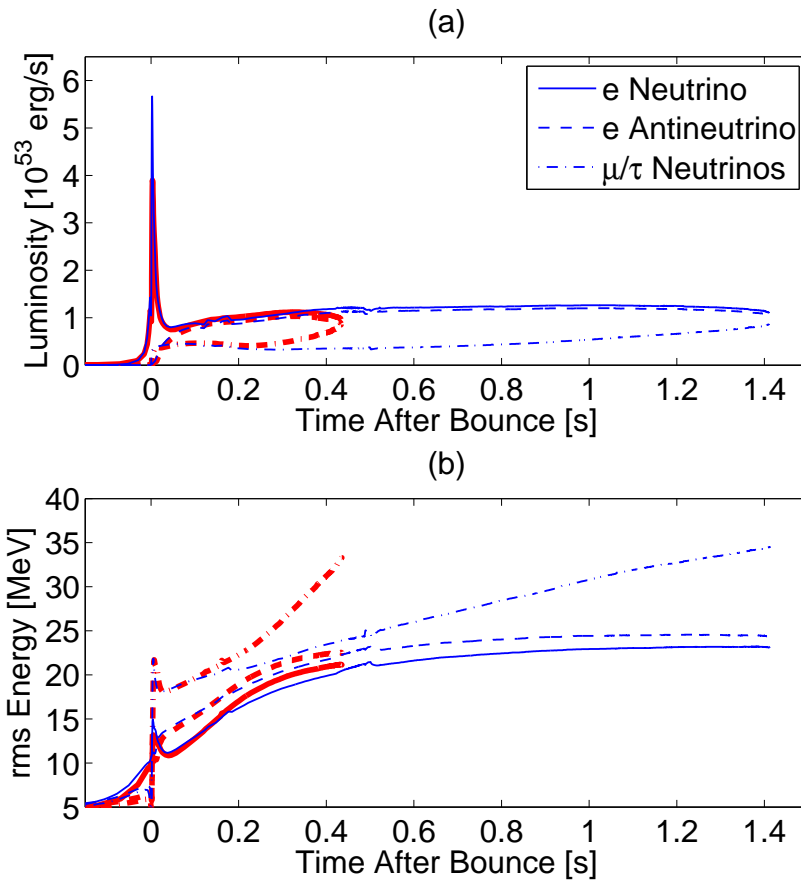Figure 3.21: Luminosities and mean energies during the post-bounce phase of a core collapse simulation of a 40 $M_\odot$ progenitor model from Woosley and Weaver (1995). Comparing EoS1 (red thick lines) with EoS2 (blue thin lines).
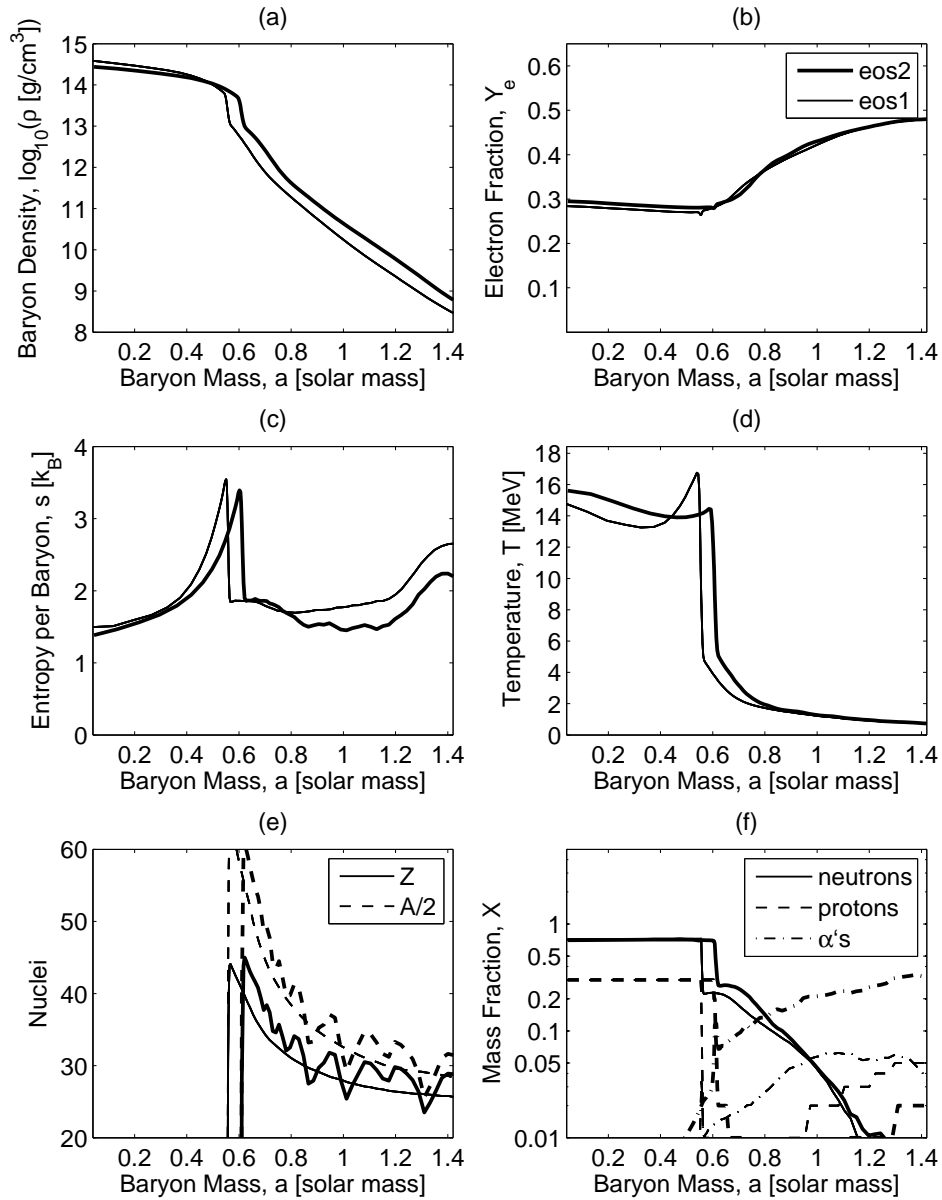
Figure 3.22: Bounce conditions for the core collapse simulation of a 40 $M_\odot$ progenitor model from Woosley and Weaver (1995), comparing EoS1 (thin lines) with EoS2 (thick lines).

(a) EoS1   (b) EoS2

Figure 3.23: The last stable configuration of the PNSs (solid lines) before becoming gravitationally unstable and starting to collapse (dashed lines) to a black hole (dash-dotted lines), using the 40 $M_\odot$ progenitor model from Woosley and Weaver (1995).

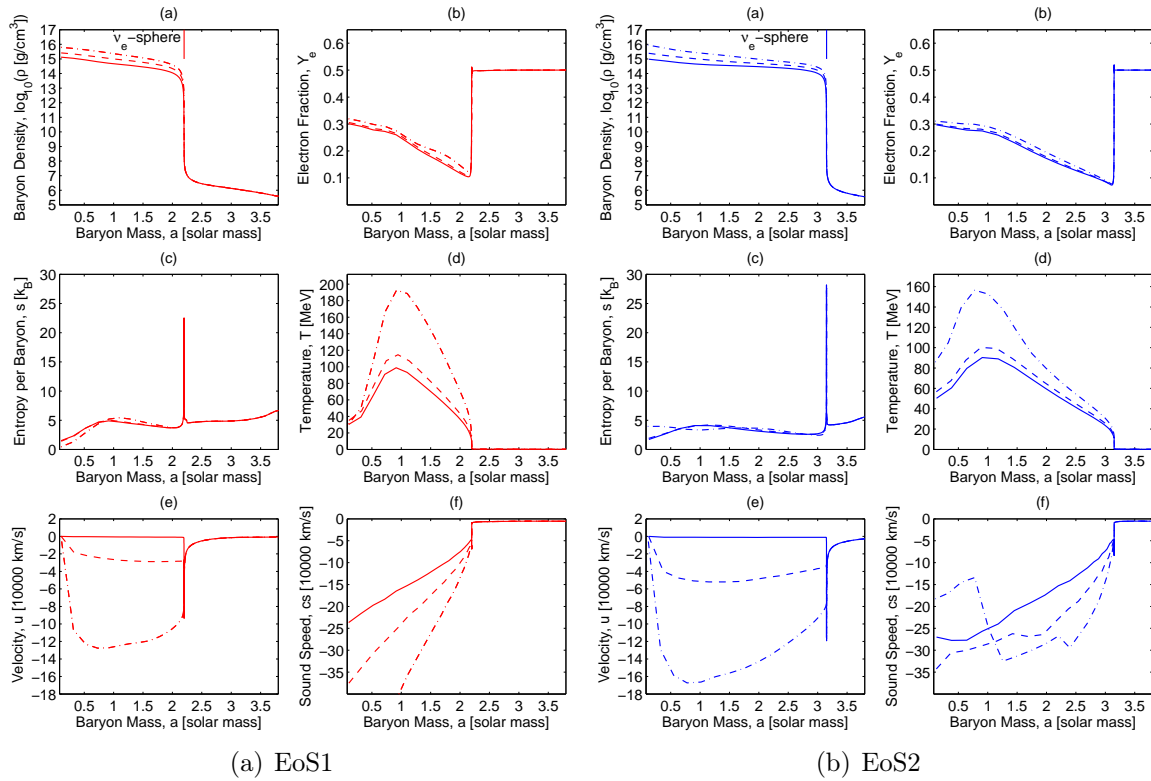| EoS	T	ρ	Y_e
	[MeV]	10^{14} [g/cm^3]	
eos1 (a)	29.78	12.0	0.299
eos1 (b)	96.05	5.86	0.270
eos2 (a)	50.27	9.16	0.297
eos2 (b)	92.04	4.37	0.271

Table 3.1: Thermodynamic conditions of the PNSs in Fig. 3.23, comparing the central data (a) with data corresponding to the maximum temperatures obtained (b).

conditions are a direct hydrodynamic consequence of the more compact bouncing core using EoS1 (see the higher central density in graph (a)), which results in a larger central deleptonisation in graph (b). The corresponding entropy and temperature profiles are shown in graphs (c) and (d) respectively. At intermediate densities and temperatures, heavy nuclei appear with slightly larger average atomic charge and number using EoS1 (see graph (e)). On the other hand, the fractions of light nuclei in graph (f) differ quite a lot. This is a deficit of EoS1 and has been noticed by the authors J. Lattimer and F. D.Swesty. During the postbounce phase, the simulation using the soft EoS1 is characterized by a short accretion time of $\simeq 500$ ms and thus a rapid PNS contraction before becoming gravitationally unstable and collapsing to a black hole.

Fig. 3.23 illustrates the last stable configuration before the PNSs (identified via the ν_e-spheres) become gravitationally unstable. The Figure compares the baryon density, electron fraction, entropy, temperature and velocity profiles in the graphs (a) - (e) respectively with respect to the enclosed baryon mass for the two EoSs (EoS1: left panel, EoS2: right panel).

The configuration achieved using the stiff EoS2 is supported via larger pressure and nuclear forces, which stabilise the PNS against gravity and allow more mass to be accreted. The maximal masses for both (hot and dense) EoSs were found to be 2.196 $M_\odot$ for EoS1 and 3.15 $M_\odot$ for Eos2 respectively. This results in an extended PNS accretion phase of $\simeq 1.4$ s using EoS2 for the progenitor model under investigation. The corresponding thermodynamic conditions for the PNS configurations illustrated in Fig. 3.23 are shown in Tab. 3.1. (a) compares the central data with (b) the maximum temperatures achieved, illustrating the region where the PNSs become gravitationally unstable and start to collapse. However, both of the PNS collapses to a black hole proceed along similar paths although the model using EoS2 is much more massive and has reached a higher degree of deleptonisation. Note that the PNS collapse proceeds adiabatically and the higher densities found during collapse correspond to β-equilibrium that is established at a higher electron fraction in Fig. 3.23 graphs (b). In other words, the entropy per baryon in Fig. 3.23 graphs (c) should be conserved. This is not quite the case for both models using EoS1 and EoS2 due to the temperatures of $T > 100$ MeV reached during the PNS collapse, for which both EoSs are not valid for.

Our results are in qualitative agreement with an independent study on the subject of an EoS comparison, recently published by Sumiyoshi et al. (2007).

3.2.2 The electron-(anti)neutrino signal from protoneutron star accretion

The core of massive stars are optically opaque, the only sources of information that is able to leave are gravitational waves and neutrinos. An indirect insight into the happenings inside the Fe-core is given by the observed composition of the ejecta in the case of an explosion. However, gravitational waves have proven difficult to detect and nucleosynthesis calculations are model dependent. Neutrinos on the other hand (especially the electron-flavour neutrinos), are of interest for neutrino detector facilities, such as Super-Kamiokande and SNO, being able to resolve the neutrino signal from a Galactic core collapse supernova on a tens of millisecond timescale. The understanding and modeling of the neutrino emission, absorption and transport is essential in core collapse supernova models to be able to compare the predicted neutrino signal with a possible future measurement.

With special focus on multi-dimensional simulations of the post-bounce phase, we present an analysis of the electron-neutrino luminosity. We construct an electron-neutrino luminosity approximation, which depends only on the physical conditions at the electron-neutrinosphere R_{ν_e} and can be applied after the neutronisation burst after bounce has been launched. We will also compare the approximation with spherically symmetric simulations using three-flavour Boltzmann neutrino transport.

Electron-neutrino luminosity dependencies

The long term sources of energy for the electron-neutrino luminosity are the total change of the potential energy given by the amount of accreted mass per unit time (accretion luminosity)

$$L_{\dot{M}} = \frac{GM}{r} \dot{M}, \tag{3.9}$$

at R_{ν_e}. Short term neutrino emission depends on the temperature increase at the neutrinosphere (diffusion luminosity)

$$L_{\mathrm{D}} = 4\pi R_{\nu_e}^2 c \, u_{\nu_e}, \tag{3.10}$$

where $u_{\nu_e} \propto T^4$ is the thermal black body energy spectrum for ultra-relativistic fermions with matter temperature T. Hence, L_{D} depends only on the thermodynamic conditions at the electron-neutrinosphere, which are given by the PNS contraction behavior and is correlated to the mass accretion rate. The accurate neutrino number density from

Boltzmann transport is (in spherical symmetry) given by

$$\langle n_{\nu_e}\rangle|_{R_{\nu_e}} = \frac{4\pi}{(hc)^3} \int_0^\infty E^2 dE \int_{-1}^{+1} \mu d\mu f_{\nu_e}(t, a, \mu, E), \tag{3.11}$$

at the electron-neutrinosphere R_{ν_e}. $f_{\nu_e}(t, a, \mu, E)$ is the electron-neutrino distribution function, which depends (in spherical symmetry) on the phase space coordinates (t, a, μ, E) where $\mu = \cos\theta$ is the cosine of the neutrino propagation angle θ and E is the neutrino energy. We have found that the assumption of a thermal electron-neutrino number spectrum at R_{ν_e},

$$\langle n_{\nu_e}\rangle \equiv n_\nu \propto T^3,$$

does not generally apply for all progenitor models. The measure of deviation is denoted as

$$\beta = \frac{\langle n_\nu\rangle}{n_\nu}. \tag{3.12}$$

Comparing the electron-neutrino luminosity from Boltzmann transport calculations (outside the neutrinosphere at large distances; typically of the order of a few 100 km or more) with the luminosities given by Eq. (3.9) and Eq. (3.10), we find the following approximation for the electron-neutrino luminosity

$$L_{\nu_e} = \min\left(\frac{1}{4}L_D, \beta L_{\dot{M}}\right). \tag{3.13}$$

The pre-factor 1/4 is in agreement with Janka (2001) (see §6.1) and expresses the approximate amount of outward directed transported thermal neutrinos. These neutrinos are assumed to carry information about the local thermodynamic matter conditions, since the neutrino temperature can be approximated by the matter temperature at R_{ν_e}.

Due to the lack of the neutrino momenta in approximate neutrino transport calculations, it is usually not possible to calculate the coefficient β. However, since β depends only on the mass accretion induced deviation of the neutrino spectrum from a black body spectrum, an exponential behavior of the quotient of the accretion luminosity and the diffusion luminosity was empirically found

$$\beta \simeq \frac{1}{2} e^{\frac{L_{\dot{M}}}{L_D}}. \tag{3.14}$$

β can be understood as a function of the temperature scaled with $\dot{M}$, since the temperature at R_{ν_e} is adjusted by the PNS contraction given by the mass accretion rate.

In the following subsections, I will compare the approximation Eq. (3.13) with three-flavour Boltzmann neutrino transport during the postbounce evolution of different progenitor models.

Thermal electron-neutrino spectra

The large mass accretion rates of $\simeq 1 - 2$ M$_\odot$/s of the 40 and 50 M$_\odot$ progenitor models from Woosley and Weaver (1995) in Fig. 3.24(a) and from Tominaga et al. (2007); Umeda and Nomoto (2005) in Fig. 3.24(b) respectively (see graphs (c)) result in fast contracting PNSs (see graphs (d)). The electron-neutrino number densities differ only slightly from a thermal spectrum after the neutrino burst has been launched after about 50 ms post-bounce. Hence, the electron-neutrino luminosities at large distances (here 500 km) in the graphs (b) are dominated by the diffusion luminosity over the accretion luminosity due to the limiter in Eq. (3.13). Graphs (a) compare β from Boltzmann transport calculations via Eq. (3.12) and via Eq. (3.14). β were found to be 0.7, increasing after 100 ms after bounce up to 0.8.

Finally, the fast contracting PNSs become gravitationally unstable rather quickly (due to the soft EoS *eos1* and the large mass accretion rate) and collapse to black holes after 435.5 ms after bounce for the 40 M$_\odot$ progenitor model and after 487.3 ms after bounce for the 50 M$_\odot$ progenitor model.

Non-thermal electron-neutrino spectra

Here I will continue the analysis from above and present data from core collapse simulations of massive progenitors with small mass accretion rates. These models show a different electron-neutrino luminosity dependency with respect to the approximation Eq. (3.13) during the post-bounce phase. Fig. 3.24(c) and Fig. 3.24(d) illustrate the post-bounce evolution of a 40 M$_\odot$ progenitor model from Woosley et al. (2002) and a 50 M$_\odot$ progenitor model from Umeda and Nomoto (2008) respectively (both using EoS1).

We have found the electron-neutrino luminosities are initially (until $\simeq 150$ ms post-bounce) dominated by the diffusion approximation of Eq. (3.13), as the matter temperatures are moderately high. This is in agreement with an earlier study by Liebendörfer et al. (2004). However, as the accretion rates in Fig. 3.24(c) and Fig. 3.24(d) graphs (c) decrease drastically after $\simeq 150$ ms post-bounce (even below 0.5 M$_\odot$/s). The temperature at R_{ν_e} increases less rapidly and the neutrino number density at R_{ν_e} differs from a thermal spectrum. β in Fig. 3.24(c) and Fig. 3.24(d) graphs (a) were found to be generally smaller, between 0.6 and 0.7. The PNS contraction times exceed more than 1 second, as can be seen from the slowly contracting neutrinospheres in graphs (d). The electron-neutrino luminosities in Fig. 3.24(c) and Fig. 3.24(d) graphs (b) are generally smaller (< 0.5 erg/s) in comparison to the thermal dominated spectra in Fig. 3.24(a) and Fig. 3.24(b). For low accretion rates, the electron-neutrino luminosities are dominated by the accretion luminosity as described by the limiter in Eq. (3.13).

As an example of an intermediate mass progenitor model with a small mass accretion rate, we apply the same analysis to a core collapse simulation of the 15 M$_\odot$ progenitor from Woosley and Weaver (1995) in Fig. 3.25 (using EoS2), which often served as a reference model (e.g. Liebendörfer et al. (2005)). Due to the small mass accretion

(a) 40 M$_\odot$ (Woosley and Weaver (1995)).

(b) 50 M$_\odot$ (Tominaga et al. (2007)).

(c) 40 M$_\odot$ (Woosley et al. (2002)).

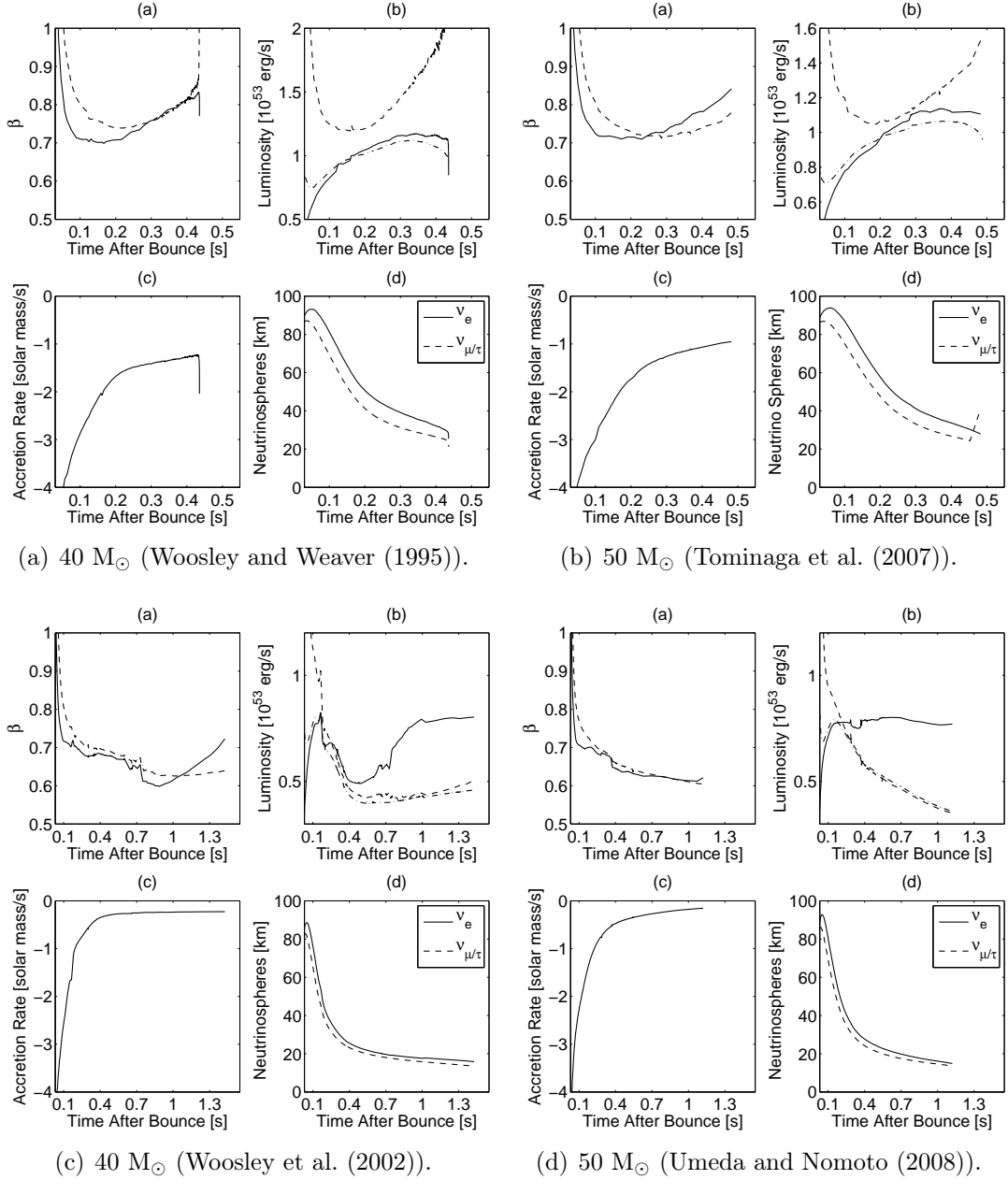(d) 50 M$_\odot$ (Umeda and Nomoto (2008)).

Figure 3.24: The electron-neutrino luminosity approximation and Boltzmann neutrino transport calculations during the post-bounce evolution for several massive progenitors, comparing β in the graphs (a) from simulations with Boltzmann neutrino transport Eq. (3.12) (dashed line) and Eq. (3.14) (solid line) and the graphs (b) illustrate the different luminosities separately (solid line: diffusion part of Eq. (3.13), dashed: accretion part of Eq. (3.13), dash-dotted: Boltzmann neutrino transport). In addition, graph (c) shows the mass accretion rate at the radius of the electron-neutrinosphere and graph (d) shows the contracting electron- and (μ/τ)-neutrinospheres.

rate in graph (c), the neutrinospheres in graph (d) contract on timescales of hundreds of milliseconds. In contrast to the massive progenitors with a small mass accretion rate, the neutrino number spectrum at the electron-neutrinosphere differs only slightly from the thermal one and β in graph (a) was found to be quite large, between 0.7 increasing up to 0.8 as for the massive progenitors with a large mass accretion rate. The electron-neutrino luminosity in graph (b) agrees initially (until 200 ms post-bounce) with the approximation Eq. (3.13) due to the limiter and is dominated by the diffusion luminosity. Note, although the electron-neutrino Luminosity can be approximated by the accretion luminosity after 200 ms post-bounce, the difference from the diffusion luminosity is only $\simeq 10\%$. On a longer timescale, the accretion luminosity becomes too large.
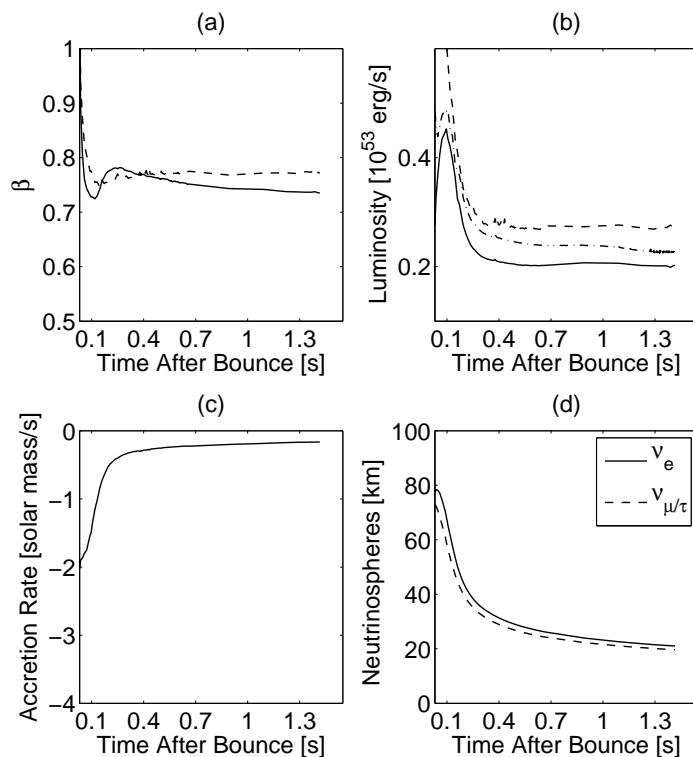

Figure 3.25: The same presentation as Fig. 3.24(d) for a 15 $M_\odot$ progenitor model from Woosley and Weaver (1995) with a small mass accretion rate. In contrast to the massive progenitors with a comparable mass accretion, the electron-neutrino luminosity is dominated by the diffusion part of Eq. (3.13).

So far, it has been demonstrated that the electron-neutrino luminosity in the post-bounce phase of core collapse supernovae depends sensitively on the progenitor model induced neutrino-spherical data and does not generally follow a thermal spectrum.

3.2.3 Dependency of the emitted neutrino signal on the progenitor model

The shock dynamics during the post-bounce evolution of failed core collapse supernova explosions take place in the innermost $\simeq 200$ km in spherical symmetry. Note that present axially symmetric core collapse models are more optimistic. The dynamical evolution outside the Fe-core is determined by the progenitor structure and does not evolve significantly during the simulation time. Material from the gravitationally unstable surrounding regions continues to fall onto the SAS. Nuclei dissociate into free nucleons and light nuclei, which accrete slowly onto the PNS at the centre. The PNS contraction is determined by the evolution of the baryon mass

$$\left.\frac{\partial a}{\alpha \partial t}\right|_{R_{\nu_e}} = \frac{4\pi r^2 u \rho}{\Gamma} \tag{3.15}$$

at the radius of the electron-neutrinosphere R_{ν_e}. $u = \partial r / \alpha \partial t$ is the radial velocity of the accreting matter, ρ is the matter density, Γ is the relativistic factor and α is the lapse function. For the derivation of the expression for the evolution of the gravitational mass, see the appendix of Liebendörfer et al. (2001a).

Above, we have discussed the connection between the emitted neutrino spectra and the matter properties at the neutrinospheres. In the following, we will explore whether there is a correlation between the different neutrino spectra and the structure of the progenitor.

The progenitor models under investigation are the 40 $M_\odot$ from Woosley and Weaver (1995) (40WW95), the 40 $M_\odot$ from Woosley et al. (2002) (40W02), the 40 $M_\odot$ from Umeda and Nomoto (2008) (40U08), the 50 $M_\odot$ from Umeda and Nomoto (2008) (50U08) and the 50 $M_\odot$ from Tominaga et al. (2007); Umeda and Nomoto (2005) (50T07). All are non-rotating and of solar metallicity. These models differ in the size of the iron-cores (see Tab. 3.2). The masses of the iron-cores are thereby determined intuitively, as Fe-group nuclei (^{52}Fe, ^{53}Fe, ^{56}Fe and ^{56}Ni) are more abundant then ^{28}Si and ^{32}S.

Fig. 3.26(a) and Fig. 3.26(b) illustrate the post-bounce luminosities and mean neutrino energies of the progenitor models listed in Tab. 3.2. As discussed above, the different mass accretion rates result in different PNS contraction timescales and different electron-neutrino luminosity dependencies.

The models 40WW95, 40U08 and 50T07 with large mass accretion rates at the PNS surface are identified with a short accretion phase after bounce before black hole formation. This corresponds to large luminosities ($L_{\nu_e} > 0.5 - 1$ erg/s, $L_{\mu/\tau} > 0.4$ erg/s) in the graphs (a) and (c). The (μ/τ)-(anti)neutrino mean energies in the graphs (c) increase rapidly after bounce and reach 34 MeV. On the other hand, the models 40W02 and 50U08 with small mass accretion rates at the neutrinospheres show before black hole formation an extended accretion phase of more than 1 second with smaller
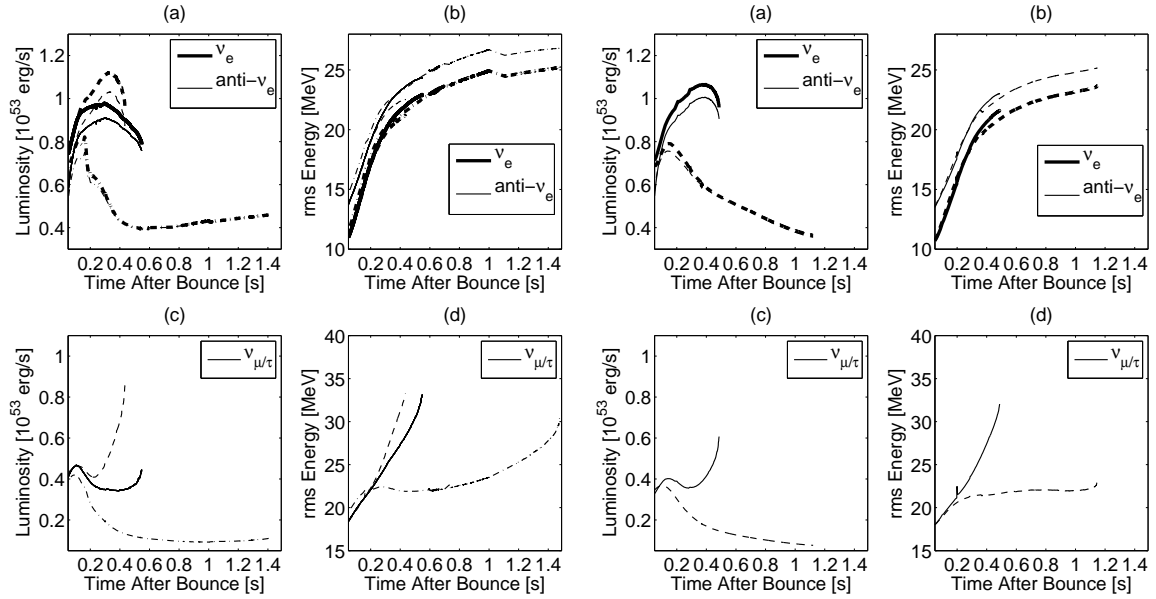
(a) The 40 $M_\odot$ progenitor models from 40U08 (b) The 50 $M_\odot$ progenitor models from 50T07 (solid lines), 40WW95 (dashed lines) and 40W02 (solid lines) and 50U08 (dashed lines). (dash-dotted lines).

Figure 3.26: Neutrino luminosities in the graphs (a) and (c) and mean neutrino energies in the graph (b) and (d) for the different progenitor under investigation with respect to time after bounce.

luminosities after the neutrino burst has been launched ($L_{\nu_e} < 0.5$ erg/s, $L_{\mu/\tau} < 0.2$ erg/s). The electron-neutrino flavour mean energies in the graphs (b) and (d) follow a similar behavior for all progenitor models while the (μ/τ)-(anti)neutrino energies increase over a longer timescale during the PNS contraction. For the model 40W02, the (μ/τ)-(anti)neutrino energies increase only after 700 ms after bounce from 22 MeV up to only 30 MeV. For the model 50U08, the PNS does not reach equivalent compactness during the post-bounce accretion phase before becoming gravitationally unstable and collapsing to a black hole. The (μ/τ)-(anti)neutrino energies increase from 22 MeV to 24 MeV only after 1.1 s after bounce. The progenitor models under investigation are based on different stellar evolution models. They involve different treatments of, for instance, nuclear burning, mixing, neutrino losses and the EoS. Hence, all models show differences at the final stage of stellar evolution, as illustrated in Fig. 3.27(a) for the 40 $M_\odot$ progenitor models under investigation and Fig. 3.27(b) for the 50 $M_\odot$ progenitor models under investigation. To be able to compare the progenitors, we evolve each model until the same central densities are reached. These are 9.12×10^9 g/cm^3 for the 40 $M_\odot$ and 1.58×10^{10} g/cm^3 for the 50 $M_\odot$ progenitor models.

Consequently, the central region of all models are very similar. The 40 $M_\odot$ pro-

Model	Fe-core	t_{bh}
	[$M_\odot$]	[ms]
40WW95	1.76	435.5
40W02	1.56	1476.5
40U08	1.74	548.4
50U08	1.89	1147.6
50T07	Unknown	487.3

Table 3.2: The size of the iron core and time between bounce and black hole formation for the different progenitor models.

genitors have electron factions of $Y_e \simeq 0.44$, temperatures of $\simeq 0.85$ MeV and infall velocities of ~ 1000 km/s. The more massive 50 $M_\odot$ progenitors have similar infall velocities but higher central temperatures of 0.9 MeV and are slightly more deleptonised with $Y_e \simeq 0.43$. Note that the central hydrodynamical variables are rather similar compared to the properties outside the Fe-cores (see Fig. 3.27(a) and Fig. 3.27(b)). There, the differences of the baryon density can be more than one order of magnitude for the same progenitor mass while temperatures and infall velocities can differ by a factor of 2. These differences are responsible for the different dynamical evolution in the post-bounce phase and will be discussed in the following paragraph.

The central regions evolve in a similar manner and are synchronised at core bounce for all progenitor models, as illustrated in Fig. 3.28(a) and Fig. 3.28(b). As demonstrated above, the PNS contraction behavior and the subsequent electron-neutrino luminosity are determined by the mass accretion rate at the neutrinosphere, which depends on the amount of mass that falls through the SAS from regions outside the Fe-core. Hence, the mass accretion rate at the neutrinosphere is given by the progenitor structure at bounce as illustrated in Fig. 3.28(a) and Fig. 3.28(b).

The infall velocities in Fig. 3.28(a) and Fig. 3.28(b) (a) are similar for all progenitor models. On the other hand, for the same progenitor mass differ the matter densities in the graphs (b) outside the Fe-cores substantially, comparing the models from the different stellar evolution groups.

The models 40WW95, 40U08 and 50T07 have high matter densities outside the Fe-cores. This corresponds to large mass accretion rates at the neutrinospheres and short post-bounce accretion times before the PNSs reach the critical masses and collapse to black holes (see Fig.3.26(a) and Fig.3.26(b)). The electron-neutrino luminosities correspond to thermal spectra.

The opposite holds for the models 40W02 and 50U08, with small matter densities outside the Fe-cores. This leads to small mass accretion rates at the neutrinospheres and consequently extended post-bounce accretion phases (see Fig.3.26(a) and Fig.3.26(b)). The electron-neutrino luminosities correspond to accretion spectra.

We have found a correlation between the electron flavour neutrino luminosities and

(a) 40 M$_\odot$: 40U08 (solid lines), 40WW95 (dashed lines), 40W02 (dash-dotted lines)

(b) 50 M$_\odot$: 50U08 (solid lines), 50T07 (dashed lines)
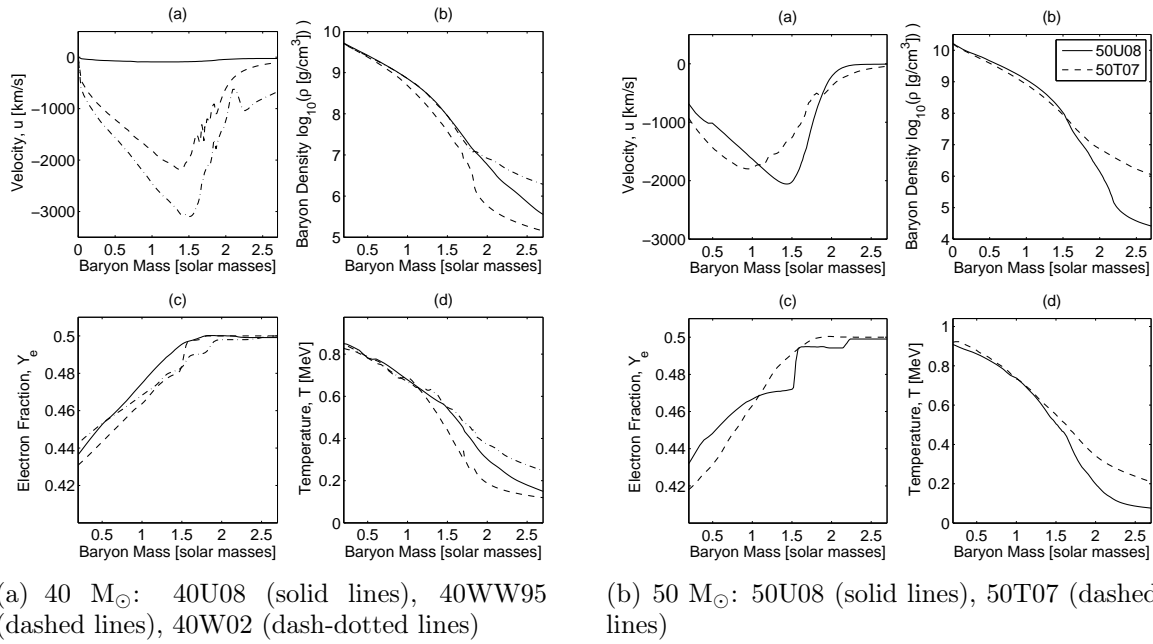
Figure 3.27: Selected hydrodynamic variables for the different progenitor models under investigation at the final stage of stellar evolution, evolved until the same central densities are reached.

(a) 40 M$_\odot$: 40U08 (solid lines), 40WW95 (dashed lines), 40W02 (dash-dotted lines)

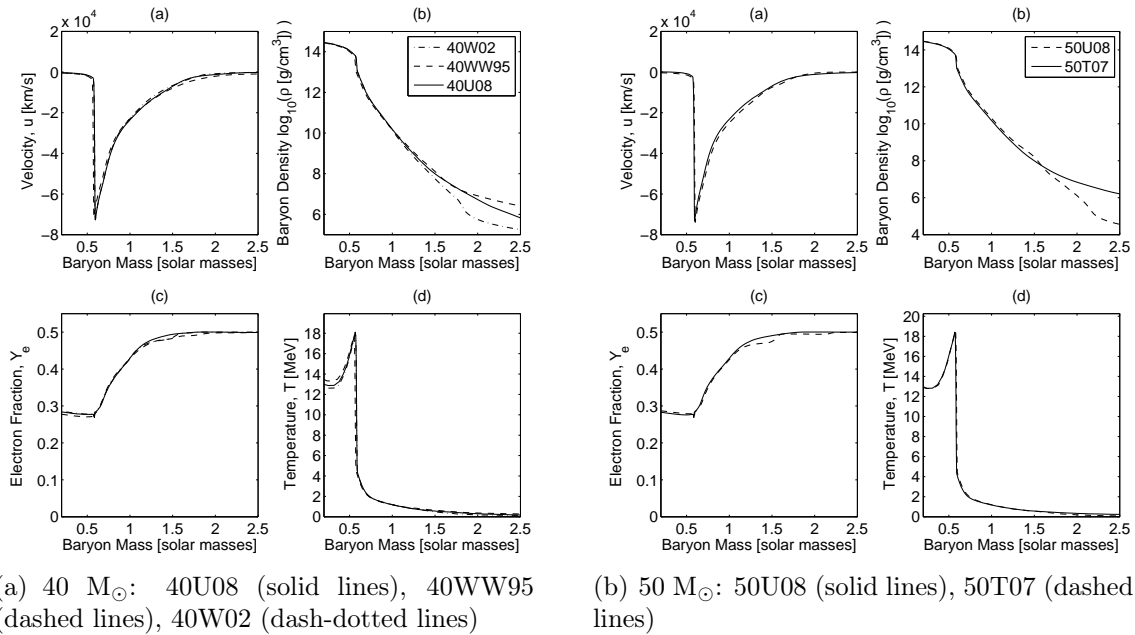(b) 50 M$_\odot$: 50U08 (solid lines), 50T07 (dashed lines)

Figure 3.28: Selected hydrodynamic variables for the different progenitor models under investigation at core bounce.

the progenitor structure. The latter has a direct impact on the mass accretion rate at the neutrinosphere and hence on the electron-neutrino spectra. We find that the structure of the progenitor has a non-negligible influence on the emitted neutrino spectra. This is in contradiction to Sumiyoshi et al. (2008), who attribute differences in the emitted neutrino emission mainly to the properties of the EoS. This is due to their selective choice of progenitor models, which all have large accretion rates producing thermal electron-neutrino spectra. However, for models that have been used in both studies, e.g. 40WW95 and 50T07, the results are qualitatively similar.

3.2.4 The (μ/τ)-neutrino signal

In the following, the analysis of Liebendörfer et al. (2004) is extended, who investigated the drastic (μ, τ)-(anti)neutrino luminosity increase during the late PNS accretion phase of failed core collapse supernova explosions of massive progenitors.

The evolution of the neutrino luminosities depends on the production rates and the diffusion timescale, which in turn depend on the assumed matter conditions. These conditions and the production rates for all neutrino flavours are plotted in Fig. 3.29 for a core collapse simulation of a 40 M$_\odot$ progenitor model applying the full set of pair, i.e. electron-positron annihilation, $N - N$-Bremsstrahlung and the annihilation of trapped electron-flavour neutrino pairs. In order to separate the different regimes, we plot all quantities with respect to the baryon density. Note, that the electron-(anti)neutrinospheres are at lower densities than the (μ/τ)-neutrinospheres, since the latter do not interact via charged current reactions.

Most (μ, τ)-(anti)neutrino pairs are produced at $\rho \simeq 10^{13}$ g/cm^3. This finding remains rather constant during the late accretion phase, because the matter temperature T and the electron fraction Y_e do not change at that density, as can be seen in Fig. 3.29 (e) and (f). In contrast, at the (μ/τ)-neutrinosphere ($\rho \simeq 10^{11}$ g/cm^3) we find a drastic increase in temperature and Y_e. Due to the continuous contraction of the PNS, the electron-degeneracy reduces which favours more electron-positron-pairs. These thermalised electron-positron-pairs increase the (μ/τ)-neutrino pair reaction rates in graph (d) via electron-positron annihilation), which increases the (μ/τ)-(anti)neutrino luminosity contribution from lower densities. In addition, the diffusion time scale of the (μ/τ)-neutrinos is reduced during the PNS contraction. The corresponding optical depths (at 300 km distance) are shown in graph (c).

3.2.5 Improvements of the neutrino opacities

Finally, we will investigate corrections of the standard neutrino opacities (Bruenn (1985)), following the suggestions by Horowitz (2002) regarding the effect of weak magnetism, nucleon recoil and corrections for the strangeness of nucleons, as already briefly explored in Liebendörfer et al. (2003) using a 15 M$_\odot$ progenitor model. We will illus-

trate the effects using the example of a failed supernova explosion of a 40 $M_\odot$ progenitor model from Umeda and Nomoto (2008) during the post-bounce evolution.

The separate consideration of weak magnetism is a higher order extension of the zeroth order scattering cross section, which reduces the antineutrino and increases the neutrino cross sections. On the other hand, recoil reduces both neutrino- and antineutrino cross sections, as discussed in Horowitz (2002). The total modified cross section for the electronic charged current reactions

$$\nu_e + n \rightarrow p + e^-,$$

$$\bar{\nu}_e + p \rightarrow n + e^+,$$

can be written as

$$\sigma = \sigma_0\, R(E),$$

with zeroth order cross section σ_0. R depends on the neutrino energy E. For average neutrino energies, $R \simeq 1$ for the electron-neutrinos, and $R < 1$ for the electron-antineutrinos. As discussed in Horowitz (2002), this effect reduces the electron-antineutrino opacity from regions inside the neutrinosphere, as illustrated in Fig. 3.30 resulting in a larger electron-antineutrino luminosity in graph (a) and larger mean neutrino energies in graph (b). The electron-neutrino luminosity and mean neutrino energies remain almost unaffected. This phenomenon becomes important during the PNS accretion phase, as the matter density rises and more neutrinos are found at higher energies, where the higher order corrections become significant. The electron-antineutrino luminosity rises above the electron neutrino luminosity, here after 400 ms post-bounce, as the PNS contraction reaches a certain level of compactness.

The correction from the strange quark contributions are taken into account by a modified axial-vector coupling constant, for (anti)neutrino-nucleon scattering

$$\nu + N \rightarrow \nu + N.$$

The larger electron-antineutrino cooling rates inside the neutrinosphere result in a more compact PNS supporting higher matter temperatures, compared to core collapse simulations of the same progenitor model with otherwise identical input physics. The largest differences are found at the (μ/τ)-neutrinosphere, while the contribution from lower matter densities remains unaffected. The higher matter temperatures are directly reflected in larger neutrino-pair reaction rates at regions near the (μ/τ)-neutrinosphere, while the contribution from high matter density at $\rho \sim 10^{13}$ g/cm^3 remains constant. The larger (μ/τ)-neutrino pair reaction rate increases the (μ/τ)-neutrino luminosity from regions with intermediate matter density $\rho \sim 10^{11} - 10^{12}$ g/cm^3. This increases the effect of cooling, which supports a more compact PNS. The more rapidly contracting PNS at the centre consequently leads to a shorter PNS accretion time, before becoming gravitationally unstable and collapsing to a black hole. For the model considered here, the difference is $\simeq 20$ ms as can be seen in Fig. 3.30.
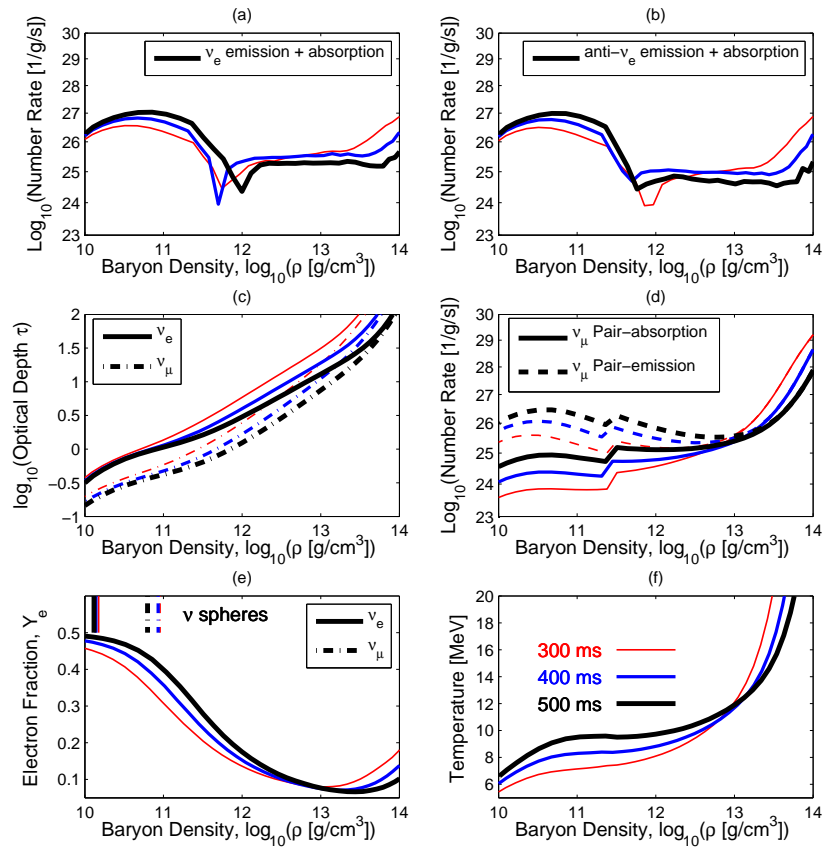
Figure 3.29: Different post-bounce snap shots (thin red lines: 300 ms intermediate blue lines: 400 ms thick black lines: 500 ms), illustrating the effects of the PNS contraction to the number fluxes, the optical depths τ, the matter temperature and the electron fraction Y_e.
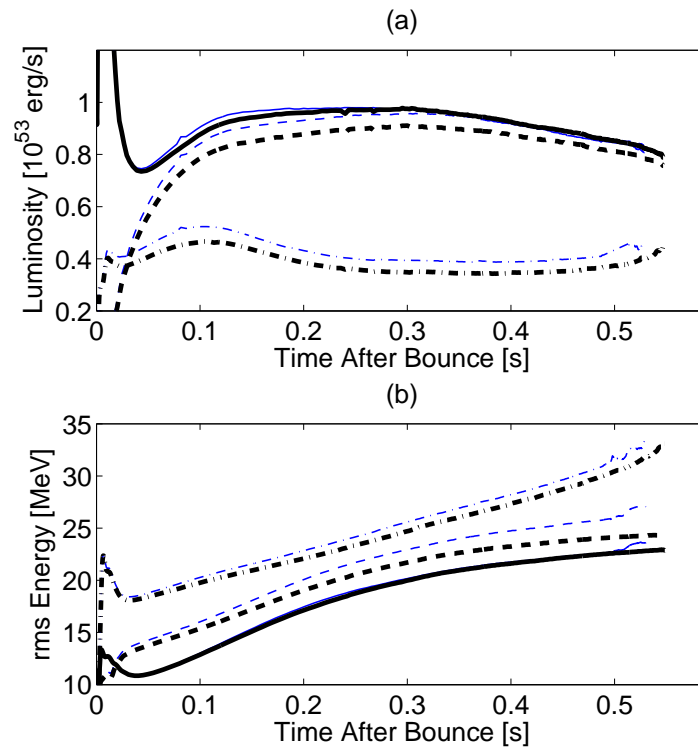
Figure 3.30: Comparing the standard neutrino opacities (thick black lines) (see Bruenn (1985)) with the corrections (thin blue lines) given in Horowitz (2002), plotting the neutrino luminosities and the mean neutrino energies as a function of time after bounce, for all three neutrino flavours (solid line: ν_e, dashed: $\bar{\nu}_e$, dash-dotted: μ/τ-neutrinos) at 500 km distance.

3.3 The quark-hadron phase transition in core collapse supernovae

After the deleptonisation burst has been launched $10 - 20$ ms post bounce and the bounce shock has turned into the SAS, the post bounce evolution of massive progenitor stars is determined by mass accretion on timescales of 100 ms. The mass accretion rate is given by the progenitor model and the consequent PNS contraction behaviour depends on the EoS for hot and dense nuclear matter, during which the central density and temperature increase continuously. The post bounce PNS evolution is illustrated in Fig. 3.37 for the 10.8 $M_\odot$ model from Woosley et al. (2002) and in Fig. 3.32 for the 40 $M_\odot$ model from Woosley and Weaver (1995). The figures show selected properties of mass shells between 0.1 and 1.5 $M_\odot$ from the innermost PNS domain. The graphs (a) show the infalling material before bounce and the post bounce contraction at the centre, during which the temperature in the graphs (b) increases above 10 MeV and the density in the graphs (c) increase above nuclear saturation density ρ_0 (vertical dashed line). On the timescale of 100 ms, the two progenitor models evolve very similar. For the more massive 40 $M_\odot$ progenitor, the post bounce temperatures are slightly higher and reach 20 MeV at the centre (in comparison to 15 MeV for the 10.8 $M_\odot$ progenitor) as well as slightly higher central densities, up to $5 \times \rho_0$ (in comparison to $1.5 \times \rho_0$ for the 10.8 $M_\odot$ progenitor). Furthermore, matter at the central part of the PNSs is high iso-spin asymmetric. The proton-to-baryon ratio (give by the electron fraction Y_e obtained at core bounce even reduces to $Y_e \simeq 0.25$. Matter at such conditions inside PNS interiors is treated in core collapse supernova simulations as normal nuclear matter. However, one may ask on the validity of this description at densities above nuclear saturation and temperatures of tens of MeV. At such conditions, the transition from hadronic matter to quark matter might occur. For that reason, we apply a quark matter EoS based on the well known and widely applied MIT bag model (see §2.7.3) to simulations of low and intermediate mass Fe-core progenitors.

The first attempt investigating the quark-hadron phase transition in simulations of massive stars goes back to Takahara and Sato (1988). They try to find a relation between the appearance of quark matter and the multi-peaked neutrino signal from SN1987a (see e.g. Hirata et al. (1988), Bionta et al. (1987)), applying general relativistic hydrodynamics in spherical symmetry and a parametrised EoS. More sophisticated input physics was applied to the investigation of Gentile et al. (1993). They applied general relativistic hydrodynamics and a description of deleptonisation during the Fe-core collapse as well as a sophisticated EoS for both hadronic and quark phases. The transition between these two phases was constructed via a co-existence region, i.e. the quark-hadron mixed phase. They found a significant softening of the EoS in the mixed phase as well as the formation of an additional shock wave which appeared due to the quark-hadron phase transition. The additional shock follows and finally mergers
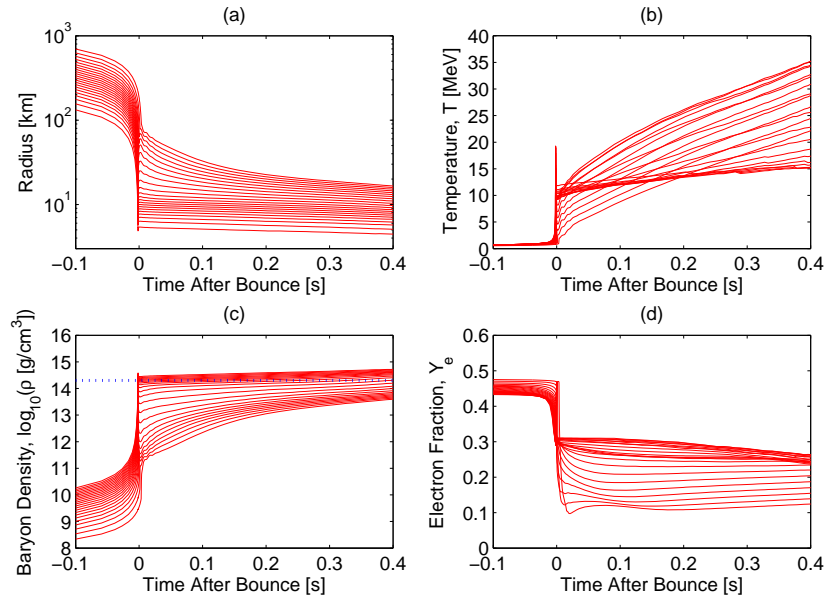
Figure 3.31: PNS evolution of selected mass elements between 0.1 to 1.15 $M_\odot$ for the low mass 10 $M_\odot$ Fe-core progenitor model. The dashed line in the graphs (c) illustrates nuclear saturation density.
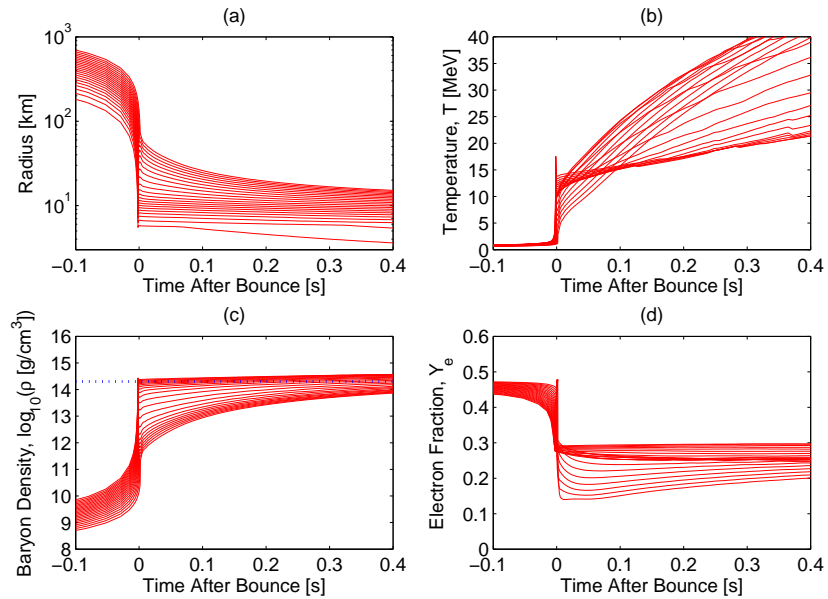

Figure 3.32: The same configuration as Fig. 3.37 but for the massive 40 $M_\odot$ progenitor model.

with Fe-core bounce shock, shortly after its appearance. Both studies could not make predictions of possible features in the neutrino signal emitted due to the lack of neutrino transport post bounce. Simulations of the QCD phase transition of extremely massive 100 $M_\odot$ Fe-core progenitors have recently been studied by Nakazato et al. (2008). Their core collapse model is based on general relativistic three-flavour Boltzmann neutrino radiation hydrodynamics in spherical symmetry and employs the sophisticated EoS from Shen et al. (1998a) for hadronic matter. They applied the MIT bag model with a large bag constant and hence a high critical density. The transition from hadronic matter to free quarks was modelled via an extended mixed phase applying a Gibbs conditions. They confirmed a significant softening of the EoS in the mixed phase due to the reduced adiabatic index. They could also not conclude to the neutrino signal emitted due to the immediate formation of a black hole during the phase transition.

In the following subsections, results from core collapse simulations will be presented where the quark-hadron phase transition takes place during the early post bounce evolution. The EoS applied is based on the hadronic model from Shen et al. (1998a), which was extended by a quark EoS for strange quark matter developed by Sagert et al. (2009a) based on the MIT bag model (see §2.3.7) at high densities and temperatures. The resulting EoS table contains contributions from hadrons and quarks. The phase transition is constructed applying Gibbs conditions, which results in an extended mixed phase. The conditions (i.e. T, Y_e, ρ_c) for the phase transition, i.e. the critical points in the phase diagram (in other words the critical density which depends on the temperature and the electron fraction), are already introduced in §2.3.7 and depend on the bag constant. In order to agree with data from heavy ion collision (HIC) experiments [3] and neutron star mass measurements [4], we chose the two values $B^{1/4} = 162$ and 165 MeV for the bag constants which provide neutron stars with maximum stable masses of 1.56 and 1.50 $M_\odot$ of baryon mass for the two bag constants $B^{1/4} = 162$ and 165 MeV respectively. These two values result in critical densities of the order ρ_0 (see the phase diagrams in §.2.3.7 Fig. 2.7), which is not in contradiction with HIC data due to the high iso-spin asymmetry in core collapse supernova matter.

First, the dynamical evolution of the PNS during the QCD phase transition will be discussed. The PNSs are modelled as central object in core collapse supernova simulations of low and intermediate mass progenitors in spherical symmetry where no explosions could be obtained. Below, the consequences of the QCD phase transition and the possible observation in the neutrino signal emitted will be illustrated. The very first results of this investigation based on core collapse supernova simulations of 10.8 and 15 $M_\odot$ progenitor models are already published in Sagert et al. (2009b).

---

[3]HIC matter is more or less iso-spin symmetric with $Y_e \simeq 0.5$ and considered of only up- and down-quarks, which results in a high critical density typically $\rho_c > 2 \times \rho_o$. Hence, HIC matter differs from form supernova matter and the critical density reduces significantly for the latter case discussed here.

[4]At present, the most precise neutron star mass measurement, Hulse-Taylor pulsar with 1.44 $M_\odot$

3.3.1   The dynamics of the phase transition

The simulations are launched from low and intermediate mass Fe-core progenitors of 10, 13 and 15 $M_\odot$, using models from the series of Woosley et al. (2002) which we evolve through the Fe-core collapse, bounce and early post-bounce phases. Without the enhanced neutrino heating as discussed in §3.1, such progenitor stars will not explode during the post-bounce evolution and the PNSs will contract on a timescale of 100 ms.

Remark 18 *The conditions for the appearance of quark matter are monitored by the quark volume fraction X_Q as follows*

$$
\begin{aligned}
Hadronic\ phase &\rightarrow& X_Q = 0, \\
Mixed\ phase &\rightarrow& 0 < X_Q < 1, \\
Quark\ phase &\rightarrow& X_Q = 1.
\end{aligned}
$$

The appearance of strange quarks can be understood via flavour changes (exchange of $W^\pm$ bosons) and is justified since β-equilibrium conditions are fulfilled

$$ u + d \leftrightarrow u + s. $$

The two values chosen of the bag constant already produce $X_Q > 0$ for the conditions obtained at core bounce. However, X_Q stays small ($< 10\%$) and reduces again due to the density decrease during the shock expansion shortly after bounce. It only increases again as the PNS starts to contract.

Fig. 2.8 illustrates the final baryon EoS (hadrons and quarks) with respect to the baryon density. For matter elements that reach the mixed phase during the PNS contraction, the adiabatic index (i.e. the pressure gradient) reduces. This softens the EoS and higher densities are favoured in comparison to the pure hadronic EoS. In addition to the softening of the baryon EoS for matter in the mixed phase, the higher densities and temperatures result in a different electron degeneracy. β-equilibrium is established at a lower value of the electron fraction during the post-bounce accretion phase, in comparison to simulations where the pure hadronic EoS was used. In this sense, also the electron pressure reduces for matter in the mixed phase during the post-bounce accretion phase. However, the timescale for this softening of the EoS during the post-bounce accretion phase is correlated with the density and temperature increase of the PNS due to mass accretion (given by the progenitor model) and hence of th order 100 ms. Only when a certain fraction of the PNS is in the mixed phase where $X_Q > 0.5$ ($\sim 0.2\ M_\odot$) during the PNS contraction, the reduced adiabatic index causes matter in the mixed phase to contract. This is illustrated in Fig. 3.33, graphs (a) where the quark fraction in the graphs (d) increases and the PNS starts to contract (middle panel). The
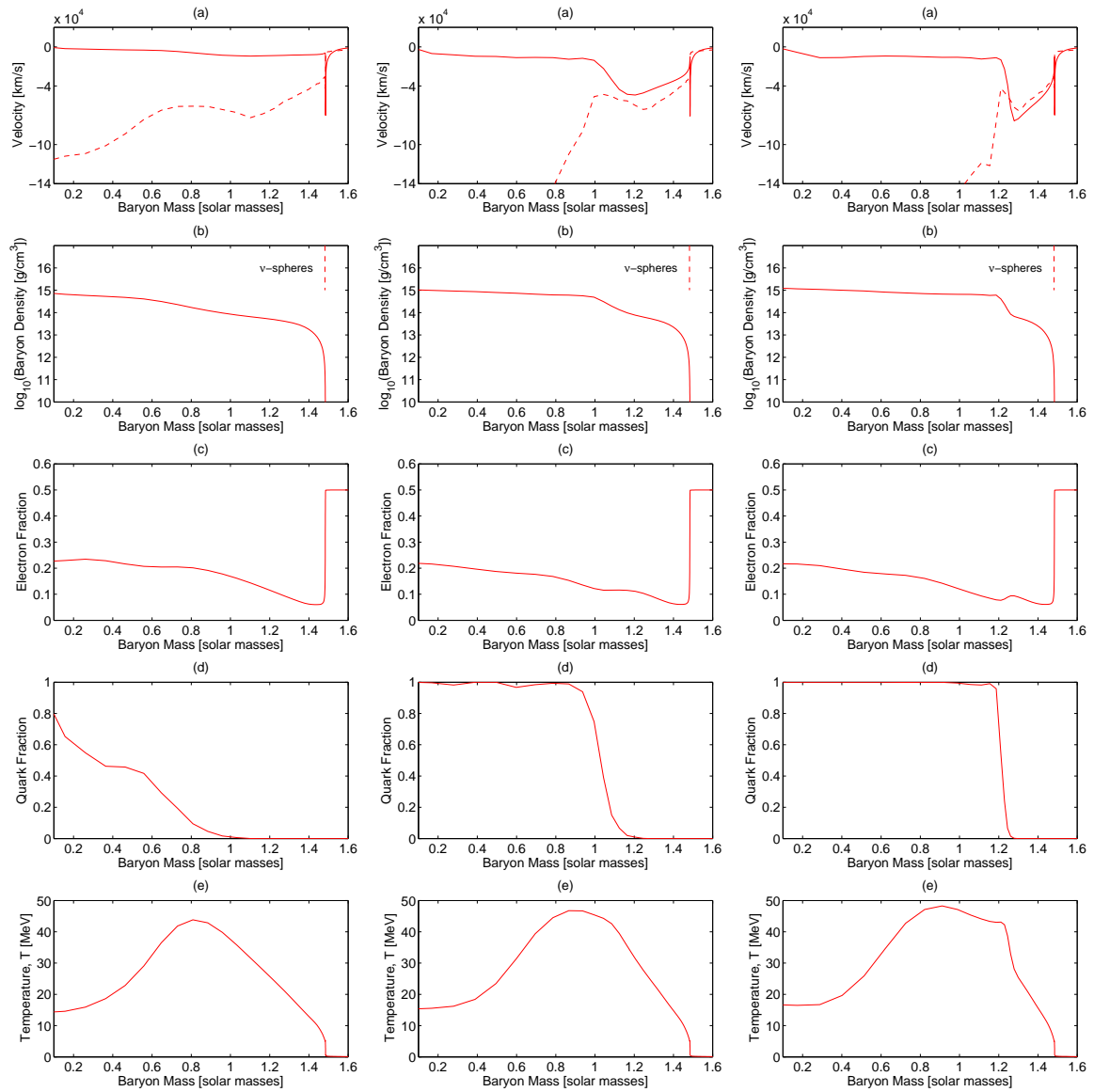
Figure 3.33: PNS collapse during the QCD phase transition due to the reduced adiabatic index in the mixed phase.

contraction proceeds into an adiabatic collapse with supersonic infall velocities (right panel) as more and more matter is converted into the mixed phase. The increased densities in the graphs (b) and temperatures in the graphs (d) cause β-equilibrium to be established at a lower value of the central electron fraction, from initially $Y_e \simeq 0.25$ to 0.2. However, the additionally emitted neutrinos can not escape because the matter conditions are such that neutrinos are fully trapped. The collapse only halts as matter that has gone through the mixed phase during the PNS collapse and reach the pure quark phase, where the adiabatic index increases again (see Fig. 2.8). In other words, the EoS stiffens for matter in the pure quark phase. Consequently, a stagnation wave forms at the boundary between the pure hadronic and quark phases. It propagates outwards and turns into a shock front at the sonic point. This additional accretion shock is standing at the phase boundary between the soft mixed phase and the stiff pure quark phase, while the first SAS remains unaffected from the happenings inside the PNS at about 100 km. The timescale is reduced from 100 ms during the post bounce accretion (PNS contraction) to milliseconds, similar to the discussion of black hole formation via PNS collapse in §3.2. The accretion shock inside the PNS will be referred to as *quark shock* in the following, in order to distinguish both shocks inside the simulated domain.

The subsequent evolution of the quark shock is determined by the dissociation of infalling nucleons into up-, down- and strange quarks, which in turn is given by the balance between ram pressure ahead of the quark shock and thermal pressure from the appearance of free quarks behind the quark shock. For all situations studied, i.e. the two choices of the bag constant and progenitor models of 10, 13 and 15 $M_\odot$, the thermal pressure behind the quark shock dominates and causes the quark shock to expand slowly (see Fig.3.34 graph (a) left panel). The presence of the quark shock (i.e. matter is shock heated) reduces the electron degeneracy and β-equilibrium changes to a larger value of the electron fraction, as can be seen in Fig.3.34 graph (c) left panel. As soon as the expanding quark shock reaches the steep density gradient between the mixed and the pure hadronic phase, the quark shock detaches from the mixed phase and turns into a dynamic shock with positive matter outflow (Fig.3.34 graph (a) and (d) middle panel). In this expanding regime, the central density and temperature reduce slightly (see Fig.3.34 graph (b) and (c) middle panel). On the other hand, the temperature of the shock heated hadronic material increases from 8 MeV to 25 MeV. This reduces the electron degeneracy and β-equilibrium establishes at an even higher value of the electron fraction, i.e. from $Y_e = 0.1$ to $Y_e = 0.3$ (compare Fig.3.34 graphs (c) and (e) middle and right panels). The situation differs from the early shock propagation after the Fe-core bounce where heavy nuclei are dissociated into light nuclei and nucleons. The matter falling onto the quark shock is already fully dissociated and composed of free nucleons only. The impact of the additional shock heating are higher Fermi-levels of the nucleons that are occupied. There are no energy losses due to dissociation processes. Even further, an additional difference to the situation after core bounce is the much steeper density gradient at the PNS surface which allows for a significantly
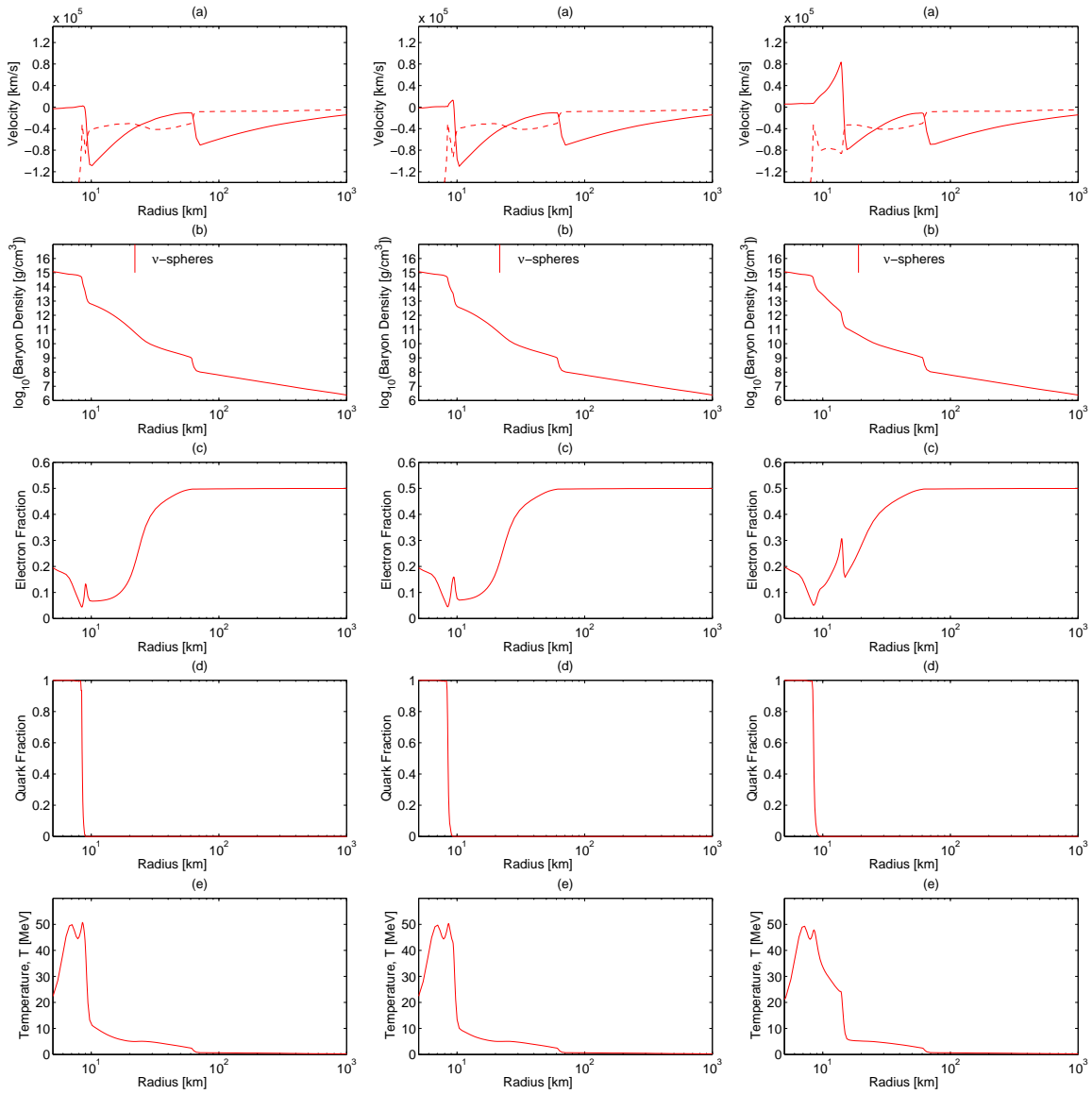
Figure 3.34: Early post quark evolution of the PNS, determined by the quark shock propagation and acceleration.

larger acceleration of the quark shock. The expanding and dynamic quark shock takes over the SAS (that can be found at $\simeq$ 70 km) (see Fig. 3.35), after which the density gradient decrease is less intense and the shock expansion slows down.

Remark 19 *The matter outflow reaches velocities at its maximum of about 1.5×10^5 km/s, which is 50% the vacuum speed of light. At such high matter velocities, kinetic relativistic effects become important and must be taken into account for both fluid dynamics and radiation transport.*

After the quark shock has taken over the SAS, an explosion can be obtained. Additionally, a region of neutrino cooling develops between the expanding (now) explosion shock and the PNS surface at the centre. There, matter outflow stagnates and proceeds into infall. This infalling matter develops into a standing accretion shock on top of the PNS surface on a timescale of 100 ms while the explosion shock continues to expand to large radii (see Fig. 3.35 dashed line). The obtained explosion energies and PNS masses are illustrated in Table 3.3 for all models under investigation. The post bounce time t_{pb} is chosen at the quark-hadron phase transitions induced PNS collapse. The PNS masses are given in baryon mass. Please note that the simulations are not carried out long enough for several models to finally estimate the explosion energy and PNS masses conclusively. In other words, the explosion energies and PNS masses might change slightly if evaluated at some later post bounce times.

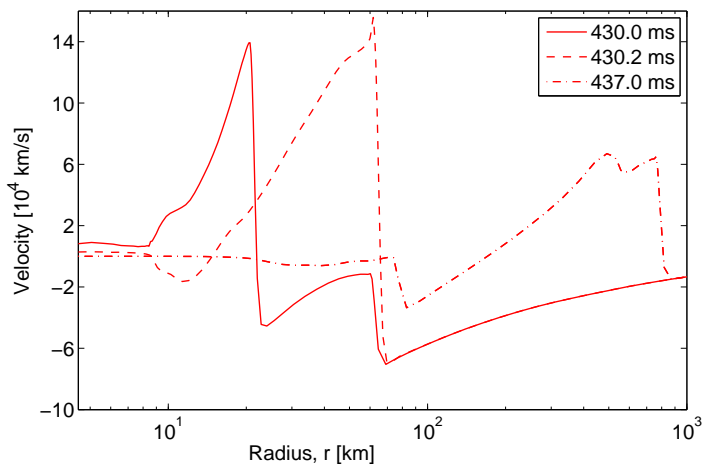Figure 3.35: Velocity profiles during the explosion phase at three different times post-bounce.

A special case is the 15 M$_\odot$ progenitor model using the quark EoS based on the large bag constant $B^{1/4} = 165$ MeV. The PNS exceeds the maximum stable mass given by the quark EoS. Consequently and similar to the study by Nakazato et al. (2008), the PNS collapse due to the softening of the EoS for matter in the mixed phase can

Prog. [$M_\odot$]	bag constant [MeV]	t_{pb} [ms]	M_{PNS} [$M_\odot$]	E_{expl} [10^{51} erg]	ρ_{c} [10^{14} g/cm^3]	T_{c} [MeV]	Y_e
10.8	162	248	1.434	0.361	7.364	13.561	0.225
10.8	165	429	1.482	1.080	7.688	14.214	0.225
13	162	241	1.467	0.146	8.525	13.666	0.221
13	165	431	1.498	0.323	8.346	14.121	0.221
15	162	209	1.608	0.420	8.166	14.433	0.223
15	165	330[5]	1.700	unknown[6]	8.437	13.966	0.217

Table 3.3: Selected properties of the PNSs for the different models under investigation.

not be halted again sufficiently due to the stiffening for matter at higher densities in the pure quark phase. The collapse proceeds into the formation of a black hole after the QCD phase transition when the quark shock has already formed. Nevertheless, the simulations could be carried out for long enough to turn the quark shock into a dynamic shock. Due to our co-moving coordinate choice, the lapse function approaches zero and no (stable) solutions for the equations of energy and momentum conservation could be obtained. However, an explosion can not be excluded for this model. The time t_{pb} in Table 3.3 for this model determines the time of black hole formation and the PNS mass is the enclosed baryon mass before the formation of the apparent horizon.

3.3.2 The neutrino signal from the QCD phase transition

The dynamical aspects from the quark-hadron phase transition discussed and illustrated above are interesting but relay strongly on the quark model and the description of the transition between the hadronic and quark phases. In other words, since the EoS at such conditions is uncertain the predictions from phenomenological calculations are highly speculative. On the other hand, if it was possible to reduce the QCD phase transition and the dynamical features observed to observables that could possible be detectable, one could use these observations to constrain the nuclear physics input and the EoS. Most interesting uncertainties are the thermodynamic conditions, i.e. the temperature and asymmetry dependent critical density, for the onset of the phase transition. For the range of parameters applied to the present study, a strong phase transition is predicted. In such a scenario, the critical conditions correspond to the formation of the quark shock inside the PNS. These conditions are reached via the PNS contraction which in turn is given by the mass accretion rate (i.e. the progenitor model) and the compressibility of nuclear matter (hadronic EoS). Although the latter is uncertain, the density and temperature increase (as well as the Y_e decrease) can be approximated for a given progenitor model with respect to time after bounce. Furthermore, the additional shock heating of the previously dissociated matter due to the quark shock propagation causes

Y_e to increase (as discussed above) due to the lifted degeneracy. As soon as the quark shock propagates crosses over the neutrinospheres, the additionally emitted neutrinos can escape, which cause a second burst of neutrinos (see Fig. 3.36). This burst is dominated by electron-antineutrinos that are emitted via positron captures which are favoured in the shock heated neutron-rich environment. If such a second neutrino burst will be confirmed by observations of a future Galactic event from ground based neutrino detector facilities, its delay after the first deleptonisation burst provides correlated information about the progenitor model, the hadronic EoS and the thermodynamic state for the quark phase transition. In other words, for a given progenitor model and an assumed PNS contraction behaviour, the conditions for the quark-hadron phase transition can be extracted from the neutrino signal emitted. In order to illustrate this argument, Fig. 3.36 shows the neutrino signal for the 10.8 $M_\odot$ progenitor model using the two quark EoS. The model using $B^{1/4} = 162$ MeV (left panel) corresponds to the early onset of the phase transition (i.e. the low critical density and low temperature) and hence the second neutrino burst (in other words the quark-hadron phase transition) occurs already at about 248 ms post-bounce. For the model using $B^{1/4} = 162$ MeV (right panel), the phase transition is delayed to about 429 ms post-bounce due to the higher density and temperature required for the quark-hadron phase transition. The central conditions (ρ_c, T_c, Y_e) for all models are listed in Table 3.3. This is a powerful way of reprocessing constraints on nuclear physics from astronomical observations using astrophysical models. Unfortunately, the only observed neutrino signal from a core collapse supernova explosion, i.e. SN1987a (see Hirata et al. (1988)), did provide only very few (namely 12) events and does allow therefore only poor statistics.

The post quark oscillation of the neutrino signal is due to the formation of the additional accretion shock on top of the PNS surface due to neutrino cooling. This shock is oscillating, i.e. expanding via neutrino heating and descending due to cooling. This behaviour is reflected in the neutrino signal since the dominant source for the neutrinos is the mass accretion (as discussed in §3.2.2). The significant increase in the mean neutrino energies, especially for the μ/τ-neutrinos (see Fig. 3.36 (c)), is due to the quark shock expansion of the shock heated material over the position of 500 km where the neutrino observables are measured in a co-moving reference frame. After the quark shock (and hence the ejecta) have passed the radius of 500 km, the mean energies return to the pre-quark values on a timescale of 100 ms except for the decay (luminosities and mean energies) which is due to the explosion obtained.

3.3.3   Relevance for nucleosynthesis investigations

If the assumption holds true that quark matter can be found in compact stars, it is natural to investigate all possible phases. On its evolution from a massive star on the main sequence between 9 - 75 $M_\odot$ to an isolated neutron star, quark matter can appear. Since nuclear physic models rely on mostly phenomenological attempts to
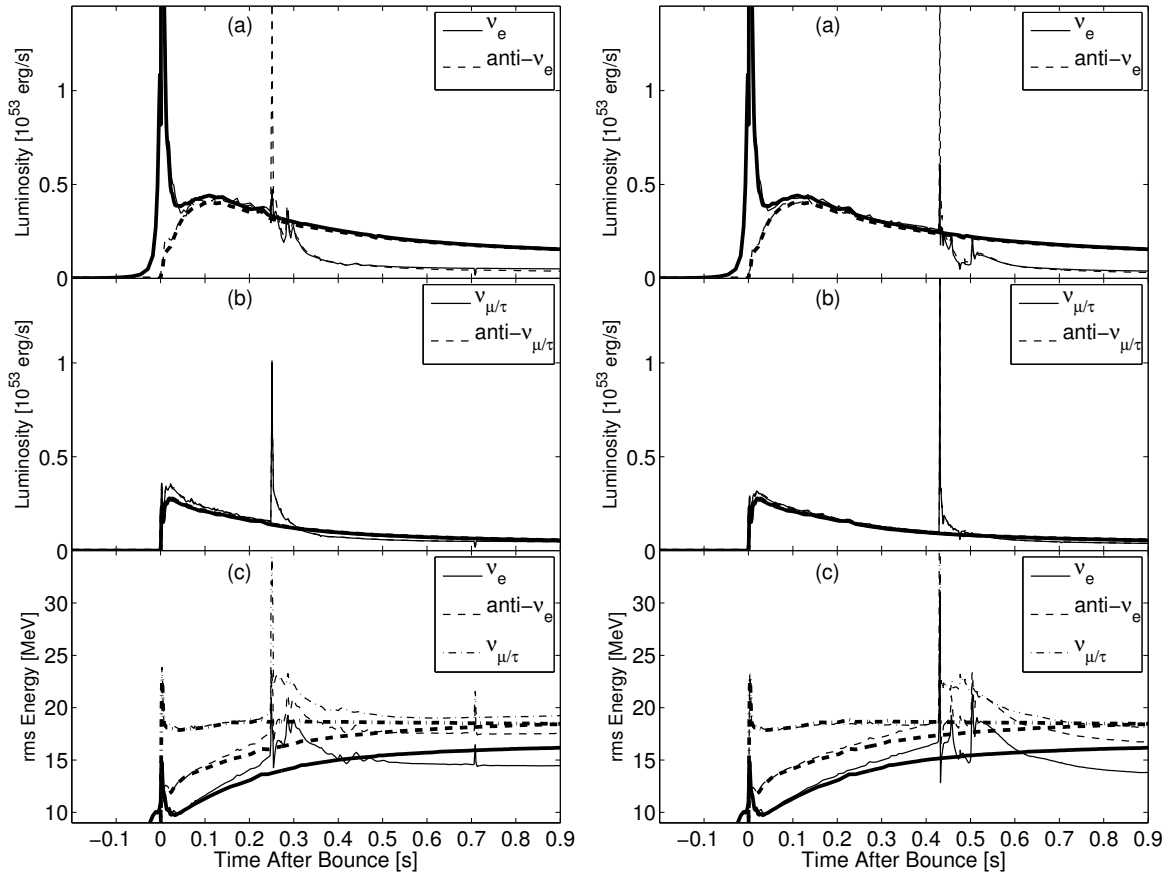
Figure 3.36: Neutrino luminosities and mean neutrino energies taken in a co-moving reference frame at 500 km, comparing the quark EoSs (thin lines) with $B^{1/4} = 162$ MeV (left panel) and $B^{1/4} = 165$ MeV (right panel) with the pure hadronic EoS (thick lines) for the 10.8 M$_\odot$ progenitor model.

answer the question about the conditions for the quark-hadron phase transition, the wide parameter range used in such models can be explored to investigate the appearance of quark matter in astrophysical scenarios. A comparison with observations is required to favour one set of parameters over the other. It can thereby not only be due to the neutrino signal. Other observables are for example

1. The gravitational waves emitted from the quark-hadron phase transition,

2. The consequent nucleosynthesis of the ejecta due to the presence,

3. Explosion energies and the kinetics of the ejecta,

4. Remnant properties, such as the maximum stable mass and the possible kick velocity.

Picking one of these additional aspects(evidences) for the appearance of quark matter and the subsequent hydrodynamic evolution discussed above, the nucleosynthesis of the ejecta is a very powerful indication to exclude or confirm particular aspects.

The main focus of nucleosynthesis investigations, which are done via post processing of ejected mass elements, is to explain the abundances observed. In order to illustrate thermodynamic properties of selected mass elements that will be ejected, Fig. 3.37 shows results from the 10.8 $M_\odot$ progenitor model that has gone through the quark-hadron phase transition as discussed above. Notice the low electron fraction of the innermost ejecta where $Y_e \simeq 0.4$ in graph (d). This was a first strong evidence for the possibility of the r-process, which takes place during the expansion below temperatures where the charged particle reactions freeze out typically below 0.5 MeV. (for the post bounce time, see the temperature trajectories in graph (b)). However, the low entropies in graph (e) of $s \simeq 28 - 40$ k_B/baryon indicate the low entropy r-process. These speculations have to be confirmed via full r-processes nucleosynthesis calculations, taking effects of the short timescale into account.

After about 1.5 s post bounce the second post quark accretion shock on top of the PNS surface is revived via the continuous neutrino energy deposition, after which the neutrino driven wind appears in the same manner as introduced and discussed above in §3.1. Material on top of the PNS is accelerated in the wind where it becomes proton-rich and mixes with the neutron-rich ejecta of the explosion shock. This increases the electron fraction and the entropies per baryon of the innermost ejecta. The formation of the neutrino driven wind can be identified at the slight density and temperature increase in the graphs (c) and (b) respectively after about 2 s post-bounce. The strong increase in entropy after about 4 s post-bounce in graph (e) is due to the formation of the reverse shock. Unfortunately the simulation setup was not ideally suited for the neutrino driven wind evolution, especially the formation of the reverse shock and the simulations are not carried out much further. Long story short, the appearance of the neutrino driven wind might lead to a less successful r-process scenario in the context of the quark-hadronic phase transition induced explosion mechanism. Alternative scenarios should be explored, e.g. first a neutrino driven explosion where matter becomes proton-rich at high entropies per baryon followed by the quark-hadron phase transition during or after the neutrino driven wind phase.
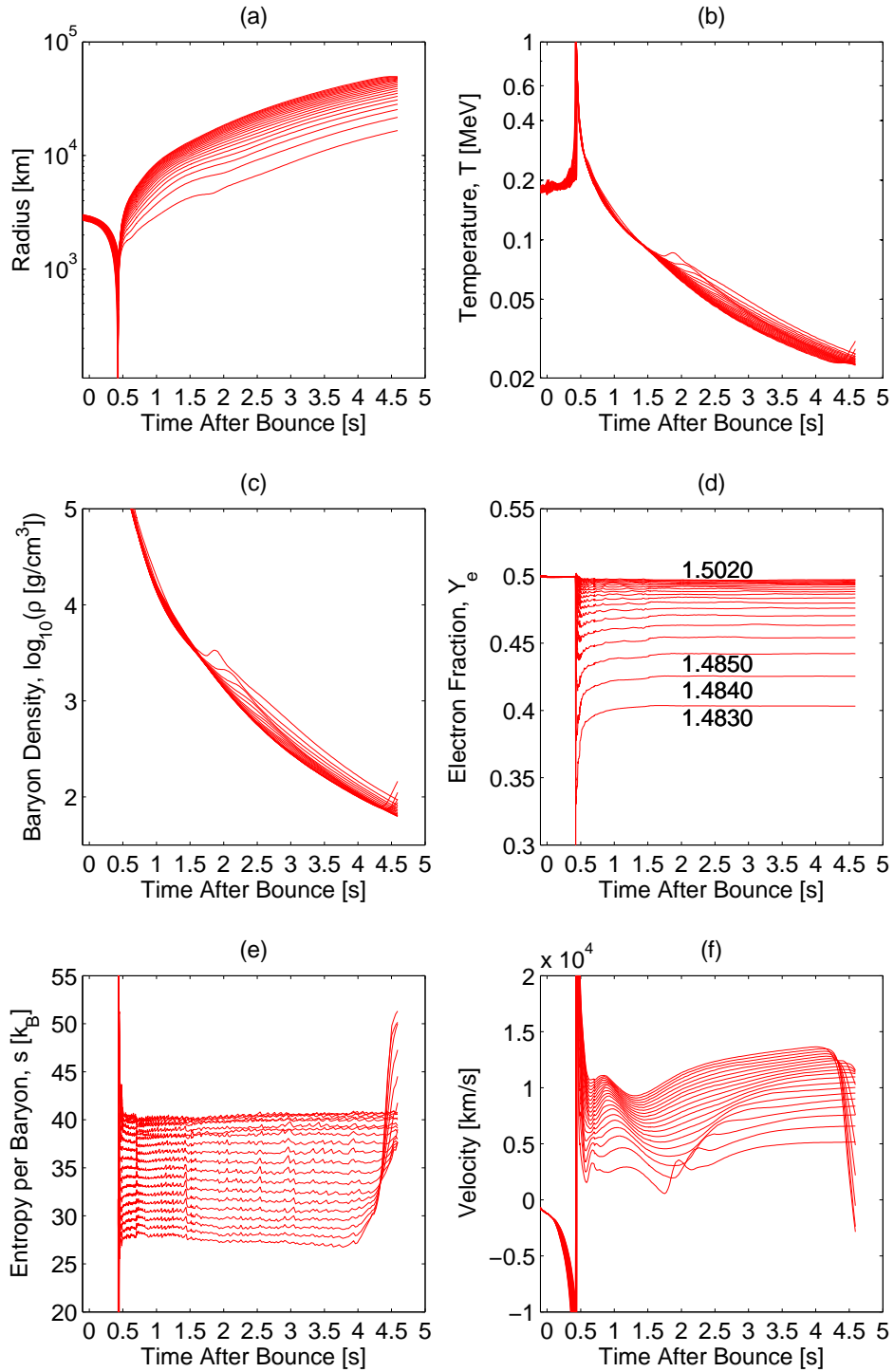
Figure 3.37: Thermodynamic properties of selected mass shells from 1.4830 to 1.5020 $M_\odot$ with respect to time after bounce of the 10.8 $M_\odot$ progenitor model using the quark EoS based on $B^{1/4} = 165$ MeV. The peaked behaviour at $t = 429$ ms after bounce corresponds to the quark-hadron phase transition and the formation of the quark shock.

Chapter 4

Summary

One of the most important topics in astrophysics is the origin of heavy elements, next to the origin and character of dark energy and dark matter. The production of heavy elements in astrophysical processes can be understood from nucleosynthesis considerations which are based the theory of weak and strong interactions. Such nucleosynthesis models simulate the evolution of a subset of elements of the nuclear chart based on thermodynamic trajectories, which in turn are given from simulations of astrophysical processes such as explosions of massive stars. The latter is known as supernovae (SNe) which can be divided into two subclasses: (a) Thermonuclear (SN Ia) and (b) core collapse (SN Ib, Ic, II). The explosion mechanism of SN Ia is understood to a large degree where the progenitor remains a mystery and is an active subject of research. On the other hand, the progenitor models for core collapse SNe are well known from stellar evolution calculations but the explosion mechanism is uncertain. Such stellar evolution calculations predict progenitors with high central densities and temperatures where a large fraction of Fe-group nuclei are produced at the end of stellar evolution, which causes the Fe-core to become gravitationally unstable and collapse. That is the origin of the classification *core collapse* SN, because all progenitor stars more massive than $\simeq 8$ $M_\odot$ suffer the same fate at the end of stellar evolution. The lower central temperatures obtained in stars less massive than 8 $M_\odot$ (such as our sun) leave a degenerate C-O white dwarf as remnant and heavy elements such as ^{56}Fe and ^{56}Ni cannot be produced in such low mass stars. Hence, core collapse supernovae of massive stars are investigated as one of the main sources for the production of the elements heavier than ^{56}Fe in the Universe.

The final composition of the ejecta of such SNe are obtained when the explosion reaches the stellar surface, where the theoretically predicted results from explosive nucleosynthesis calculations can be compared with observations. Of particular interest are the well known solar abundances. We explore the evolution of stellar cores of massive progenitor stars consistently in core collapse supernova simulations based on general relativistic neutrino radiation hydrodynamics. For the post processing nucleosynthesis

investigations, the dynamical evolution of the proton-to-baryon ratio, which is given by the electron fraction Y_e, is required. Since Y_e depends not only on the charged current reaction rates but also on the neutrino and antineutrino fluxes, accurate three flavour Boltzmann neutrino transport becomes essential at high densities where neutrinos can only diffuse as well as at intermediate densities where neutrinos transfer form the trapping to the free streaming regimes. Y_e determines which nuclear process are favoured over the other, e.g. neutron(proton) captures are favoured in a neutron(proton)-rich environment. Three-flavour Boltzmann neutrino transport is computationally very expensive and can only be applied in spherical symmetry where we use the numerical model AGILE-BOLTZTRAN. With this approach we can explore general relativistic effects, which become important in the presence of strong gravitational fields and relativistic matter velocities, and the input physics, such as neutrino reactions and the equation of state (EoS), to a high accuracy. This would be beyond the state-of-the-art of present multi-dimensional core collapse models due to the present computational limitations.

During the detailed studies of the past 4 years, I have began to develop a systematic understanding of the fate of massive stars and the importance and relevance of the involved microphysics. The results obtained are summarised in the following sections.

Neutrino driven explosions and the long term evolution of low and intermediate mass stars

For the first time, spherically symmetric core collapse supernova simulations based on general relativistic radiation hydrodynamics and three-flavour Boltzmann neutrino transport are performed consistently for more than 20 seconds. We follow the dynamical evolution of low and intermediate mass progenitors of 8.8, 10.8 and 18 $M_\odot$ through the collapse, bounce, postbounce, explosion and neutrino driven wind phases. The neutrino driven explosions of the 10.8 and 18 $M_\odot$ Fe-core progenitors are modelled by applying artificially enhanced opacities, while the explosion of the 8.8 $M_\odot$ O-Ne-Mg-core was obtained using the standard opacities. For all models under investigation, we confirmed the formation and illustrated the conditions required for the appearance of a neutrino driven wind during the dynamical evolution after the explosion has been launched.

A comparison with approximate and static steady-state as well as parametrized dynamic wind models leads to a discrepancy in the physical properties of the neutrino driven wind. Although the evolution of the hydrodynamic variables are in general agreement, we find smaller neutrino luminosities and a different behavior of the mean neutrino energies in comparison to steady-state and parametrised dynamic wind models. In particular, the differences between the neutrino and antineutrino luminosities and mean neutrino energies are smaller. These differences reduce with time as the PNS contracts on a much longer timescale and results in a generally proton-rich neutrino

driven wind for more than 10 seconds. Hence, the suggestion that the physical conditions found in the neutrino driven wind could be favourable for the r-process could not be confirmed.

The simulations are carried out until the neutrino driven wind settles down to a quasi-stationary state and the neutrino heating rates become negligible. We illustrate the disappearance of the neutrino driven wind and discuss the quasi-static PNS evolution, which corresponds to the initial and neutrino dominated PNS cooling phase. Unfortunately, important neutrino cooling processes are not yet taken into account but a smooth connection to isolated neutron or protoneutron star cooling studies comes into reach for future work (Henderson and Page (2007)).

This work has recently been submitted to the journal Astronomy & Astrophysics and is currently under revision, see Fischer et al. (2009b).

The evolution of massive stars and the formation of black holes

Additionally, we performed spherically symmetric core collapse simulations of massive progenitors. In the absence of an earlier explosion, the continuous mass accretion of material onto the central object, a protoneutron star (PNS), will eventually lead to the formation of a solar mass black hole, on timescales up to seconds for progenitors in the mass range of 40 to 50 $M_\odot$.

The neutrinos emitted during core collapse supernovae are, besides gravitational waves and nucleosynthesis yields, the only source of information leaving the stellar core. In addition, the available neutron star (NS) properties from observations provide information about the remnants of core collapse supernova explosions. However, gravitational waves are difficult to detect, nucleosynthesis calculations are model dependent and NS mass measurements provide information about the EoS of hot and dense nuclear matter. Hence, we believe that up to now neutrinos are the most promising source of information that gives a direct insight into the happenings inside the stellar interiors. The understanding of the emission, absorption and transport of neutrinos is essential for the accurate modeling of core collapse supernovae. Special focus is devoted to the cooling at the sphere of last scattering where neutrinos decouple from matter, the neutrino energy dependent neutrinospheres, and heating between the neutrinospheres and the expanding shock during the post-bounce evolution.

We confirm the results from Sumiyoshi et al. (2007), that a stiff EoS for hot and dense nuclear matter leads to an extended accretion phase of several seconds (as has been explored here at the example of a 40 $M_\odot$ progenitor model).

However, comparing progenitors of the same mass from different stellar evolution groups shows that a small mass accretion rate at the electron-neutrinosphere also leads to an extended accretion phase of several seconds. For the same progenitor mass but

different mass accretion rates at the electron-neutrinosphere, we even find a different electron-neutrino luminosity dependency. Models with large mass accretion are determined by a diffusion dominated electron-neutrino spectrum, while small mass accretion rates lead to accretion dominated spectra. Different EoSs of hot and dense nuclear matter are unable to change a diffusion dominated electron-neutrino spectrum into an accretion dominated one. Different EoSs might extend or delay the accretion phase due to different compressibilities and asymmetry energies or may provide a different composition. However, the electron-neutrino spectra will always stay either diffusion or accretion dominated, determined only by the progenitor model. In this sense, the progenitor model has a non-negligible influence on the emitted neutrino spectra. This is in contradiction to the recently published work by Sumiyoshi et al. (2008). They investigated different progenitor models with similar mass accretion rates and thus find the progenitor dependency less relevant for the emitted neutrino signal. We would like to point out that the emitted neutrino signal contains correlated information about the EoS, the progenitor star and the neutrino physics. If analysing the neutrino luminosities, one has to take all these dependencies into account.

Finally, three-dimensional core collapse models have to make use of some form of neutrino transport approximation scheme due to present computational limitations. For that reason, we introduced an electron-neutrino luminosity approximation which can be applied to any progenitor model and for large distances, typically from a few 100 km to the remaining physical domain of the progenitor. This approximation depends only on the mass accretion rate, given by the progenitor model, and the temperature at the electron-neutrinosphere. We compared this approximation with accurate three-flavour Boltzmann neutrino transport calculations for several different massive progenitor models and find qualitatively good agreement.

In addition to the electron-flavour neutrino spectra, the (μ/τ)-neutrinos are analysed in the full Boltzmann model and their importance with respect to cooling at the (μ/τ)-neutrinosphere is explored. We compared different (μ/τ)-neutrino pair reactions separately and during the accretion phase of failed core collapse supernova explosions of massive progenitors. A large (μ/τ)-neutrino luminosity corresponds to a large cooling rate and consequently supports a more compact PNS as well as a shorter PNS accretion phase of the order of a few milliseconds. In addition, the connection between the drastic (μ/τ)-neutrino luminosity increase during the accretion phase and the PNS contraction has been investigated. We find that the changing thermodynamic conditions (especially the increasing temperature) at the (μ/τ)-neutrinosphere establish β-equilibrium at a larger value of the electron fraction, which leads to an increase of the (μ/τ)-neutrino pair reaction rate. This increases the (μ/τ)-neutrino luminosity from regions with low and intermediate densities. Additionally, following Horowitz (2002), an update of the standard neutrino emissivities and opacities has been investigated, using the example of a failed core collapse supernova of a massive 40 $M_\odot$ progenitor.

This analysis has been published recently in Fischer et al. (2009a) and addresses a

deeper understanding of the origin and the dependencies of the emitted neutrino signal of all three-flavours, examined using failed core collapse supernova explosions of massive stars and the formation of solar mass black holes.

Strange quark matter in core collapse supernovae

The properties of the internal nucleon substructures are well understood from deep-inelastic lepton-nucleon scattering experiments and are known as quarks. The nucleon is composed of two quark flavours, up- and down-quarks. The additional quark flavours strange, bottom, top and charm are known today. The description of quark matter properties based on quantumchromodynamics (QCD) is difficult and by the present standard knowledge limited to describe the phase diagram. One of the most studied subjects in QCD is the transition from hadronic matter to quark matter and the related thermodynamic state given by temperature, baryon chemical potential (or equivalent density) and iso-spin asymmetry energy. However, confinement which allows for the interpretation of the bound state of quarks as hadrons cannot be provided by QCD calculations at present. The current models are either of phenomenological nature, such as e.g. MIT bag, NJL, PNJL, or have to relay on numerical solutions of the QCD equations in a discrete from on a lattice, which are computationally extremely expensive to obtain. Several models predict a smooth transition from hadronic matter to quark matter at high temperatures ~ 100 MeV and low baryon densities, defining so called critical point(s) in the phase diagram. However, the behaviour of the phase boundary between the hadronic and quark phases at finite and even large baryon densities is uncertain. Based on the MIT bag model, our collaborators Sagert et al. (2009b) constructed an EoS for strange quark matter and replaced and extended the hadronic EoS from Shen et al. (1998a) at high baryon densities and temperatures where appropriate. A smooth transition between these two phases is modelled following the Gibbs construction which results in an extended quark-hadron mixed phase. This approach is not unique and turns out to be very powerful and extremely useful in developing EoSs for astrophysical applications where matter properties change according to a phase transition. The behaviour of the critical density, which defines the quark-hadron phase boundary, in the phase diagram depends not only on the temperature but also on the iso-spin asymmetry which in turn is given by the electron fraction. Based on the MIT bag model, it has been demonstrated that high temperatures and a low electron fraction favour a lower critical density. Note that this behaviour of the critical density might change if different nuclear models are used for the description quark matter. However, Sagert et al. (2009b) constructed two combined hadron-quark EoSs where the free parameter (based on the MIT bag model for quark matter) is the bag constant, which determines the confinement and in this sense the temperature and electron fraction dependent critical density in the phase diagram. Since the EoS is meant to be applied to astrophysical

applications, certain constraints on the bag constant must be fulfilled. Observations of isolated (or in a binary system) neutron star (NS) mass measurements indicate maximum NS masses above 1.44 $M_\odot$ (Hulse-Taylor pulsar Lattimer and Prakash (2004)), which determines a lower limit of the bag constant. Note, that NS matter is given at $(T = 0, Y_e = 0)$. In addition, nuclear physics excludes the existence of absolutely stable strange quark matter. The EoSs must also not violate heavy ion collision experiments, where the situation differs because matter is iso-spin symmetric (i.e. $Y_e \simeq 0.5$) and matter is composed of up- and down-quarks only because the timescales are too short to produce strangeness. The two values for the bag constant chosen, i.e. $B^{1/4} = 162$ MeV and $B^{1/4} = 162$ MeV, give stable NSs with maximum baryon masses of 1.56 $M_\odot$ and 1.50 $M_\odot$ respectively. Since top-, bottom-, and charm-quarks have large rest masses, only strange quarks are taken into account next to the mass-less considered up- and down-quarks. A strange quark mass of 100 MeV is assumed, in accordance with the Particle Data Group and Eidelman (2004).

The two resulting EoSs have been implemented into our spherically symmetric core collapse model. With this approach, we assume that general relativistic effects on both fluid dynamics and neutrino radiation transport are more important than the development of fluid instabilities and multi-dimensional effects. In fact, this turns out to be the case. The domain above or near nuclear saturation density and high temperatures, where the QCD phase transition takes place, lays inside the deep gravitational potential of the central PNS where the lapse function is found to be $\alpha << 1$ and strong general relativistic effects can be observed. The simulations are launched from low and intermediate mass Fe-core progenitors in the range of 10.8 to 15 $M_\odot$, and are carried out through the core collapse, bounce and postbounce phases. The thermodynamic state at core bounce already produces free quarks. In terms of mass fractions, about 10% quarks are produced. In this sense, no phase transition has taken place at core bounce only a softening of the EoS due to the appearance of the quark-hadron mixed phase. During the early post-bounce shock expansion, this small fraction of quarks reduces again due to the slight density and temperature decrease. Only when the expanding shock turns into the SAS (due to neutrino losses and the dissociation of heavy nuclei) and hence the central density and temperature increase as well as the electron fraction decreases, the quark fraction rises on a timescale of 100 ms (corresponding to the PNS contraction timescale due to mass accretion). Since the adiabatic index reduces for matter in the mixed phase, the EoS is much softer. As a certain fraction of the PNS (typically $\simeq 0.7$ $M_\odot$) is in the mixed phase where more than 50% of quarks are produced, nuclear forces and pressure fail to keep the PNS stable against gravity and the PNS starts to contract. The contraction proceeds into a collapse which halts as matter reaches the pure quark phase where the EoS stiffens. A second accretion shock forms at the phase boundary between the mixed and infalling hadronic phases. This second shock accelerates to positive velocities of the order 1.5×10^5 km/s (= 50% the vacuum speed of light!) as it propagates outwards along the decreasing density gradient at the

PNS surface. The second shock overtakes the first SAS which remains unaffected at about 80 km by the happenings inside the central PNS. A new explosion mechanism for low and intermediate mass progenitor stars was discovered, which leads to explosions even in spherical symmetry where moderate explosion energies of 1×10^{51} erg could be obtained.

The question about the detectability and hence observational indications of the QCD phase transition remains to be answered. The primary goal of the initial investigation was to find evidence in the emitted neutrino signal from the QCD phase transition. Our first estimate was motivated by the densities above nuclear saturation where the QCD phase transition occurs, which means the neutrinos are fully trapped and their transport to lower densities is given by diffusion only on a timescale of seconds. However, the presence of a dynamic shock as a direct consequence of the phase transition changes everything. As soon as this shock propagates across the neutrinospheres, where neutrinos decouple from matter, additional neutrino-matter interactions emit a large number of neutrinos due to shock heating and the changed β-equilibrium. These neutrinos escape and become observable in the neutrino spectrum as an additional burst of neutrinos, accompanied by a significant increase in the mean neutrino energies. The first neutrino burst from the Fe-core bounce is a deleptonisation burst and only due to electron-neutrinos emitted via additional electron captures. The second neutrino burst is dominated by electron-antineutrinos and (μ/τ)-neutrinos due to the reduced degeneracy and hence increased number of charges. The burst has a width of about $5 - 20$ ms and can be observed at present neutrino detector facility such as Super-Kamiokande and SNO for a future Galactic event (see therefore the analysis from Dasgupta et al. (2009)). The delay of the second neutrino burst with respect to the first one provides correlated information about the thermodynamic state of the critical density for the onset of the phase transition, the EoS for hadronic matter and the progenitor model. Additional observations, e.g. gravitational waves, remnant properties and the composition of the ejecta, can be considered to sharpen the constraints on the involved nuclear physics. This way of back-tracing engineering science is a powerful technique and may provide, in addition to experimental evidence from detector facilities such as the LHC, RHIC and FAIR at the GSI, incontrovertible constraints on the nuclear physics.

Bibliography

Arcones, A.; Janka, H.-T. and Scheck, L. 2007, Nucleosynthesis-relevant conditions in neutrino-driven supernova outflows. I. Spherically symmetric hydrodynamic simulations, *A&A*, 467, 1227

Audi, G.; Wapstra, A. H. and Thibault, C. 2003, The Ame2003 atomic mass evaluation (II). Tables, graphs and references, *Nuclear Physics A*, 729, 337

Baumgarte, T. W.; Shapiro, S. L. and Teukolsky, S. A. 1996, Computing the Delayed Collapse of Hot Neutron Stars to Black Holes, *ApJ*, 458, 680

Beacom, J. F.; Boyd, R. N. and Mezzacappa, A. 2001, Black hole formation in core-collapse supernovae and time-of-flight measurements of the neutrino masses *PRD*, 63 (7), 073011

Bethe, H. A. and Wilson, J. R. 1985 Revival of a stalled supernova shock by neutrino heating, *ApJ*, 295, 14

Bionta, R. M.; Blewitt, G.; Bratton, C. B.; Caspere, D. and Ciocio, A. 1987, *Phys. Rev. Lett.*, 58, 1494,

Bisnovatyi-Kogan, G. S. 1971 The Explosion of a Rotating Star As a Supernova Mechanism, *Soviet Astronomy*, 14, 652

Bruenn, S. W. 1985 Stellar core collapse - Numerical model and infall epoch, *ApJS*, 58, 771

Bruenn, S.W.; Dirk, C. J.; Mezzacappa, A.; Hayes, J. C.; Blondin, J. M.; Hix, W. R. and Messer, O. E. B. 2006 Modeling core collapse supernovae in 2 and 3 dimensions with spectral neutrino transport, *Journal of Physics Conference Series*, 46, 393

Buras, R.; Janka, H.-T.; Keil, M. T.; Raffelt, G. G. and Rampp, M. 2003 Electron Neutrino Pair Annihilation: A New Source for Muon and Tau Neutrinos in Supernovae, *ApJ*, 587, 320

Burrows, A.; Hayes, J. and Fryxell, B. A. 1995, On the Nature of Core-Collapse Supernova Explosions, *ApJ*, 450, 830

Burrows, A.; Livne, E.; Dessart, L.; Ott, C. D. and Murphy, J. 2006, An acoustic mechanism for core-collapse supernova explosions, *New Astronomy Review*, 50, 487

Castor, J. I. 1972, Radiative Transfer in Spherically Symmetric F, *ApJ*, 178, 779

Dasgupta, B.; Fischer, T.; Horiuchi, S.; Liebendörfer, M.; Mirizzi, A.; Sagert, I. and Schaffner-Bielich, J. 2009, Detecting the QCD phase transition in the next Galactic supernova neutrino burst *Phys. Rev. Lett.* submitted, (astro-ph/0912.2568)

Dicus, D. A. 1972 Stellar Energy-Loss Rates in a Convergent Theory of Weak and Electromagnetic Interactions, *PRD*, 6, 941

Duncan, R. C.; Shapiro, S. L. and Wasserman, I. 1986, Neutrino-driven winds from young, hot neutron stars, *ApJ*, 309, 141

Durand, D.; Surand, E. and Tamain, B. 2000, Nuclear Dynamics in the Nucleonic Regime Series in Fundamental and Applied Nuclear Physics

Fischer, T.; Liebendörfer, M. and Mezzacappa, A. 2007, *Journal of Physics Conference Series*, 66, 2043

Fischer, T.; Whitehouse, S. C.; Mezzacappa, A.; Thielemann, F.-K. and Liebendörfer, M. 2009a, The neutrino signal from protoneutron star accretion and black hole formation, *A&A*, 499, 1

Fischer, T.; Whitehouse, S. C.; Mezzacappa, A.; Thielemann, F.-K. and Liebendörfer, M. 2009b, Protoneutron star evolution and the neutrino driven wind in general relativistic neutrino radiation hydrodynamics simulations, *ArXiv e-print*, 0908.1871,

Fuller, G. M.; Fowler, W. A. and Newman, M. J. 1982, Stellar weak interaction rates for intermediate mass nuclei. III - Rate tables for the free nucleons and nuclei with A = 21 to A = 60, *ApJS*, 48, 279

Fröhlich, C.; Hauser, P.; Liebendörfer, M.; Martínez-Pinedo, G.; Thielemann, F.-K.; Bravo, E.; Zinner, N. T.; Hix, W. R.; Langanke, K.; Mezzacappa, A. and Nomoto; K. 2006a, *ApJ*, 637, 415

Fröhlich, C.; Hix, W. R.; Martínez-Pinedo, G.; Liebendörfer, M.; Thielemann, F.-K.; Bravo, E.; Langanke, K. and Zinner, N. T. 2006b, *New Astronomy Review*, 50, 496

Fröhlich, C.; Martínez-Pinedo, G.; Liebendörfer, M.; Thielemann, F.-K.; Bravo, E.; Hix, W.-R.; Langanke, K. and Zinner, N. T. 2006c, *Physical Review Letters*, 96 (14), 142502

Gentile, N. A.; Aufderheide, M. B.; Mathews, G. J.; Swesty, F. D. and Fuller, G. M. 1993, The QCD phase transition and supernova core collapse, *ApJ*, 414, 701

Gögelein, P. 2007, Private communications,

Goldreich, P. and Weber, S. V. 1980, Homologously collapsing stellar cores, *ApJ*, 238, 991

Greiner, W. and Müller, B. 1986, Eichtheorie der schwachen Wechselwirkung, Theoretische Physik Band 8.

Greiner, W. and Schäfer, A. 1989, Quantenchromodynamik, Theoretische Physik Band 10,

Hannestad, S. and Madsen, J. 1995, *PRD*, 52, 1764

Hannestad, S. and Raffelt, G. 1998, Supernova Neutrino Opacity from Nucleon-Nucleon Bremsstrahlung and Related Processes, *ApJ*, 507, 339

Heger, A. and Woosley, S. E. 2002, *ApJ*, 567, 532

Henderson, J. A. and Page, D. 2007, *APSS*, 308, 513

Herant, M.; Benz, W.; Hix, W. R.; Fryer, C. L. and Colgate, S. A. 1994, Inside the supernova: A powerful convective engine, *ApJ*, 435, 339,

Hirata, K. S.; Kajita, T.; Koshiba, M.; Nakahata, M.; Oyama, Y.; Sato, N.; Suzuki, A.; Takita, M.; Totsuka, Y.; Kifune, T.; Suda, T.; Takahashi, K.; Tanimori, T.; Miyano, K.; Yamada, M.; Beier, E. W.; Feldscher, L. R.; Frati, W.; Kim, S. B.; Mann, A. K.; Newcomer, F. M.; van Berg, R.; Zhang, W. and Cortez, B. G. 1988, *PRD*, 38, 448

Hirschi, R. 2007, Very low-metallicity massive stars:. Pre-SN evolution models and primary nitrogen production, *A&A*, 461, 571

Hix, W. R.; Messer, O. E. B.; Mezzacappa, A.; Liebendörfer, M.; Sampaio, J.; Langanke, K.; Dean, D. J. and Martínez-Pinedo, G. 2003, Consequences of Nuclear Electron Capture in Core Collapse Supernovae, *Physical Review Letters*, 91(20), 201102

Hoffman, R. D.; Pruet, J.; Fisker, J. L.; Janka, H.-T.; Burras, R. and Woosley, S. E. 2007, *ArXiv e-prints* 0712.2847

Hoffman, R. D.; Woosley, S. E. and Qian, Y. Z. 1997, Nucleosynthesis in Neutrino-driven Winds. II. Implications for Heavy Element Synthesis, *ApJ*, 482, 951

Horowitz, C. J. 2002, Weak magnetism for antineutrinos in supernovae, *PRD*, 65(4), 043001

Itoh, N.; Asahara, R.; Tomizawa, N.; Wanajo, S. and Nozawa, S. 2004, Ion-Ion Correlation Effect on the Neutrino-Nucleus Scattering in Supernova Cores, *ApJ*, 611, 1041

Janka, H.-T. 2001, Conditions for shock revival by neutrino heating in core-collapse supernovae, *A&A*, 368, 527

Janka, H.-T.; Marek, A.; Müller, B. and Scheck, L. 2008, Supernova Explosions and the Birth of Neutron Stars, In C. Bassa, Z. Wang, A. Cumming, and V. M. Kaspi, editors, *40 Years of Pulsars: Millisecond Pulsars, Magnetars and More*, volume 983 of *American Institute of Physics Conference Series*, 369

Janka, H.-T. and Mueller, E. 1995, The First Second of a Type II Supernova: Convection, Accretion, and Shock Propagation, *ApJL*, 448, L109

Janka, h.-T. and Mueller, E. 1996, Neutrino heating, convection, and the mechanism of Type-II supernova explosions, *A&A*, 306, 167

Kitaura, F. S.; Janka, H.-T. and Hillebrandt, W. 2006, Explosions of O-Ne-Mg cores, the Crab supernova, and subluminous type II-P supernovae, *A&A*, 450, 345

Langanke, K.; Martínez-Pinedo, G.; Sampaio, L. M.; Dean, D. J.; Hix, W. R.; Messer, O. E. B.; Mezzacappa, A.; Liebendörfer, M.; Janka, H.-T. and Rampp, M. 2003, Electron Capture Rates on Nuclei and Implications for Stellar Core Collapse, *Physical Review Letters*, 90(24), 241102

Lattimer, J. M. and Prakash, M. 2004, The Physics of Neutron Stars, *Science*, 304, 536

Lattimer, J. M. and Swesty, D. F. 1991, A generalized equation of state for hot, dense matter, *Nuclear Physics A*, 535, 331

LeBlanc, J. M. and Wilson, J. R. 1970, A Numerical Example of the Collapse of a Rotating Magnetized Star, *ApJ*, 161, 541

Liebendörfer, M.; Mezzacappa, A.; Thielemann, F.-K.; Messer, O. E. B.; Hix, W. R. and Bruenn, S. W. 2001a, Probing the gravitational well: No supernova explosion in spherical symmetry with general relativistic Boltzmann neutrino transport, *PRD*, 63(10), 103004

Liebendörfer, M.; Mezzacappa, A.; Thielemann, F.-K.; Messer, O. E. B.; Hix, W. R. and Bruenn, S. W. 2001b, Conservative general relativistic radiation hydrodynamics in spherical symmetry and comoving coordinates, *PRD*, 63(10), 104003

Liebendörfer, M.; Rosswog, S. and Thielemann, F.-K. 2002, An Adaptive Grid, Implicit Code for Spherically Symmetric, General Relativistic Hydrodynamics in Comoving Coordinates, *ApJS*, 141, 229

Liebendörfer, M.; Mezzacappa, A.; Messer, O. E. B.; Martinez-Pinedo, G.; Hix, W. R. and Thielemann, F.-K. 2003, The neutrino signal in stellar core collapse and post-bounce evolution, *Nuclear Physics A*, 719, 144

Liebendörfer, M. 2004, *eprint*, astro-ph/0405029

Liebendörfer, M. 2004, Fifty-Nine Reasons for a Supernova to not Explode, *ArXiv Astrophysics e-prints* 0405029

Liebendörfer, M.; Messer, O. E. B.; Mezzacappa, A.; Bruenn, S. W.; Cardall, C. Y. and Thielemann, F.-K. 2004, A Finite Difference Representation of Neutrino Radiation Hydrodynamics in Spherically Symmetric General Relativistic Spacetime, *ApJS*, 150, 263

Liebendörfer, M. 2005, A Simple Parameterization of the Consequences of Deleptonization for Simulations of Stellar Core Collapse, *ApJ*, 633, 1042

Liebendörfer, M.; Rampp, M.; Janka, H.-T. and Mezzacappa, A. 2005, Supernova Simulations with Boltzmann Neutrino Transport: A Comparison of Methods, *ApJ*, 620, 840

Liebendörfer, M.; Whitehouse, S. C. and Fischer, T. 2009, The Isotropic Diffusion Source Approximation for Supernova Neutrino Transport, *ApJ*, 698, 1174

Lindquist, R. W. 1966, Relativistic transport theory, *Annals of Physics*, 37, 487

Marek, A. and Janka, H.-T. 2009, Delayed Neutrino-Driven Supernova Explosions Aided by the Standing Accretion-Shock Instability, *ApJ* 694, 664

Marek, A.; Janka, H.-T. and Müller, E. 2009, Equation-of-state dependent features in shock-oscillation modulated neutrino and gravitational-wave signals from supernovae, *A&A*, 496, 475

May, M. M. and White, R. H. 1966, Hydrodynamic Calculations of General-Relativistic Collapse, *Physical Review*, 141, 1232

Mayle, R. and Wilson, J. R. 1988, *ApJ*, 334, 909

Messer, O. B. E. 2000, Ph.D. thesis,

Messer, O. B. E. and Bruenn, S. W. 2003, private communications

Mezzacappa, A. and Bruenn, S. W. 1993a, A numerical method for solving the neutrino Boltzmann equation coupled to spherically symmetric stellar core collapse, *ApJ*, 405, 669

Mezzacappa, A. and Bruenn, S. W. 1993b, Type II supernovae and Boltzmann neutrino transport - The infall phase, *ApJ*, 405, 637

Mezzacappa, A. and Bruenn, S. W. 1993c, Stellar core collapse - A Boltzmann treatment of neutrino-electron scattering, *ApJ*, 410, 740

Miller, D. S.; Wilson, J. R. and Mayle, R. W. 1993, Convection above the neutrinosphere in Type II supernovae, *ApJ*, 415, 278

Misner, C. W. and Sharp, D. H. 1964, Relativistic Equations for Adiabatic, Spherically Symmetric Gravitational Collapse, *Physical Review*, 136, 571

Nakazato, K.; Sumiyoshi, K. and Yamada,S. 2008, Astrophysical implications of equation of state for hadron-quark mixed phase: Compact stars and stellar collapses, *PRD*, 77(10), 103006

Nomoto, K. 1983, Presupernova evolution of 8-12 solar mass stars and the Crab Nebula's progenitor, Supernova Remnants and their X-ray Emission, *IAU Symposium*, 101, 139

Nomoto, K. 1984, Evolution of 8-10 solar mass stars toward electron capture supernovae. I - Formation of electron-degenerate O+NE+MG cores, *ApJ*, 277, 791

Nomoto, K. 1987, Evolution of 8-10 solar mass stars toward electron capture supernovae. II - Collapse of an O+NE+MG core *ApJ*, 322, 206

Nomoto, K. and Hashimoto, M. 1988, Presupernova evolution of massive stars, *Phys. Rev.*, 163, 13

Otsuki, K.; Tagoshi, H.; Kajino, T. and Wanajo, S. Y. 2000, General Relativistic Effects on Neutrino-driven Winds from Young, Hot Neutron Stars and r-Process Nucleosynthesis, *ApJ*, 533, 424

Panov, I. V. and Janka, H.-T. 2009, *A&A*, 494, 829

Particle Data Group and S. et al. Eidelman 2004, Gauge Higgs boson summary table, *Physics Letters B*, 592, 31

Qian, Y. Z.; Fuller, G. M.; Mathews, G. J.; Mayle, R. W.; Wilson, J. R. and Woosley, S. E. 1993, Connection between flavor mixing of cosmologically significant neutrinos and heavy element nucleosynthesis in supernovae, *Physical Review Letters*, 71, 1965

Qian, Y. Z. and Woosley, S. E. 1996, Nucleosynthesis in Neutrino-driven Winds. I. The Physical Conditions, *ApJ*, 471, 331

Sagert, I.; Fischer, T.; Hempel, M.; Pagliara, G.; Schaffner-Bielich, J.; Mezzacappa, A.; Thielemann, F.-K. and Liebendörfer, M. 2009a, Signals of the QCD Phase Transition in Core-Collapse Supernovae, *Physical Review Letters*, 102(8), 081101

Sagert, I; Hempel, M.; Pagliara, G. and Schaffner-Bielich, J. 2009b, *Private communications*

Scheck, L.; Kifondis, K.; Janka, H.-T. and Müller, E. 2006, Multidimensional supernova simulations with approximative neutrino transport. I. Neutron star kicks and the anisotropy of neutrino-driven explosions in two spatial dimensions, *A&A*, 457, 963

Schinder, P. J. and Shapiro, S. L. 1982, Neutrino emission from a hot, dense, plane-parallel atmosphere in hydrostatic equilibrium. II - Numerical methods and interaction functions, *ApJS*, 50, 23

Shen, H.; Toki, H.; Oyamatsu, K. and Sumiyoshi, K. 1998a, Relativistic equation of state of nuclear matter for supernova and neutron star, *Nuclear Physics A*, 637, 435

Shen, H.; Toki, H.; Oyamatsu, K. and Sumiyoshi, K. 1998b, Relativistic equation of state of nuclear matter for supernova and neutron star, *Progress of Theoretical Physics*, 100, 1013

Stephani, H.; Kramer, D.; MacCallum, M.; Hoenselaers, C. and Herlt, E. 2003, Exact solutions of Einstein's field equations,

Sumiyoshi, K.; Yamada, S. and Suzuki, H. 2007, Dynamics and Neutrino Signal of Black Hole Formation in Nonrotating Failed Supernovae. I. Equation of State Dependence, *ApJ*, 667, 382

Sumiyoshi, K.; Yamada, S. and Suzuki, H. 2008, Dynamics and Neutrino Signal of Black Hole Formation in Nonrotating Failed Supernovae. II. Progenitor Dependence, *ApJ*, 688, 1176

Takahara, M. and Sato, K. 1988, *Progress of Theoretical Physics*, 80, 861,

Takahashi, K.; Witti, J. and Janka, H.-T. 1994, Nucleosynthesis in neutrino-driven winds from protoneutron stars II. The r-process, *ApJ*, 286, 857

Thielemann, F.-K. Physik in Sternen I+II, *lecture notes in theoretical physics*,

Thielemann, F.-K.; Brachwitz, F.; Höflich, P.; Martinez-Pinedo, G. and Nomoto, K. 2004, *New Astronomy Review*, 48, 605

Thompson, T. A. and Burrows, A. 2001, Neutrino processes in supernovae and the physics of protoneutron star winds, *Nuclear Physics A*, 688, 377

Thompson, T. A.; Burrows, A. and Meyer, B. S.2001, The Physics of Proto-Neutron Star Winds: Implications for r-Process Nucleosynthesis, *ApJ*, 562, 887

Timmes, F. X. and Arnett, D. 1999, The Accuracy, Consistency, and Speed of Five Equations of State for Stellar Hydrodynamics, *ApJS*, 125, 277

Timmes, F. X. and Swesty, F. D. 2000, The Accuracy, Consistency, and Speed of an Electron-Positron Equation of State Based on Table Interpolation of the Helmholtz Free Energy, *ApJS*, 126, 501

Tominaga, N.; Umeda, H. and Nomoto, K. 2007, Supernova Nucleosynthesis in Population III 13-50 $M_\odot$ Stars and Abundance Patterns of Extremely Metal-poor Stars, *ApJ*, 660, 516

Tubbs, D. L. and Schramm, D. N. 1975, Neutrino Opacities at High Temperatures and Densities, *ApJ*, 201, 467

Tubbs, D.L. 1978, Direct-simulation neutrino transport - Aspects of equilibration, *ApJS*, 37, 287.

Umeda, H. and Nomoto, K. 2005, Variations in the Abundance Pattern of Extremely Metal-Poor Stars and Nucleosynthesis in Population III Supernovae, *ApJ*, 619, 427

Umeda, H. and Nomoto, K. 2008, How Much ^{56}Ni Can Be Produced in Core-Collapse Supernovae? Evolution and Explosions of 30-100 $M_\odot$ Stars, *ApJ*, 673, 1014

Wanajo, S. 2006a, The r-Process in Proto-Neutron Star Winds with Anisotropic Neutrino Emission, *ApJL*, 650, L79

Wanajo, S. 2006b, The rp-Process in Neutrino-driven Winds, *ApJ*, 647, 1323

Whitehouse, S. C. and Liebendörfer, M. 2010, Three-dimensional models of core-collapse supernovae with spectral neutrino transport, *in preparation*

Wilson, J. R. and Mayle,W. R. 1993, *Phys. Rep.*, 227, 97

Witti, J.; Janka, H.-T. and Takahashi, K. 1994, Nucleosynthesis in neutrino-driven winds from protoneutron stars I. The α-process, *A&A*, 286, 841

Woosley, S. E. and Baron, E. 1992, The collapse of white dwarfs to neutron stars, *ApJ*, 391, 228

Woosley, S. E. and Weaver, T. A. 1995, The Evolution and Explosion of Massive Stars. II. Explosive Hydrodynamics and Nucleosynthesis, *ApJS*, 101, 181

Woosley, S. E.; Wilson, J. R.; Mathews, G. J.; Hoffman, R. D. and Meyer, B. S. 1994, *ApJ*, 433, 229

Woosley, S. E.; Heger, A. and Weaver, T. A. 2002, The evolution and explosion of massive stars, *Reviews of Modern Physics*, 74, 1015

Yamada, S.; Janka, H.-T. and Suzuki, H. 1999, Neutrino transport in type II supernovae: Boltzmann solver vs. Monte Carlo method, *A&A*, 344, 533

Yueh, W. R. and Buchler, J. R. 1976a, Neutrino processes in dense matter, *APSS*, 41, 221

Yueh, W. R. and Buchler, J. R. 1976b Scattering functions for neutrino transport, *APSS*, 39, 429

Yueh, W. R. and Buchler, J. R. 1977, Neutrino transport in supernova models - S_N method, *ApJ*, 217, 565

CURRICULUM VITAE

Tobias Fischer
Department of Physics, University of Basel
Klingelbergstrasse 82
CH-4056 Basel, Switzerland
Tel. +41 61 267 3740
email: tobias.fischer@unibas.ch
homepage: phys-merger.physik.unibas.ch/~tobias

Research interests

Core collapse supernovae and the explosion mechanism of massive stars, in particular:

1. Radiation hydrodynamics,

2. Neutrino interactions and neutrino transport,

3. The properties of matter below and above nuclear saturation density,

4. General relativity (gravitational waves, gravitational collapse, black hole formation)

Employment

Dates	Organisation and position held	Type of appointment
05.2010	The GSI, post doctoral fellow	stipend, full-time
11.2009 - 04.2010	University of Basel, post doctoral fellow	contract, full-time

Academic education

Dates	Department/University	Degree
10.2005 - 10.2009	Graduate student, Department of Physics, University of Basel, Switzerland	Ph. D. (**summa cum laude**), title: *Neutrino radiation hydrodynamics in hot and dense nuclear matter and the role of microphysics in simulations of massive stars*, (supervision: M. Liebendörfer, F.-K. Thielemann, J. Schaffner-Bielich)
10.2004 - 03.2006	Master student, Royal Institute of Technology, Stockholm, Sweden	Master of Science in Quantum Physics, title: *The evolution of galactic nuclei under numerical N-body simulations* (supervision: B. Gustafsson, T. Ohlsson)
10.1998 - 11.2003	Undergraduate student, Faculty of Physics and Earth Science, University of Leipzig, Germany	Diploma of Physics, title: *Investigations of axisymmetric and stationary spacetime using algebraic-geometric methods* (supervision: O. Richter, G. Rudolph)

Schools and training programs

08. - 10.2007	Summer school at the ECT*, Doctoral training program "PHYSICS OF COMPACT STARS"; Trento, Italy
11.2005 - 04.2010	Member of the European Graduate School Basel-Tübingen-Graz "HADRONS IN VACUUM, IN NUCLEI AND STARS"

Collaborations

1. J. Schaffner-Bielich, University of Heidelberg (Germany)
   "Quark matter in supernovae I - explosions of massive stars"

2. D. Blaschke, University of Wroclaw (Poland),
   "Quark matter in supernovae II - long term protoneutron star evolution"

3. D. Page, University of Mexico City (Mexico),
   "A consistent description of protoneutron star cooling"

4. R. Hirschi, Keele University (UK)
   "New progenitor models for core collapse supernova investigations"

Teaching experience

Teaching assistance	Theoretical Physics courses (Classical Mechanics, Electrodynamics, Special Relativity, Thermodynamics and Statistical Physics)	University of Basel, 2005 - 2009
	Special courses (Computational Astrophysics, Waves and Mixing in Astrophysical Plasma)	University of Basel, 2005 - 2009
Temporary lecturing	Classical Mechanics, Electrodynamics, General Relativity	University of Basel, 2005 - 2009

Programming skills [1]

FORTRAN	fluent (scientific computing, parallel programming experience: OpenMP)
MATLAB	fluent (data analyzing and visualization)
MATHEMATICA	fluent (data analyzing and visualization)
LATEX	fluent
PERL	beginner

---

[1]Familiar operating systems: LINUX (Ubuntu, SuSe, ManDrake), MICROSOFT WINDOWS, MACINTOSH OS

Language experience

German (native)

English (fluent)

Swedish (beginner)

Russian (absolute beginner)

Conferences and Seminars

Invited talks

2010.03. **The neutrino driven wind in radiation hydrodynamics simulations based on Boltzmann neutrino transport**
The 10th. International Symposium on "Origin of Matter and Evolution of the Galaxies", RCNP Osaka University (Japan)

2009.10. **Quark matter in supernova explosions**
"Dense QCD Phases in HIC and Supernovae", HIC for FAIR Workshop, Prerow (Germany)

2009.04. **Core collapse supernova simulations in spherical symmetry: state of the art of present models**
The GSI, Theory Seminar, Darmstadt (Germany)

Conference talks

2009.05. **Exploring the QCD phase transition in core collapse supernova simulations**
Conference on "Compact stars in the QCD phase diagram II", KIAA, Peking University, Beijing (China)

2008.12. **Exploring the possibility of the QCD phase transition in core collapse supernovae**
Meeting of the Swiss Society of Astronomy and Astrophysics, Zuerich (Switzerland)

2008.07. **Exploring the possibility of a phase transition from Hadronic matter to quark matter in core collapse supernovae**
"The Physics of Neutron stars", St. Petersburg (Russia)

2008.02. **On the possible fate of massive progenitor stars**
Advanced School followed by a Workshop on "The Complex Physics of Compact Stars", Ladek Stroj (Poland)

2007.12. **The accretion phase of core collapse supernovae**
OMEG07, 10th International Symposium on "Origin of Matter and the Evolution of Galaxies", Hokkaido University, Sapporo (Japan)

2006.09. **The expected neutrino signal from the formation of black holes via protoneutron star collapse**
XXIX Spanish Relativity Meeting E.R.E., Majorca (Spain)

2006.03. **Neutrino-electron(positron) scattering in core collapse supernovae**
13th Workshop on Nuclear Astrophysics, Ringberg Castle, (Germany)

Posters

2008.07. **The Formation of the neutrino driven wind termination shock in 1D core collapse Supernovae using Boltzmann neutrino transport**
10th Symposium on Nuclei in the Cosmos Mackinac Island, Michigan (USA)

2007.01. **Supernova explosion models via 1D GR core collapse simulations with artificially enhanced absorption rates**
"Workshop on Neutrino Physics", University of Tokyo (Japan)